4 Results for Prehydrided Cladding Alloys

High-burnup operation results in cladding outer-surface corrosion (oxidation) and hydrogen pickup. Hydrogen can reduce significantly the ductile-to-brittle transition ECR, especially at high oxidation temperatures. Baseline data are needed on the effects of hydrogen on embrittlement. Such data are generated with non-irradiated cladding, which has been prehydrided prior to testing. As tests with non-irradiated cladding are much easier to conduct, a relatively large number of tests can be conducted to map out embrittlement as a function of hydrogen content, oxidation temperature, oxidation level (e.g., CP-ECR), and quench temperature. The data generated using prehydrided cladding samples help in both planning and interpreting the results of tests conducted with high-burnup cladding.

In this section, post-quench ductility data are presented for prehydrided Zry-4 cladding oxidized at 1200ºC and either slow cooled to RT or quenched at 800ºC, 700ºC, or 600ºC. The reference test conditions are the same as those for the as-fabricated alloys: oxidize 25-mm-long samples at 1200ºC to the desired CP-ECR level, cool at ≈11-13ºC/s from 1200ºC to 800ºC, rapidly cool (by means of bottom-flooding quench water flow) from 800ºC to 100ºC, slow cool from 100ºC to RT, section 8-mm-long rings sectioned from the oxidation sample, and compress the rings at 135ºC and 0.0333 mm/s.

4.1 Prehydrided Zircaloy-4 oxidized at 1200ºC and quenched at 800ºC

Two methods have been used to introduce hydrogen into Zry-4 segments. During the period of June – October 2004, prehydriding was performed at 400ºC in a closed quartz chamber (1.5-liter volume) with a gas mixture of 4% H_2 in argon at near ambient pressure. The 100-mm-long segments were wrapped in aluminum foil to prevent oxide film buildup while allowing hydrogen atoms to permeate to the surface of the Zry-4 sample. The exposure times used to introduce 200-600 wppm of hydrogen into the segment were 1500 to 4500 s. This simple procedure resulted in circumferential hydrides uniformly distributed through the wall of the Zry-4 segments (see Figure 103).

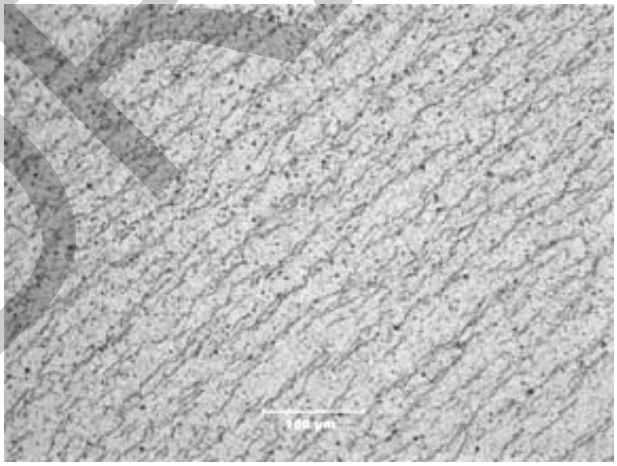

Figure 103. Uniform distribution of circumferential hydrides across the wall of HBR-type 15×15 Zry-4 prehydrided to 400 wppm H.

However, due to furnace temperature gradients and non-uniform cladding surface conditions, the hydrogen-concentration gradients in the axial and circumferential directions were significant. For a segment with a target hydrogen content of 500 wppm, the axial gradient was ≈4 wppm/mm, and the circumferential gradient varied from ≈0.6 to 6 wppm/mm for a 25-mm-long sample. The procedure for

homogenization of the hydrogen calls for heating the sample to 400ºC for ≤72 hours in an inert atmosphere with temperature cycling between 300 and 400 ºC. However, even high-purity argon contains trace impurities of oxygen, moisture, and nitrogen, which would result in the growth of surface oxide layers and possible nitrogen-contamination of these layers. As it was desirable to avoid surface modification during sample preparation for steam-oxidation tests, this homogenization step was not used for the LOCA test samples. In planning the oxidation tests for prehydrided cladding alloys, we assumed that homogenization of hydrogen would occur during the oxidation heating ramp.

Early test results indicated that the circumferential and axial gradients in hydrogen content remained after the oxidation tests conducted at 1200ºC. It has been demonstrated that redistribution of hydrogen across the wall of the cladding is very rapid as the wall is thin (0.57-0.77 mm), and the beta layer has a very high affinity for hydrogen. However, it was surprising to discover that no significant redistribution of hydrogen occurred in the longer axial direction (25 mm) or the circumferential direction (≈30 mm). Figure 104 shows the hydrogen distribution for a prehydrided HBR-type Zry-4 oxidation sample before and after oxidation-quench testing. Prior to oxidation, hydrogen levels were measured for 2-mm-long rings cut from both sides of a 30-mm-long sample. Following oxidation of the remaining 25-mm-long sample to 5% CP-ECR (92 s from beginning of ramp to the end of the 1200ºC hold time), hydrogen readings were obtained from the center of the oxidized sample and from the 8-mm-long rings used in the ring compression tests. These post-oxidation hydrogen measurements were corrected for weight gain for comparison to pretest values.

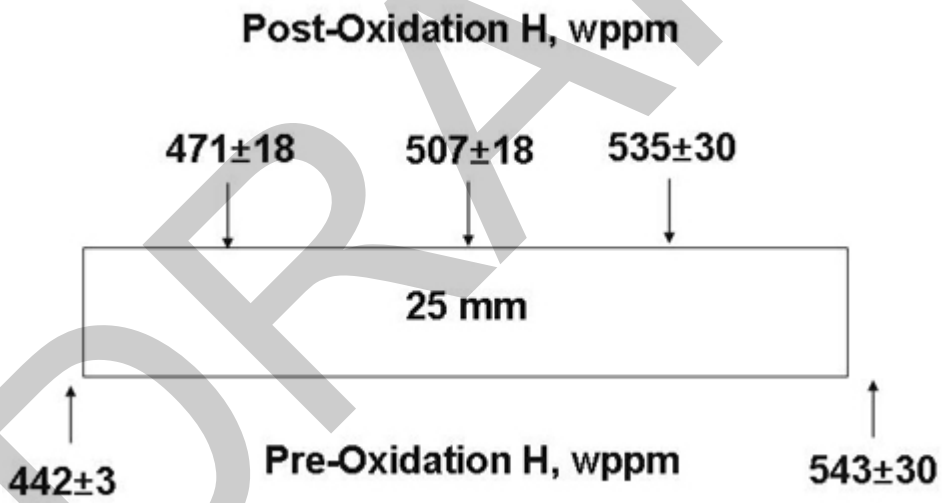

Figure 104. Hydrogen concentration in a prehydrided HBR-type 15×15 Zry-4 sample before and after oxidation at 1200ºC to 5% CP-ECR. Hydrogen contents after oxidation were corrected for sample weight gain to allow direct comparison with pre-test hydrogen contents.

The gradients following high-temperature oxidation were comparable to the pretest gradients, indicating that hydrogen did not homogenize under these test conditions. Although gradients in hydrogen concentration are not desirable for controlled studies, the relative immobility of the hydrogen allowed ANL to study the local effects of hydrogen concentration on post-quench ductility for samples oxidized to the same CP-ECR levels. The approach is reasonable even for samples with more uniform distribution of hydrogen. As prehydriding Zry-4 is more of an art than a science, prehydrided Zry-4 used in other

LOCA-relevant studies (e.g., CEA, JAEA) does have some axial gradient that leads to sample-to-sample variation in hydrogen for samples cut from the same prehydrided segment.

Modern 17×17 Zry-4 and HBR-type 15×15 Zry-4 segments were prehydrided by the closed-system method. Due to limited material availability, more 15×15 Zry-4 segments were prehydrided for oxidation tests. The baseline data generated for HBR-type 15×15 Zry-4 were used to plan the in-cell oxidation tests with high-burnup HBR cladding (see Section 5.1).

The improved and more recent method used for prehydriding cladding alloys utilizes a three-stage furnace for temperature control and flowing gas containing either 4% H_2 - 96% Ar mixture, 30% H_2 - 70% Ar mixture, or 100% H_2. Prehydriding was conducted at 350ºC with this furnace. Segments of HBR-type 15×15 Zry-4 were 50-to-100 mm long and prehydrided to 180-880 wppm. Because of the temperature uniformity in the new furnace, better homogenization of hydrogen was achieved in the axial and circumferential direction. It was difficult to control the final hydrogen content for segments prehydrided with 100% H_2, which was both flowing and at a slightly elevated pressure (0.1113 MPa absolute). Hydrogen uptake progressed very slowly for the first 4.5 hours of exposure, with hydrogen contents ranging from ≈70 wppm at 2-hours exposure to ≈180 wppm at 4.75-hours exposure. Within the test period of 5 to 8 hours, hydrogen uptake increased dramatically from 200 wppm to 900 wppm, but duplicate tests conducted for the same time-temperature history did not result in the same hydrogen contents (e.g., for a 7-hour hold time at 350ºC, one sample picked up 140 wppm while another sample picked up 730 wppm). Also, for >200-wppm-H pickup, a dense hydride rim formed on or near the inner surface of the cladding (see Figure 105), even though hydrogen flowed along both the inside and outside of the segment. As the HBR-type cladding inner surface had been pickled as a final fabrication step, this effect may explain why higher hydrogen pickup was observed at the inner surface. Several oxidation samples were prepared by this technique. The dense hydride rim near the inner-cladding surface was not considered to be an issue for oxidation tests because hydrogen redistribution across the wall of the cladding is expected to be rapid in the beta phase, and this phase has a high affinity for hydrogen. However, circumferential variation in hydride rim thickness led in some cases to circumferential variation in hydrogen content.

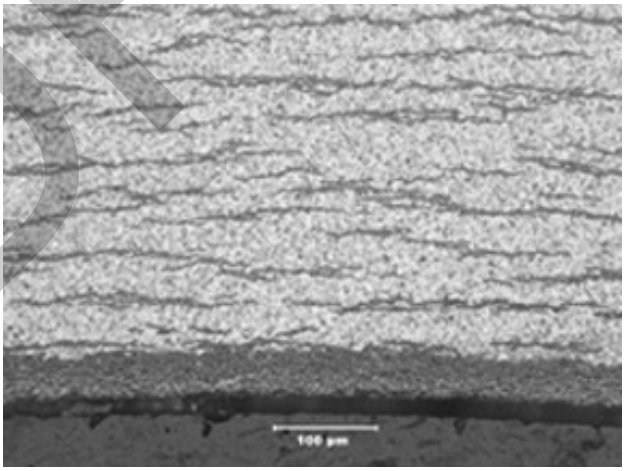

Figure. 105. Hydride morphology for prehydrided (435±50 wppm) HBR-type 15x15 Zry-4 showing the dense hydride rim (≈46 µm) at the cladding inner surface.

Better control was achieved by using the 4% H_2 - 96% Ar gas mixture at the same hold temperature (350ºC) and absolute pressure (0.1113 MPa). However, the segments had to be pre-wrapped in aluminum foil to reduce test time and to inhibit oxide buildup on the cladding segment surfaces. This process was used to generate prehydrided HBR-type Zry-4 samples for post-quench ductility studies.

4.1.1 Post-quench ductility of prehydrided 17×17 Zry-4 oxidized at 1200ºC

The ANL tests with prehydrided 17×17 Zry-4 samples were conducted during June-October 2004 with samples prepared by the old prehydriding method. Because of ANL's limited supply of 17×17 Zry-4 and the old oxidation test train used, the results should be used more for scoping purposes to determine ranges of hydrogen contents and CP-ECR levels for which post-quench ductility was retained. There were indications from foreign partners that hydrogen contents of 300-600 wppm were enough to completely embrittle Zry-4 after exposures to 1200ºC for test times <60 s and CP-ECR levels <5%. These test results were later published by Mardon et al. [21]. The results were generated by an approach using very rapid heating to 1200ºC, oxidation at 1200ºC for various hold times, and direct quench at 1200ºC. Thus, it was important to conduct companion tests with the ANL test protocol (slow ramp from about 1150ºC to 1200ºC, hold at 1200ºC for various test times, cool at ≈13ºC/s, quench at 800ºC, slow cool from 100ºC to RT, and ring-compress at 135ºC). Because of the axial gradients in the ANL prehydrided samples, the approach used was to study the effects of hydrogen on embrittlement at two target CP-ECR values: 7.5% and 10%. The thermal history for the test train used for oxidation is given in Figure 20. However, because so many tests had been conducted with this test train, it was re-benchmarked during the testing of the prehydrided 17×17 Zry-4 samples.

Table 46 summarizes the post-quench ductility results for prehydrided 17×17 Zry-4 oxidized at 1200ºC to target CP-ECR levels of 7.5% and 10%. Test times were selected based on the thermal history in Figure 20. Calculated CP-ECR levels were later corrected based on the thermal re-benchmarking for the old test train. The hydrogen contents listed in Table 46 were determined from 2-mm-long rings cut from prehydrided segments prior to oxidation and post-oxidation samples cut before and after ring-compression testing. For the post-oxidation hydrogen readings, the hydrogen concentration was corrected for weight gain to reference the hydrogen content to the pre-oxidized sample weight. The nominal CP-ECR values used for plotting trend curves are 7.5% and 10%. The lower CP-ECR values for the prehydrided samples are 7.5-7.6%. The 7.8% CP-ECR for the as-fabricated sample (no prehydriding) is not significantly different from 7.5% because the ductility is so high. The higher CP-ECR values for the prehydrided samples are 9.4-10.1% and 10.8% for the as-fabricated sample (no prehydriding). Given the sparse data set, the variable hydrogen content along the samples, and the condition of the test train used, the CP-ECR groupings are reasonable.

The offset strain data and the trend curves are plotted in Figure 106. At 7.5% CP-ECR, the ductile-to-brittle transition occurs between 314-wppm and 412-wppm hydrogen. The ductile-to-brittle transition is interpolated to occur at 375±25 wppm for 7.5% CP-ECR oxidation level. At 10% CP-ECR, Zry-4 is ductile at 274-wppm H and brittle at 335-wppm H. The ductile-to-brittle transition is interpolated to occur at 300±25 wppm H for 10% CP-ECR oxidation level. These results are not inconsistent with the results presented by Mardon et al. [21]. The hydrogen content for their samples was 600 wppm (most likely 600±50 wppm) in 17×17 Zry-4 with 0.57-mm-wall thickness. Their samples were oxidized (one-sided) at 1200ºC under isothermal conditions and were quenched at 1200ºC.

Table 46 Ring Compression Test Results for Prehydrided 17×17 Zry-4 Cladding Oxidized at 1200˚C, Cooled at ≈13ºC/s to 800˚C, and Quenched. ECR = 1.538 Wg for 0.57-mm-wall cladding. Tests were performed on ≈8-mm-long samples at 135ºC and 0.0333-mm/s displacement rate.

Test Conditions		ECR, %		Plastic Displacement, mm		Plastic Strain, %	
H Content wppm	Ox. Test Time,[a] s	CP	Meas.	Offset	Permanent	Offset	Permanent
5	100	7.8	8.2	5.48	4.82	58	51
247	95	7.6	8.5	3.30	3.02	35	32
278	95	7.6	8.5	1.13	---	12	---
314	95	7.6	8.5	1.95	---	21	---
412	100	7.5	8.8	0.05	0.07	0.5	0.7
438	100	7.5	8.8	0.06	0.08	0.6	0.8
524	100	7.5	8.8	0.06	---	0.6	---
5	151	10.8	11.9	2.14	---	23	---
5	151	10.8	11.9	>2.41	>1.92	>25	>20
154	136	9.4	9.9	2.87	2.58	30	27
209	136	9.4	9.9	0.52	0.31	5.5	3.3
274	136	9.4	9.9	0.27	---	2.8	---
335	141	10.1	12.8	0.06	0.04	0.6	0.4
462	141	10.1	11.2	0.04	0.08	0.4	---
499	141	10.1	11.2	0.05	0.04	0.5	0.4

[a]Includes time for ramp from 300ºC and hold time.

More data are needed for modern 17×17 Zry-4 to map out combinations of hydrogen content, oxidation temperature, and CP-ECR leading to embrittlement; to determine the influence of heating rate on post-quench ductility; and to determine the influence of cooling rate and quench temperature on post-quench ductility. The database for HBR-type 15×15 Zry-4 oxidized at 1200ºC is more extensive and is presented in Section 4.1.2 for quench at 800ºC and in Section 4.2 for quench at 700ºC and 600ºC vs. slow cooling to RT. The HBR-type Zry-4 data base is important as it is used to aid in interpreting the results of tests with high-burnup HBR Zry-4.

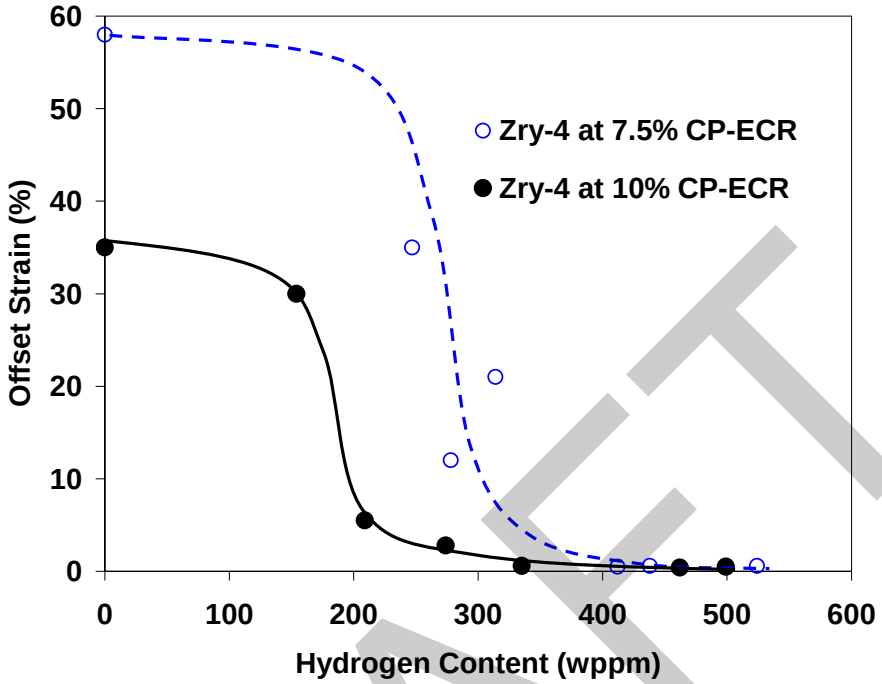

Figure 106. Variation of post-quench ductility with pre-test hydrogen content for modern 17×17 Zry-4 oxidized at 1200ºC to 7.5% and 10% CP-ECR (see Figure 20 for temperature history), cooled at ≈13ºC/s, quenched at 800ºC, and ring-compressed at 135ºC and 0.0333 mm/s.

4.1.2 Post-quench ductility of prehydrided HBR-type 15×15 Zry-4 oxidized at 1200ºC

The tests with prehydrided 15×15 Zry-4 samples were conducted with well-benchmarked test trains. Tests conducted during June-December 2004 used the test train with the temperature history shown in Figure 10. Tests conducted from January-June 2006 used the thermal history presented in Figure 107, which is very similar to the one in Figure 10. Tests conducted during June-October 2006 are characterized by the thermal history shown in Figure 108, which has a faster ramp to 1200ºC and a temperature overshoot of 16ºC early in the transient. This temperature history resulted in earlier-than-expected embrittlement due to the fast ramp and the temperature overshoot. Tests conducted after October 2006 used a thermal history more similar to the one in Figure 107. The test protocol for HBR-type Zry-4 was the same as the one used for oxidizing prehydrided 17×17 Zry-4. However, because as-fabricated HBR-type Zry-4 exhibited low ductile-to-brittle-transition CP-ECR (16%), the target CP-ECR values were reduced to 5% and 7.5%. The 7.5% CP-ECR oxidation level allowed a direct comparison of the two data bases. In evaluating the ANL data, note that 5% CP-ECR was reached for most samples during the slow part of the heating ramp with a peak temperature of 1190ºC (Figure 10) or 1180ºC (Figure 107) prior to cooling. The oxidation level of 7.5% was achieved for most samples at the end of a 55-s hold time at 1204ºC. Tables 47 and 48 summarize post-quench ductility results for prehydrided 15×15 Zry-4 oxidized to target CP- ECR levels of 5% and 7.5%, respectively. The footnotes to Tables 47 and 48 identify the thermal history for the tests conducted in 2006.

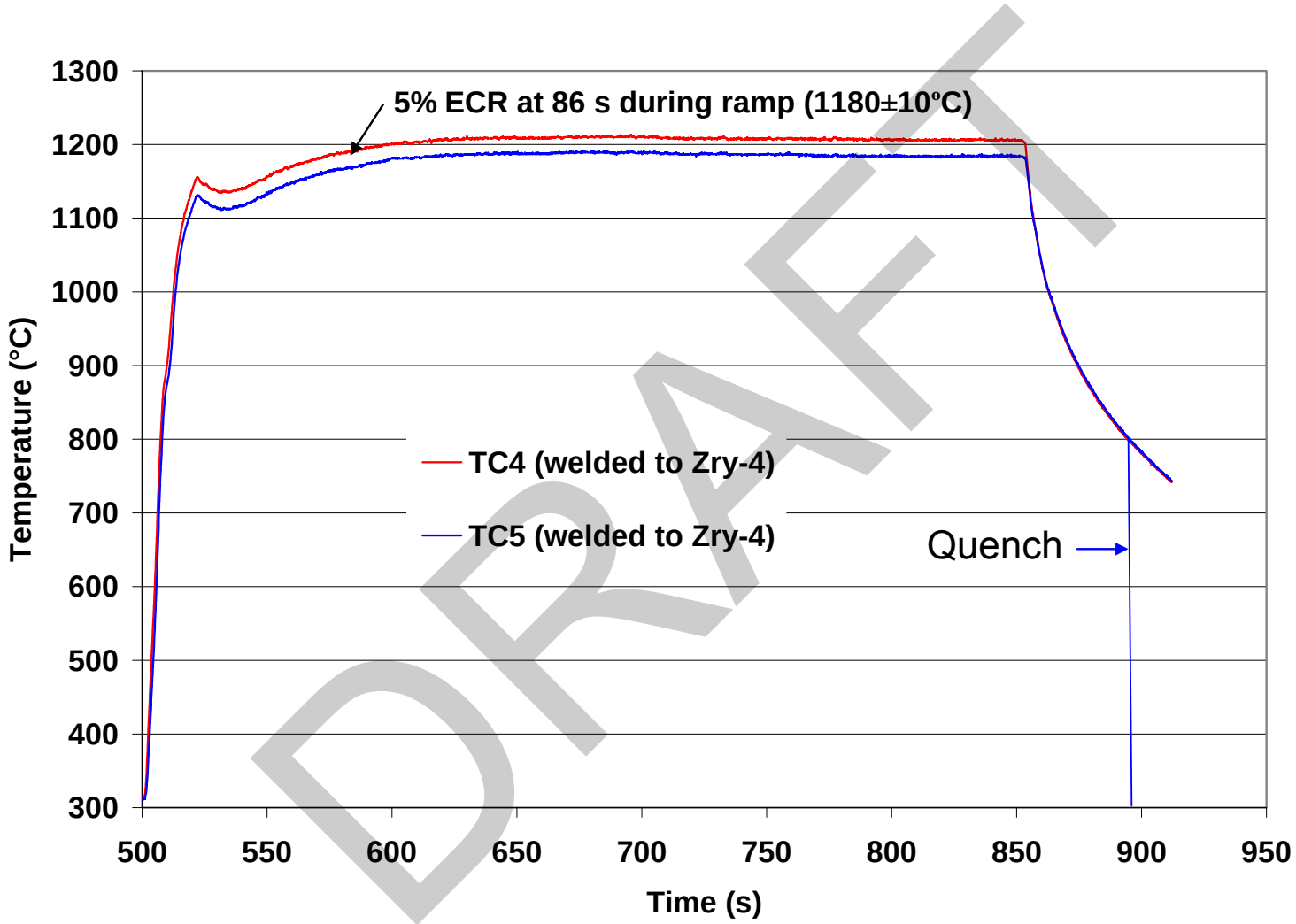

Figure 107. March 2006 thermal benchmark results for HBR-type 15×15 Zry-4 with a target oxidation temperature of 1200ºC.

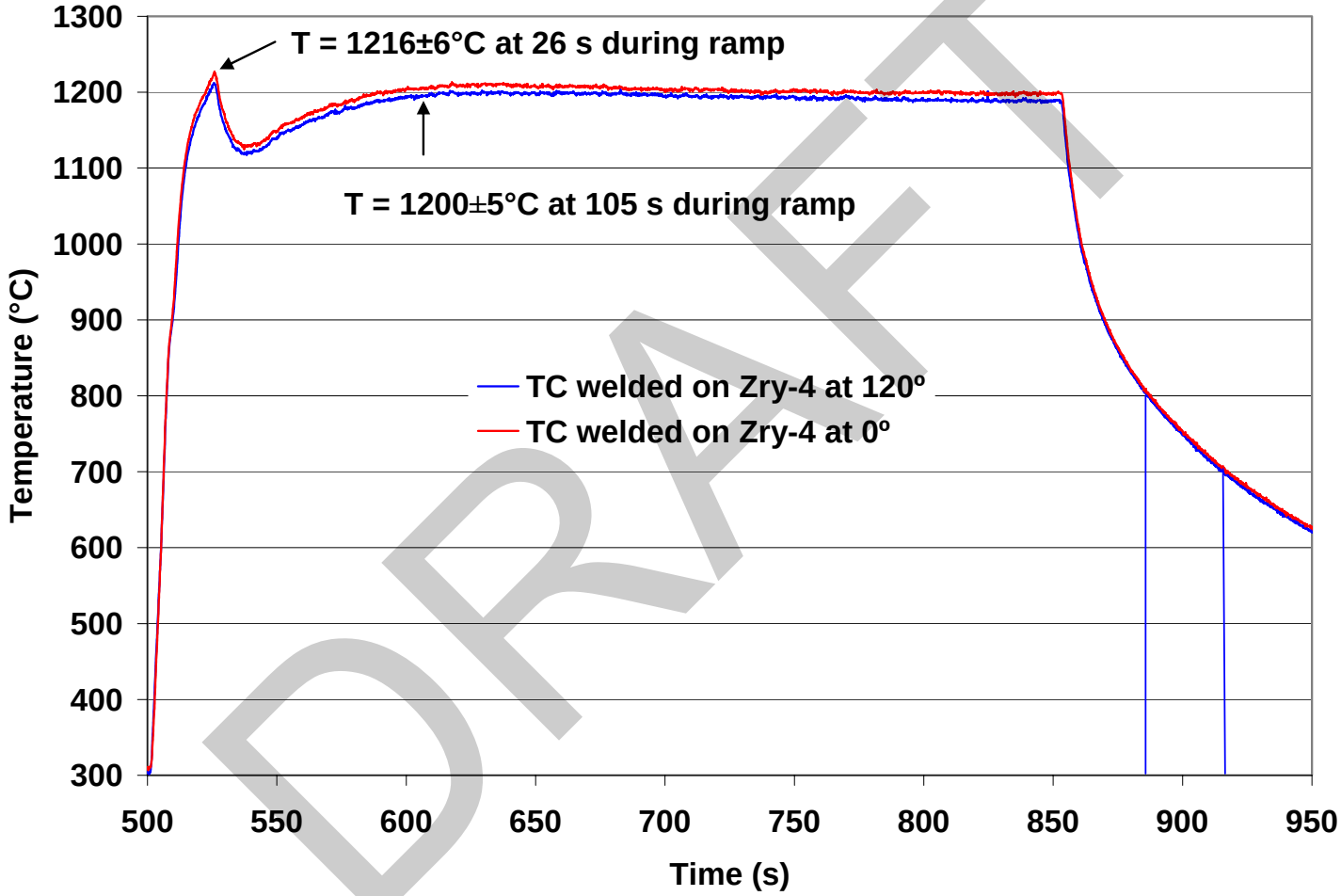

Figure 108. June 2006 thermal benchmark results for HBR-type 15×15 Zry-4 with a target oxidation temperature of 1200ºC.

Data and trend curves for offset strain vs. pre-oxidation hydrogen content are given in Figures 109 and 110 for the 5% and 7.5% CP-ECR oxidation levels, respectively. For 5% CP-ECR test conditions, Zry-4 exhibits post-quench ductility up to ≈550-wppm hydrogen and is definitely brittle at ≈640-wppm hydrogen. Although the ductile-to-brittle-transition hydrogen content at 5% CP-ECR is not precisely determined, 600-wppm hydrogen appears to be a reasonable value based on interpolation. The transition CP-ECR and/or the hydrogen content would decrease for tests with faster heating ramps and longer hold times at ≈1200ºC.

For the 7.5% CP-ECR oxidation level, one Zry-4 sampled exhibited ductility at 400-wppm hydrogen. However, embrittlement occurred at 335-wppm hydrogen for the more aggressive temperature ramp shown in Figure 108. For lower heating rate (Figures 10 and 107), the ductile-to-brittle transition hydrogen level is 375±25 wppm. The HBR-type Zry-4 offset strains are lower than the strains for 17×17 Zry-4 at <315 wppm H, but the ductile-to-brittle transition hydrogen content appears to be the same (375±25 wppm) at 7.5% CP-ECR for both types of Zry-4 (see Figure 111). Thus, within the data scatter, the higher transition CP-ECR for as-fabricated 17×17 Zry-4 does not appear to lead to higher transition values for prehydrided 17×17 Zry-4, as compared to HBR-type 15×15 Zry-4. .

Table 47 Post-quench Ductility of Prehydrided HBR-type 15×15 Zry-4 Cladding Oxidized to 5% CP-ECR with T = 1180-1190ºC at End of Heating Ramp, Cooled at ≈11ºC/s to 800˚C, and Quenched (Q). Ring-compression tests were performed on ≈8-mm-long samples at 135ºC and 0.0333-mm/s displacement rate; ECR = 1.1535 Wg for 0.76-mm-wall and 1.1385 Wg for 0.77-mm wall; displacements were normalized to 10.77-mm OD for 0.76-mm-wall and 10.76-mm OD for 0.77-mm wall.

Sample and Test Conditions			ECR, %		Plastic Displacement, mm		Plastic Strain, %	
Q-T, ºC	Test Time,[a] s	H, wppm	CP	Meas.	Offset	Permanent	Offset	Permanent
800	93	22	5.0	5.1	>6.0	>5.5	>56	>51
800	92	320	5.0	5.4	5.49	---	51	---
800	92	375	5.0	5.4	3.38	3.36	31	30
800	92	400	5.0	5.4	3.91	3.56	36	33
800	92	400	5.0	5.4	2.98	3.02	28	28
800	92	480	5.0	5.4	0.68	---	6.3	---
800	92	517	5.0	5.4	0.57	---	5.4	---
800	92	545	5.0	5.4	1.45	---	13.5	---
800	92	636	5.0	5.6	0.06	0.04	0.5	0.4
800[b]	**96**	**710**	**5.0**	**5.7**	**0.06**	**0.07**	**0.5**	**0.6**
800[b]	**96**	**730**	**5.0**	**5.7**	**0.05**	**---**	**0.5**	**---**
800[b]	**96**	**760**	**5.0**	**5.7**	**0.03**	**---**	**0.3**	**---**
800	92	800	5.0	5.4	0.03	---	0.3	---

[a]From beginning of ramp at 300ºC to end of hold time at 1204ºC (see Figure 10 for thermal history).

[b]See Figure 107 for thermal history of these tests conducted in 2006; ECR = 1.1385 Wg.

Table 48 Post-quench Ductility of Prehydrided HBR-type 15×15 Zry-4 Cladding Oxidized at 1200˚C to 7.5% CP-ECR, Cooled at ≈11ºC/s to 800˚C, and Quenched (Q). Ring-compression tests were performed on ≈8-mm-long samples at 135ºC and 0.0333-mm/s displacement rate. ECR = 1.1535 Wg for 0.76-mm wall and 1.1385 Wg for 0.77-mm wall; displacements were normalized to 10.77-mm OD for 0.76-mm wall and 10.76-mm OD for 0.77-mm wall.

Sample and Test Conditions			ECR, %		Plastic Displacement, mm		Plastic Strain, %	
Q-T, ºC	Test Time,[a] s	H, wppm	CP	Meas.	Offset	Permanent	Offset	Permanent
800 800	154 145	22 22	7.5 7.5	8.1 7.6	>4.7 5.53	>4.3 ---	>43 51	>40 ---
800[b]	**144**	**185**	**7.4**	**8.1**	**1.41**	**1.2**	**13**	**11**
800[c] **800[c]**	**132** **132**	**335** **335**	**7.4** **7.4**	**7.7** **7.7**	**0.08** **0.12**	**---** **0.08**	**0.7** **1.1**	**---** **0.7**
800	145	360	7.5	7.6	0.54	---	5.0	---
800	145	386	7.5	7.7	0.20	---	1.9	---
800	145	386	7.5	7.7	0.11	0.07	1.0	0.6
800	145	386	7.5	7.7	0.06	0.04	0.6	0.4
800	145	390	7.5	7.6	0.09	---	0.8	---
800	145	400	7.5	7.6	0.23	0.11	2.1	1.0
800[b]	**144**	**435**	**7.4**	**8.0**	**0.05**	**0.03**	**0.5**	**0.3**
800[b]	**144**	**435**	**7.4**	**8.0**	**0.05**	**0.03**	**0.5**	**0.3**
800	145	533	7.5	8.1	0.05	---	0.5	---
800	145	600	7.5	8.1	0.04	---	0.4	---

[a]From beginning of ramp at 300ºC to end of hold time at 1204ºC (see Figure 10 for thermal history).

[b]Tests conducted with thermal history shown in Figure 107; ECR = 1.1385 Wg.

[c]Tests conducted with thermal history shown in Figure 108; ECR = 1.1385 Wg.

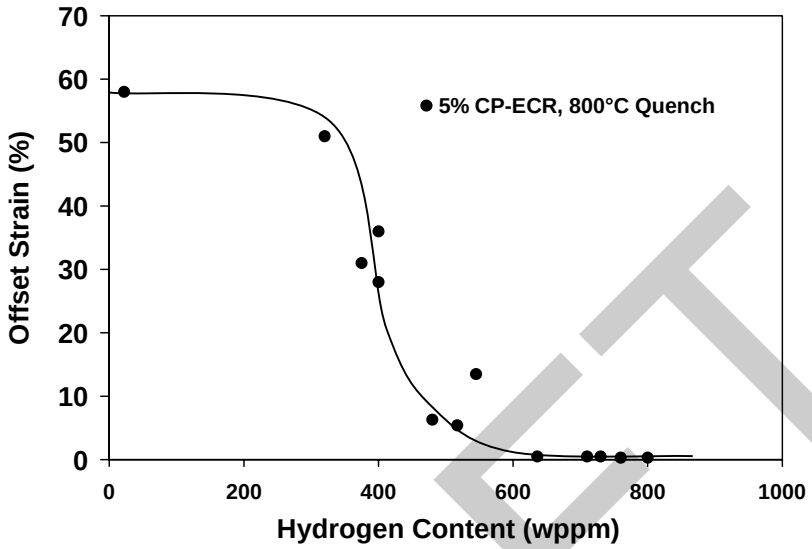

Figure 109. Variation of post-quench ductility with pre-test hydrogen content for HBR-type 15×15 Zry-4 oxidized to 5% CP-ECR with an end-of-heating temperature of 1180-1190ºC (see Figures 10 and 107), cooled at ≈11ºC/s, quenched at 800ºC, and ring-compressed at 135ºC.

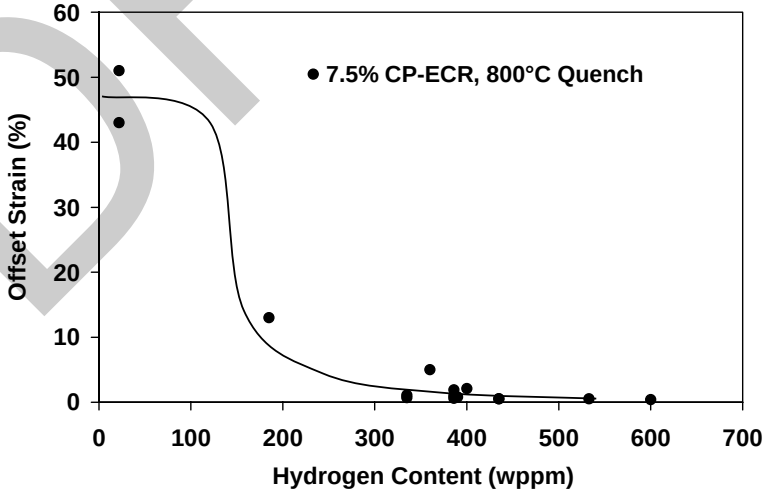

Figure 110. Variation of post-quench ductility with pre-test hydrogen content for HBR-type 15×15 Zry-4 oxidized at 1204ºC to 7.5% CP-ECR (see Figures 10, 107, and 108), cooled at ≈11ºC/s, quenched at 800ºC, and ring-compressed at 135ºC.

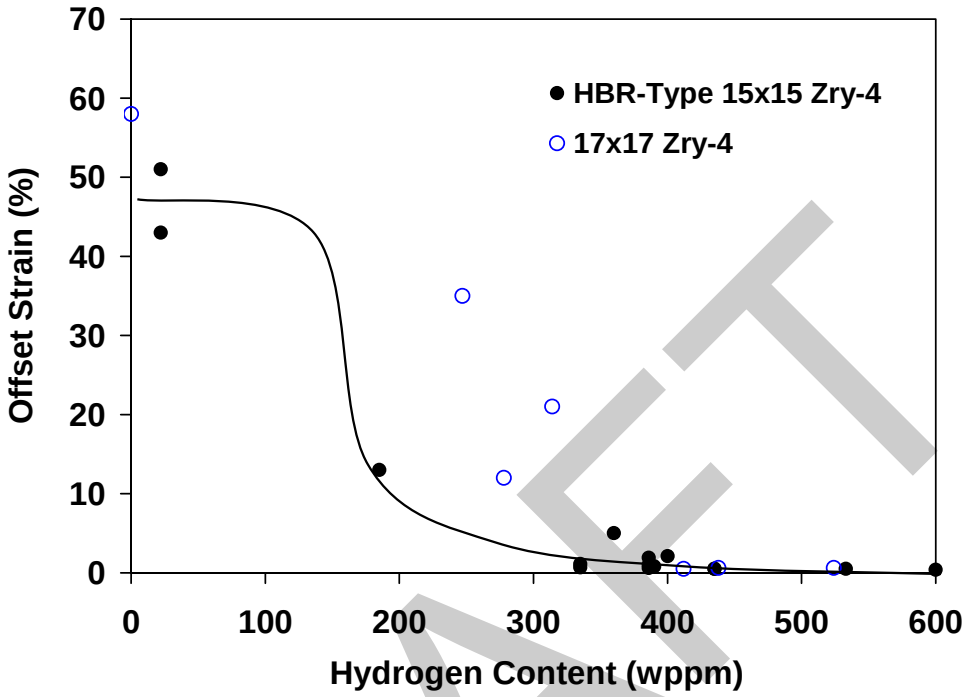

Figure 111. Post-quench ductility vs. pre-test hydrogen content for modern 17×17 and HBR-type 15×15 Zry-4 oxidized at 1200ºC to 7.5% CP-ECR, cooled at ≈11-13ºC/s, quenched at 800ºC, and ring-compressed at 135ºC.

To better understand the significant decrease in post-quench ductility with increasing hydrogen content, metallography and microhardness were performed on as-received HBR-type Zry-4 and prehydrided (600 wppm) HBR-type Zry-4, both oxidized at ≈1200ºC to 7.5% CP-ECR. Figures 112a and 112b show typical cross sections (one out of eight circumferential locations) of the as-received and prehydrided samples, respectively, following oxidation and quench at 800ºC. Although both samples show evidence of alpha incursions precipitated during cooling in the prior-beta layer, these incursions appear to be larger and more pronounced in the as-received Zry-4. The layer thicknesses are comparable and do not suggest that one sample was highly ductile and the other sample was highly brittle. Table 49 summarizes measured sample weight gains, layer thicknesses determined from metallographic images, weight gains determined from the layer thicknesses, and post-quench ductility. The presence of 600-wppm hydrogen resulted in embrittlement (nil-ductility) of Zry-4 oxidized to 7.5% CP-ECR, whereas the as-received Zry-4 sample exhibited a very high offset strain (>43%, which is the limit of this particular test) at 135ºC ring-compression temperature. The prior-beta-layer microhardness profiles shown in Figure 113 reveal significant differences between the two samples. The local and average microhardness values in the prior-beta layer for the prehydrided sample are significantly higher than the ones for the as-received sample. These results are consistent with the post-quench ductility results.

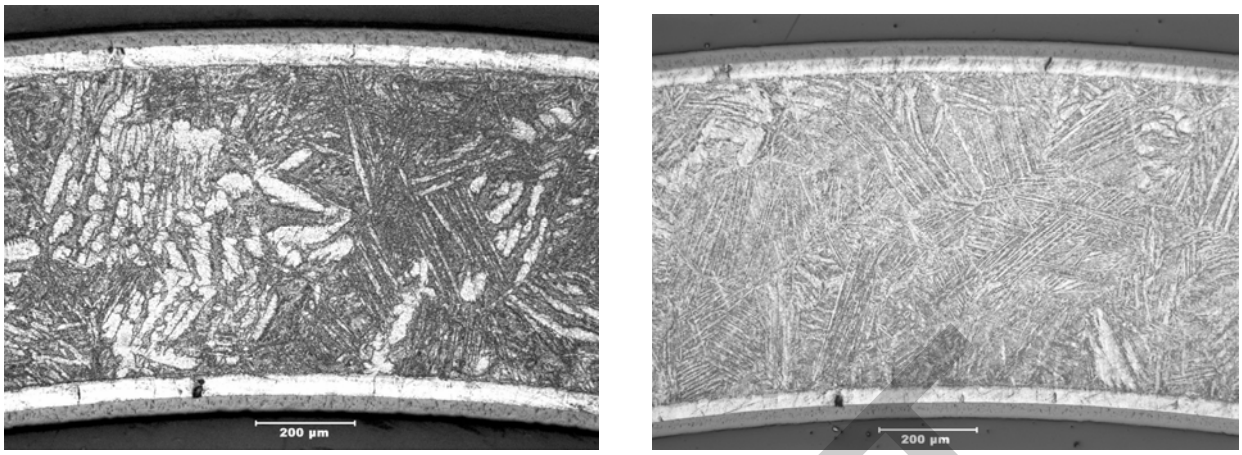

(a) As-received (b) 600-wppm hydrogen

Figure 112. Metallographic images of HBR-type 15×15 Zry-4 following oxidation at ≈1200ºC to 7.5% CP-ECR, cooling at ≈11ºC/s to 800ºC, and quench at 800ºC: (a) as-received and (b) 600-wppm hydrogen.

Table 49 Comparison of Results for As-received and 600-wppm-prehydrided HBR-type 15×15 Zry-4 Samples after Exposure to Steam at ≈1200˚C to 7.5% CP-ECR, Cooling at ≈11ºC/s to 800˚C, and Quench at 800˚C

Parameter	**HBR-Type 15x15 Zry-4**	
	As-received	**Prehydrided**
Hydrogen Content, wppm	≈10	600
Hold Temperature, ˚C	1200±17	1204±10
CP-ECR, %	7.5	7.5
CP Weight Gain, mg/cm^2	6.5	6.5
Measured Weight Gain based on Change in Sample Weight, mg/cm^2	6.94	6.75
Measured ECR, %	8.0	7.8
Outer-surface Oxide Layer, µm	35	33
Outer-surface Alpha Layer, µm	41	38
Prior-beta Layer, µm	636	640
Inner-surface Alpha Layer, µm	40	39
Inner-surface Oxide Layer, µm	36	34
Weight Gain Determined from Metallography, mg/cm^2	---	6.7
Post-Quench Ductility, % (Offset Strain)	>43	0.4

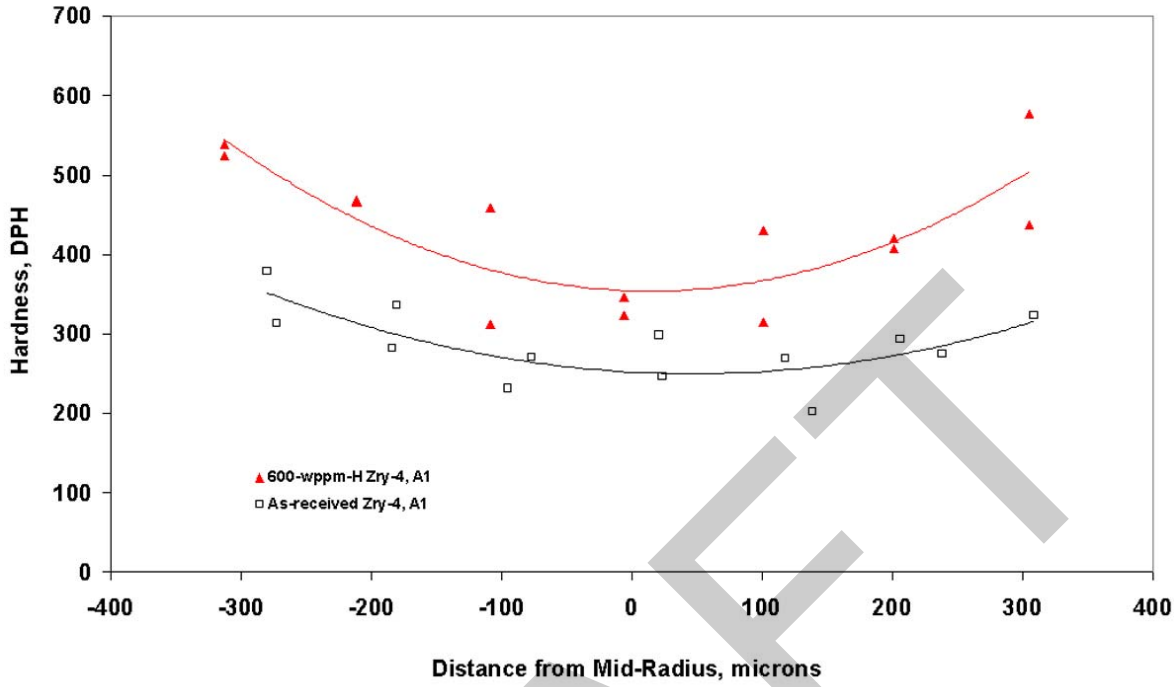

Figure 113. RT microhardness profiles across the prior-beta layer of two samples oxidized at ≈1200˚C to 7.5% CP-ECR, cooled at ≈11ºC/s to 800˚C, and quenched at 800˚C: as-received and 600-wppm-hydrogen HBR-type 15×15 Zry-4.

The elevated RT microhardness for the prehydrided sample suggests that hydrogen increases the rate of oxygen diffusion into the beta layer during oxidation at elevated temperature, and/or that hydrogen has a direct effect on increasing hardness and embrittlement. Based on the results of Mardon et al. [21, Figure 16], 600 wppm of hydrogen causes the solubility limit of oxygen in the prior-beta layer to increase by 0.4±0.1 wppm relative to as-received material oxidized at 1200ºC. If the Chung and Kassner [18] solubility limit of 0.57-wt.% oxygen at 1200˚C were used for as-received Zry-4, then the oxygen solubility limit for 600-wppm-H Zry-4 would be 1.0±0.1 wt.%. The oxygen concentration in the beta layer at the alpha-beta boundary would increase from ≈0.6 wt.% to ≈1.0 wt.%. Using the oxygen diffusivity determined by Pawel et al. [26], the solubility limit for the oxygen concentration at the alpha-beta boundary, the as-received oxygen concentration for the "zero-time" oxygen concentration across the beta layer, and the end-of-oxidation beta-layer thickness (approximation to bypass the more complicated moving-boundary problem), the oxygen profiles were calculated and compared to the microhardness profiles across the beta layer for as-received and 600-wppm-prehydrided Zry-4. The results are given in Figure 114 for as-received (a) and prehydrided (b) Zry-4 oxidized at ≈1200˚C to 7.5% CP-ECR. These calculated oxygen concentrations do not agree very well with the microhardness vs. oxygen-content results of Mardon et al. [21, Figure 16]. The results of Mardon et al. show a linear relationship between microhardness and oxygen concentration for samples oxidized long enough at 1000-1200ºC to approach the solubility limit. The non-linear relationships shown in Figures 114a and 114b suggest that the model and oxygen diffusivity used to calculate the oxygen profiles may need some improvement.

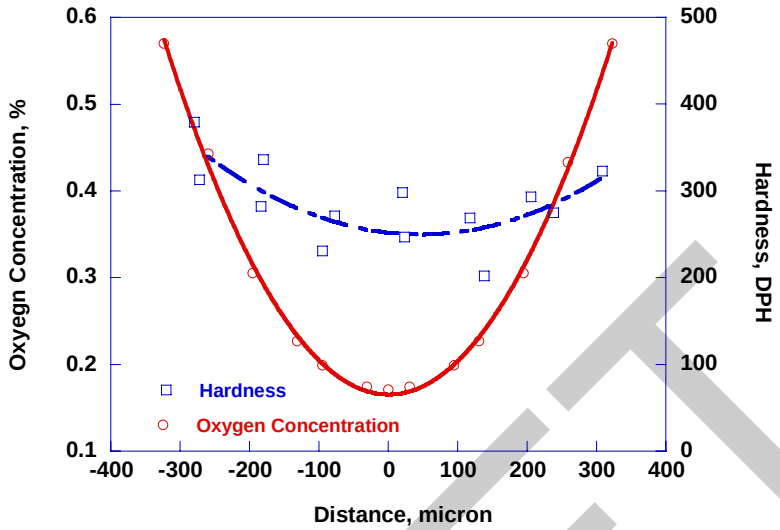

(a)

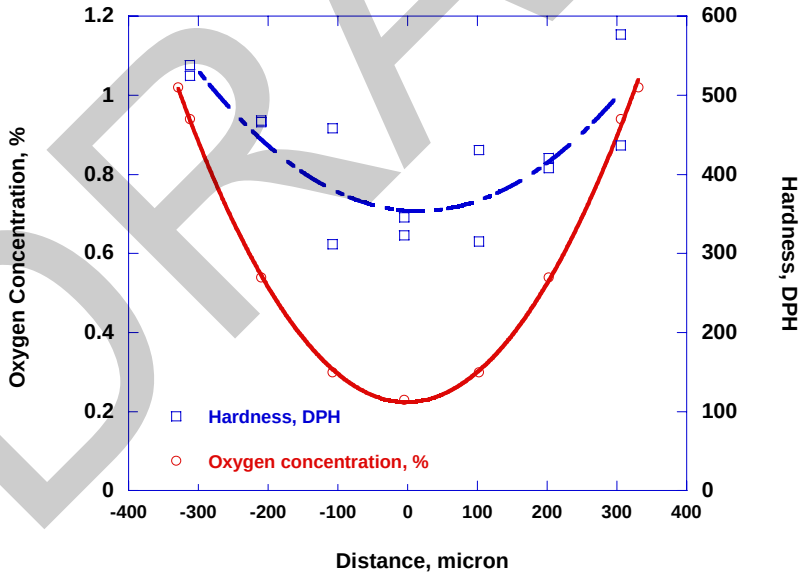

(b)

Figure 114. RT microhardness and oxygen-concentration profiles across the beta layers of HBR-type 15×15 Zry-4 oxidized at ≈1200˚C to 7.5% CP-ECR, cooled at ≈11ºC/s to 800˚C, and quenched at 800˚C: (a) as-received and (b) 600-wppm hydrogen.

4.2 Effects of quench temperature on post-quench ductility

Heating-rate effects on post-quench ductility and ductile-to-brittle transition CP-ECR are reasonably well understood qualitatively. However, systematic studies have not been performed to quantify the transition CP-ECR vs. temperature ramp rate. Also, modeling oxygen diffusion into the beta layer during transient heating is challenging because of the temperature-dependent increase in beta-layer oxygen concentration at the alpha-beta boundary. At a fixed CP-ECR, cladding oxidized at a low heating rate to 1200ºC will exhibit higher post-quench ductility than cladding oxidized at a very high heating rate to 1200ºC. The rapidly heated sample would experience more time at 1200ºC and would pick up more oxygen in the beta layer due to higher diffusivity and solubility at 1200ºC as compared to lower oxidation temperatures. However, the effects of cooling rate and quench temperature on post-quench ductility are not well understood. In Section 3.6, it was shown that as-fabricated Zry-4, ZIRLO, and M5 samples quenched at 800ºC after oxidation at 1200ºC exhibited the same ductile-to-brittle-transition CP-ECR as samples cooled from 1200ºC to RT without quench. The transitions occurred at 17-20% CP-ECR and corresponded to relatively long test times. For oxygen-induced embrittlement of as-fabricated cladding alloys, the cooling rate from 800ºC to RT appears to be insignificant. However, tests needed to be conducted with prehydrided and high-burnup samples before conclusions could be drawn with regard to cooling-rate and quench-temperature effects on post-quench ductility.

In order to address these issues for prehydrided samples, tests were conducted with prehydrided HBR-type 15×15 Zry-4 to determine the effects of quench temperature on post-quench ductility for samples oxidized at 1200ºC. Prehydrided samples were oxidized to the same CP-ECR level and, cooled at an average rate of 11ºC/s to 800ºC and quenched (Q); or cooled at an average rate of 7.3ºC/s to 700ºC and quenched; or slow cooled (SC) from 1200ºC to RT. The relevant temperature histories for these tests are shown in Figures 107 and 108. Because of the significant database presented in Section 4.1.2 for HBR-type 15x15 Zry-4 at 5% and 7.5% CP-ECR, the same oxidation levels were used in this study. The results for Zry-4 oxidized to 5% CP-ECR are listed in Table 50 and shown in Figure 115, along with the data in Table 47. The 7.5% CP-ECR results are listed in Table 51 and shown in Figure 116, along with the data in Table 48.

The prehydrided (710-760 wppm) samples quenched at 800ºC were brittle after oxidation to 5% CP-ECR. Slow-cooled samples with the same hydrogen content and oxidized to the same CP-ECR had marginally higher offset and permanent strains. Nevertheless, the difference is significant as all six samples exhibited low ductility (offset strain ≥ 2.0%, permanent strain ≥ 1.4%). Quenching at 800ºC essentially "freezes" in the distribution of oxygen within the high-oxygen-containing alpha incursions precipitated during very rapid cooling from 800ºC to 100ºC and the low-oxygen-containing prior-beta matrix. For the slow-cooled samples, oxygen diffusion is very slow below 800ºC and is not predicted to occur. However, most of the hydrogen is expected to be in solution in the low-oxygen-containing part of the prior-beta layer. Hydrogen has more mobility than oxygen at <800ºC. It can move to the interfaces of these two regions and form small precipitates. If the oxygen concentration remains the same in the low-oxygen-containing prior-beta matrix and the hydrogen concentration decreases with slow cooling, the ductility results suggest that hydrogen causes a small amount of embrittlement beyond what is expected due to its enhancement of oxygen solubility in the prior-beta layer. If hydrogen is given time to migrate out of the low-oxygen prior-beta regions, then the ductility of these regions appears to be enhanced.

The results following oxidation to 7.5% CP-ECR are also interesting. These prehydrided samples were at ≈1200ºC hold temperature for ≈60 s. Depending on the heating rate (Figure 10, 107, or 108), embrittlement for 800ºC-quenched Zry-4 samples occurred in the range of 335-wppm (Figure 108 heating rate) to 400-wppm H (one sample with Figure 10 heating rate). However, slow-cooled samples exhibited

low ductility for hydrogen contents up to ≈550 wppm, with one sample marginally brittle at 530 wppm and another one ductile at 570 wppm. As with the prehydrided 5% CP-ECR samples, the enhancement in offset and permanents strains is small but significant. For the aggressive heating rate in Figure 108, samples with ≈330 wppm H were brittle following quench at 800ºC, brittle (2 out of 3 samples) following quenching at 700ºC, and marginally ductile following slow cooling to RT.

Table 50 Post-quench Ductility of Prehydrided HBR-type 15×15 Zry-4 Cladding Oxidized to 5% CP-ECR with T = 1180ºC at End of Heating Ramp, Cooled at ≈11ºC/s to 800˚C, and either Quenched (Q) at 800ºC or Slow Cooled to RT. ECR = 1.1385 Wg; ring-compression tests performed on ≈8-mm-long samples at 135ºC and 0.0333 mm/s displacement rate.

Sample and Test Conditions			ECR, %		Plastic Displacement, mm		Plastic Strain, %	
Q-T, ºC or SC	Test Time,[a] s	H, wppm	CP	Meas.	Offset	Permanent	Offset	Permanent
800	96	710	5.0	5.7	0.06	0.07	0.5	0.6
SC	96	720	5.0	5.7	0.37	0.29	3.4	2.7
SC SC SC	96 96 96	720 720 720	5.0 5.0 5.0	5.6 5.6 5.6	0.18 0.22 0.21	0.14 0.19 0.17	2.3 2.1 2.0	1.4 1.8 1.6
800	96	730	5.0	5.7	0.05	---	0.5	---
SC	96	740	5.0	5.7	0.30	0.25	2.8	2.3
800	96	760	5.0	5.7	0.03	---	0.3	---
SC	96	760	5.0	5.7	0.32	0.17	3.0	1.6

[a]From beginning of heating ramp at 300ºC to time at 1180ºC (see Figure 107 for thermal history).

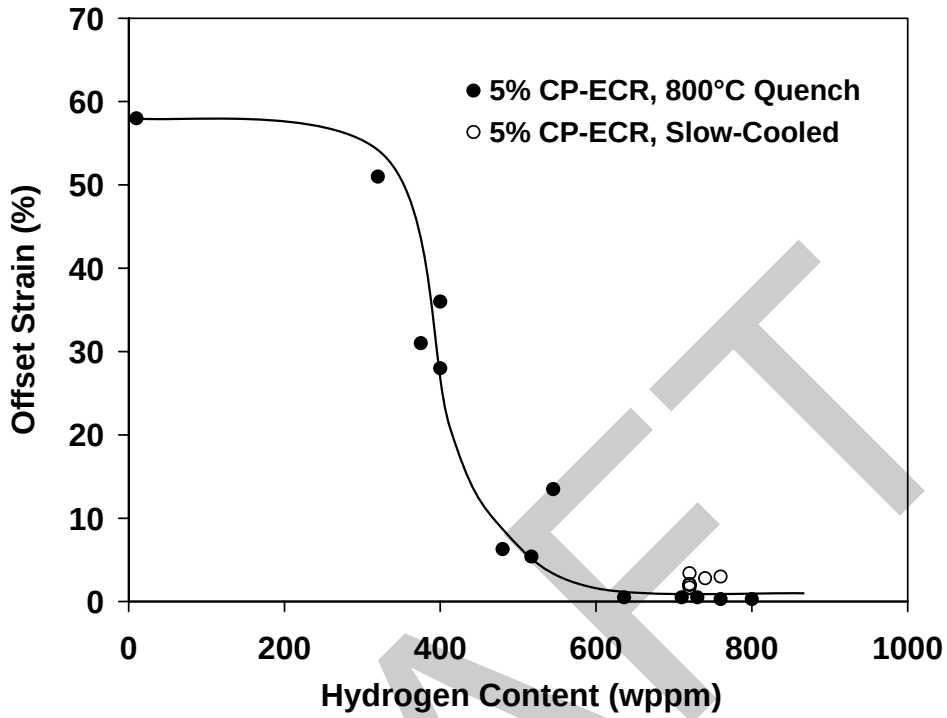

Figure 115. Effects of slow cooling vs. quench at 800ºC on the post-test ductility at 135ºC for HBR-type 15x15 Zry-4 oxidized to 5% CP-ECR at a peak temperature of 1180-1190ºC prior to cooling. Plot includes data shown in Figure 109.

The CP-ECR values reported throughout Sections 3 and 4 are based on the integrated value up through the end of the heating phase. For the rapid cooling in the ANL experiments, oxygen diffusion into the beta layer is negligible during cooling. However, the calculated weight gain for the cooling phase does add a little to the CP-ECR value. The CP weight gain for the cooling phase from 1200ºC to 800ºC is 1.52 mg/cm^2. Because of the parabolic nature of diffusion and weight gain, the contribution of the cooling weight gain is not linear. Let $(Wg)_t$ be the total weight gain prior to quench at 800ºC, $(Wg)_h$ be the weight gain at the end of the heating phase, and $(Wg)_c$ be the weight gain calculated from the cooling curve by ignoring the heating phase. Then, $(Wg)_t = [(Wg)_h^2 + (Wg)_c^2]^{0.5} = [(Wg)_h^2 + 2.3]^{0.5}$. Using the conversion factors for weight gain to ECR and the same notation for total, heating, and cooling, we can write $ECR_t = [(ECR_h)^2 + (ECR_c)^2]^{0.5}$. For the 17×17 Zry-4 results in Table 46, the 7.5% heating-phase CP-ECR converts to a total CP-ECR of 7.9%, and the 10% heating-phase CP-ECR \converts to a total CP-ECR of 10.3%. For the HBR-type 15×15 Zry-4 results in Tables 47, 48, and 50-52, the heating-phase CP-ECR values of 5%, 6%, and 7.5% convert to total CP-ECR values of 5.2%, 6.2%, and 7.7%, respectively.

Table 51 Post-quench Ductility of Prehydrided HBR-type 15×15 Zry-4 Cladding Oxidized to 7.5% CP-ECR at 1204ºC, Cooled at ≈11ºC/s to 800˚C, and Quenched (Q) at 800ºC, or Quenched at 700ºC, or Slow Cooled to RT, ECR = 1.1385 Wg; ring-compression tests performed on ≈8-mm-long samples at 135ºC and 0.0333-mm/s displacement rate.

Sample and Test Conditions			ECR, %		Plastic Displacement, mm		Plastic Strain, %	
Q-T, ºC or SC	Test Time,[a] s	H, wppm	CP	Meas.	Offset	Permanent	Offset	Permanent
800[b]	144	185	7.4	8.0	1.41	1.2	13	11
SC[b]	144	180	7.4	8.1	1.40	1.2	13	11
SC[b]	144	185	7.4	8.1	2.04	1.8	19	17
800[c]	132	335	7.4	7.7	0.12	0.08	1.1	0.7
800[c]	132	335	7.4	7.7	0.08	---	0.7	---
700[c]	132	335	7.4	7.6	0.24	0.11	2.2	1.0
700[c]	132	335	7.4	7.6	0.11	0.08	1.0	0.7
700[c]	132	335	7.4	7.6	0.15	0.09	1.3	0.8
SC[c]	132	327	7.4	7.6	0.45	0.27	4.2	2.5
SC[c]	132	327	7.4	7.6	0.31	0.23	2.8	2.1
800[b]	144	435	7.4	8.0	0.05	0.03	0.5	0.3
800[b]	144	435	7.4	8.0	0.05	0.03	0.5	0.3
SC[b]	144	490	7.4	8.0	0.36	0.26	3.3	2.4
SC[b]	144	530	7.4	8.0	0.15	0.10	1.4	0.9
SC[b]	144	570	7.4	8.0	0.19	0.14	1.8	1.3

[a]From beginning of ramp at 300ºC to end of hold time at ≈1200ºC.

[b]Tests conducted with thermal history shown in Figure 107.

[c]Tests conducted with thermal history shown in Figure 108.

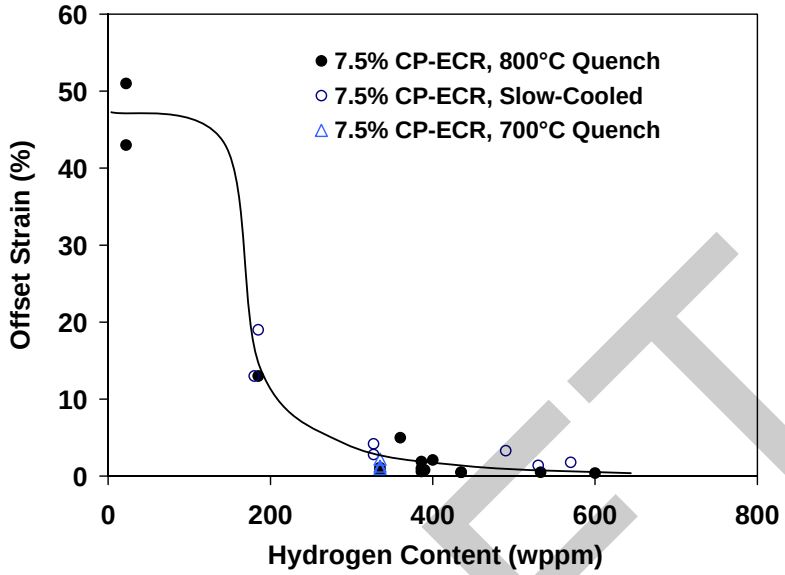

Figure 116. Effects of slow cooling vs. quench at 700ºC and 800ºC on ductility at 135ºC for HBR-type 15×15 Zry-4 oxidized to 7.5% CP-ECR at 1204ºC prior to cooling. Plot includes data shown in Figure 110.

In order to better understand the effects of quench temperature on post-quench ductility, an additional set of tests was conducted with a heating rate comparable to the ones shown in Figures 10 and 107, which were used to oxidize most of the prehydrided samples prior to conducting post-quench ductility tests. Figure 117 shows the thermal history for these additional tests. The lower heating rate to 1200ºC is comparable to the heating rates shown in Figures 10 and 107, as well as the ones used to oxidize high-burnup Zry-4 samples (see Section 5).

Previous data for prehydrided HBR cladding were generated for samples oxidized to 5% and 7.5% CP-ECR. Additional tests were conducted with Zry-4 samples containing 450-470 wppm hydrogen oxidized to 6% CP-ECR. During the oxidation phase, the samples were at 1200-1204ºC for 17 s and >1180ºC for 86 s. The uniformity of hydrogen content from sample to sample allowed for a good comparison of ductility for Zry-4 quenched at 800ºC (450±20 wppm H), 700ºC (450±20 wppm H), and 600ºC (460±30 wppm H), as well as the sample that was slow cooled to RT (470±30 wppm H). The post-test ductility results are given in Table 52. The samples quenched at 600-800˚C were all brittle by both the offset and permanent strain criteria. The slow-cooled samples were ductile with 3.5±1.4% offset strain and 2.7±1.0% permanent strain. Although the average cooling rates decreased from 11˚C/s (1200˚C to 800˚C) to 3˚C/s (800˚C to 700˚C) to 2˚C/s (700˚C to 600˚C), it is only the very slow cooling at <<2˚C/s from 600˚C to RT that resulted in ductility enhancement. Oxygen redistribution at 600˚C to RT is highly unlikely due to the slow diffusivity of oxygen. The phase change from (beta + alpha) → alpha is complete by about 750˚C, so no further phase change is expected from 600˚C to RT. However, hydrogen diffusivity is much faster than oxygen diffusivity. Thus, hydrogen can come out of solid solution and precipitate as very small hydrides during very slow cooling from 600˚C to RT.

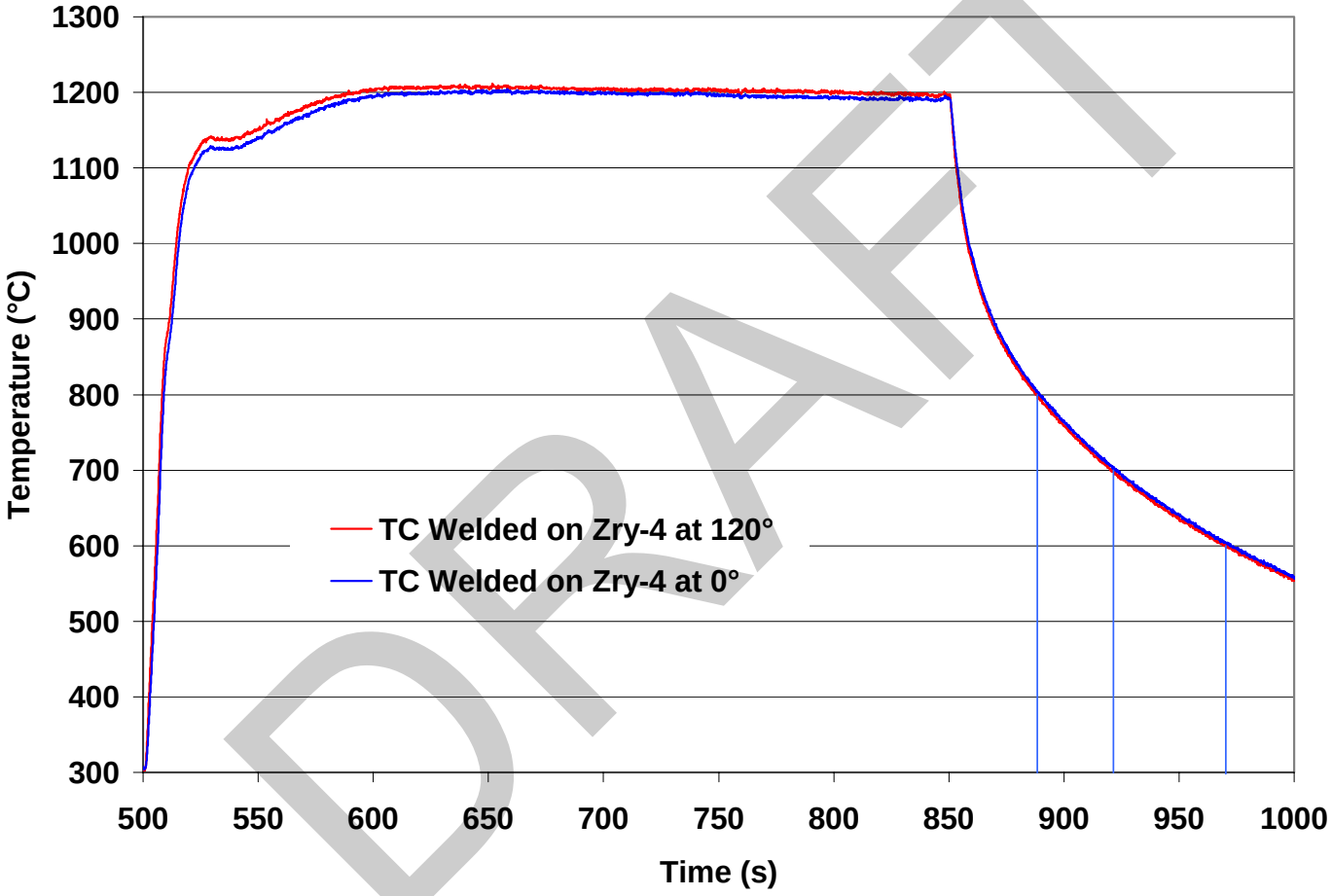

Figure 117. November 2006 thermal benchmark results for HBR-type 15×15 Zry-4 with a sample oxidation temperature of 1201±3ºC. Vertical blue lines indicate different quench temperatures for tests with prehydrided Zry-4 samples.

Table 52 Post-quench Ductility of Prehydrided HBR-type 15×15 Zry-4 Cladding Oxidized to 6% CP-ECR at 1200ºC, Cooled at ≈11ºC/s to 800˚C and Quenched (Q) at 800˚C, Cooled from 800˚C to 700˚C at 3˚C/s and Quenched at 700˚C, Cooled from 700˚C to 600˚C at 2˚C/s and Quenched at 600˚C, or Slow Cooled from 600˚C to RT at <2˚C/s. Thermal history is shown in Figure 117; CP-ECR is calculated from beginning of ramp to end of hold time; ring-compression tests performed on ≈8-mm-long samples at 135ºC and 0.0333-mm/s displacement rate.

Sample and Test Conditions			ECR,[b] %		Plastic Displacement, mm		Plastic Strain, %	
Q-T, ºC or SC	Test Time,[a] s	H, wppm	CP	Meas.	Offset	Permanent	Offset	Permanent
800	106	450	6.0	6.5	0.10	0.08	0.9	0.7
800	106	450	6.0	6.5	0.09	0.07	0.8	0.7
700	106	450	6.0	6.6	0.07	0.05	0.6	0.5
700	106	450	6.0	6.6	0.10	0.05	0.9	0.5
600	106	460	6.0	6.5	0.08	0.05	0.7	0.5
600	106	460	6.0	6.5	0.13	0.08	1.2	0.7
SC	106	470	6.0	6.4	0.22	0.18	2.1	1.7
SC	106	470	6.0	6.4	0.53	0.39	4.9	3.6

[a]From beginning of ramp at 300ºC to end of hold time at ≈1200ºC.
[b]Total CP-ECR, including cooling phase is 6.2%.

The ductility enhancement with slow cooling to RT is important to incorporate in data interpretation (see Section 5), but it may not be relevant to LOCA post-quench ductility for quench temperatures ≥600˚C.

Additional data for prehydrided HBR-type Zry-4 were needed to determine the embrittlement threshold within the narrow CP-ECR range of 4.5-6.0% for samples cooled with quench at 800˚C. The prehydrided samples included ones with small (<±30 wppm) and large (≥±100 wppm) circumferential variations in hydrogen. A new test train was constructed and carefully benchmarked to generate these data. The thermal benchmark results shown in Figure 118 give the temperature history used to generate these results. Results of the additional tests are summarized in Table 52a. The embrittlement threshold vs. hydrogen content derived from all the ductility data for prehydrided Zry-4 is shown in Figure 118a for samples cooled with or without (i.e., slow cooling [SC]) quench (Q) at 800ºC. Embrittlement results in Figure 118a are for the heating rates used in this study and are expressed in terms of the total transient CP-ECR, including oxidation during the heating ramp, the hold time and the cooling phase. The database used to determine embrittlement threshold is based on samples with relatively uniform hydrogen content in the circumferential direction (< ±30 wppm). A few samples were tested with circumferential variations (±100 wppm) as large as anticipated for high-burnup Zry-4. Although these samples were predicted to be ductile based on average hydrogen content, they were brittle: 510±100 wppm hydrogen oxidized to 5.2% CP-ECR and 610±100 wppm hydrogen oxidized to 4.7% CP-ECR. To quantify embrittlement effects of large circumferential variations in hydrogen, a very extensive dataset would be needed with multiple oxidation-quench tests conducted at the same CP-ECR and hydrogen content.

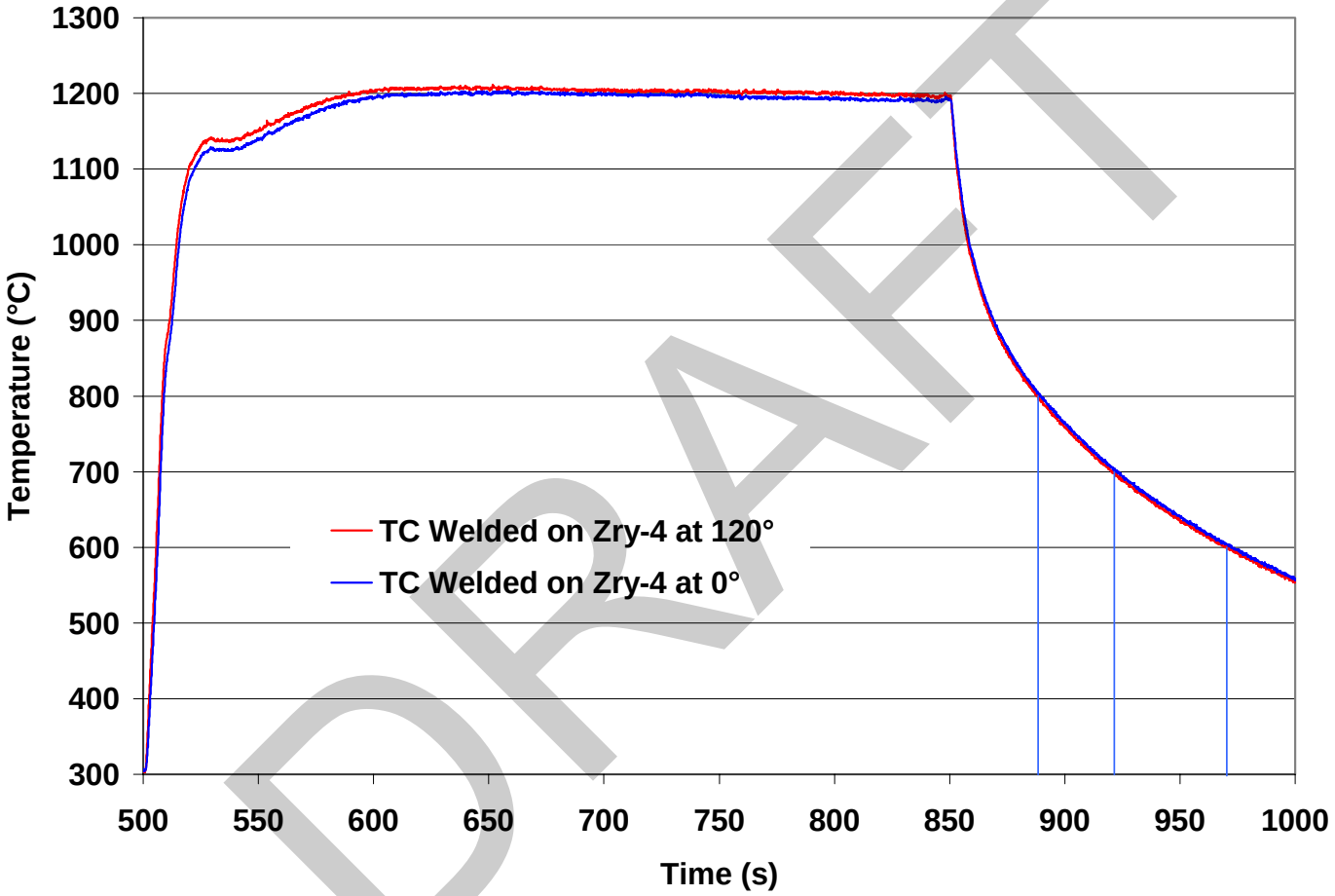

Figure 118. March 2007 thermal benchmark results for HBR-type 15×15 Zry-4 with a sample oxidation temperature of 1201±3ºC. Vertical blue lines indicate different quench temperatures for tests with prehydrided Zry-4 samples.

Table 52a Post-quench Ductility of Prehydrided HBR-type 15×15 Zry-4 Cladding Oxidized to 4.5-5.5% CP-ECR at 1200ºC, Cooled at ≈11ºC/s to 800˚C and Quenched (Q) at 800˚C. Thermal history is shown in Figure 118; CP-ECR is calculated from beginning of ramp to end of hold time; ring-compression tests performed on ≈8-mm-long samples at 135ºC and 0.0333-mm/s displacement rate.

Sample and Test Conditions			CP-ECR,[b] %	Plastic Displacement, mm		Plastic Strain, %	
Test Time,[a] s	T_{max}, ºC	H, wppm		Offset	Permanent	Offset	Permanent
74	1185	610±100 640±100 630±80	4.5	0.11 0.03 0.09	 0.03 	1.0 0.3 0.8	--- 0.4 ---
83	1191	490±20 470±20 460±20	5.0	0.30 0.33 0.44	--- --- ---	2.8 3.1 4.1	--- --- ---
83	1191	510±100 >510±100 >510±100	5.0	0.11 0.03 0.09	0.10 0.04 0.07	1.0 0.3 0.8	0.9 0.4 0.7
93	1193	470±20 470±20 490±20	5.5	0.33 0.21 0.09	--- --- ---	3.1 2.0 0.8	--- --- ---

[a]From beginning of ramp at 300ºC to end of hold time at ≈1200ºC.
[b]Total CP-ECR values, including cooling phase, are 4.7%, 5.2% and 5.7%, respectively.

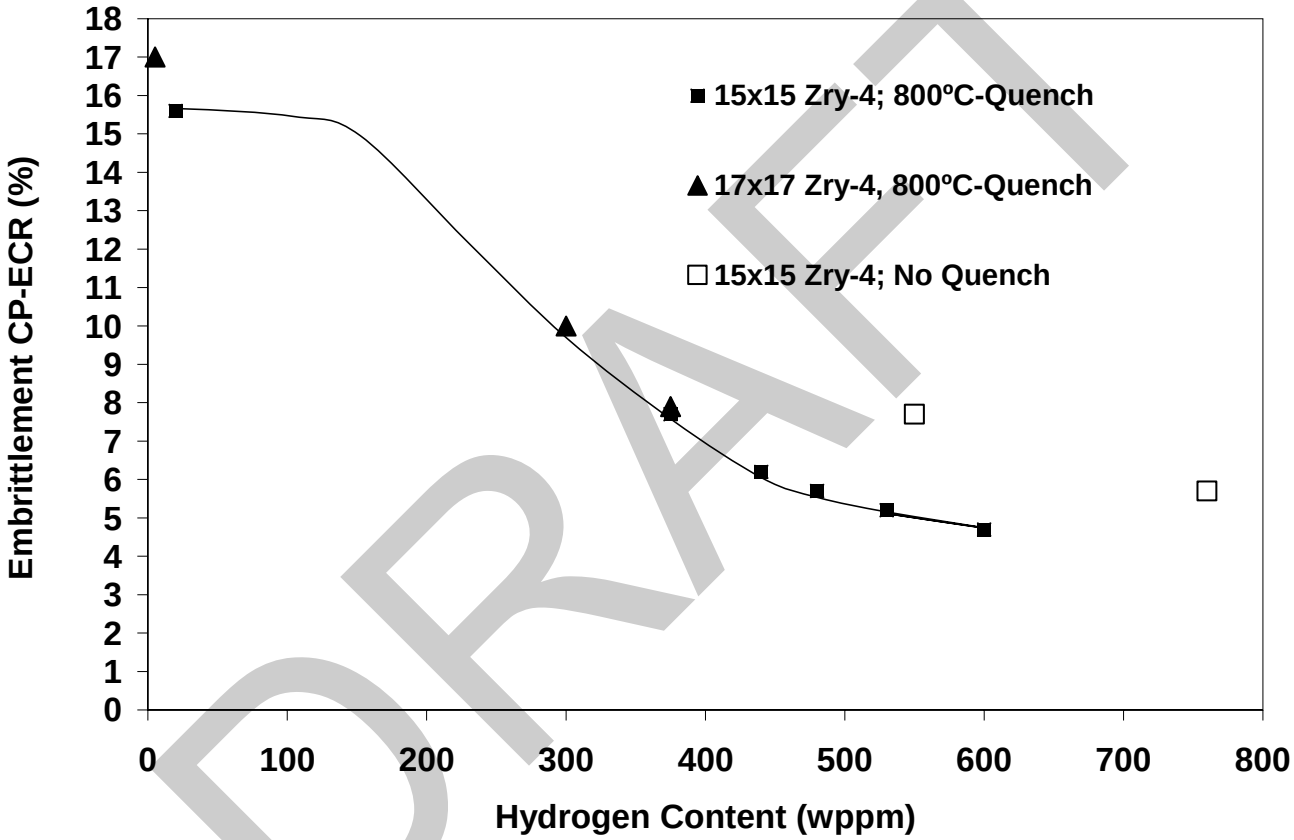

Figure 118a. Embrittlement oxidation level (CP-ECR) vs. hydrogen content for 17×17 Zry-4 and 15×15 HBR-type Zry-4 oxidized at ≤1200ºC, cooled at 11-13ºC/s to 800ºC and quenched. Results for samples with large circumferential distributions in hydrogen content (±100 wppm) are not included in this figure.

The test results show that slow cooling gives a small enhancement in ductility that increases the ductile-to-brittle transition CP-ECR for a given hydrogen content. At 7.7% total transient CP-ECR, the hydrogen content needed to embrittle the cladding appears to increase from ≈370 wppm to ≈550 wppm.

4.3 Discussion on cooling rate and quench temperature effects

Results similar to those in Table 52 were generated by CEA-AREVA-EdF. Preliminary results were presented by Mardon [27] in July 2005, and additional results were presented by V. Maillot et al. [28]. The tests were performed by CEA with prehydrided (600 wppm) 17×17 Zry-4 samples oxidized to ≈6.2% ECR based on the measured weight gain (i.e., measured ECR). A comparison between ANL and CEA test samples, test conditions, and results is given in Table 53. If the cladding materials and test conditions were the same, one would expect the ANL samples to be more ductile because of the lower hydrogen content. However, the cooling rate prior to quench appears to have a dominant effect on the post-quench ductility for samples quenched at 600-700ºC. The cooling time from 1200ºC to 800ºC is much longer (≈1000 s) for the CEA tests as compared to the ANL tests (38 s). However, both ANL and CEA data sets indicate the same results for Zry-4 samples quenched at 800ºC: the samples were brittle. The 38 s cooling time for the ANL tests is long enough for oxygen redistribution during the partial phase change from beta-to-(alpha + beta) in this temperature range. Based on the work of Brachet et al. [29], the beta-to-alpha phase transformation is expected to be ≈50% complete at 800ºC for Zry-4 with as-fabricated levels of oxygen and with 300-600 wppm hydrogen. The ANL and CEA post-oxidation ductility data are also consistent for samples that were slow cooled from 1200ºC to RT, even though the total cooling time from 1200ºC to 150ºC was much greater for the CEA samples. Both cooling scenarios appear to give hydrogen enough time to come out of solution and precipitate as fine hydrides outside the low-oxygen-content prior-beta material responsible for ductility.

The primary differences between the two sets of results are for quench temperatures of 700ºC and 600ºC. The ANL results show no enhancement in post-quench ductility for quench at these temperatures for a cooling times of 33 s (800→700ºC) + 50 s (700→600ºC) = 83 s, as compared to ≈1200 s for the CEA samples. Although the exponential-decay cooling curves for the ANL and CEA tests have the opposite curvature as compared to LOCA transients, the ANL cooling times appear to be more LOCA relevant. For the ANL cooling times, ductility is not increased by lowering the quench temperature from 800ºC to 600ºC. The ductility enhancement observed for samples cooled with no quench implies that time-dependent phenomena (e.g., hydrogen diffusion and precipitation) do indeed occur for long cooling times below 600ºC. This enhancement is important in data interpretation for the ANL and CEA tests, but more data are needed to establish the magnitude of this ductility enhancement for LOCA-relevant cooling rates and quench temperatures.

Vendor-predicted wetting (i.e., film boiling) temperatures – temperatures at which rapid cooling occur – are in the range of 400-800ºC. It is also possible that some small-break LOCAs are terminated without quench. Possible enhancement of ductility for quench temperatures in the range of 400-600ºC should be investigated with LOCA-relevant cooling rates prior to quench.

Table 53 Comparison between ANL and CEA Test Samples, Test Conditions, and Results for Post-quench Ductility of Prehydrided Zry-4 as a Function of Quench Temperature

Parameter	ANL	CEA	Comment
Cladding Test Samples	15×15 Zry-4 (low-tin) 0.77-mm wall ≈0.3-μm roughness 1370 wppm O 460±10 wppm H	17×17 Zry-4 (low-tin) 0.57-mm wall ≈0.3-μm roughness ≈1200 wppm O 600 wppm H	
Oxidation Test	Two-sided	One-sided (OD)	
Oxidation Time at 1200ºC, s	17	50	
Oxidation Time at ≥1180ºC, s	86	90	Includes heating and cooling ramps
Cooling Times, s 1200→800ºC 800→600ºC 600→150ºC	 38 83 >600	 1000 1180 9000	CEA values estimated from average cooling rates
Post-quench Ductility Offset Strain, % (Permanent Strain, %)			
800ºC Quench	0.8 (0.7)	1.0±0.2 (---)	Brittle
700ºC Quench	0.8±0.15 (0.5)	10.4±0.9 (---)	ANL Brittle CEA Ductile
600ºC Quench	1.0±0.2 (0.6±0.1)	13 (---)	ANL Brittle CEA Ductile
No Quench	3.5±1.4 (2.7±1.0)	6.6±2.4 (---)	Results remarkably close (ductile)

4.4 Summary of post-quench ductility results for prehydrided Zry-4

Hydrogen has a significant effect on reducing post-quench ductility. For HBR-type 15×15 Zry-4 oxidized to 5% CP-ECR at a maximum oxidation temperature of ≈1190ºC and quenched at 800ºC, the ductile-to-brittle transition hydrogen content was determined to be ≈600 wppm. For both 17×17 Zry-4 and HBR-type 15×15 Zry-4 oxidized to 7.5% CP-ECR at slow heating rates from ≈1150ºC to ≈1200ºC and no temperature overshoot, the ductile-to-brittle-transition hydrogen content was determined to be ≈370 wppm. However, for a more aggressive heating rate with an early temperature peak of 1216ºC, embrittlement at 7.5% CP-ECR occurred in HBR-type Zry-4 with a hydrogen content of ≈340 wppm. For 17×17 Zry-4 oxidized at 1200ºC to ≈10% CP-ECR, the embrittlement hydrogen concentration was determined to be ≈300 wppm.

As-received HBR-type 15×15 Zry-4 has a very high post-quench ductility at 7.5% CP-ECR following oxidation at ≈1200ºC and quench at 800ºC, while the same material prehydrided to 600-wppm hydrogen has essentially no post-quench ductility. The as-received and prehydrided samples were characterized and compared following oxidation and quench. The RT microhardness profile was significantly higher for the prehydrided Zry-4 sample as compared to the as-received sample. In particular, the 600-wppm-H Zry-4 has higher microhardness values in the prior-beta layer at the boundary of the alpha and beta layers. The ANL results are consistent with the results presented by Mardon et al. [21], demonstrating that hydrogen increases the hardness and oxygen-solubility limit in the Zry-4 prior-beta phase. This effect also results in higher oxygen concentration gradients and higher early-time diffusion rates of oxygen into the beta layer.

Although the embrittlement CP-ECR of as-fabricated alloys oxidized at 1200ºC was relatively insensitive to quench at 800ºC vs. slow cooling to RT, the same was not true for prehydrided HBR-type 15×15 Zry-4. Slow cooling to RT resulted in a small, but significant, increase in ductility. At 5% CP-ECR, slow cooling increased the hydrogen embrittlement threshold from ≈600 wppm to ≈750 wppm. At 7.5% CP-ECR, slow cooling increased the embrittlement hydrogen threshold from ≈370 wppm to ≈550 wppm.

Based on two series of tests conducted with prehydrided Zry-4 oxidized to 6% and 7.5% CP-ECR at ≈1200ºC, lowering the quench temperature from 800ºC to 700ºC to 600ºC had no effect on post-quench ductility for hydrogen contents of 450 wppm and 340 wppm, respectively. All quenched samples were brittle under these conditions, while the samples that were slow cooled from 1200ºC to RT retained a small level of ductility. These results indicate that the ductility enhancement arises from slow cooling at <<2ºC/s from 600ºC to RT. During this interval, hydrogen would have time to diffuse short distances out of the matrix of prior-beta grains and precipitate as fine hydrides. If this were the case, then the results suggest intrinsic hydrogen embrittlement for hydrogen dissolved in the prior-beta matrices, as well as enhancement in oxygen-induced embrittlement caused by increased solubility of oxygen in beta layers with dissolved hydrogen.

5 Results for High-Burnup Zry-4, ZIRLO, and M5

Two-sided oxidation tests were conducted at a target temperature of 1200ºC with defueled cladding samples sectioned from a high-burnup H. B. Robinson (HBR) rod with a rod-averaged burnup of 64 GWd/MTU. Characterization of the samples is presented in Section 5.1.1. The characterization of the as-irradiated samples includes gamma scanning, corrosion-layer-thickness measurements (metallography), hydrogen-content measurements (LECO), and oxygen-content measurements (LECO). Five oxidation tests were conducted at 1200ºC to ≈3-9% CP-ECR followed by slow cooling to room temperature (RT) and ring-compression testing at 135ºC. In the as-irradiated condition, these samples had a corrosion layer thickness in the range of 70-75 μm and a hydrogen content of 550 wppm. The samples were slow cooled to ensure that the three thermocouples welded to the test-train holder would remain intact. A sixth test was conducted with oxidation at 1200ºC to 7.5% CP-ECR and quench at 800ºC. This sample had a corrosion-layer thickness of 95 μm and a hydrogen content of 740 wppm. Post-oxidation characterization and ring-compression results are presented in Section 5.1.2 for the two-sided oxidation tests.

One-sided oxidation tests were conducted at 1200ºC with defueled cladding samples sectioned from another HBR rod, which had a similar location within the HBR assembly and the same burnup as the rod used to section the two-sided oxidation test samples. The purpose of these tests was to determine steam-oxidation layer growth and post-oxidation ductility of high-burnup cladding away from the balloon region. Four oxidation tests were conducted at 1200ºC to 5-9% CP-ECR (one-sided) with samples characterized by a 70-μm corrosion-layer thickness and 550-wppm hydrogen. Two tests were conducted were samples from lower grid span locations and ≈42-μm corrosion layers. The six samples were slow cooled following oxidation. Characterization of the as-irradiated Zry-4 cladding is given in Section 5.1.1 and the post-oxidation results are given in Section 5.1.3.

{Two-sided oxidation tests were conducted at 1200ºC with high-burnup ZIRLO (5.2) and M5 (5.3). Because of the lower hydrogen content of the ZIRLO and M5 cladding samples and the higher ductile-to-brittle transition CP-ECR values (19-20% vs. 14% for HBR-type Zry-4) for as-fabricated alloys, these samples were oxidized to higher CP-ECR values (7.5-13%) than the high-burnup Zry-4 samples (3-9%). Three samples were slow cooled to determine an upper bound on post-quench ductility. The fourth sample, which was oxidized to an intermediate CP-ECR, was quenched at 800ºC.}

5.1 Results for high-burnup H. B. Robinson 15×15 Zry-4

5.1.1 Characterization of high-burnup H. B. Robinson 15×15 Zry-4

Seven high-burnup HBR rods (64-67 GWd/MTU) were received by ANL in May 2001 for LOCA-related testing. Ruzaukas and Fardell [30] and Van Swam et al. [31] give a detailed description of the as-fabricated cladding, the irradiation history, the nondestructive testing results (eddy current, profilometry, fission-gas release, etc.), and the fuel isotopic content for these rods. EPRI, in cooperation with Framatome ANP Richland (now AREVA ANP), arranged for the shipment of the rods from the Robinson plant to GE Vallecitos Nuclear Center (VNC) to ANL. The seven rods, along with five other HBR rods, were sectioned into ≈0.9-m (≈35-in.) lengths by GE-VNC and shipped to ANL in DOE T-2 casks.

Characterization was performed on HBR rod A02 (67 GWd/MTU) as part of the NRC spent-nuclear-fuel program [32]. This rod was irradiated in an edge-next-to-corner position within the assembly. HBR rod R01 (67 GWd/MTU), also an edge-next-to-corner rod, was characterized for a spent-nuclear fuel program conducted by Sandia National Laboratories and sponsored by DOE, NRC, and international partners. Fuel ceramography, cladding metallography, and hydrogen concentration

measurements for A02 and R01 indicated significant circumferential temperature variation in the fuel and cladding. The circumferential variation in hydrogen content at 0.5-0.9 m above the core midplane was ±100 wppm based on four quadrant measurements. Metallography of circumferential sections, which showed regions of very dense hydrides across the cladding wall, suggested that the circumferential variation of hydrogen was >200 wppm. This variation was a concern for LOCA oxidation tests because experience with prehydrided HBR-type Zry-4 (see Figure 104) indicated that hydrogen did not homogenize in the circumferential direction during oxidation to 1200ºC for short test times corresponding to 5-7.5% CP-ECR. Large circumferential variation in hydrogen content would make interpretation of test data difficult.

Interior rods F07 and G10 were selected for two-sided and one-sided oxidation tests, respectively. These rods were not near the assembly edge, nor were they next to guide tubes. The expectation was that these rods would have smaller circumferential temperature variation and more uniform hydrogen concentration and hydride morphology. Based on data for rods A02 and R01, cladding at the fuel midplane was expected to have a corrosion layer thickness of ≈70 μm and a hydrogen content of ≈550 wppm. Based on the results for prehydrided HBR-type Zry-4 (see Figures 109 and 110), embrittlement was anticipated for samples with >600-wppm hydrogen oxidized at 1200ºC to 5-7.5% CP-ECR. These were important factors in the decision to section oxidation samples primarily from near the core midplane.

The fuel midplane is located near the top of grid span #3 and close to one end of the middle fuel-rod segment. It is labeled in the gamma scanning profile for the middle segments of rods F07 (Figure 119) and G10 (Figure 120); the locations of grid spacer #4 and grid span #4 are also labeled. The gamma-scan results were used to select samples from uniform burnup regions, away from the cut ends and away from regions under grid spacers.

The sectioning diagram for characterization samples and test samples for two-sided oxidation tests is show in Figure 121. The same basic sectioning diagram was used for the one-sided tests, except that the test samples were longer (Figure 122). The characterization results for rods F07 and G10, along with the A02 and R01 results, are summarized in Table 54. For short (1.5-mm-long) F07 cladding samples, the circumferential variation in hydrogen content was in the range of ±70 to ±90 wppm (standard deviation of four data points per location). Taking the average of the eight sets of hydrogen readings, a reasonable hydrogen content to use for the near-midplane samples is 550±100 wppm (includes circumferential and axial variations in hydrogen concentration) for oxidation test samples sectioned from a span of 140 mm from near the fuel midplane. This hydrogen level is consistent with the hydrogen measurement for the G10 near-midplane sample (550±90 wppm) and the A02 near-midplane sample (580±65 wppm). These hydrogen concentrations are referenced to the weight of the corroded cladding. Converting to hydrogen concentration for the weight of the cladding metal alone would result in a small increase in hydrogen concentration. However, this correction was not made because of the uncertain amount of corrosion layer lost during cutting and snipping used to prepare small samples for LECO hydrogen determination.

The F07 hydrogen measurement (545±90 wppm) taken at 320 mm above the fuel midplane is consistent with the R01 measurement (550±80 wppm) taken at 360 mm. The F07 measurement (800±110 wppm after high-temperature oxidation) taken at 650 mm above the fuel midplane is higher than the A02 and R01 measured values with comparable corrosion-layer-thickness values. Based on the corrosion layer thickness (95 μm) for the F07 sample at this elevation, a hydrogen content of 730-750 wppm was expected. However, when corrected for the sample weight loss due to spallation of the corrosion layer during the oxidation test, the hydrogen content would be reduced from 800 wppm to ≈715 wppm. Given

the uncertainty in this measurement, a hydrogen content of 740±110 wppm was chosen on the basis of scaling the A02 and R01 results.

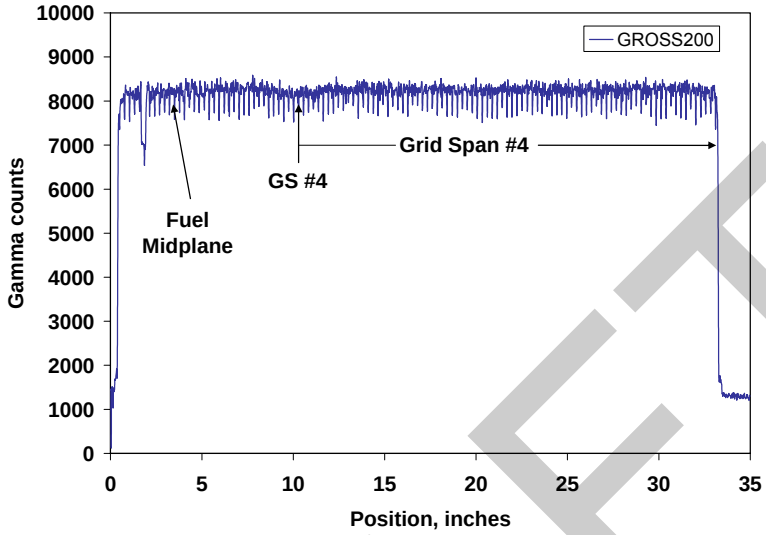

Figure 119. Gamma scan profile for HBR rod F07, from which samples were sectioned for hydrogen-content analysis, oxygen-content analysis, metallography, and two-sided oxidation tests.

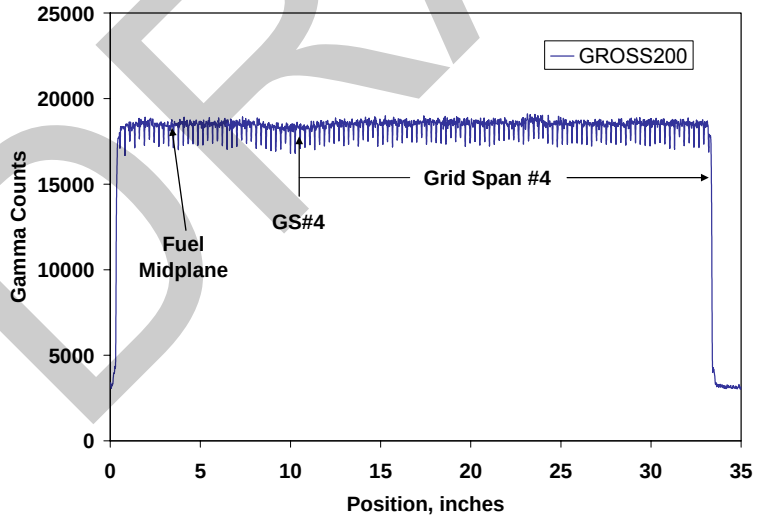

Figure 120. Gamma scan profile for HBR rod G10, from which samples were sectioned for hydrogen-content analysis, oxygen-content analysis, metallography, and one-sided oxidation tests.

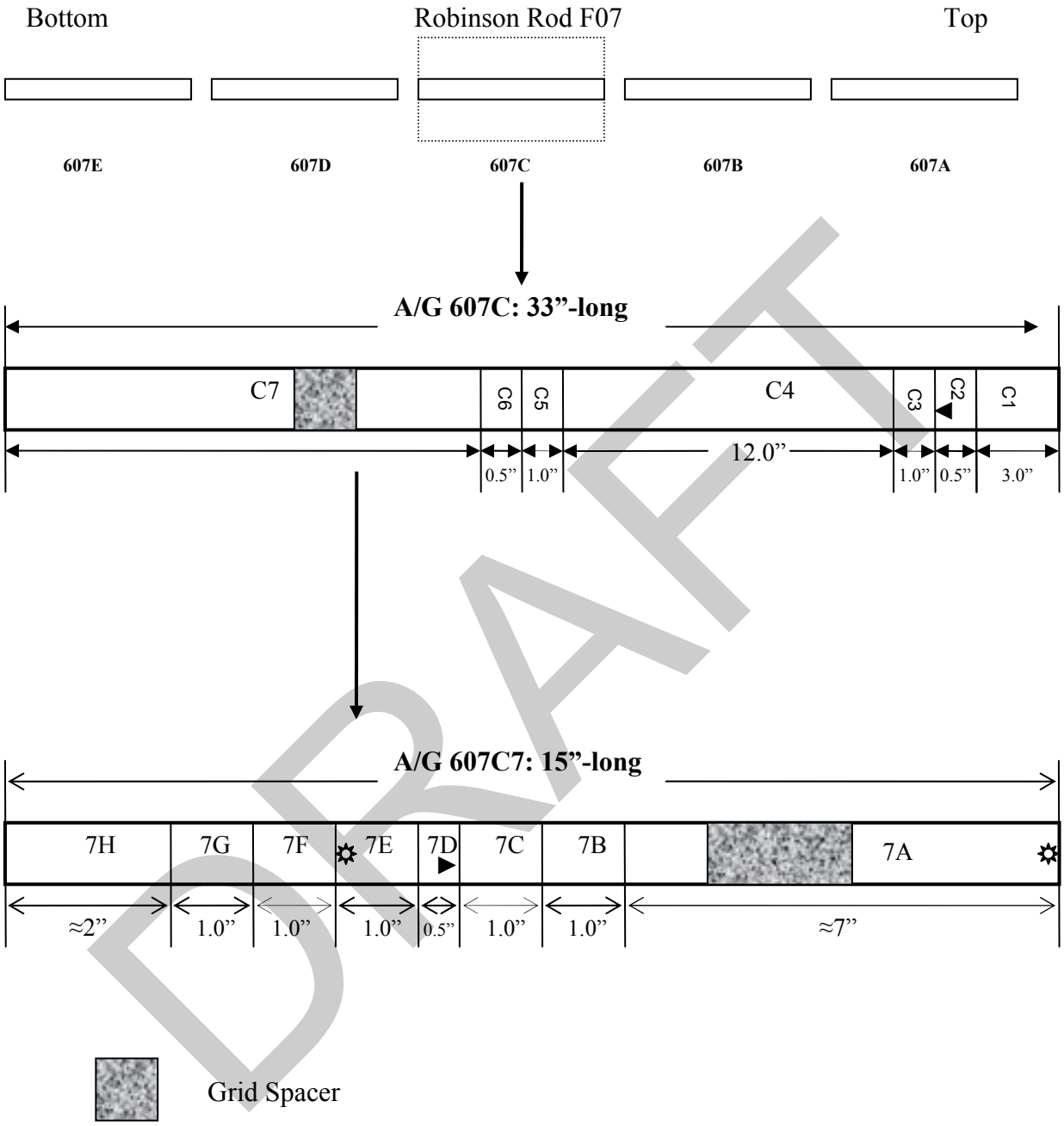

Figure 121. Sectioning diagram for characterization samples and two-sided-oxidation test samples. Eight 1.5-mm-long hydrogen-content samples were cut from 7H. One 13-mm-long sample (7D) was prepared for metallography, one 25-mm-long sample was cut for hydrogen and oxygen analyses (7E), and four 25-mm-long samples (7B, 7C, 7F, and 7G) were sectioned from near the core midplane for oxidation tests. C2 and C6 were used as metallography samples, and C3 and C5 were used as oxidation test samples.

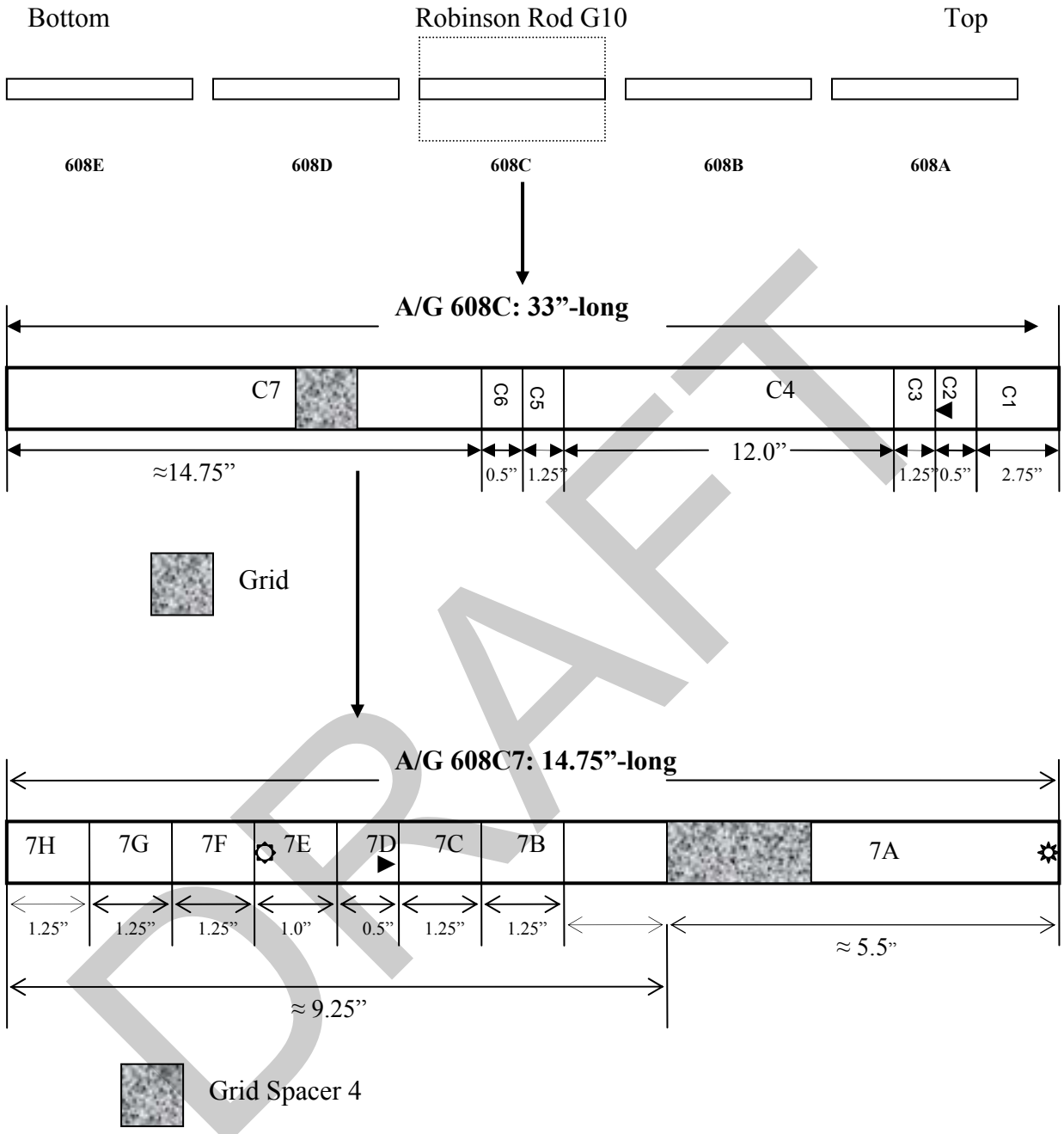

Figure 122. Sectioning diagram for characterization samples and one-sided-oxidation test samples. Sample 7E was used for hydrogen and oxygen analysis. Sample 7D was used for metallographic analysis. Four 32-mm-long samples (7B, 7C, 7F, and 7G) were sectioned from near the core midplane for oxidation tests.

Table 54 Corrosion Layer Thickness and Hydrogen Content Results for H. B. Robinson Rods F07 and G10 and for Rods A02 and R01. Axial locations are relative to the midplane of the 3658-mm-long fuel column.

Axial Location Relative to Fuel Midplane. mm	Rod F07 H Content (Corrosion Layer)	Rod G10 H Content (Corrosion Layer)	Rod A02 H Content (Corrosion Layer)	Rod R01 H Content (Corrosion Layer)
-920		≈360[a] (≈40[a])		
-580		≈400[a] (44±2)		
±50	545±85 wppm 530±80 wppm 530±90 wppm 535±85 wppm 555±85 wppm 575±80 wppm 535±80 wppm 565±70 wppm 550±100 wppm (71±5 μm)	550±90 wppm (68±2 μm)	580±65 wppm (70 μm)	
+320	545±80 wppm (74±5 μm)			
+360				550±180 wppm (77 μm)
+510				650±150 wppm (89 μm)
+650	740±110 wppm[a] (95±4 μm)			
700			750±90 wppm (98 μm)	
740				770±125 wppm (98 μm)

[a]Estimated by interpolation/extrapolation and scaling. Hydrogen measurements following oxidation and ring-compression tests were higher for rod F07 at +650 mm (800±110 wppm) due to weight loss from corrosion-layer spalling and higher for rod G10 at -920 mm (550±70 wppm) and at -580 mm (570±70 wppm) due to inner-surface hydrogen pickup during one-sided oxidation tests.

The corrosion layer thicknesses measured for rods F07 and G10 are in good agreement with those measured for rods A02 and R01 at the axial locations examined. For the F07 and G10 samples oxidized and slow cooled, the corrosion layer thickness is ≈70 μm (68-74 μm). The two-sided oxidation sample that was quenched had a corrosion layer thickness of 95 μm.

Half of sample 7E in Figure 121 was sectioned for LECO oxygen determination. The measured oxygen concentration (2.08±0.19 wt.%) is in good agreement with the ≈70-μm corrosion layer thickness if the Pilling-Bedworth ratio (1.75) recommended by Van Swam et al. [33] is used for the HBR corrosion layer. The 1.75 ratio is consistent with ≈10% porosity in the HBR corrosion layer.

Detailed characterization was performed for the midplane region of the F07 rod to determine the fuel, fuel-cladding bond, corrosion layer, and hydride morphology. Figure 123 shows a low magnification image of the fuel morphology. The central darkened region is not symmetric with respect to the center of the pellet. This result indicates asymmetric power distribution and fuel temperature, as well as circumferential variation in cladding temperature.

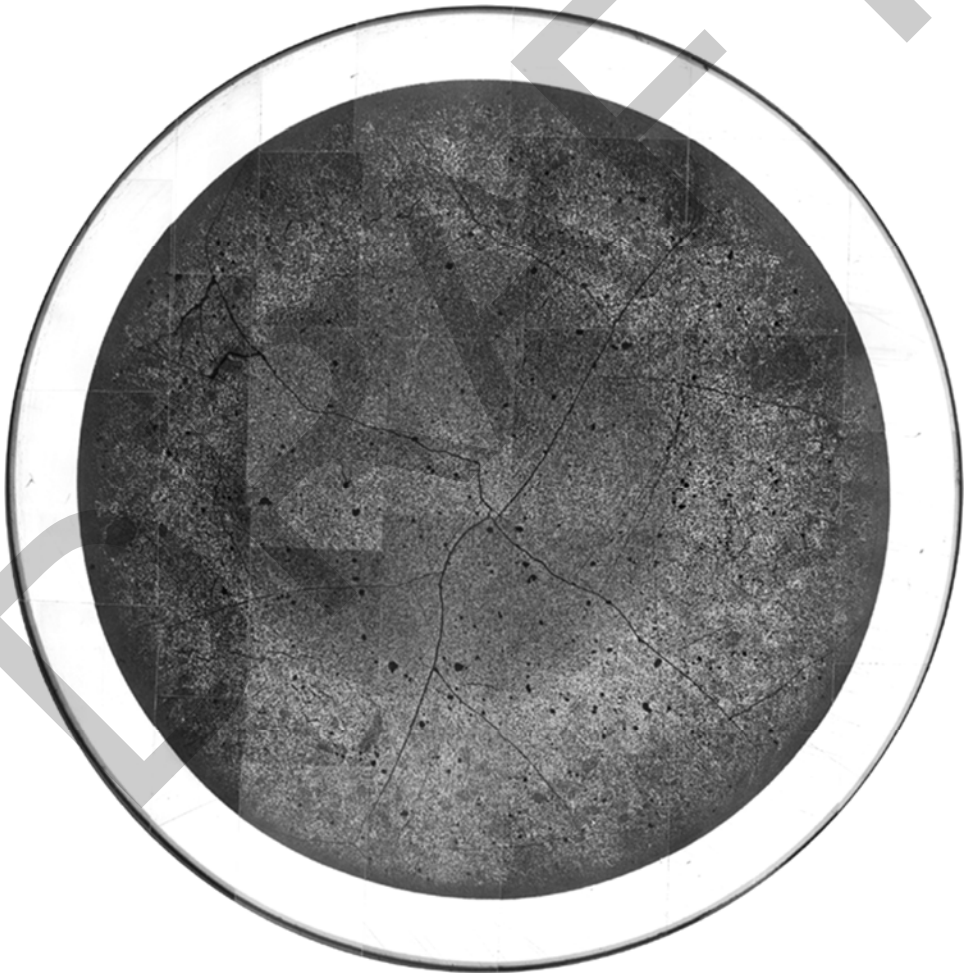

Figure 123. High-burnup HBR fuel morphology for the fuel midplane cross section of rod F07 showing indications of asymmetric power and temperature distributions relative to the center of the pellet.

The fuel-cladding bond appears to be well developed at the F07 rod midplane. This finding is consistent with characterization results for the A02 and R01 HBR rods. Figure 124 shows the fuel-cladding bond within one circumferential sector of the fuel shown in Figure 123. The bond thickness is 11±4 μm. A higher magnification image is shown in Figure 125 for the fuel-cladding bond in rod A02. The fuel-cladding bond layer remains intact and adherent to the cladding inner-surface after nitric-acid defueling. This bond layer has been demonstrated for high-burnup Limerick BWR cladding (see Figure 126). It is an additional source of oxygen, beyond the oxygen from steam, during two-sided oxidation tests. For one-sided (outer-surface) oxidation tests, it is the primary source of oxygen on the inner surface of defueled cladding. According to Une et al. [34], the bond layer is primarily ZrO_2 with some UO_2 in solid solution. Whether or not all of the UO_2 in the bond remains following nitric-acid defueling is not clear.

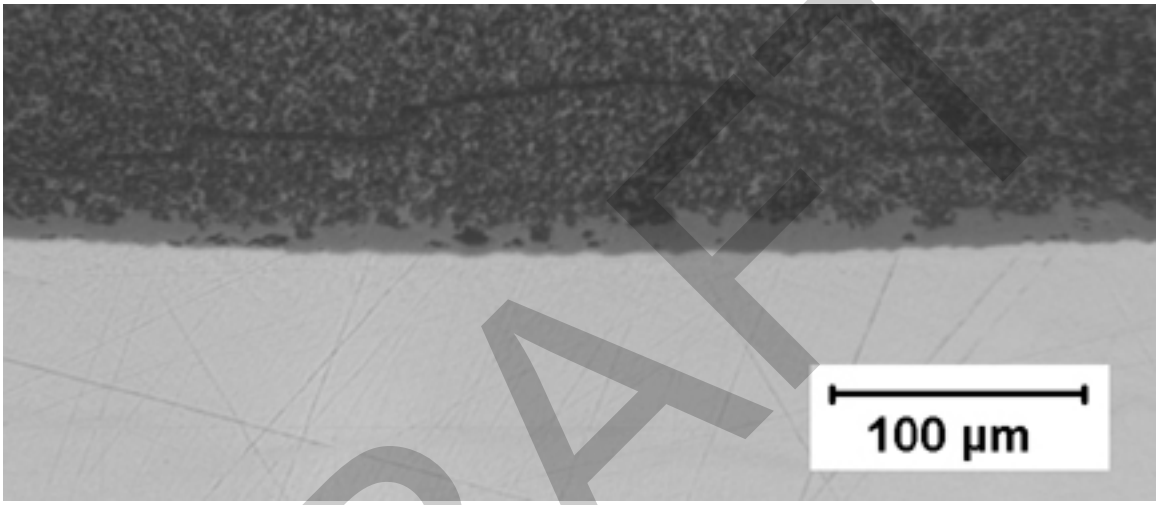

Figure 124. Fuel (dark region), cladding (light region), and fuel-cladding bond layer (gray) at the midplane of HBR rod F07. The image is a magnification of a small region from the fuel cross section shown in Figure 123.

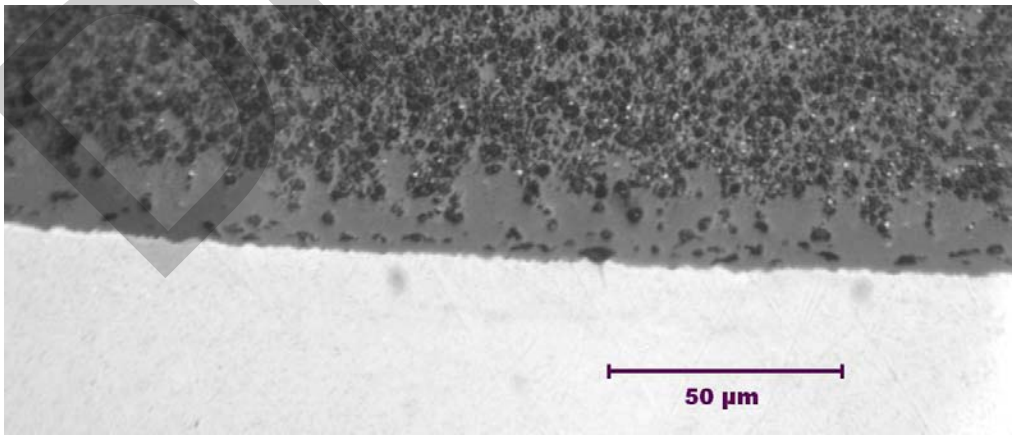

Figure 125. High-magnification image of fuel-cladding bond layer at the fuel midplane of HBR rod A02.

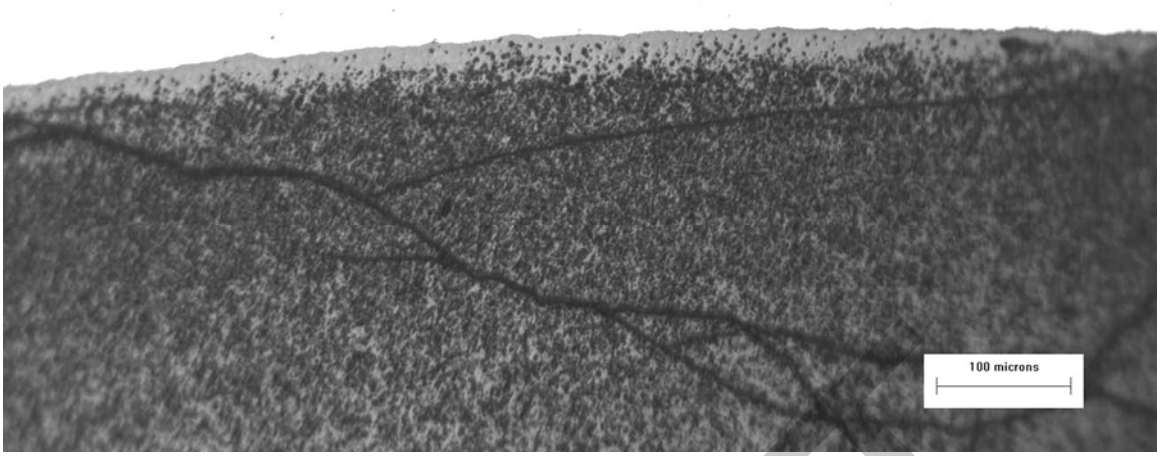

(a)

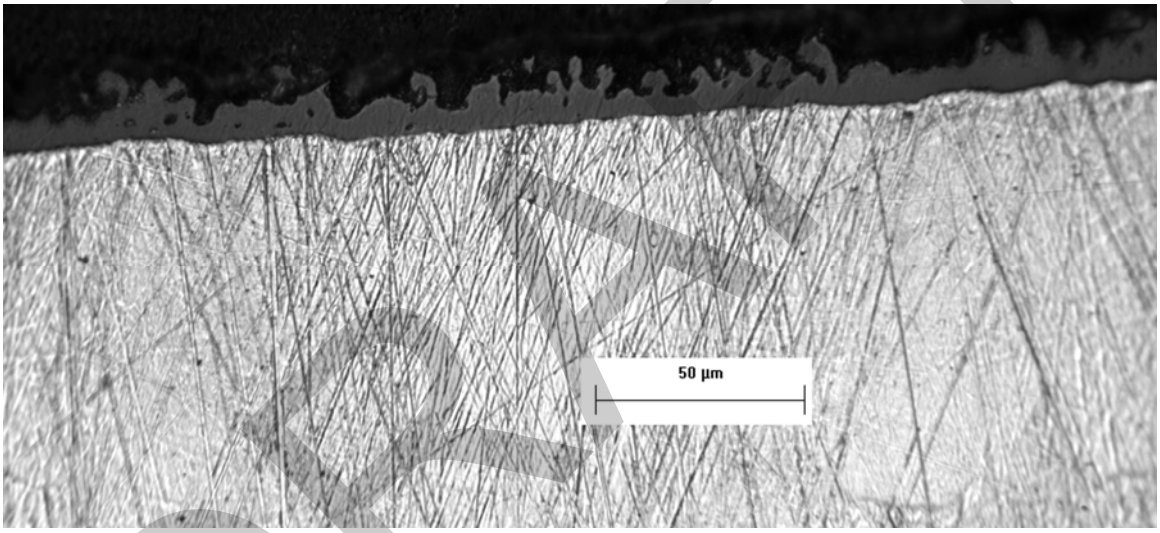

(b)

Figure 126. Images of high-burnup Limerick BWR fuel-cladding bond at fuel-midplane location: (a) prior to defueling in nitric acid and (b) after defueling in nitric acid.

High-magnification images were taken from three axial locations of the HBR rod F07 to determine the corrosion layer thickness, the cladding metal thickness, and the hydride distribution and morphology. At each axial location, eight circumferential regions were magnified to obtain the data. The corrosion layer thickness was measured to be 71±5 µm at the midplane (in grid span #3); 74±5 µm at 320 mm above the midplane (in grid span #4); and 95±4 µm at 650 mm above the midplane (in grid span #4). From the metallography, we determined that the average cladding wall thickness at the midplane was 0.712 mm for rod F07 and 0.720 mm for rod G10. These wall thicknesses were used in the determination of test times and CP-ECR values. Samples of metallographic images of the corrosion layer at three relevant axial locations along rod F07 are shown in Figure 127.

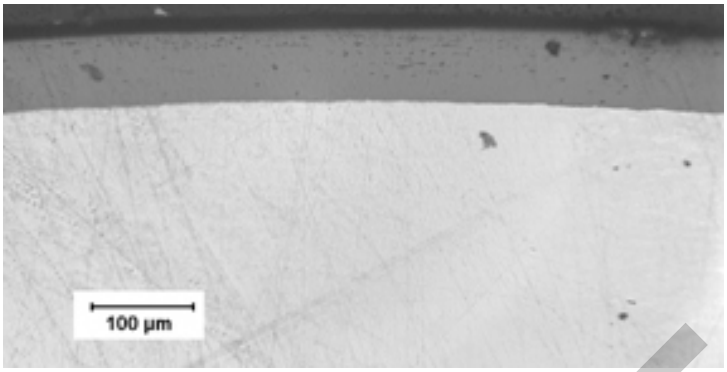

(a) Midplane

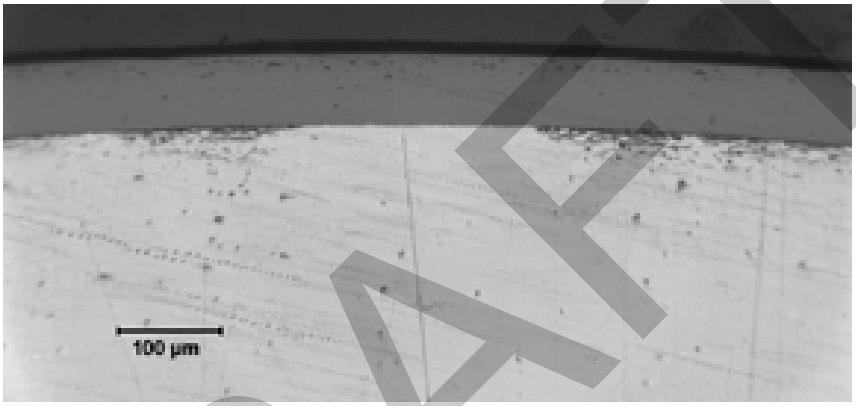

(b) 320 mm above midplane

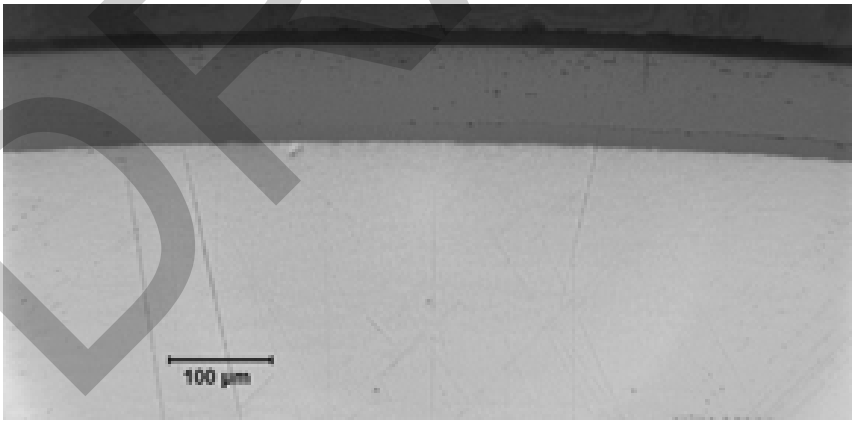

(c) 650 mm above midplane

Figure 127. Outer-surface corrosion layer for two-sided-oxidation test samples from HBR rod F07: (a) fuel midplane (71 µm); (b) 320 mm above midplane (74 µm); and (c) 650 mm above midplane (95 µm).

Hydride distribution and morphology are important parameters for oxidation and post-oxidation ductility tests. Images of etched samples are shown in Figure 128 for the three axial locations of interest for HBR rod F07. Of the eight images taken at each axial location, no unusual hydride morphology was observed.

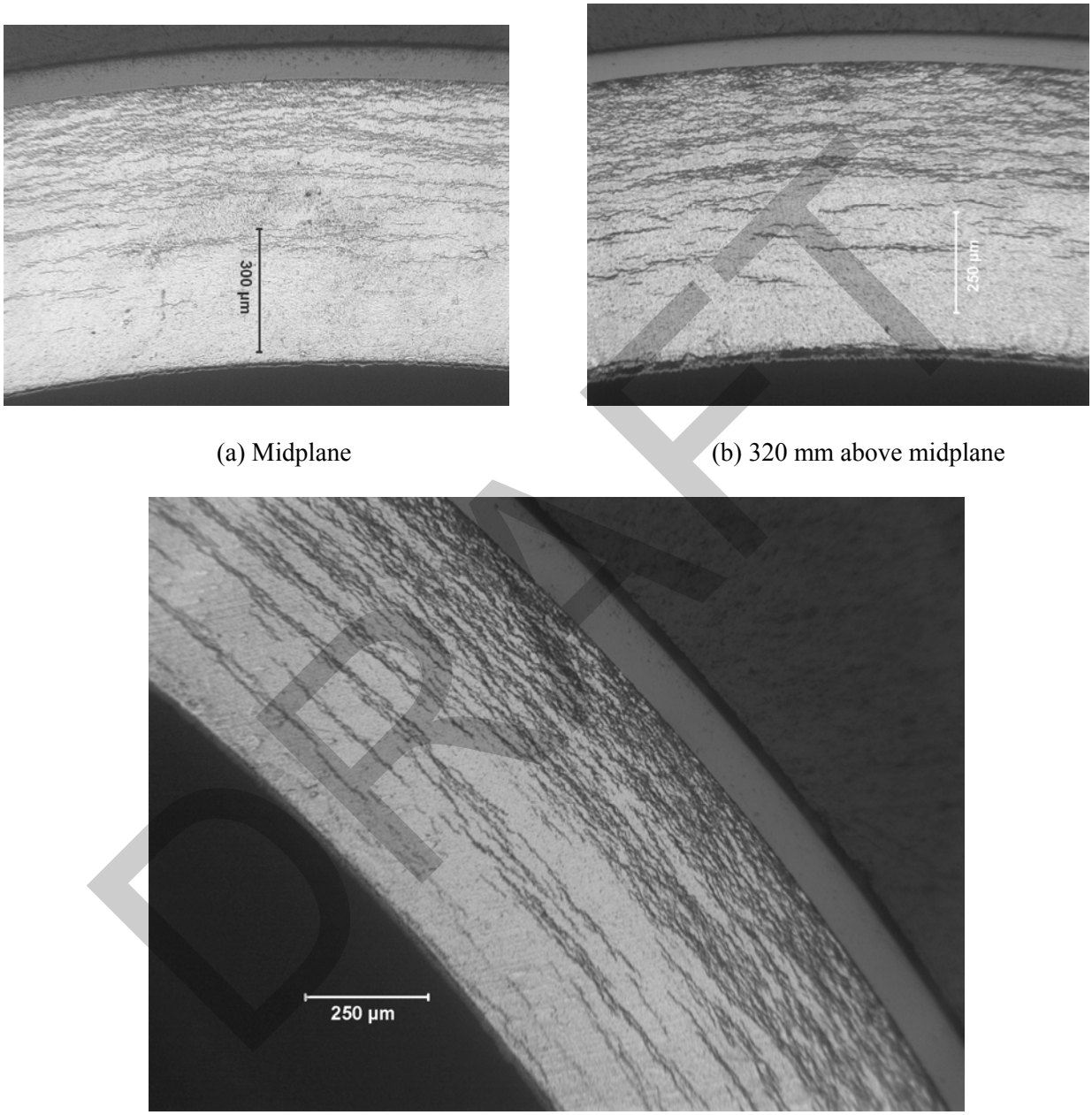

(a) Midplane

(b) 320 mm above midplane

(c) 650 mm above midplane

Figure 128. Hydride distribution and morphology in HBR rod F07 cladding near locations used to section two-sided-oxidation test samples: a) fuel midplane (550-wppm H); b) 320 mm above midplane (550-wppm H); and c) 650 mm above midplane (740-wppm H).

For HBR Rod G10, from which one-sided oxidation samples were sectioned, metallographic images from etched cladding areas at the fuel midplane location revealed areas of typical (Figure 129a) and atypical (Figure 129b) hydride distribution and morphology. The hydrides in Figure 129b appear to be much denser across the cladding wall and appear to have more hydrogen than the region shown in Figure 129a. This observation was confirmed for rod R01, which had circumferential variations of 450-770 wppm hydrogen with atypical hydride morphology within about 50% of the cross section.

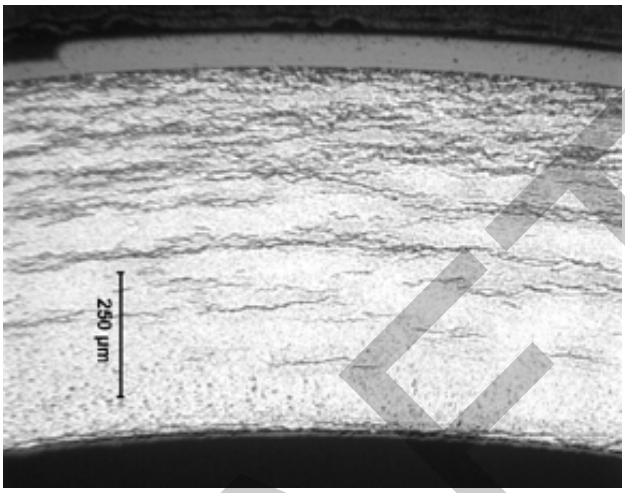

(a) Typical hydride morphology

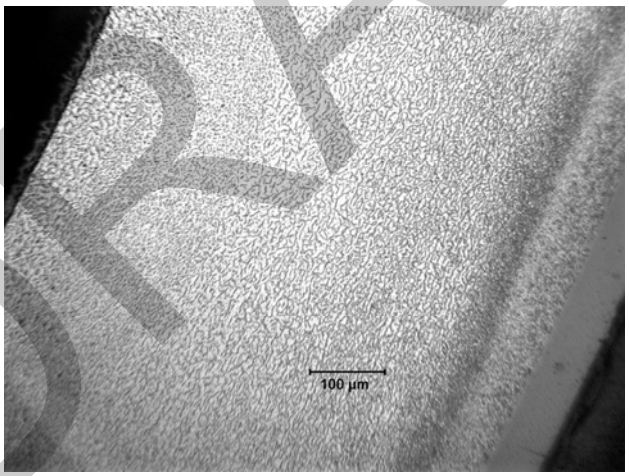

(b) Atypical hydride morphology

Figure 129. Hydride distribution and morphology in HBR rod G10 cladding at the core midplane: (a) typical hydride distribution across cladding wall and (b) atypical hydride distribution with a very dense hydride band near the outer surface and smaller dense hydrides across the wall.

Table 55 summarizes the data used to plan and interpret the test results for the two-sided and one-sided oxidation tests.

Table 55 Summary of Cladding Characterization for HBR Fuel Rod Segments Used for Pre- and Post-test Analysis of Two-sided and One-sided Oxidation Tests

Test Type	Sample ID	Corrosion Thickness, μm	Corrosion ECR, %	Hydrogen Content, wppm	Cladding Thickness, mm	Cladding OD,[a] mm
Two-sided	Rod F07 C7B, C7C C7F, C7G	71	5.4	550±100	0.712	10.58
Two-sided	Rod F07 C5	74	5.6	550±100	0.714	10.58
Two-sided	Rod F07 C3	95	7.1	740±110	0.702	10.54
One-sided	G10 C7B, C7C C7F, C7G	68	5.1	550±100	0.720	10.60
One-sided	D3 D5	44 ≈40	3.3 ≈3.0	≈400 ≈360	0.740 0.742	10.65 10.65

[a]Deduced from interpolation of outer diameters reported in Ref. 30 minus two times the corrosion layer thickness measured by ANL. A reasonable value to use for all these samples is 10.6 mm for normalizing the offset and permanent displacements to determine strains.

5.1.2 Results of two-sided oxidation tests for high-burnup HBR 15×15 Zry-4

Six two-sided oxidation tests were conducted during January-February 2005 in the in-cell LOCA oxidation-quench apparatus. Because of the limited availability of the Alpha-Gamma Hot Cell (AGHC) at ANL, the tests had to be planned carefully and conducted quickly. If time had permitted, these tests would have been conducted sequentially with a full post-test data set (metallography and post-oxidation or post-quench ductility) from the previous test used to plan the next test. A new test train was constructed; benchmarked in an out-of-cell test with non-irradiated cladding samples to determine the temperature history and verify that the measured weight gain and oxide-layer thickness were within 10% of the CP predicted values; and benchmarked in an in-cell test with a nonirradiated cladding sample to demonstrate that the same weight gain results were obtained using the in-cell furnace. The weight gains measured following the out-of-cell and in-cell tests were in excellent agreement with the CP-predicted values. The thermal history for this test train is shown in Figure 130, along with times corresponding to CP-ECR values of 3-10% for the 0.77-mm wall of the as-fabricated cladding. In planning and conducting the in-cell tests, we adjusted the test times corresponding to the target CP-ECR values for the difference in cladding wall thickness (0.71 mm vs. 0.77 mm).

As described below, the corrosion layer was found to be partially protective with regard to growth of the high-temperature oxidation layer with time. Thus, the rate of oxidation of the corroded high-burnup cladding is somewhat lower than that of the as-fabricated cladding used to generate the temperature history in Figure 130. The lower oxidation rate corresponds to the lower heat-generation rate and lower cladding temperatures during the ramp from 300ºC to 1200ºC. Consequently, additional thermal benchmark tests were conducted after the in-cell tests were completed to better determine the temperatures to use for interpretation of the high-burnup results.

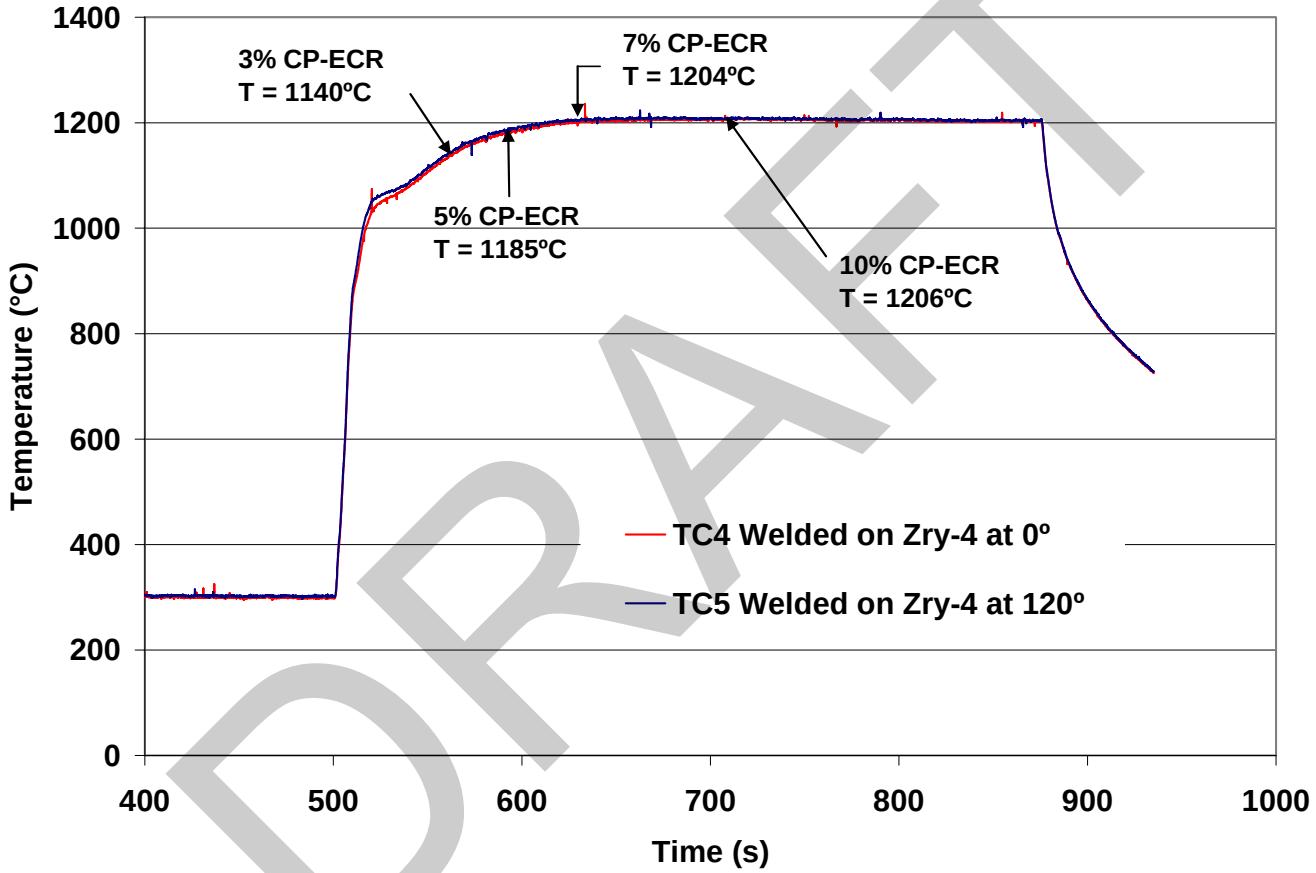

Figure 130. Out-of-cell thermal benchmark results for as-fabricated cladding in the test train used to conduct in-cell two-sided oxidation tests with high-burnup HBR cladding. The results were used to plan oxidation times for two-sided tests with high-burnup HBR cladding samples.

Another test train was constructed after running the in-cell tests, and the thermal benchmark was conducted by using the same controller parameters as were used for the in-cell tests. Two tests were conducted in sequence with thermocouples welded to the cladding metal: ramp from 300ºC to 1200ºC and hold long enough to grow a 37-μm oxide on the cladding inner and outer surfaces and slow cool to RT, and repeat the ramp-and-hold test with the oxidized cladding. Figure 131 shows the temperature ramp-and-hold results for initially bare cladding, and Figure 132 shows results for cladding with initial oxide layers of 37 μm on the inner and outer surfaces. By comparing the two figures, we determined that for pre-oxidized cladding, the temperature at the end of the rapid ramp is lower (1017ºC vs. 1060ºC), the time to reach the hold temperature is about the same (140 s vs. 130 s), and the hold temperature is slightly lower (1193ºC vs. 1201ºC). Temperatures from these two benchmark runs are compared at relevant in-cell test times in Table 56 under the columns for the bare-cladding results (HBRU#73A) and the pre-oxidized cladding results (HBRU#73B). A small correction was then made to the temperature history for

Table 56 Thermal Benchmark Results for Test HBRU#44 with As-fabricated Zry-4 (Figure 130), for Test HBRU#73A with As-fabricated Zry-4 (Figure 131), and for Test HBRU#73B with Pre-oxidized Zry-4 (Figure 133). Estimated temperatures for high-burnup test samples (HBRI) are given in column 3.

HBRI Test #	Test Time,[a] s	Deduced HBRI T, ºC	HBRU#44 (Figure 130) T, ºC	HBRU#73A (Figure 131) T, ºC	HBRU#73B (Figure 133) T, ºC
2	62	1110	1141	1136	1105
1	93	1169	1186	1180	1163
3	132	1196	1204	1196	1188
5	155	1197	1206	1201	1192
6	155	1197	1206	1201	1192
4	206	1198	1206	1201	1193

[a]From beginning of ramp at 300ºC to end of hold time.

pre-oxidized cladding by accounting for differences in test trains used to conduct the in-cell tests and the bare vs. pre-oxidized cladding thermal benchmarks. Also shown in Table 56 (under the heading HBRU#44) are the bare-cladding temperatures (see Figure 130) measured at relevant test times for the test train used to conduct the in-cell tests. The difference between the two test-train results for the same controller parameters and bare cladding samples is ≈5ºC. Thus, for interpretation of in-cell tests, the temperatures in Figure 131 were increased in gradually during the ramp to give a 5ºC increase in hold temperature. The results are plotted in Figure 133 and summarized in Table 57.

The temperature history in Figure 133 represents a lower bound during the temperature ramp for high-burnup samples tested in-cell. The heat of oxidation is proportional to the oxidation rate, which is proportional to the inverse of the oxide-layer thickness for dense oxide layers grown in steam at high temperature (see Equation 1). Even if the corrosion layer ($\delta_c \approx 70$ μm) and the fuel-cladding-bond oxide layer ($\delta_b \approx 10$ μm) grown at reactor temperatures were as protective as high-temperature-grown oxide layers, the initial heat generation would be proportional to $1/\delta_c + 1/\delta_b = 0.114\ \mu m^{-1}$. For the thermal benchmark test with pre-oxidized cladding, the initial heat generation rate is proportional to $2/(37\text{-}\mu m) = 0.054\ \mu m^{-1}$. Therefore, the initial heating rate in the thermal benchmark test is <50% of the initial heat

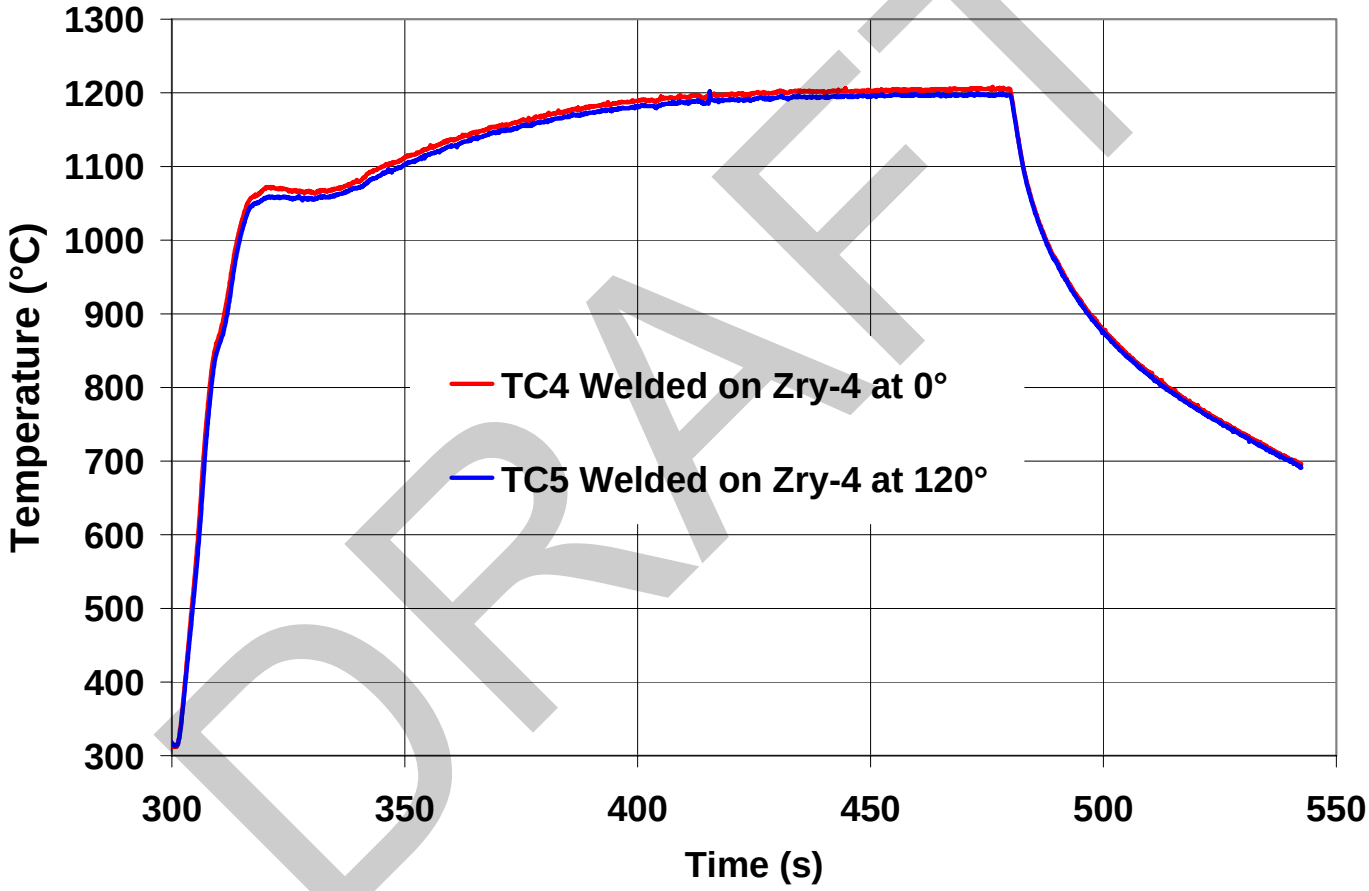

Figure 131. Results of thermal benchmark test conducted after the in-cell oxidation tests with another test train and with TCs welded onto the outer surface of as-fabricated HBR-type Zry-4 cladding. Controller parameters were the same as those used to generate Figure 130 results.

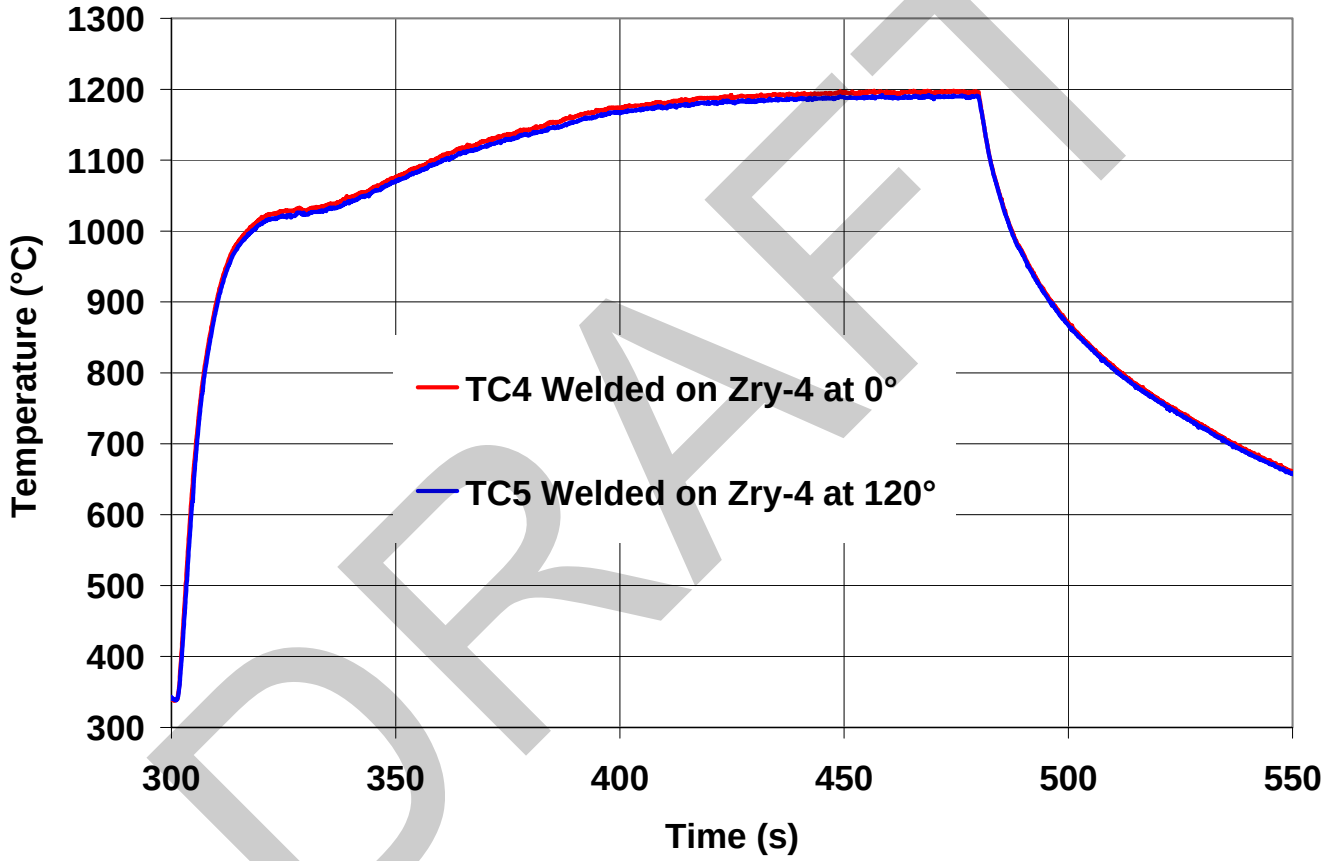

Figure 132. Thermal benchmark results for pre-oxidized HBR-type Zry-4 with TCs welded onto bare-cladding outer surface and with steam-induced oxide layers of 37 μm grown on the inner and outer surface of the cladding sample prior to the temperature ramp. Controller parameters were the same as those used to generate results in Figures 130 and 131.

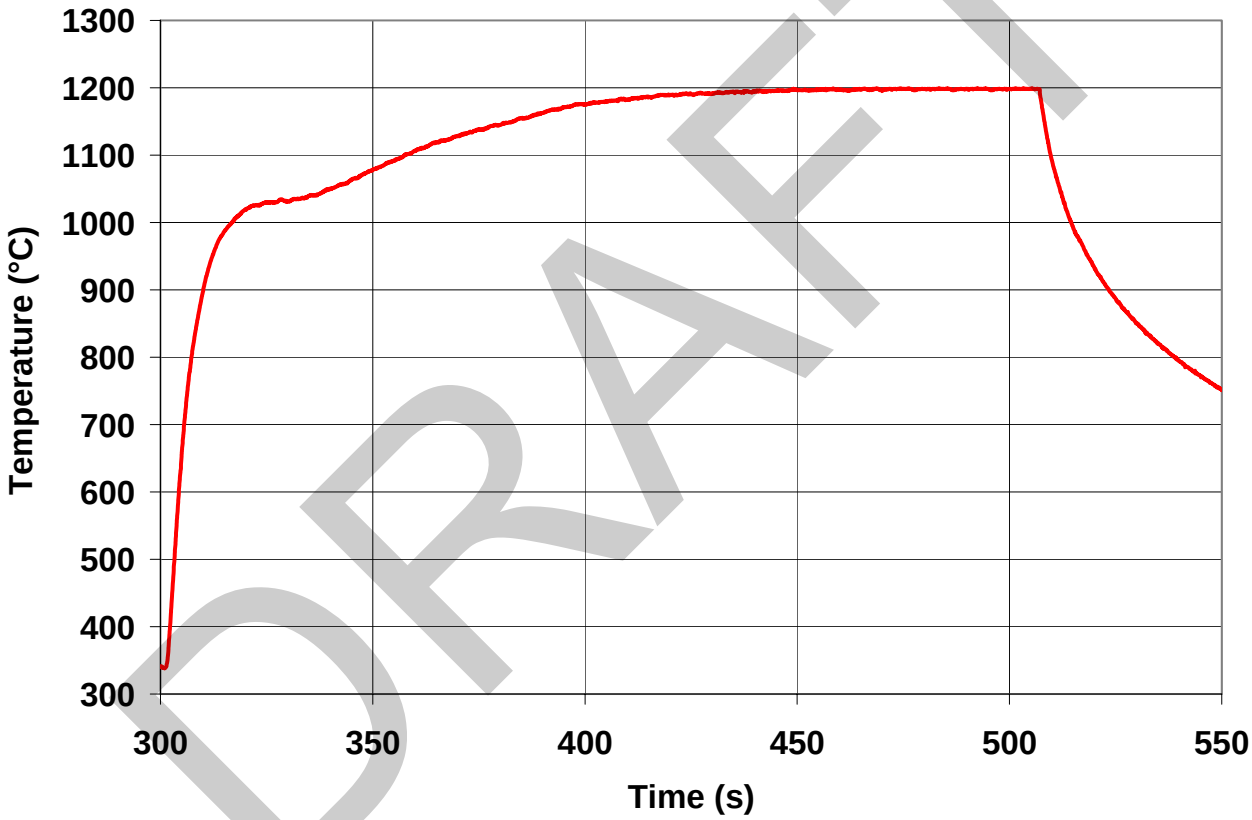

Figure 133. Temperature history used to calculate CP-ECR values and to interpret results for the in-cell two-sided oxidation tests conducted with high-burnup HBR Zry-4 cladding samples.

generated by the corroded high-burnup cladding during the in-cell tests. However, the temperature history in Figure 133 should be a reasonable lower bound because beyond a certain oxide thickness (≈10 μm) heat of oxidation is too small to have a significant effect on cladding temperatures during the heating ramp.

Table 57 Sample Characterization and Test Conditions for Two-sided Oxidation Tests Conducted with High-burnup HBR Zry-4 Cladding. SC is slow cooling, and Q is quench at 800ºC.

Test ID #	Hydrogen Content, wppm	Test Time,[a] s	Target CP-ECR, %	Corrected CP-ECR, %	Maximum T, ºC	Time at T ≥ 1180ºC, s	Cooling
2	550±100	62	3	2.7	1110	0	SC
1	550±100	93	5	4.3	1169	0	SC
3	550±100	132	7	6.4	1196	27	SC
5	550±100	155	8	7.4	1197	50	SC
6	740±110	155	8	7.5	1197	50	Q
4	550±100	206	10	9.3	1198	101	SC

[a]Includes time for ramp from 300ºC and hold time.

The target CP-ECR values were chosen by analysis of the post-quench ductility results for prehydrided HBR-type Zry-4. From Figures 100 and 101, we estimated that high-burnup cladding with 550 wppm hydrogen would be brittle at 5%< CP-ECR <7.5%. The effects of slow cooling on ductility were not known at the time the high-burnup HBR tests were planned and conducted. Tests were planned at lower (3% and 5%) and higher (7% and 10%) CP-ECR levels in order to bracket the expected ductile-to-brittle transition CP-ECR. Additional tests were conducted at 8% target CP-ECR after data for the first set of tests showed that ductility had been retained up to 7% target CP-ECR. Table 57 gives the test conditions for the two-sided oxidation tests, including the target CP-ECR values (based on Figure 130) and the corrected CP-ECR values (based on Figure 133).

Post-test measurements included sample weight, layer (corrosion, steam-oxide, and oxygen-stabilized alpha) thicknesses, hydrogen concentration, and post-test ductility at 135ºC. All test samples decreased in weight, indicating that corrosion-layer spallation (probably during cooling) resulted in greater weight loss than the gain due to oxygen pickup. The metallographic results are particularly interesting in that they reveal information regarding fundamental phenomena that influence oxygen pickup, oxygen diffusion, and post-test ductility. Based on the results of the oxidation tests with high-burnup Limerick BWR cladding (see Section 6.2 and Yan et al. [15, 35]), we concluded that the corrosion layer was non-protective and "transparent" to steam oxidation. However, the Limerick-cladding corrosion layer was only ≈10-μm thick (≈3-to-18 μm variation around the cladding circumference). Also, the one-sided oxidation tests with Limerick cladding were run for relatively long times (300-6000 s), which resulted in very thick outer-surface oxide layers. If the corrosion layer did have any effect on oxidation kinetics, it was not detectable for these sample and test conditions. In particular, the measured oxide layer thickness and the weight gain determined from layer thicknesses agreed quite well with CP-predicted values for as-fabricated cladding.

Table 58 summarizes the results of the steam-oxide-thickness measurements taken from metallographic images. Only the 7.4% and 9.3% CP-ECR oxide thicknesses are given, along with the corresponding weight gains. Because of problems encountered in mounting the lower CP-ECR samples and the difficulty in distinguishing the steam-oxide layer from the corrosion layer, the uncertainty for these samples was too high to yield reliable data. For the higher CP-ECR samples, the measured steam-oxide thickness on the outer surface of the cladding is clearly less than the inner-surface-oxide thickness and less than the CP-predicted thickness. The results indicate that the thick HBR corrosion layer is partially protective with respect to steam oxidation. The weight gains, determined from the metallographic results in Tables 58 and 59, are less than the CP-predicted weight gains. In terms of ECR based on these weight gains, the 7.4% CP-ECR sample had a measured ECR of 5.6%, and the 9.3% CP-ECR sample had a measured ECR of 7.8%. The difference in ECR is 1.5-1.8%.

Table 58 Results of Quantitative Metallography for Two-sided-oxidized, High-burnup HBR Zry-4 following Steam Oxidation. Includes oxide layer thickness (δ_{ox}) and measured ECR; data are from optical microscopy (OM) images at eight circumferential locations around sample cross section (see Figures 135-137 for images from one-of-eight locations for HBRI#4 and #5 samples).

Test ID #	Test Time,[a] s	Maximum T, ºC	CP-ECR, %	Measured ECR, %	CP-δ_{ox}, µm	Measured δ_{ox}, µm	
						OD	ID
2	62	1110	2.7	---	11	---	---
1	93	1169	4.3	---	18	---	---
3	132	1196	6.6	---	26	---	---
5	155	1197	7.4	5.6±0.2	30	19±2	26
6	155	1197	7.5	---	30	---	---
4	206	1198	9.3	7.8±0.4	38	28±4	38

[a]Includes time for ramp from 300ºC and hold time.

The effect of the fuel-cladding bond on the oxidation growth rate at the inner surface is less clear. This bond layer is only ≈11±4 µm thick, and like the thin corrosion layer on the Limerick cladding, its effect on oxide growth rate was not detectable. At 7-to-9% CP-ECR, the measured ID oxide layer equals the CP-predicted value, indicating that the thin fuel cladding bond is much less protective to steam oxidation than the thick corrosion layer.

Although the corrosion layer appears to slow down the growth of the OD high-temperature oxide, it does not appear to slow down the growth of the oxygen-stabilized alpha layer. Table 59 and Figure 134 show the measured OD and ID oxygen-stabilized alpha-layer thickness values, as compared to the CP-predicted values. Unlike the oxide layers, the OD and ID alpha layers are comparable and agree reasonably well with the CP-predicted values. The difference of 1-2 µm between measured and predicted OD alpha-layer thickness is not significant because of the uncertainty in the CP correlation due to the variable hydrogen pickup in the Cathcart et al. [13] samples. The slightly thicker (2 µm) OD vs. ID alpha

layer may or may not be significant. The results indicate that oxygen diffuses directly from the corrosion layer to the cladding metal, resulting in growth of the oxygen-stabilized alpha layer. Oxygen from this alpha layer is available for diffusion into the beta layer.

Table 59 Results of Quantitative Metallography for Two-sided-oxidized, High-burnup HBR Zry-4 following Steam Oxidation. Includes oxygen-stabilized alpha layer thickness (δ_α); data are from images at eight circumferential locations around sample cross section (see Figures 135 and 136 for OM images from one-of-eight locations for sample HBRI#5).

Test ID #	Test Time,[a] s	Maximum T, °C	CP-ECR, %	Measured ECR, %	CP- δ_α, µm	Measured δ_α, µm	
						OD	ID
2	62	1110	2.7	---	9	8.4	6.2
1	93	1169	4.3	---	16	14	12
3	132	1196	6.4	---	25	23	21
5	155	1197	7.4	5.6±0.2	29	27	25
6	155	1197	7.5	---	29	---	---
4	206	1198	9.3	7.8±0.4	37	35	33

[a]Includes time for ramp from 300ºC and hold time.

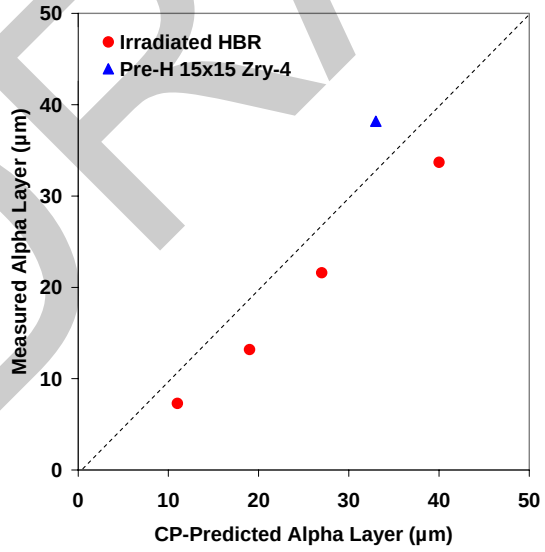

Figure 134. Measured average ([OD+ID]/2) alpha-layer thickness vs. CP-predicted value for high-burnup (550±100 wppm) HBR samples oxidized (two-sided) at 1100-1200ºC and prehydrided (600 wppm) HBR-type Zry-4 sample oxidized at ≈1200ºC to 7.5% CP-ECR.

Metallographic (optical microscopy, OM) images were taken of the oxidized high-burnup HBR Zry-4 samples. Higher quality OM images were obtained for the 7.4% and 9.3% CP-ECR samples. In addition, SEM images were taken of the 7.4% CP-ECR sample. Figure 135a shows a partial cross section emphasizing the outer surface of the 7.4% CP-ECR sample. The corrosion layer is visible, but its thickness is much smaller than the 71 μm of the as-irradiated HBR Zry-4. Some of this layer was consumed during the oxidation test, and most of it was lost during cooling (spallation). Also shown in Figure 135a are the oxide layer formed at high temperature, the oxygen-stabilized alpha layer, and part of the prior (previous) beta layer. Because the corrosion layer was not fully protective (numerous micro- and macro-cracks), the high-temperature oxide grew underneath the corrosion layer, which remained visible. Figure 135b shows the SEM image from another position along the 7.4% CP-ECR sample. The distinction between the corrosion layer and the high-temperature oxide layer is much clearer in the SEM image, which was then used to draw the boundary lines in Figure 135a.

Similar OM and SEM images were obtained for the inner-surface area of the 7.4% CP-ECR sample. Figure 136a shows the OM image, in which the oxide layer, the oxygen-stabilized alpha layer, and part of the prior-beta layer are clearly visible. No boundary is observed between the fuel-cladding-bond oxide and the high-temperature oxide. Figure 136b shows the SEM image for the 7.4% CP-ECR sample inner surface at another axial location.

The outer- and inner-surface oxide layers for the 9.3% CP-ECR high-burnup HBR Zry-4 sample are better viewed by using polished samples for OM imaging. Figure 137a shows the outer-oxide layer. The unevenness of the outer boundary and the morphology of this region suggest the presence of corrosion oxide, although the thickness is small due to partial loss of this layer. Because the epoxy was not vacuum-impregnated, there was a small gap between the outer surface and the epoxy, which allowed room for some of the corrosion layer to spall and drop below the imaged surface during grinding and polishing. Figure 137b shows the inner-surface oxide layer in the as-polished condition. There is no indication of a fuel-cladding bond layer in this image. Based on readings taken from eight circumferential areas, the average high-temperature oxide layer thickness is 28±4 μm for the outer-surface oxide and 38 μm for the inner-surface oxide (see Table 58). The variation in the outer-surface high-temperature oxide thickness is due to uncertainties in determining the interface between the corrosion layer and the high-temperature oxide layer, as well as the circumferential variation in oxide layer thickness.

The oxygen-stabilized alpha layer and the prior-beta layer are better imaged from etched surfaces. Figures 138a and 138b show the outer- and inner-surface regions, respectively, of these layers. The contrast between the oxygen-stabilized alpha layer and the prior-beta layer is quite good and allows for an accurate determination of the alpha-layer thickness. Based on readings from eight circumferential areas, the average alpha-layer thickness values (see Table 59) are about the same near the outer surface (35 μm) and the inner surface (33 μm).

Ring-compression tests were conducted at 135ºC and 0.0333-mm/s crosshead displacement rate with ≈8-mm-long samples sectioned from the oxidation and oxidation-quench samples. Offset displacements were determined from load-displacement curves and normalized to the cladding metal outer diameter (10.6 mm) to calculate offset strain. In addition, the outer diameter of the oxidized cladding was measured in the loading direction prior to, and after, compression testing. As is standard protocol for the ANL ring-compression tests, the tests were stopped after the first significant load drop to determine if through-wall failure along the length of the sample had occurred. Table 60 summarizes the results of the ring-compression tests.

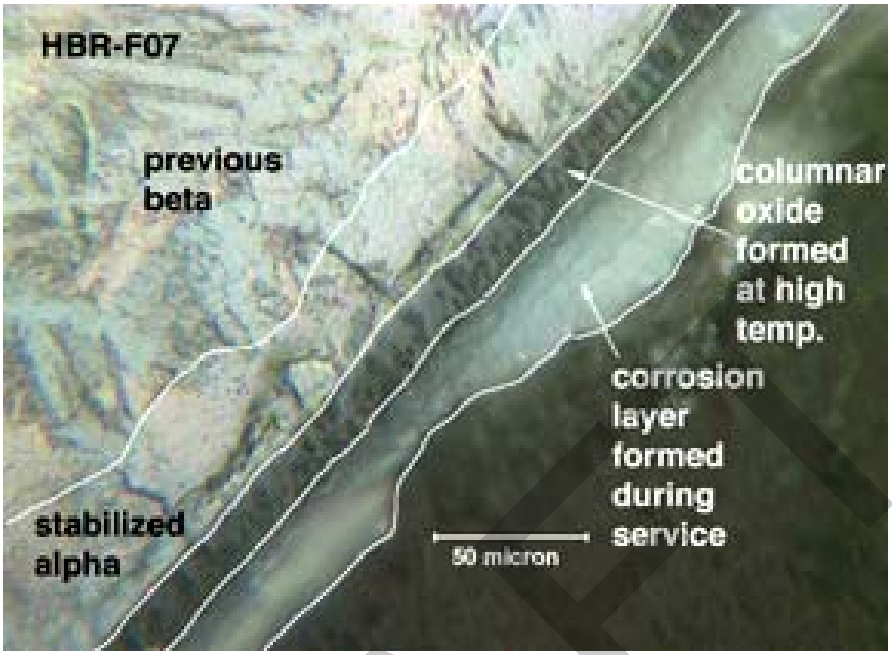

(a)

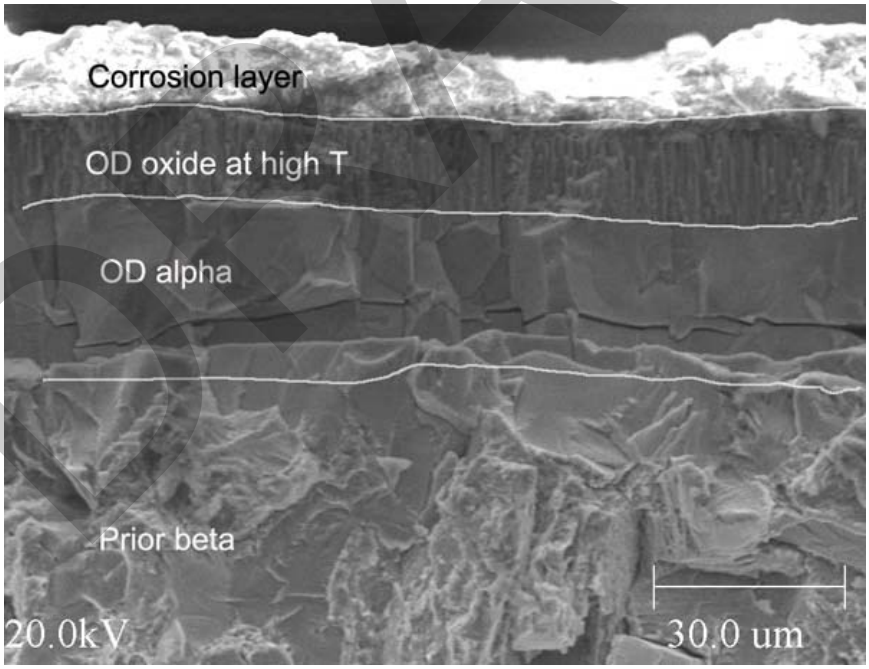

(b)

Figure 135. High-magnification images of the outer surface of high-burnup HBR Zry-4 sample following oxidation (two-sided) at 1200ºC to 7.4% CP-ECR and slow cooling to RT: (a) OM and (b) SEM.

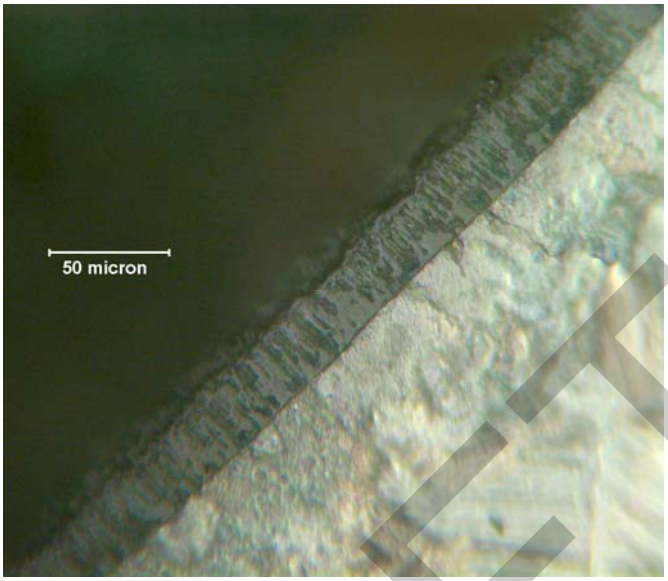

(a)

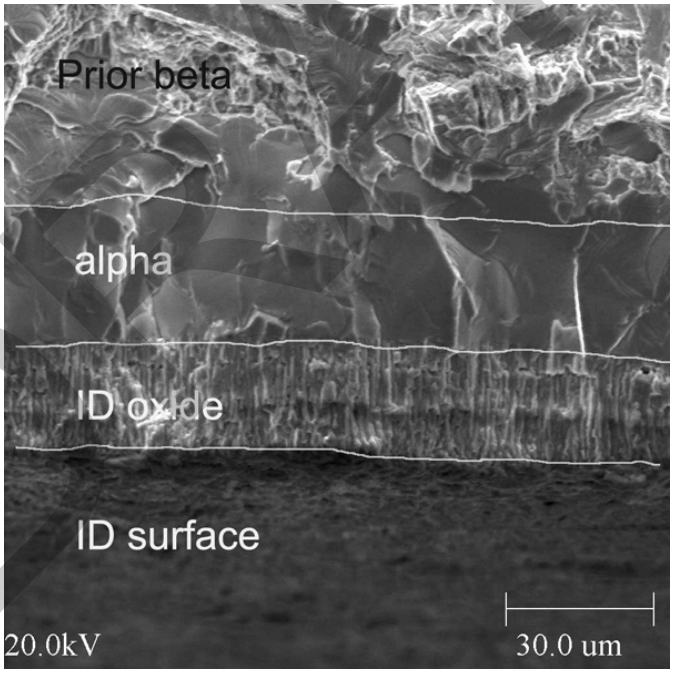

(b)

Figure 136. High-magnification images of the inner surface of high-burnup HBR Zry-4 sample following oxidation (two-sided) at 1200ºC to 7.4% CP-ECR and slow cooling to RT: (a) OM and (b) SEM.

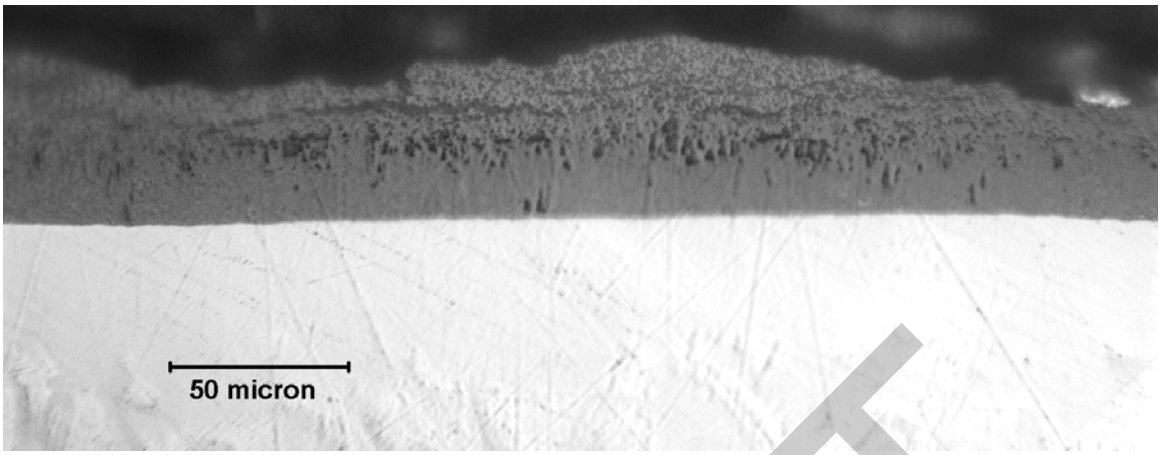

(a)

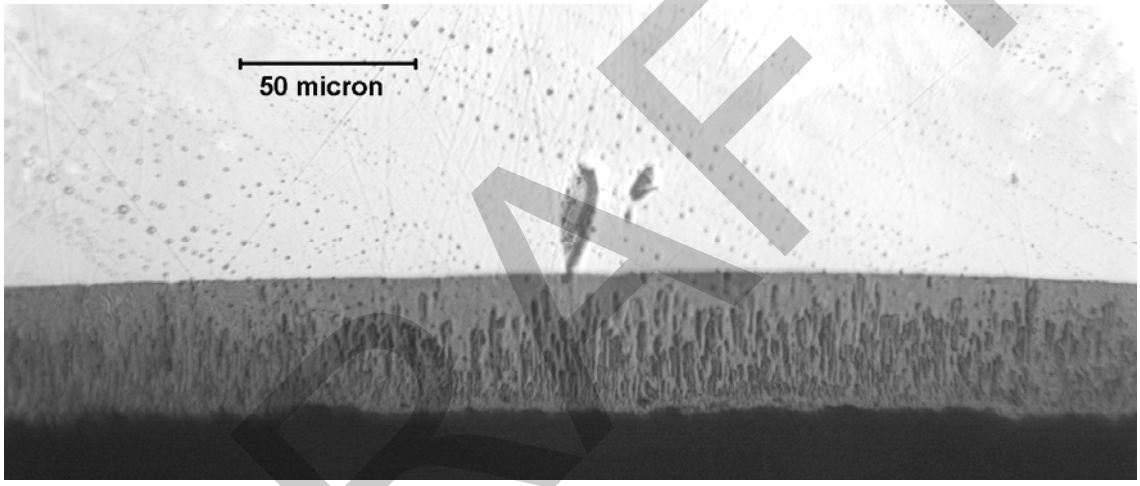

(b)

Figure 137. Optical microscopy images of the outer (a) and inner (b) surfaces of the high-burnup HBR Zry-4 sample oxidized (two-sided) at ≈1200ºC to 9.3% CP-ECR followed by slow cooling to RT. The sample is in the as-polished condition.

The CP-ECR values in Tables 57-60 were calculated for the heating phase of the transient. The total ECR (ECR_t) can be calculated from the relationship $ECR_t = [(ECR_h)^2 + (ECR_c)^2]^{0.5}$, which yields total CP-ECR values of 2.9%, 4.5%, 6.6%, 7.6%, and 9.4%, respectively, for heating-phase CP-ECR values of 2.7%, 4.3%, 6.4%, 7.4%, and 9.3%.

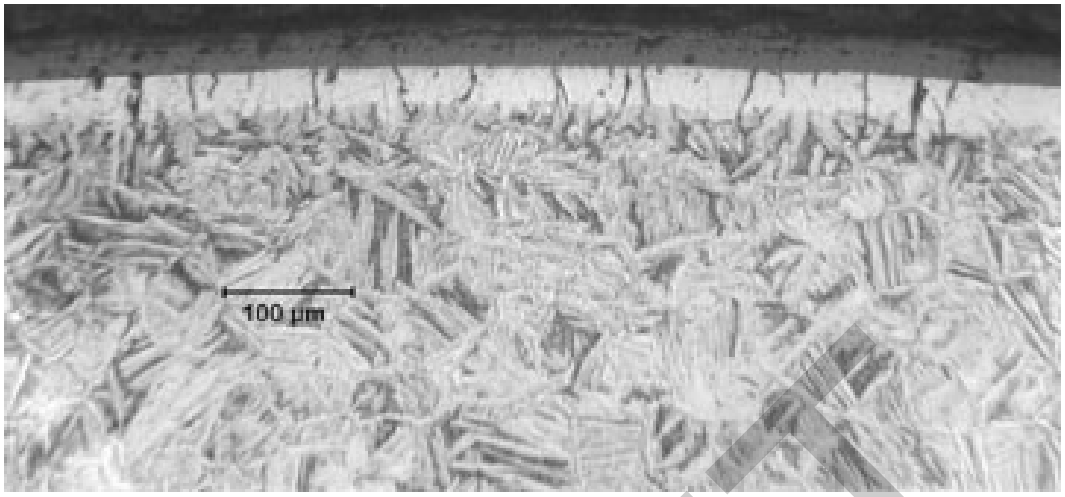

(a)

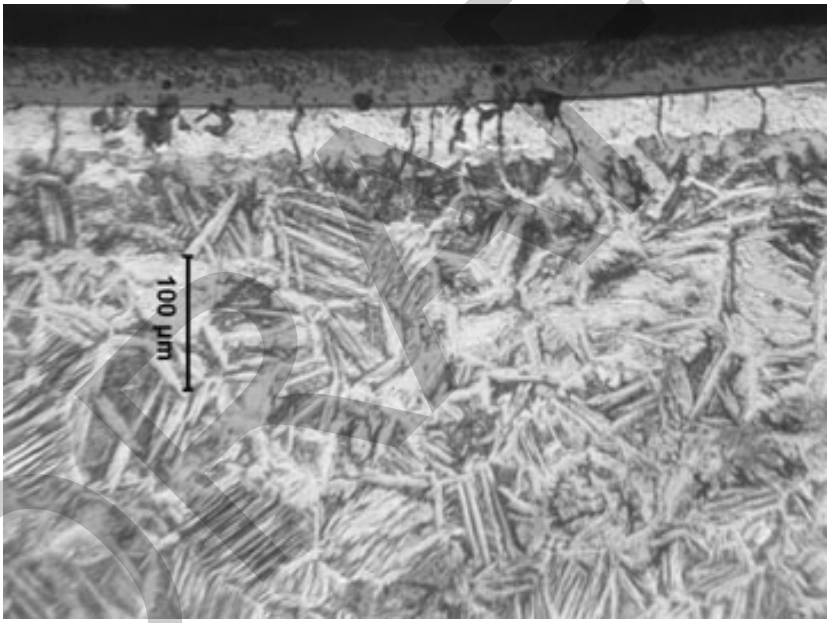

(b)

Figure 138. Optical microscopy images of the outer (a) and inner (b) surfaces of the high-burnup HBR Zry-4 sample oxidized (two-sided) at 1200ºC to 9.3% CP-ECR followed by slow cooling to RT. The sample is in the etched condition.

Table 60 Results of Ring-compression Tests for High-burnup HBR Zry-4 Cladding Samples Oxidized (Two-sided) at 1110-1198ºC to 2.7-9.3% CP-ECR and Slow Cooled (SC) to RT or Quenched (Q) at 800ºC. Tests were conducted on ≈8-mm-long rings at 135ºC and 0.0333-mm/s displacement rate; offset and permanent displacements were normalized to the cladding metal outer diameter (10.6 mm) to calculate strains.

Test ID #	Hydrogen Content, wppm	Test Time,[a] s	Cooling	CP-ECR, %	Maximum Oxidation T, ºC	Plastic Strains, %	
						Offset	Permanent
2	550±100	62	SC	2.7	1110	>45	>43
1	550±100	93	SC	4.3	1169	>12 ≈37	--- ---
3	550±100	132	SC	6.4	1196	4.0	2.6
5	550±100	155	SC	7.4	1197	4.0	2.9
6	740±110	155	Q	7.5	1197	0.2	0.8
4	550±100	206	SC	9.3	1198	0.5	0.6

[a]Includes time for ramp from 300ºC and hold time (see Figure 133 for temperature history).

The load-displacement curves are presented because they reveal more information (e.g., maximum load) than just the summary values in Table 60. Figure 139 shows the load-displacement curve for the sample oxidized to 2.7% CP-ECR at a maximum temperature of 1110ºC during the ramp. The test was stopped after an offset displacement of 4.75 mm, which is close to the geometrical limit where the top and bottom ends contact the thermocouple across the sample. The sample was intact, and the increasing load with displacement suggests that this sample had as much ductility as the as-fabricated HBR-type Zry-4 cladding. The results are significant because the presence of 550±100 wppm hydrogen had no effect on the ductility of the sample at such a low oxidation level. With a test time of only 62 s from 300ºC to 1110ºC, there was not enough time at high temperature for significant oxygen diffusion into the beta layer to occur.

Based on the post-quench-ductility results for prehydrided samples (see Figure 109), the 4.3% CP-ECR sample was expected to have low ductility. Two 8-mm-long rings were sectioned from the oxidation sample. The first ring tested experienced a sharp 40% load drop after 12% offset strain (see Figure 140a). The load drop was accompanied by a sharp cracking noise. However, the post-test sample had a crack initiating on the inner surface that did not penetrate through the wall. The second ring was tested under the same conditions (see Figure 140b). The load decrease with displacement was gradual, indicative of a highly ductile ring, and the only sharp load drop observed (and cracking sound heard) was at the end of the test at very low load. After 53% offset strain, the ring was in the shape of a bow tie (infinity symbol) with a single crack through the wall of the cladding across the length of the ring. Although a partial crack may have formed anywhere in the range of 18-53% offset strain and developed into a through-wall crack at 53% offset strain, it is more likely that the slow-growing crack penetrated the wall at an intermediate strain. Based on judgment and experience, 37% offset strain is assumed to represent the ductility of this sample. It is much higher than offset strains measured for prehydrided samples, which were quenched at 800ºC following oxidation to 5% CP-ECR. The lower peak oxidation temperature (1169ºC vs. 1180-1190ºC), the lower CP-ECR (4.3% vs. 5.0%), and the cooling history (slow cooling vs. quench) all contributed to the relatively high ductility of this sample.

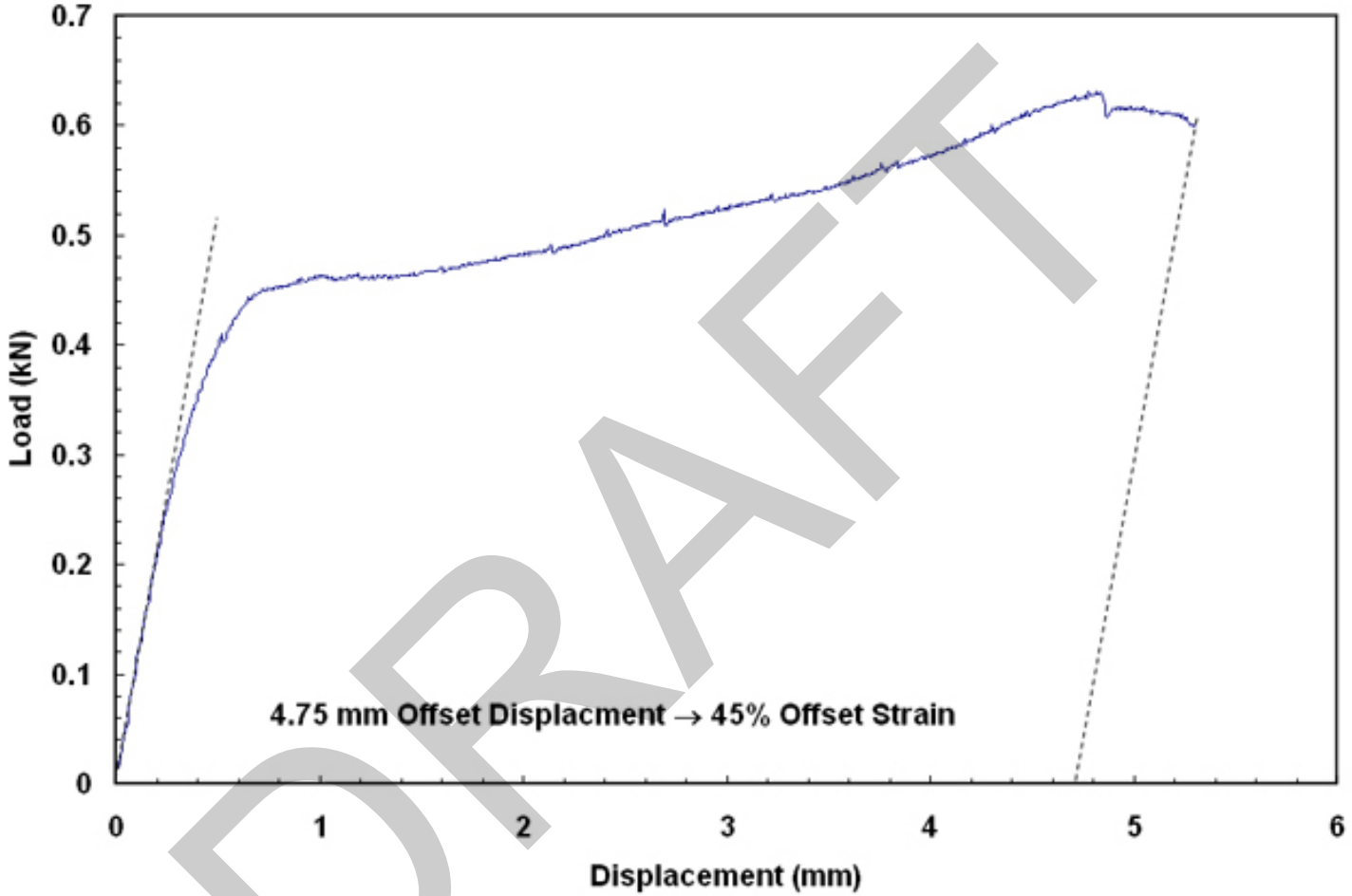

Figure 139. Load-displacement curve for high-burnup HBR Zry-4 sample (550±100 wppm H) oxidized (two-sided) at T ≤ 1110ºC to 2.7% CP-ECR and slow cooled to RT. The ring-compression test was conducted at 135ºC and 0.0333-mm/s displacement rate. The ring was intact after the test, indicating that ductility was > 45%.

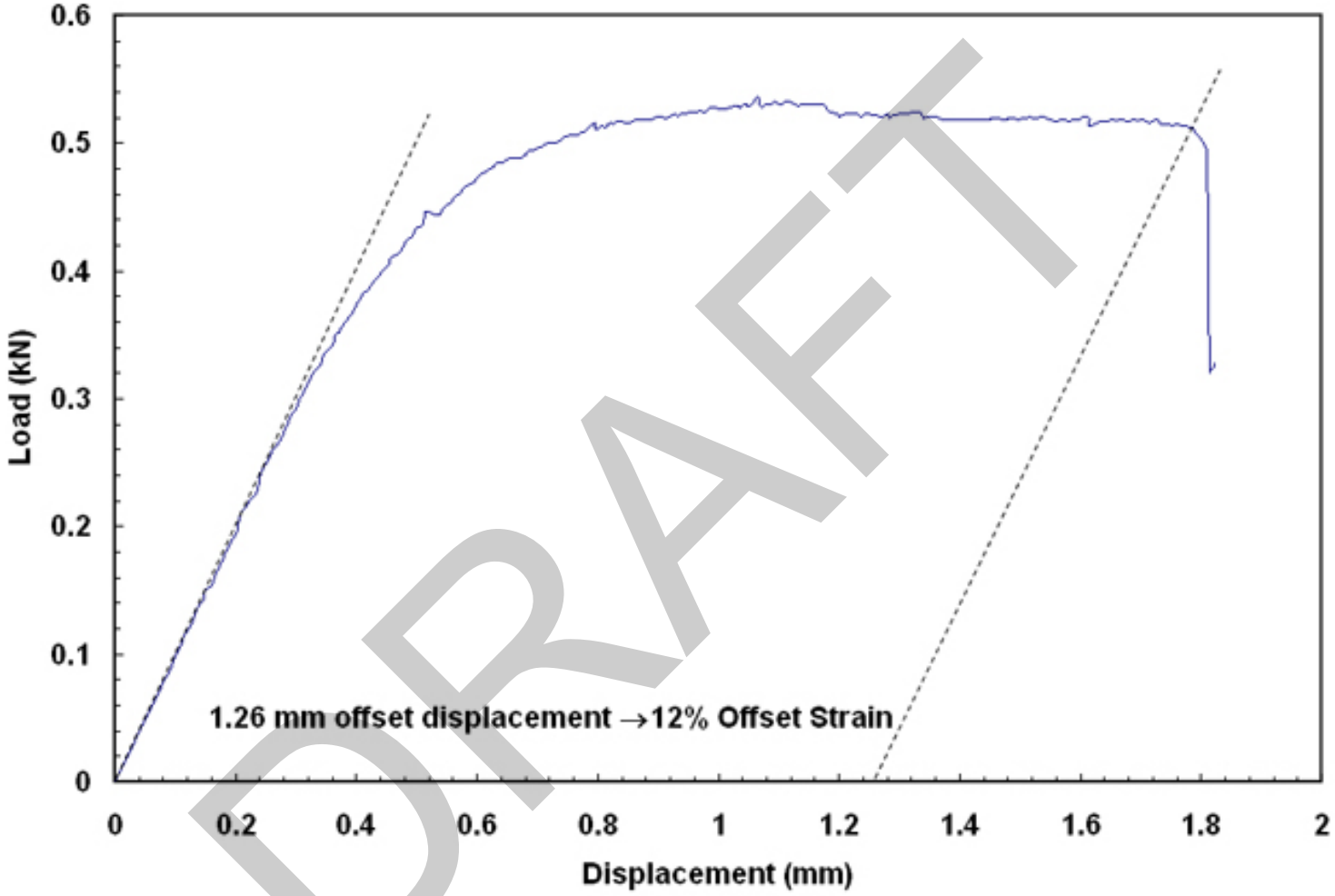

Figure 140a. Load-displacement curve for high-burnup HBR Zry-4 Ring #1 (550±100 wppm H) cut from sample oxidized (two-sided) at T ≤ 1169ºC to 4.3% CP-ECR and slow cooled to RT. The ring-compression test was conducted at 135ºC and 0.0333-mm/s displacement rate. The ring had a partial-wall crack after the first load drop, indicating that ductility was > 12%.

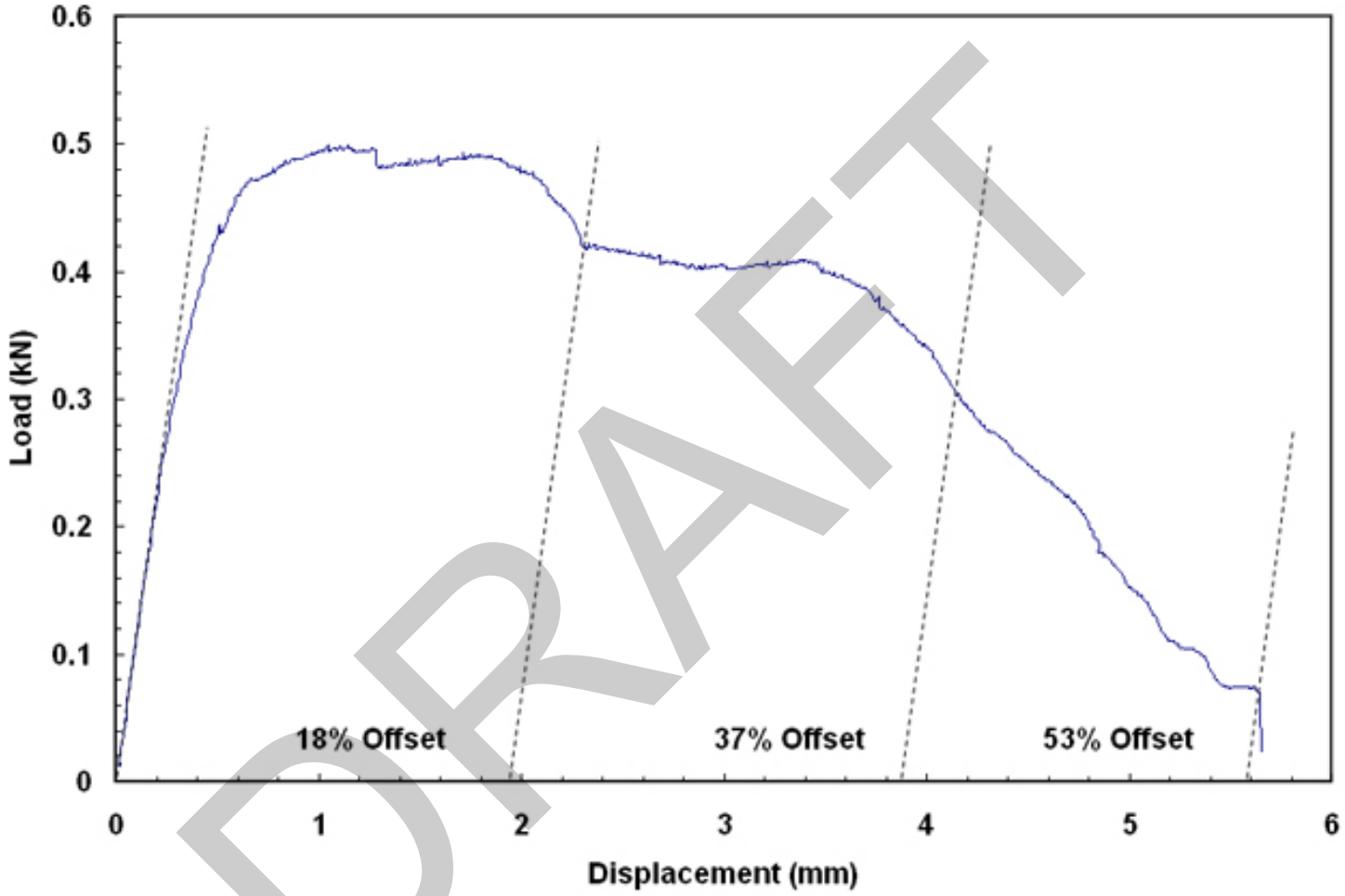

Figure 140b. Load-displacement curve for high-burnup HBR Zry-4 Ring #2 (550±100 wppm H) cut from sample oxidized (two-sided) at T ≤ 1169ºC to 4.3% CP-ECR and slow cooled to RT. The ring-compression test was conducted at 135ºC and 0.0333-mm/s displacement rate. The ring had a single through-wall crack after 53% offset strain. Because it is not clear at what strain this crack occurred, the offset strain (37%) corresponding to a 40% load drop is used to represent the ductility of the sample.

Figure 141 shows the load-displacement curve for the high-burnup HBR Zry-4 sample with 550±100 wppm hydrogen, which was oxidized to 6.4% CP-ECR at a peak oxidation temperature of 1196ºC. The results are easy to interpret because the sharp load drop did correspond to through-wall failure across the length of the ring. The offset and permanent strains for this sample are given in Table 61 as 4.0% and 2.6%, respectively. By the ANL criteria (≥2% offset strain and/or ≥1% permanent strain), the sample is ductile. However, the low ductility indicates a significant decrease in ductility between 4.3% and 6.4% CP-ECR oxidation levels.

The 7.4% CP-ECR test was conducted because it was estimated that embrittlement would occur at this oxidation level for Zry-4 with 550±100 wppm hydrogen. However, as shown in Figure 142, the offset strain (4.0%) for this sample was the same as for the 6.3% CP-ECR sample, and the permanent strain was slightly higher (2.9% vs. 2.6%). The test was repeated with another high-burnup HBR Zry-4 sample with higher hydrogen content (740±110 wppm) and with quench at 800ºC. Because of the higher corrosion level of this sample (95 μm vs. 74 μm), the cladding metal wall was slightly thinner, and the CP-ECR was slightly higher (7.5% vs. 7.4%) for the same test time. Consistent with prehydrided samples (>400 wppm H) oxidized at 1200ºC to 7.5% CP-ECR and quenched at 800ºC, this high-burnup sample was highly brittle (see Figure 143). The 9.3% CP-ECR test, which was slow cooled, was conducted before the 7.4-7.5% CP-ECR tests. As shown in Figure 144, the sample was highly brittle with an offset strain of 0.5% and a permanent strain of 0.6%.

Figure 145 shows the post-oxidation and post-quench ductility data plotted as a function of CP-ECR. A trend curve is also plotted for the slow-cooled samples with 550±100 wppm hydrogen. Using interpolation, we calculated that the ductile-to-brittle transition CP-ECR for these high-burnup samples is ≈8% following slow cooling to RT. For high-burnup Zry-4 with 740±100 wppm hydrogen, the transition CP-ECR is clearly <7.5%.

An important motivation for testing high-burnup cladding is to determine if prehydrided cladding is a good surrogate for high-burnup cladding. The post-oxidation and post-quench ductility results presented in Section 4 are compared to the high-burnup results in Table 61 for samples with comparable hydrogen content. The prehydrided samples at 5% CP-ECR have ductility values between the high- and low-ductility values for high-burnup cladding at lower (4.3%) and higher (6.4%) CP-ECR levels. For 7.4% CP-ECR oxidized samples, slow-cooled high-burnup Zry-4 has a higher ductility than the slow-cooled prehydrided Zry-4. Based on this limited comparison, prehydrided Zry-4 appears to embrittle at lower combinations of CP-ECR and hydrogen content than high-burnup Zry-4. However, a more detailed comparison of the data for slow-cooled samples indicates that the difference could be due to data scatter.

Table 61 Ductility Data from Two-sided Oxidation Tests at 1200ºC with High-burnup and Prehydrided (Unirradiated) Zry-4. Q = quench and SC= slow cooling.

Cladding Condition	H Content, wppm	CP-ECR, %	Tmax, ºC	Cooling	Offset Strain, %	Permanent Strain, %
High-burnup	550±100	4.3	1170	SC	37	---
Prehydrided	517-545	5.0	1190	Q-800ºC	9.5±4.0	---
High-burnup	550±100	6.4	1196	SC	4.0	2.6
High-burnup	550±100	7.4	1197	SC	4.0	2.9
Prehydrided	550±20	7.4	1200	SC	1.6±0.2	1.1±0.2
Prehydrided	533	7.5	1200	Q-800ºC	0.5	---

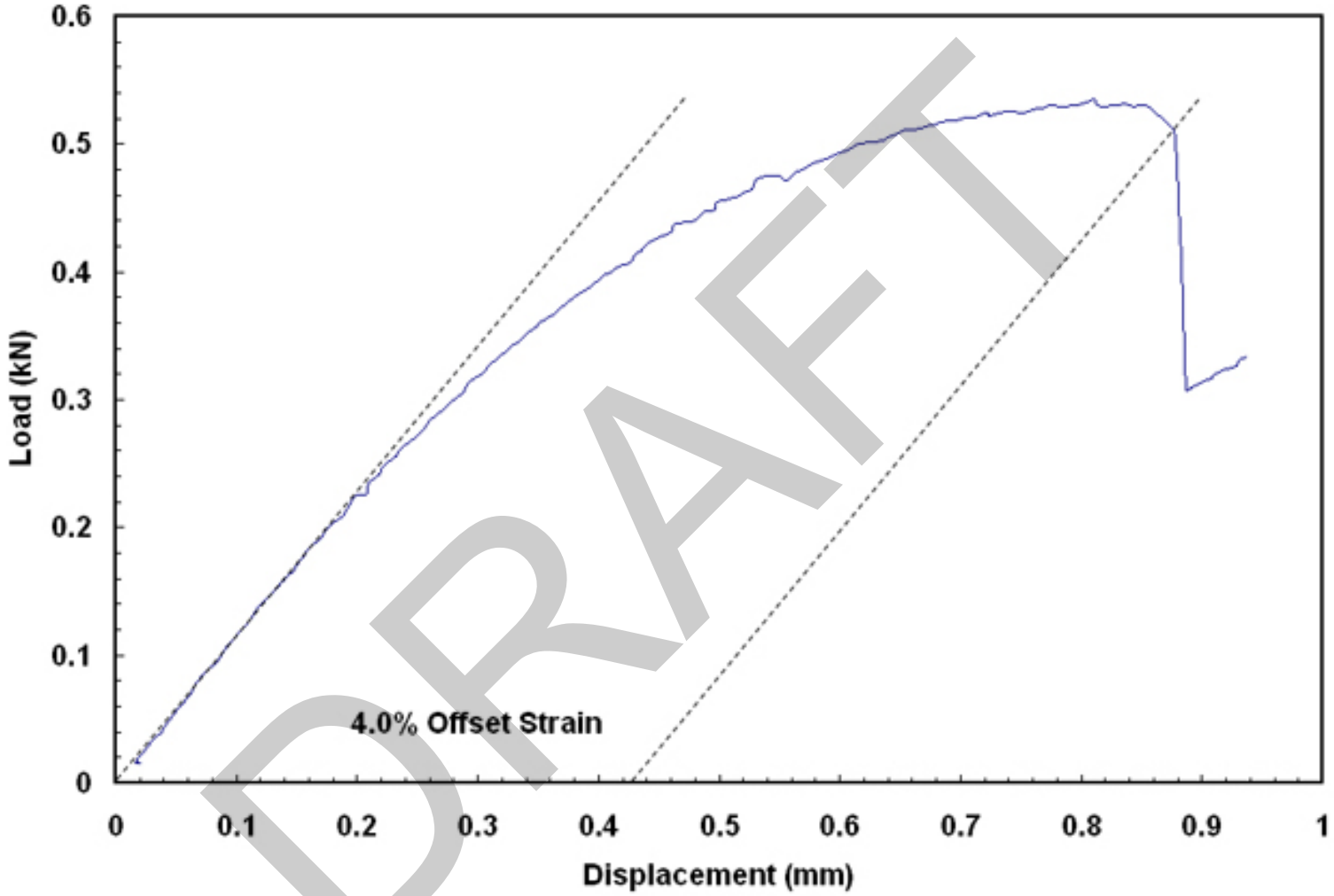

Figure 141. Load-displacement curve for high-burnup HBR Zry-4 (550±100 wppm H) sample oxidized (two-sided) at T ≤ 1196ºC to 6.4% CP-ECR and slow cooled to RT. The ring-compression test was conducted at 135ºC and 0.0333-mm/s displacement rate. The ring had a single through-wall crack along the length of the sample at 4.0% offset strain, corresponding to the sharp load drop.

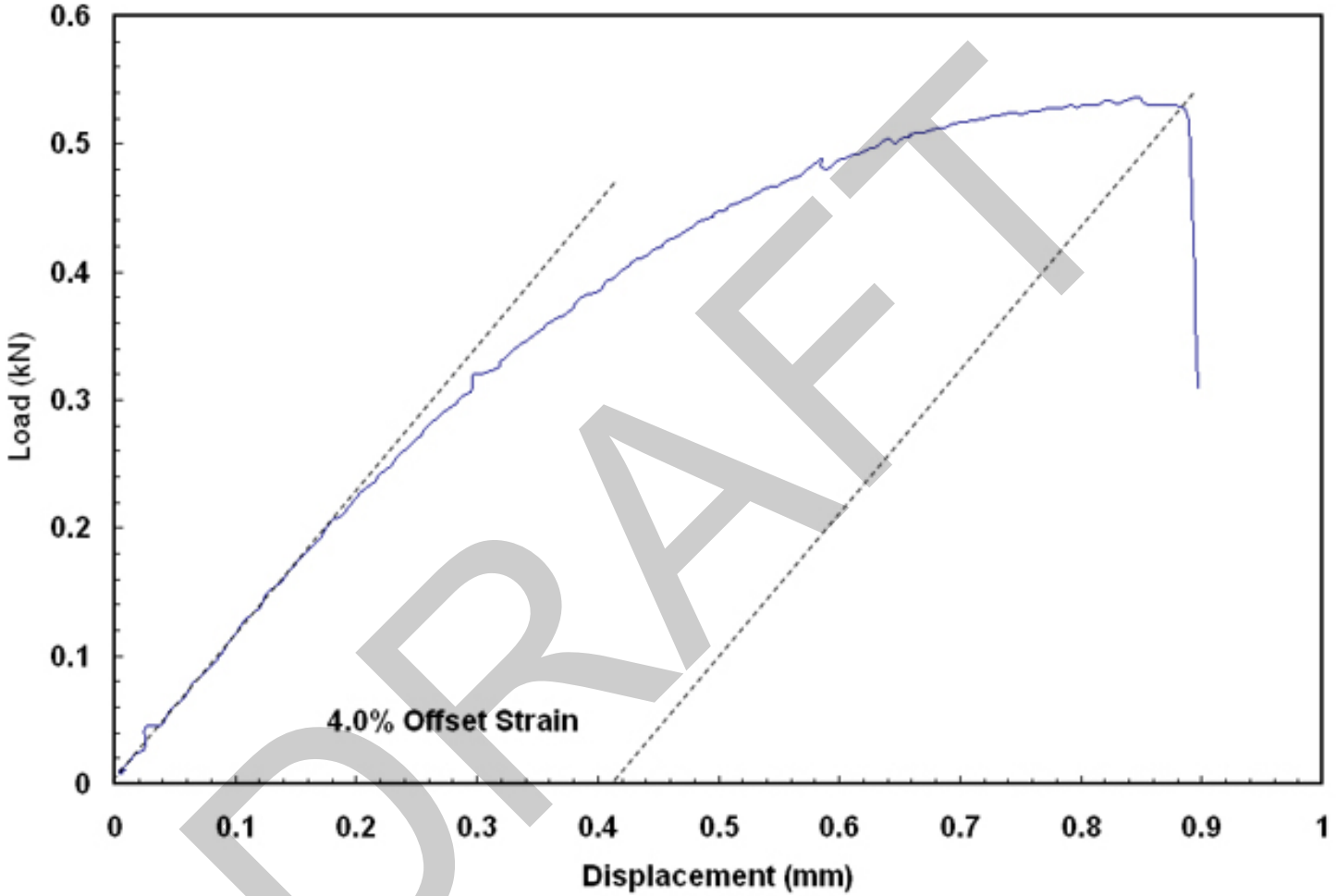

Figure 142. Load-displacement curve for high-burnup HBR Zry-4 (550±100 wppm H) sample oxidized (two-sided) at 1197ºC to 7.4% CP-ECR and slow cooled to RT. The ring-compression test was conducted at 135ºC and 0.0333-mm/s displacement rate. The ring had a single through-wall crack along the length of the sample at 4.0% offset strain, corresponding to the sharp load drop.

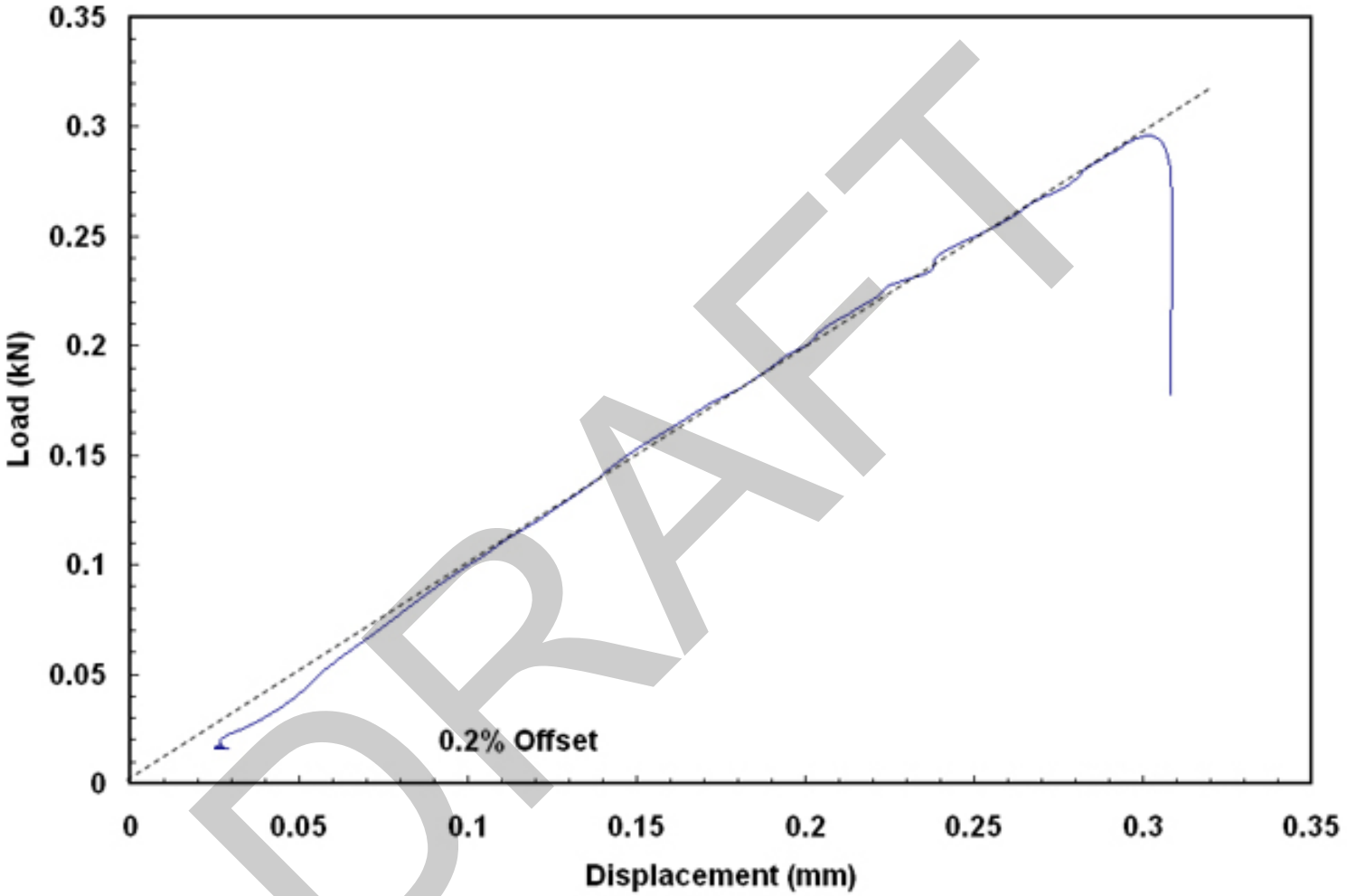

Figure 143. Load-displacement curve for high-burnup HBR Zry-4 (740±110 wppm H) sample oxidized (two-sided) at 1198ºC to 7.5% CP-ECR and quenched at 800ºC. The ring-compression test was conducted at 135ºC and 0.0333-mm/s displacement rate. The sharp load drop occurred essentially in the elastic deformation region and corresponded to a single through-wall crack along the length of the sample and no ductility.

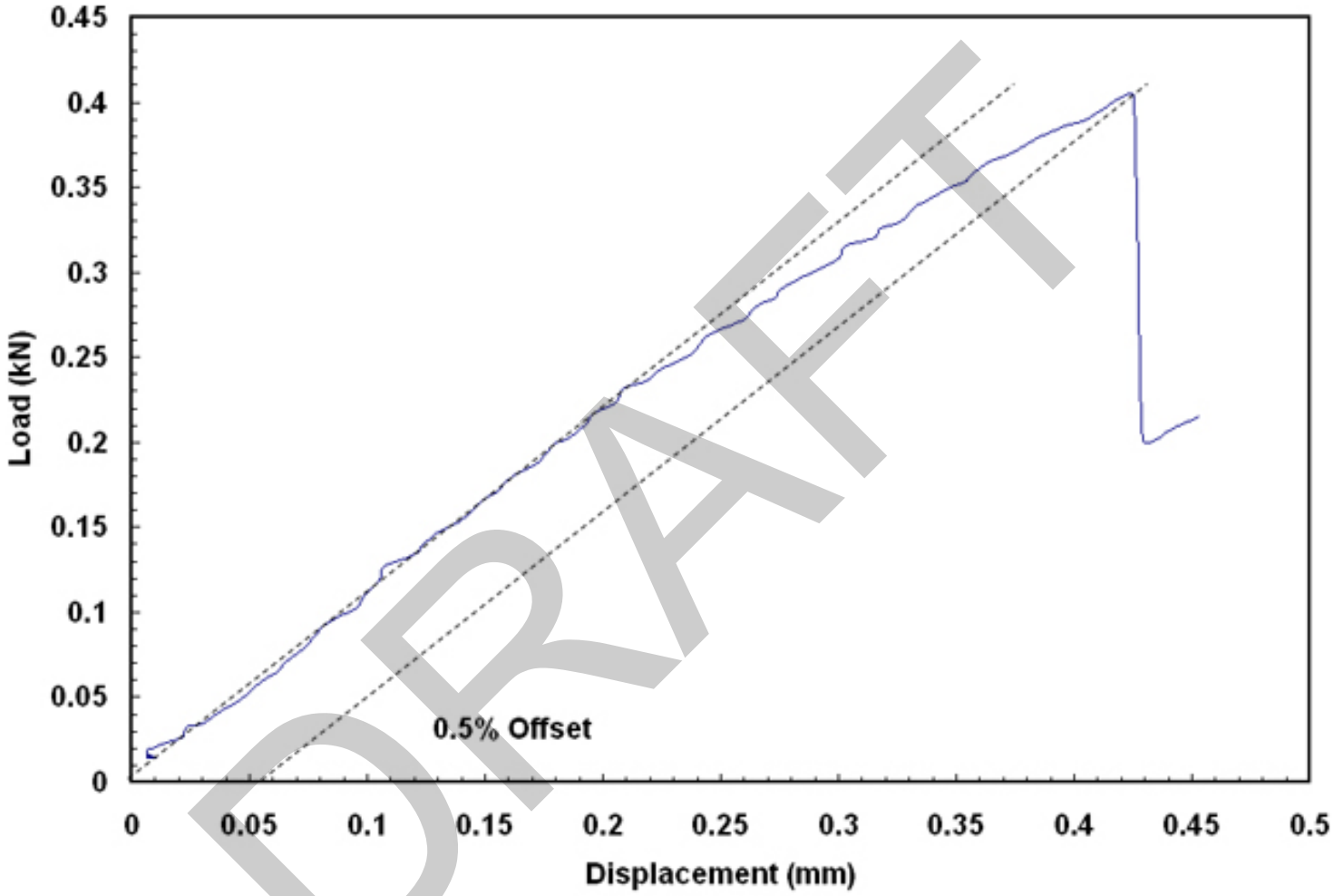

Figure 144. Load-displacement curve for high-burnup HBR Zry-4 (550±100 wppm H) sample oxidized (two-sided) at 1198ºC to 9.3% CP-ECR and slow cooled to RT. The ring-compression test was conducted at 135ºC and 0.0333-mm/s displacement rate. The ring had a single through-wall crack along the length of the sample at very low offset strain (brittle), corresponding to the sharp load drop.

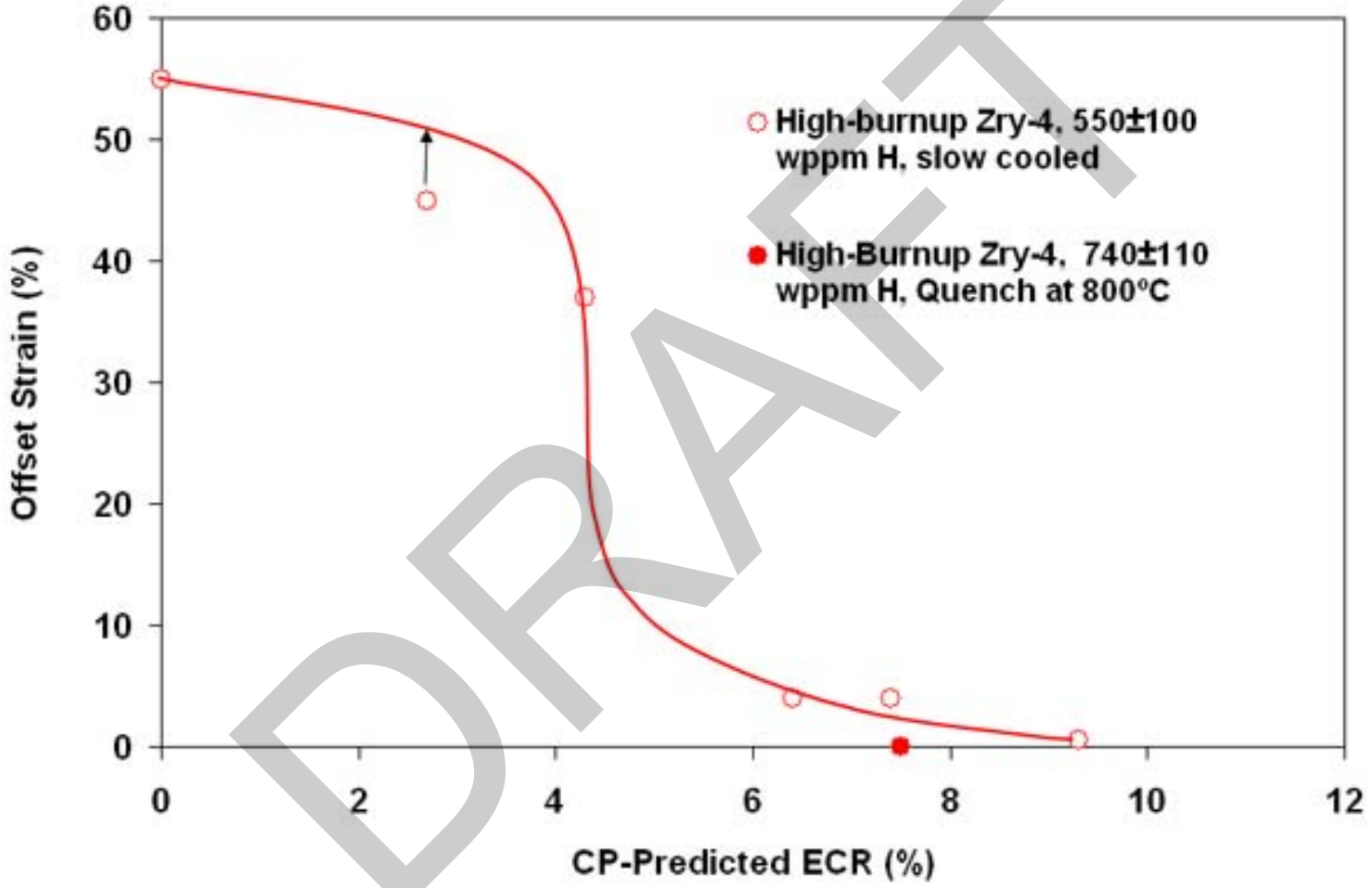

Figure 145. Ductility at 135ºC vs. CP-ECR for high-burnup HBR Zry-4 cladding following oxidation (two-sided) at ≤1200ºC and either slow cooling to room temperature or quench at 800ºC. For the slow-cooled samples, the ductile-to-brittle transition CP-ECR is ≈8%.

As shown in Figures 115 and 116, the embrittlement of prehydrided Zry-4 samples oxidized at 1200ºC and quenched at 800ºC is very sensitive to hydrogen content. The same sensitivity is expected for quench temperatures in the range of 600-800ºC. However, slow-cooled cladding samples oxidized to the same ECR levels (5%, 6%, and 7.5%) appear to maintain a small, but significant, ductility with increasing hydrogen content. This behavior of slow-cooled Zry-4 allows more latitude in comparing the ductility of oxidized prehydrided and high-burnup Zry-4 as a function of CP-ECR for hydrogen contents in the range of 470-720 wppm. The comparison is shown in Table 62 for offset and permanent strains as a function of CP-ECR (5-9.3%). Figure 146 compares the permanent strains, which are a more reliable measure of ductility for measured strains ≥1%. The results suggest that for slow-cooled samples, the ductility of prehydrided Zry-4 is comparable within data scatter to the ductility of high-burnup Zry-4.

Table 62 Ductility Data from Two-sided Oxidation Tests at 1200ºC followed by Slow Cooling for High-burnup and Prehydrided (Unirradiated) Zry-4 Cladding Samples.

Cladding Condition	H Content, wppm	CP-ECR, %	Offset Strain, %	Permanent Strain, %
Prehydrided	720	5.0	3.4	2.7
Prehydrided	470	6.0	2.1	1.7
Prehydrided	470	6.0	4.9	3.6
High-burnup	550±100	6.4	4.0	2.6
Prehydrided	490	7.4	3.3	2.4
Prehydrided	530	7.4	1.4	0.9
Prehydrided	570	7.4	1.8	1.3
High-burnup	550±100	7.4	4.0	2.9
High-burnup	550±100	9.3	0.5	0.6

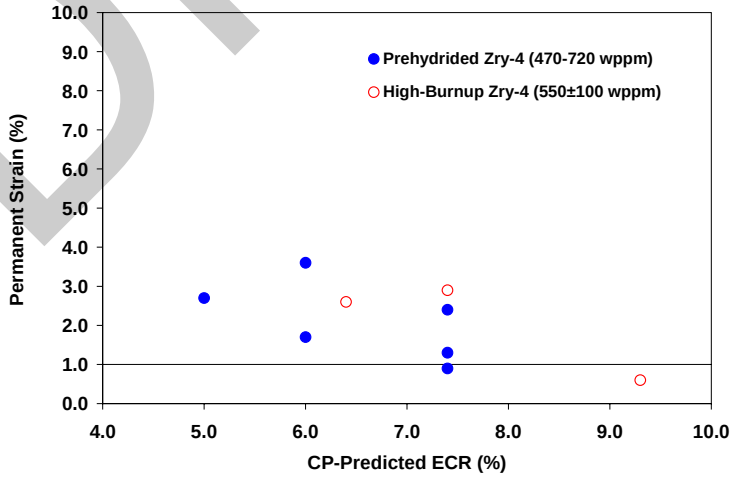

Figure 146. Permanent strain data from two-sided oxidation tests at 1200ºC followed by slow cooling to RT for high-burnup and prehydrided (unirradiated) Zry-4 cladding samples.

5.1.3 Results of one-sided oxidation tests for high-burnup HBR 15×15 Zry-4

The main purpose of conducting the one-sided oxidation tests was to investigate post-oxidation ductility of high-burnup Zry-4 cladding away from the balloon region where there would be no inner-surface steam oxidation. Of particular interest was the influence of the outer-surface corrosion layer on steam-oxidation kinetics at 1200ºC and post-test ductility. Test planning and initial data interpretation were based on the CP-ECR calculated for outer-surface steam oxidation of bare cladding, which is consistent with the manner in which LOCA embrittlement calculations are currently performed for licensing purposes. This calculation does not account for the oxygen source inside fueled-cladding samples from the fuel-cladding bond and the fuel itself. Of these two internal sources of oxygen, only the fuel-cladding bond oxygen source could be investigated in these studies with defueled cladding. Differences in ductility vs. CP-ECR between the one-sided- and two-sided-oxidized high-burnup samples, along with metallographic results, were used to infer the influence of the fuel-cladding bond oxide on embrittlement. The effects on ductility of oxygen in the fuel are discussed in Section 6.

The system used in 2001 to conduct oxidation kinetics studies with high-burnup Limerick Zry-2 was duplicated in 2005 to conduct these one-sided oxidation tests. The test train was essentially the same as the one shown in Figure 9 without the drilled holes. Steam leakage into the inner volume through the sample-gasket and gasket-spacer interfaces was a concern, but it was not a major problem with the tests conducted in 2001. The slow-flowing argon purge through the center of the samples was sufficient to minimize inner-surface oxidation at the ends of the sample to <10% of the sample length. Hydrogen pickup through the inner surface of the cladding due to hydrogen generation from the small amount of steam leakage did not appear to be a significant issue in 2001 because the hydrogen content of the as-irradiated Zry-2 cladding was ≈70 wppm, and the hydrogen content of the post-oxidation samples was <100 wppm. The 1200ºC Zry-2 samples were exposed to steam for 300-1200 s in the 2001 tests. The times for the 2005 tests with high-burnup Zry-4 were considerably shorter (174-534 s).

For the one-sided tests, the same test train was used for the out-of-cell thermal benchmarks and for the in-cell tests. Figure 147 shows the results of the thermal benchmark test using as-fabricated HBR-Type Zry-4 cladding. The controller parameters were chosen to ramp quickly to high temperature without temperature overshoot. Also shown in Figure 147 are the results of thermal benchmark tests with the starting cladding material pre-oxidized in steam at 1200ºC to outer-surface oxide layer thicknesses of 42 μm and 62 μm. Two thermocouples were welded directly to the Zry-4 metal prior to pre-oxidation for these tests. The average of the two thermocouple readings is plotted in Figure 136. The heat-of-oxidation effect on the cladding temperature appears to be negligible for pre-oxidized cladding with a 42-μm oxide layer. The temperature history for the sample with the 62-μm oxide layer is about the same as the one for the 42-μm oxide layer. The 42-μm pre-oxide-layer temperature history was used to plan and interpret test results for the one-sided high-burnup HBR Zry-4 tests. Figure 148 compares the faster-ramp temperature history for the one-sided oxidation tests to the slower-ramp temperature for the two-sided tests (see Section 5.1.2).

Table 63 summarizes the test conditions for the one-sided oxidation tests. All samples were slow cooled from 1200ºC. The test chamber inlet port, which had been used to flood the chamber with quench water in two-sided oxidation tests, was used for the argon purge in these tests. As can be seen in Table 63, all samples reached 1200ºC oxidation temperature and were at 1200ºC for substantial periods of time.

Figure 149 shows the cutting diagram for the oxidized high-burnup Zry-4 samples. Because of concern regarding inner-surface oxidation and hydrogen pickup away from the sample midplane, only one 8-mm-long ring (C2) was sectioned from the midplane region for ring-compression testing.

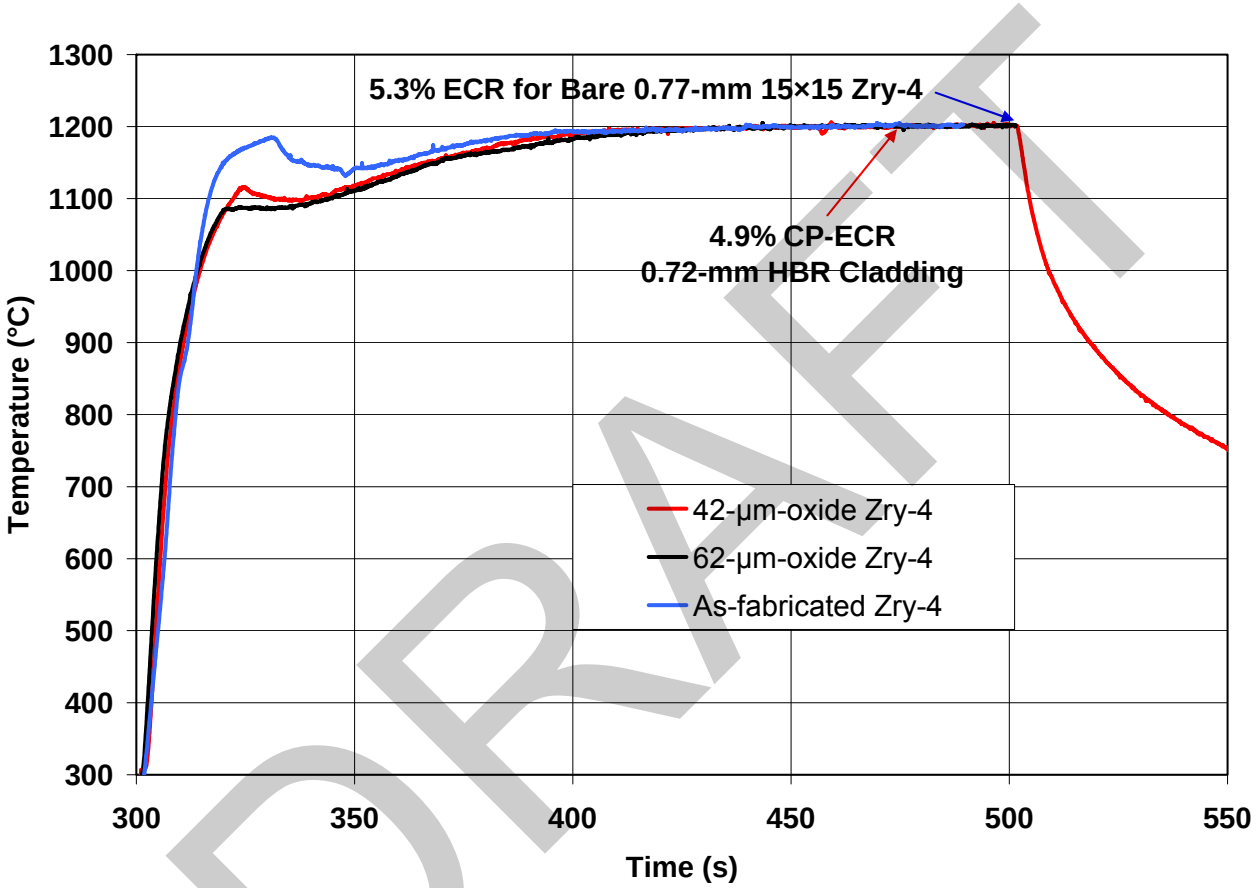

Figure 147. Thermal-benchmark results for unirradiated, HBR-type Zry-4 exposed to one-sided (outer-surface) oxidation: as-fabricated, pre-oxidized to 42-µm outer-surface oxide layer; and pre-oxidized to 62-µm outer-surface oxide layer. The temperature history for the 42-µm oxide layer benchmark was used to plan and interpret the results from the one-sided oxidation tests with corroded (68-µm), high-burnup HBR Zry-4.

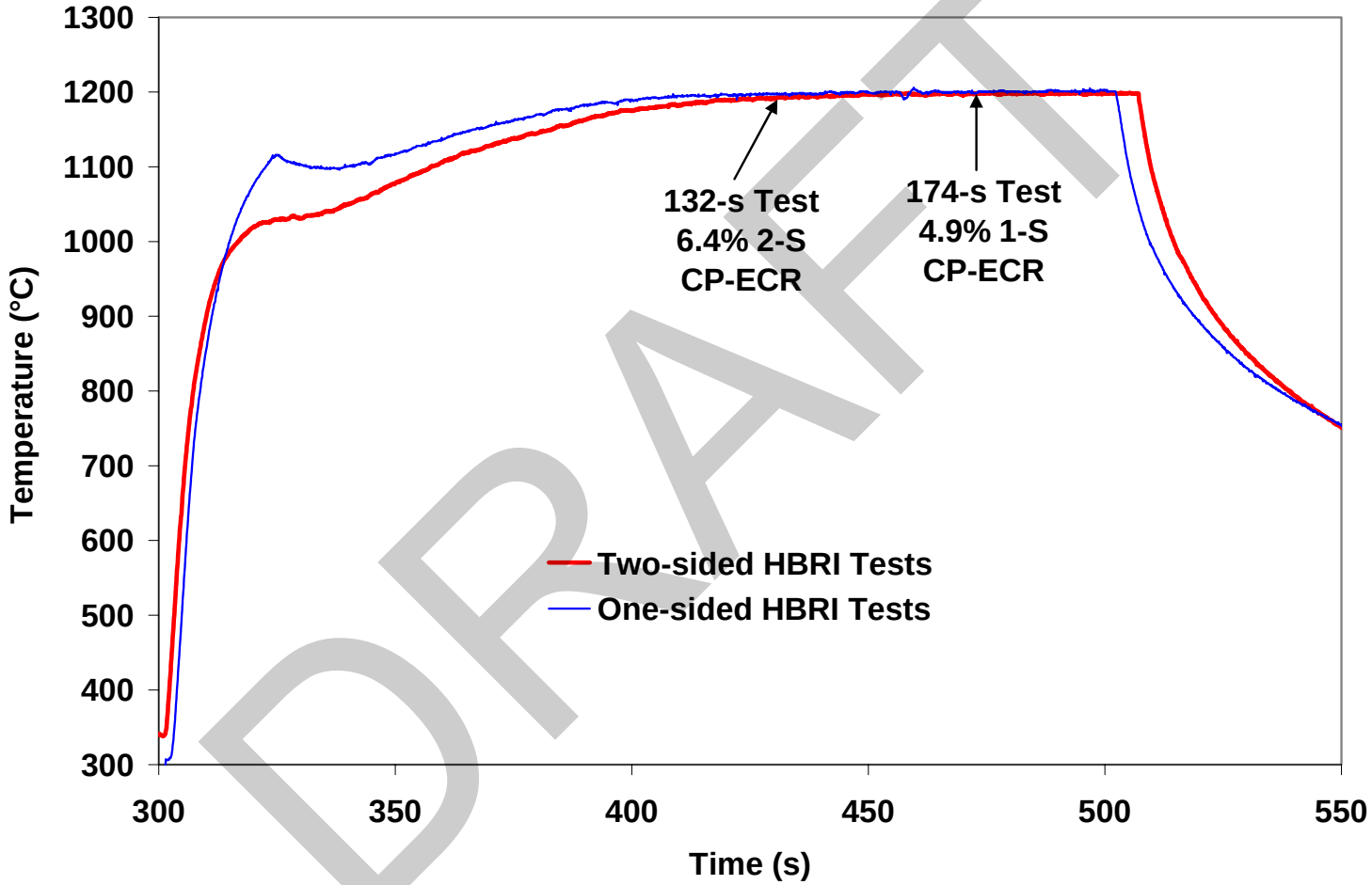

Figure 148. Temperature histories for the one-sided and two-sided steam oxidation tests using high-burnup HBR Zry-4 cladding samples.

Hydrogen analysis was performed on the ring after ring-compression testing. The samples on either side of the 8-mm-long ring (C1 and C3) were used for metallographic examination.

Table 63 Sample Characterization and Test Conditions for One-sided Steam Oxidation Tests (HBRI) Conducted with High-burnup HBR Zry-4 Cladding. SC is slow cooling.

HBRI Test ID #	Corrosion Layer, μm	Hydrogen Content, wppm	Test Time,[a] s	One-sided CP-ECR, %	Maximum T, ºC	Time at T ≥ 1180ºC, s	Cooling
7	68	550±100	174	4.9	1200	85	SC
11	44	≈400	174	4.8	1200	85	SC
8	68	550±100	323	7.3	1200	234	SC
12	≈40	≈360	323	7.1	1200	234	SC
10	68	550±100	419	8.5	1200	330	SC
9	68	550±100	534	9.7	1200	445	SC

[a]Includes time for ramp from 300ºC and hold time.

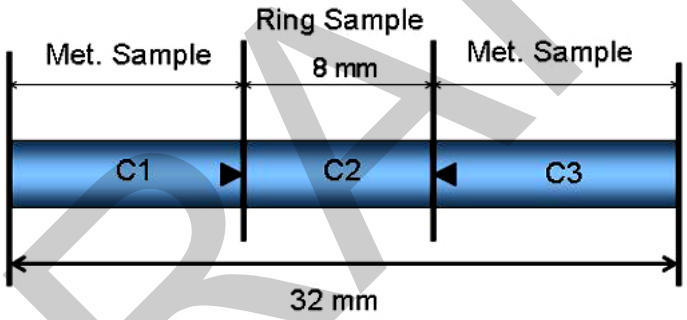

Figure 149. Sectioning diagram for high-burnup HBR Zry-4 samples after one-sided oxidation. Points of triangles indicate surfaces designated for metallographic characterization.

Table 64 summarizes the post-test results for the high-temperature oxide layer formed on the cladding outer surface and the hydrogen content of the samples. The post-test hydrogen analysis was performed on ring sectors cut from the oxidized-and-compressed rings. The hydrogen values were not corrected for weight gain due to oxidation. The weight of the post-oxidized samples was only slightly less than the weight of the pre-oxidized samples. Although the main purpose of the post-test hydrogen analysis was to determine if the samples picked up additional hydrogen due to steam leakage and inner-surface oxidation near the ends of the sample, the results indicated that fuel-mid-plane samples oxidized for 174-419 s actually lost hydrogen. The last column in Table 64 indicates whether or not inner-surface oxidation was observed at the ends of the 8-mm-long ring used for ring-compression ductility tests. No inner surface oxide was observed for the HBRI#7 (4.9% 1-S CP-ECR) and the HBRI#8 (7.3% 1-S CP-ECR) test samples. For HBRI#10 (8.5% 1-S CP-ECR) about 15% of the inner surface exhibited some oxide-layer growth from steam leakage. For HBRI#9 (9.7% 1-S CP-ECR), over 80% of the cross section at 4 mm from the ring midplane had some degree of inner-surface oxide. These observations were made on the OM-sample cross section adjacent to the cross section at the end of the ring. Although the HBRI#11-12 samples were not imaged, both samples appeared to pick up ≈180 wppm H.

Table 64 Post-test Results for High-temperature Oxide Layer Thickness and Hydrogen Content for High-burnup HBR Zry-4 Samples (HBRI) Oxidized in Steam (One-sided) at 1200ºC.

HBRI Test ID #	Pre-test H Content, wppm	Test Time,[a] s	One-sided CP-ECR, %	OD High-T Oxide, µm		Post-test H Content. wppm	ID Oxide Layer
				CP	Meas.		
7	550±100	174	4.9	38	31±6	335±31	None
11	≈400	174	4.8	--	--	570±70	---
8	550±100	323	7.3	56	42±7	190±12	None
12	≈360	323	7.1	--	--	550±70	---
10	550±100	419	8.5	65	53±7	318±44	15% of Met. Cross Section
9	550±100	534	9.7	74	63±8	767±59	>80% of Met. Cross Section

[a]Includes time for ramp from 300ºC and hold time.

Figure 150 compares the measured vs. CP-predicted values for the high-temperature oxide-layer thicknesses of the outer surface. The measured values are ≈11 µm less than the predicted values. These results are consistent with the two-sided-oxidation test results, which show an average difference of 12 µm. They confirm that the corrosion layer slows down the initial growth rate of the steam-oxide layer.

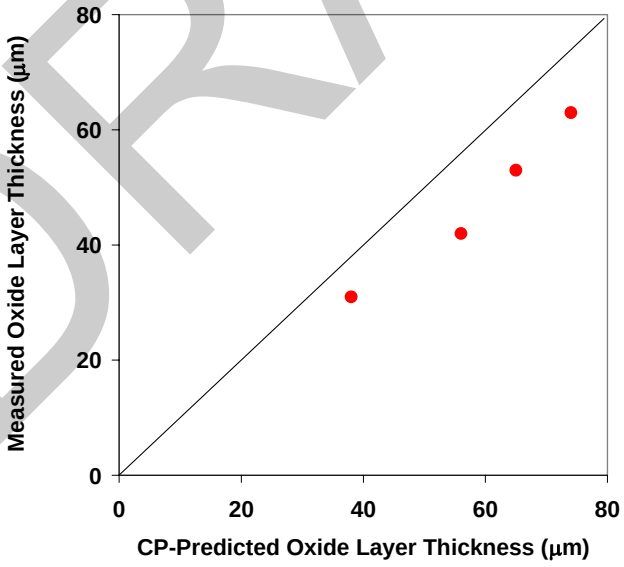

Figure 150. Comparison of measured and CP-predicted values for steam-induced outer-surface oxide layer thicknesses for high-burnup HBR Zry-4 samples oxidized at 1200ºC to one-sided CP-ECR values of 4.9-9.7%. Samples had a 68-µm pre-test corrosion layer.

Table 65 shows the CP-predicted values for the oxygen-stabilized alpha layer formed under steam oxidation conditions. Also shown in Table 65 are the measured values at the inner and outer surfaces for the HBRI#7 sample after a test time of 174 s prior to slow cooling to RT. Although there is no steam flow along the inner surface, the alpha layer formed from reduction of the fuel-cladding bond layer is comparable to the alpha layer formed at the corroded outer surface, which was exposed to steam flow.

Table 65 Post-test Results for Outer- and Inner-surface Alpha Layers Stabilized at 1200ºC for High-burnup HBR Zry-4 Samples (HBRI) Oxidized in Steam (One-sided).

HBRI Test ID #	Post-test H Content wppm	Test Time,[a] s	One-sided CP-ECR, %	Alpha Layer Thickness, μm			ID Oxide Layer
				CP OD	Meas. OD	Meas. ID	
7	335±31	174	4.9	38	42±4	36±5	None
11	570±70	174	4.8	38	---	---	---
8	190±12	323	7.3	57	58±7	35±8	None
12	550±70	323	7.1	57	---	---	---
10	318±44	419	8.5	66	70±8	--	15% of Met. Cross Section
9	767±59	534	9.7	76	77±7	---	>80% of Met. Cross Section

[a]Includes time for ramp from 300ºC and hold time.

For each test sample, up to eight metallographic images at equally spaced circumferential locations were used to obtain the data in Tables 64 and 65. Examples of metallographic images used to measure the thicknesses of the high-temperature oxide layer and alpha layer are shown in Figures 151-154. The contrast has been adjusted in Figure 151b for the 174-s test sample (HBRI#7) to allow distinction between the oxygen-stabilized alpha layer grown at 1200ºC at the outer surface as compared to the alpha incursions precipitated during cooling. The outer-surface alpha layer stabilized at 1200ºC is whiter in appearance and relatively uniform in thickness, while the alpha incursions at the outer surface are gray-white and exhibit a more uneven alpha-beta interface (see Figure 151b for outer surface). The alpha-layer thickness is more difficult to measure at the inner surface because the alpha-beta boundary is not as smooth and the color contrast is not as sharp between alpha stabilized at 1200ºC and alpha incursions. Also, recall from Figures 124 and 125 that the fuel-cladding bond layer is not uniform in thickness (11±4 μm). However, the measured alpha-layer thickness is consistent with the complete reduction of the fuel-cladding bond oxide, which is estimated to occur at ≈100 s into the 174-s test. Assuming this estimated time, the inner-surface alpha layer would continue to grow from 100 s to 174 s at a lower rate than the outer-surface alpha layer, which essentially had an infinite source of oxygen to sustain the growth of the outer-surface layer. The observed difference in alpha-layer thicknesses is relatively small. For the two-sided oxidation tests, the inner-surface alpha layer was ≈2-μm thinner than the outer-surface alpha layer. Accounting for this difference, the inner-surface alpha layer grown from reduction of the fuel-cladding bond is only ≈4 μm less than expected under flowing steam conditions. The results for the 323-s test sample (HBRI#8) are also listed in Table 65. While the OD alpha layer continues to grow from 174 s to 323 s, the ID alpha layer shows no increase in thickness within the precision of the measurements. The results are consistent with what one would expect following the complete reduction of the fuel-cladding bond at ≈100 s during the test.

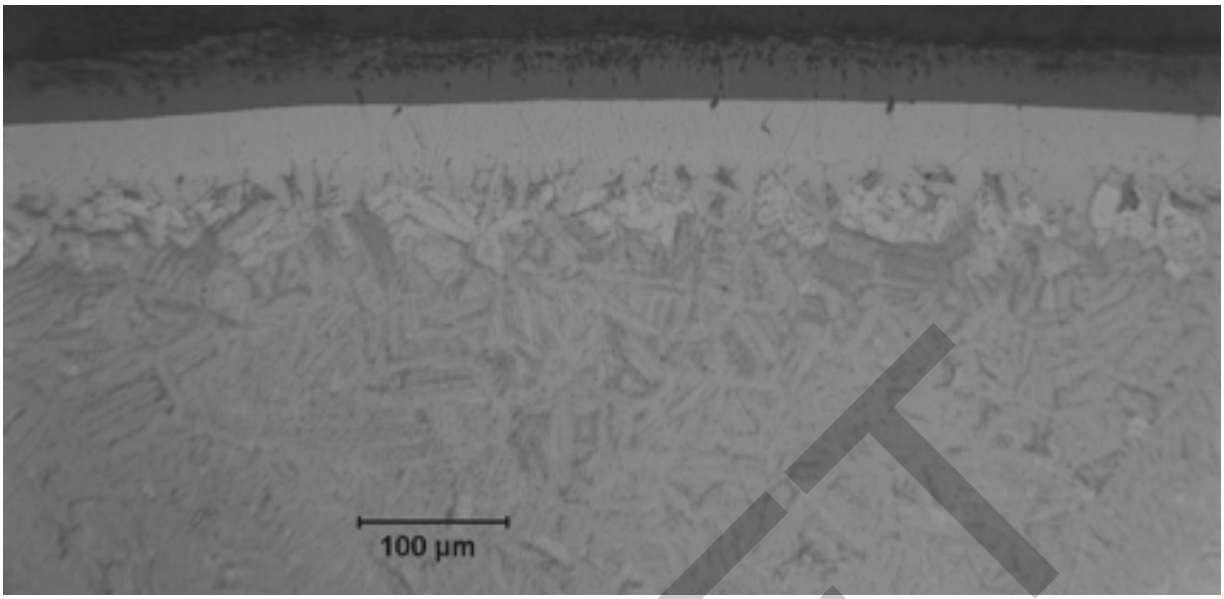

(a)

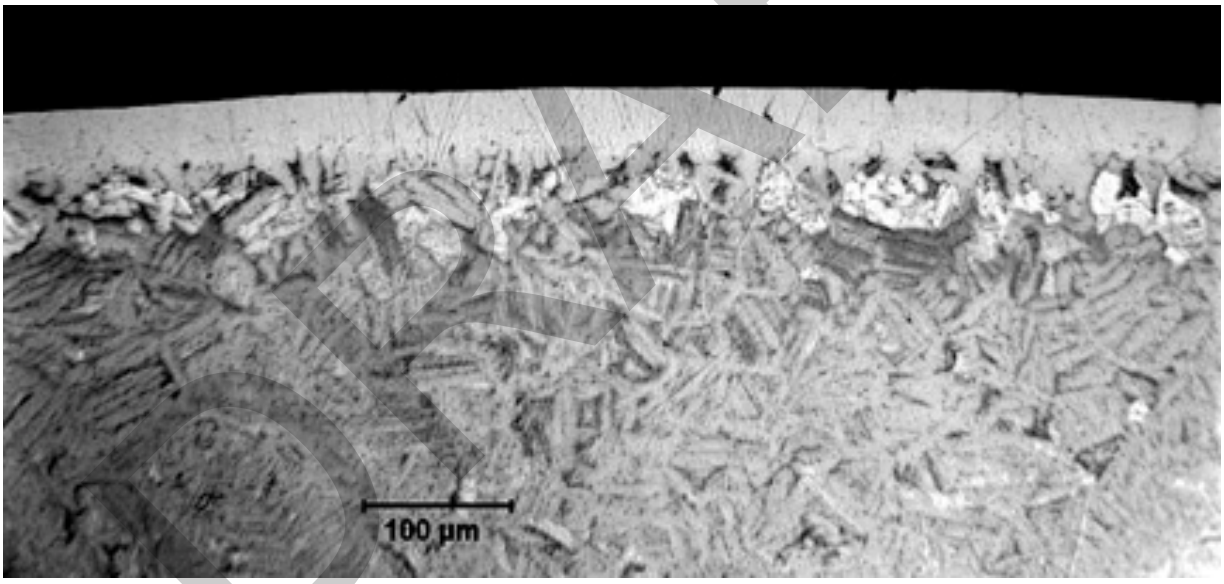

(b)

Figure 151. Outer surface of high-burnup HBR Zry-4 sample one-side oxidized at 1200ºC for 174-s test time to 4.9% CP-ECR: (a) contrast for viewing the oxide layer and (b) contrast for viewing the alpha layer.

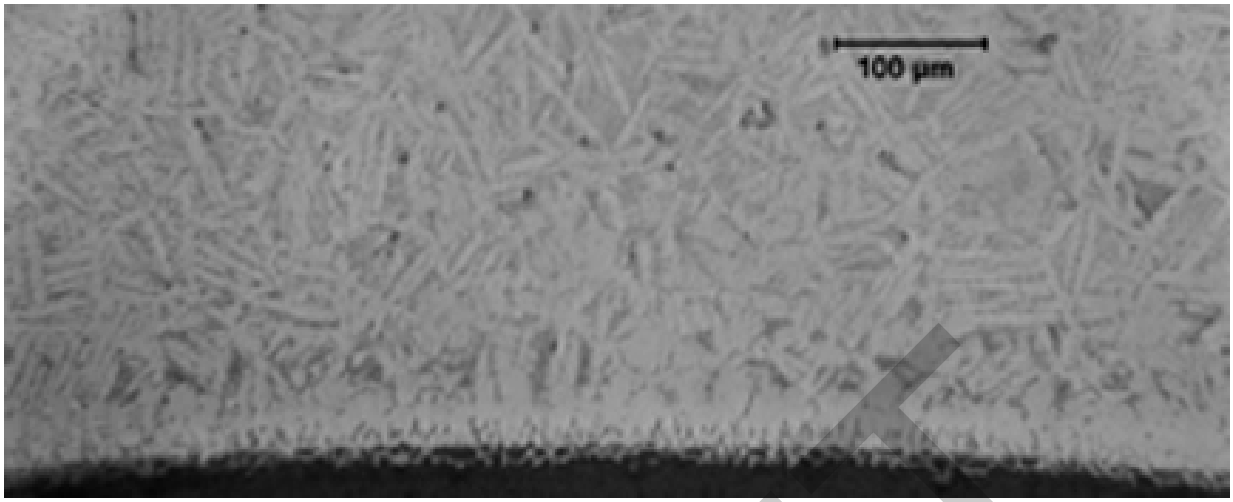

(a)

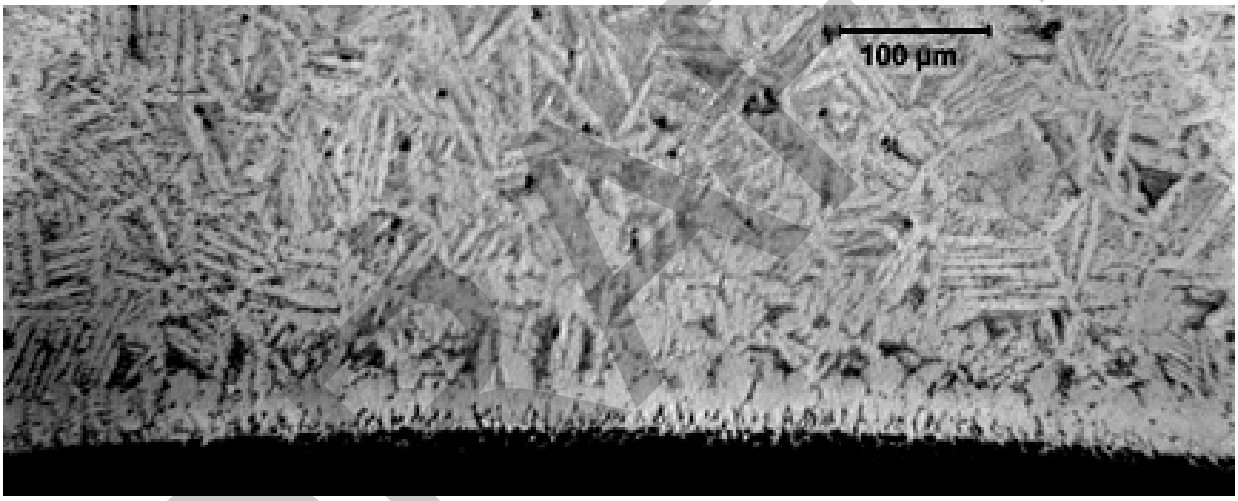

(b)

Figure 152. Inner surface of high-burnup HBR Zry-4 sample one-side oxidized at 1200ºC for 174-s test time to 4.9% CP-ECR: (a) normal contrast and (b) contrast and brightness adjusted for viewing the alpha layer in the central part of the micrograph.

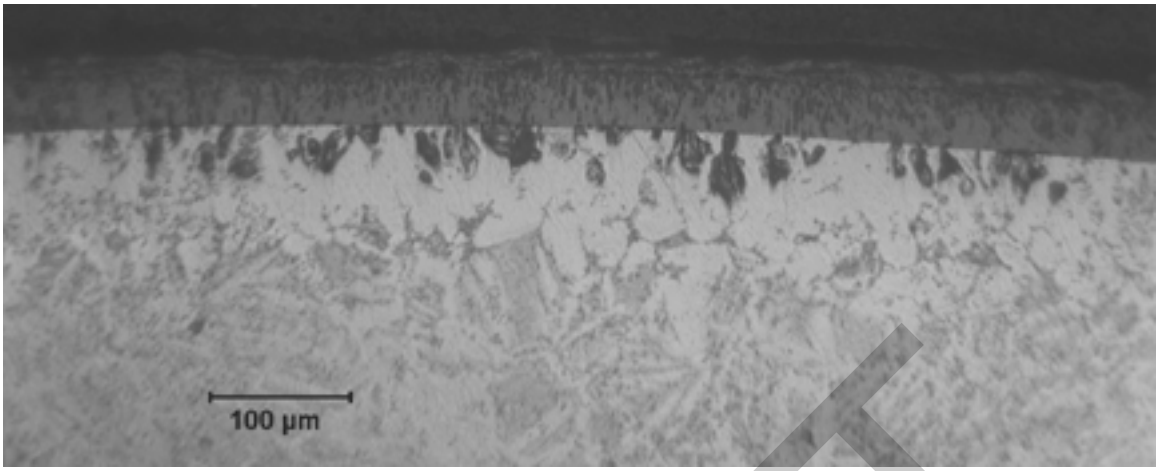

(a)

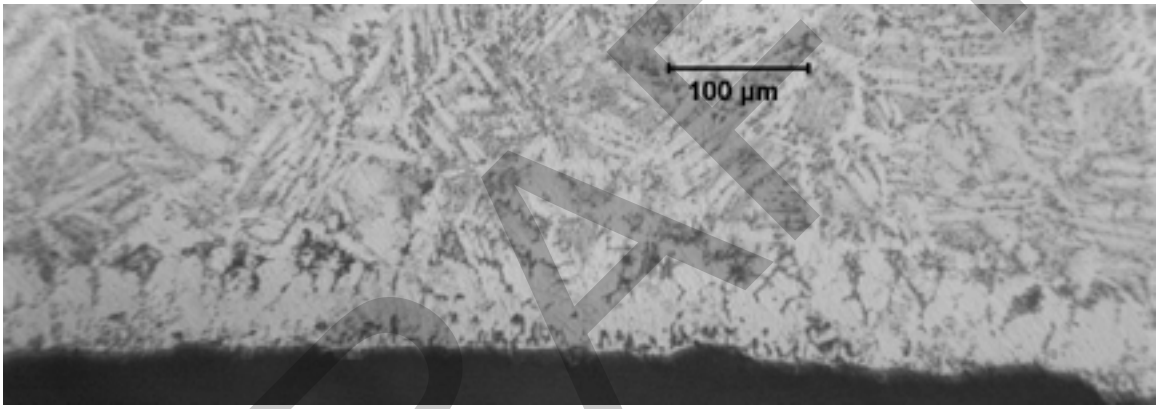

(b)

Figure 153. High-burnup HBR Zry-4 sample one-side oxidized at 1200ºC to 7.3% CP-ECR: (a) outer surface and (b) inner surface.

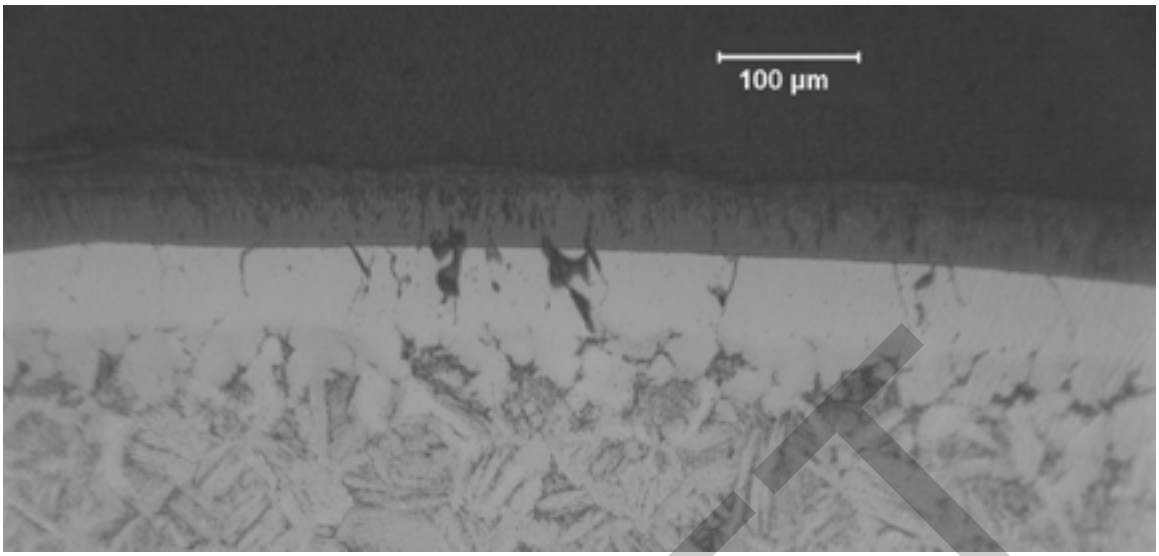

(a)

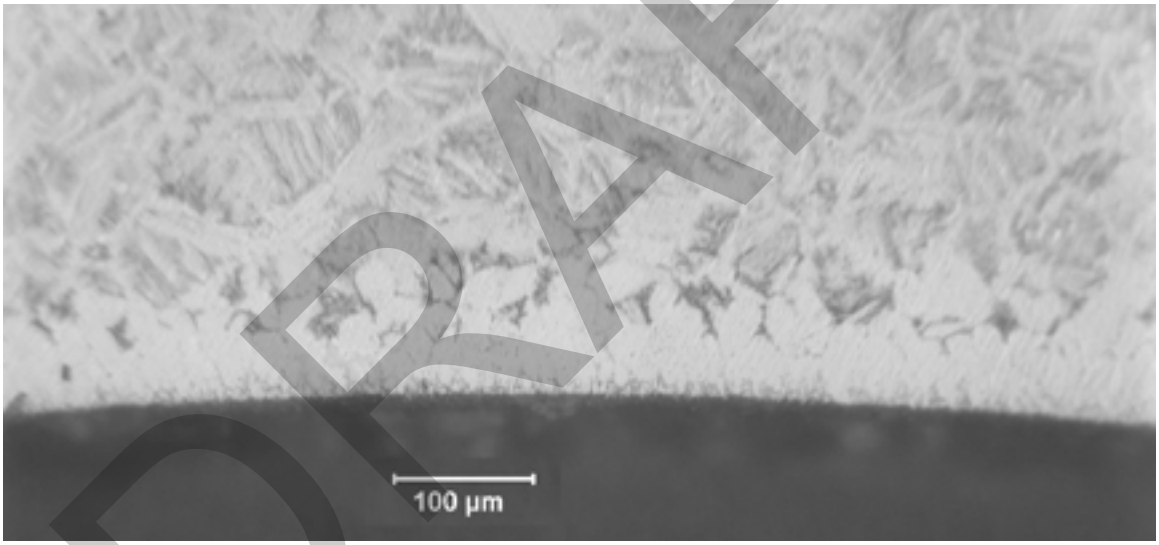

(b)

Figure 154. High-burnup HBR Zry-4 sample one-side oxidized at 1200ºC to 8.5% CP-ECR: (a) outer surface and (b) inner surface.

Post-oxidation ring-compression tests were performed with the six oxidized high-burnup HBR Zry-4 samples. Ductility data are summarized in Table 66. The results are quite interesting even though the hydrogen content was not constant during these one-sided oxidation tests.

Table 66 Ring-Compression Test Results for the Ductility at 135ºC of High-burnup HBR Zry-4 Samples Oxidized (One-sided) in Steam at 1200ºC and Slow Cooled to RT. CP-ECR values are based on outer-surface oxidation.

Test ID #	Post-test H Content, wppm	Test Time,[a] s	One-sided CP-ECR, %	Plastic Displacement, mm		Plastic Strain, %		ID Oxidation
				Offset	Perm.	Offset	Perm.	
7	335±31	174	4.9	0.89	0.65	8.4	6.1	None
11	570±70	174	4.8	0.39	0.27	3.7	2.5	---
8	190±12	323	7.3	0.47	0.39	4.4	3.7	None
12	550±70	323	7.1	0.10	0.10	0.9	0.9	---
10	318±44	419	8.5	0.40	0.33	3.8	3.1	≈15% at Ends of Ring
9	767±59	534	9.7	0.02	0.01	0.2	0.1	>80% at Ends of Ring

[a]Includes time for ramp from 300ºC and hold time.

The ductility data for the 4.9% (HBRI#7) and 7.3% (HBRI#8) 1-S CP-ECR samples were evaluated because the rings used for these tests exhibited no evidence of inner-surface oxide formation. Nevertheless, both samples had well-defined inner-surface alpha layers, which were formed by diffusion of oxygen from the fuel-cladding bond oxide. This behavior can be demonstrated by comparing the OM cross-section images (see Figure 155) from unirradiated and high-burnup Zry-4 samples oxidized to ≈5% 1-S CP-ECR. The unirradiated Zry-4 sample (0.77-mm wall) was one-side oxidized for a test time of 190 s. The outer-surface oxide and alpha layers were well developed, and the inner surface was free of oxide and alpha (see Figure 155a). By contrast, the high-burnup Zry-4 sample in Figure 155b had a well-developed alpha layer at the inner surface. Similar results were obtained for unirradiated (7.5% CP-ECR) and high-burnup (7.3% CP-ECR) samples one-side oxidized at 1200ºC.

The high-burnup Zry-4 rings from the one-sided oxidation tests failed due to a crack initiating at the inner surface and propagating towards the outer surface. The failure location was under the loading platen or above the support platen where the maximum tensile bending stress occurs at the cladding inner surface. Thus, the oxygen-stabilized alpha layer at the cladding inner surface is brittle enough to initiate the crack. With increasing ring displacement and some plastic deformation, the crack grows through the prior-beta layer and the brittle outer-surface alpha layers. These results suggest that the oxygen in the fuel-cladding bond contributes to the embrittlement of high-burnup cladding exposed to steam at the outer surface.

The test results for lower grid-span samples oxidized to 4.8% and 7.1% 1-S CP-ECR are useful for quantitative comparison purposes because their end-of-test hydrogen contents are comparable to the hydrogen content of the two-side-oxidized HBR samples. The load-displacement curves for the one-side-oxidized samples are shown in Figures 156 (4.8% CP-ECR) and 157 (7.1% CP-ECR). The ductility data from Tables 61 (two-sided results) and 66 (one-sided results) are compared in Table 67 and Figure 158 for samples with ≈550 wppm hydrogen, which were slow cooled.

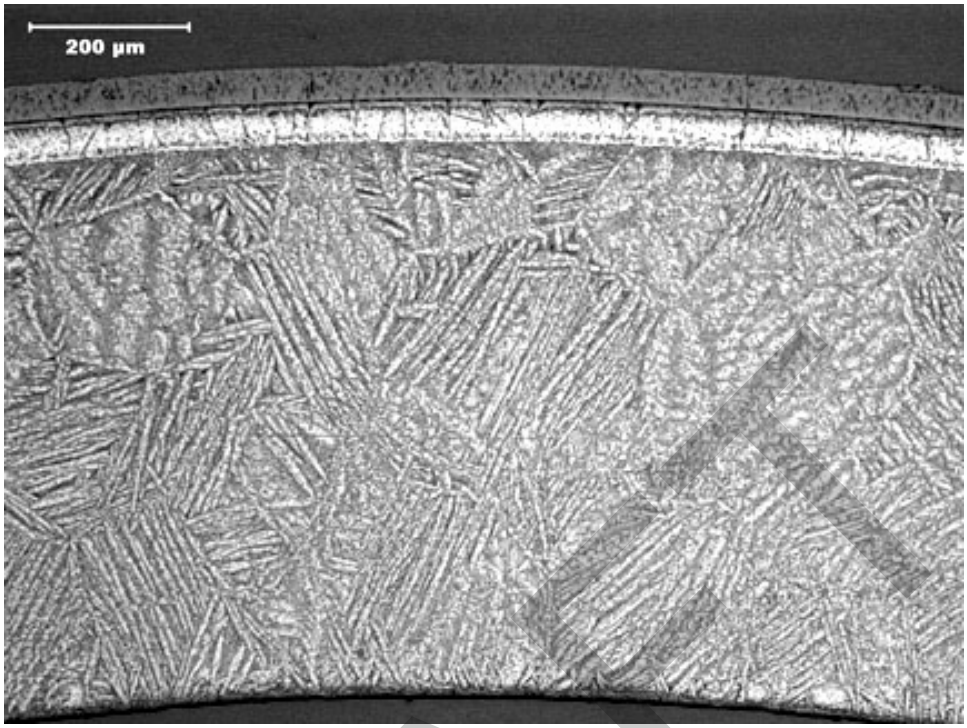

(a)

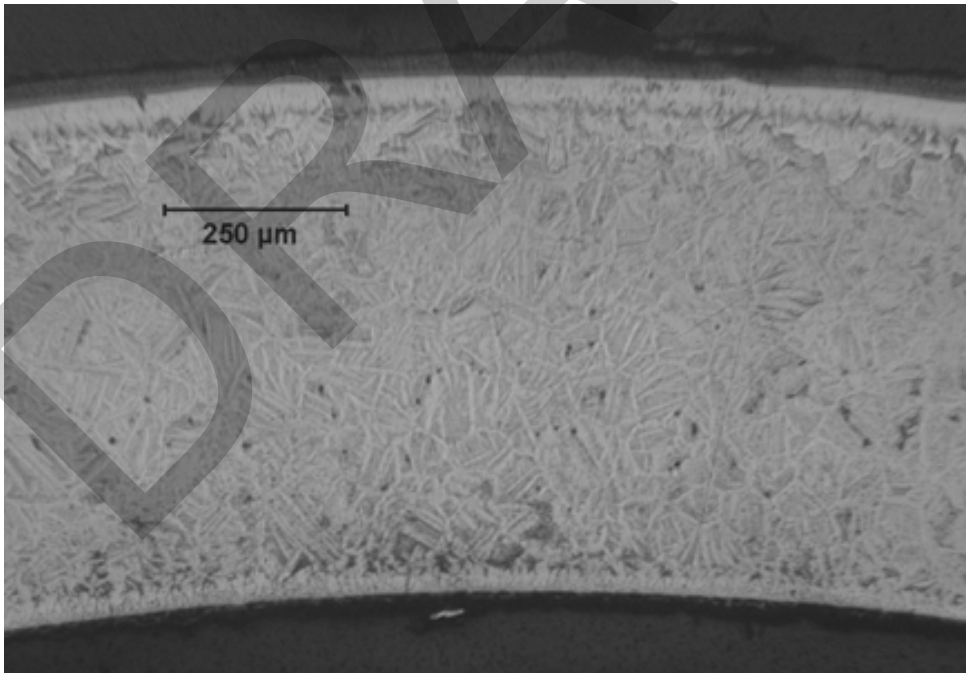

(b)

Figure 155. Comparison of Zry-4 samples oxidized (one-sided) in steam at 1200ºC to 5% CP-ECR: (a) as-fabricated HBR-type Zry-4 at 4 mm from sample midplane and (b) high-burnup HBR Zry-4 at 4 mm from sample midplane.

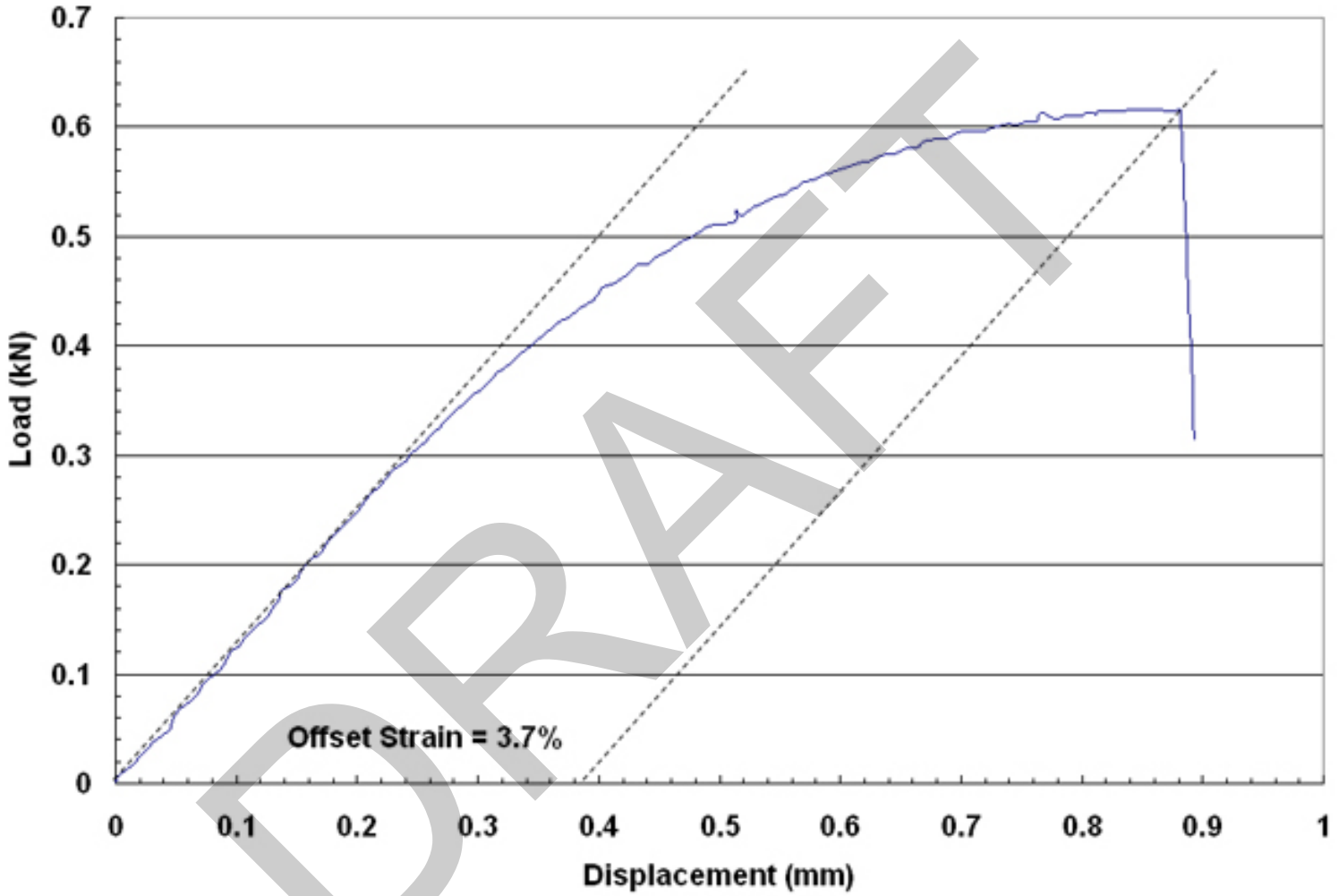

Figure 156. Load-displacement curve for HBRI#11 sample one-side oxidized to 4.8% CP-ECR at 1200ºC and ring-compressed at 135ºC and 0.0333 mm/s displacement rate. The sample developed a tight through-wall crack along the 8-mm length at the support position, with the crack initiating from the inner surface. Offset displacement was 0.39 mm, and permanent displacement in the loading direction was 0.27 mm.

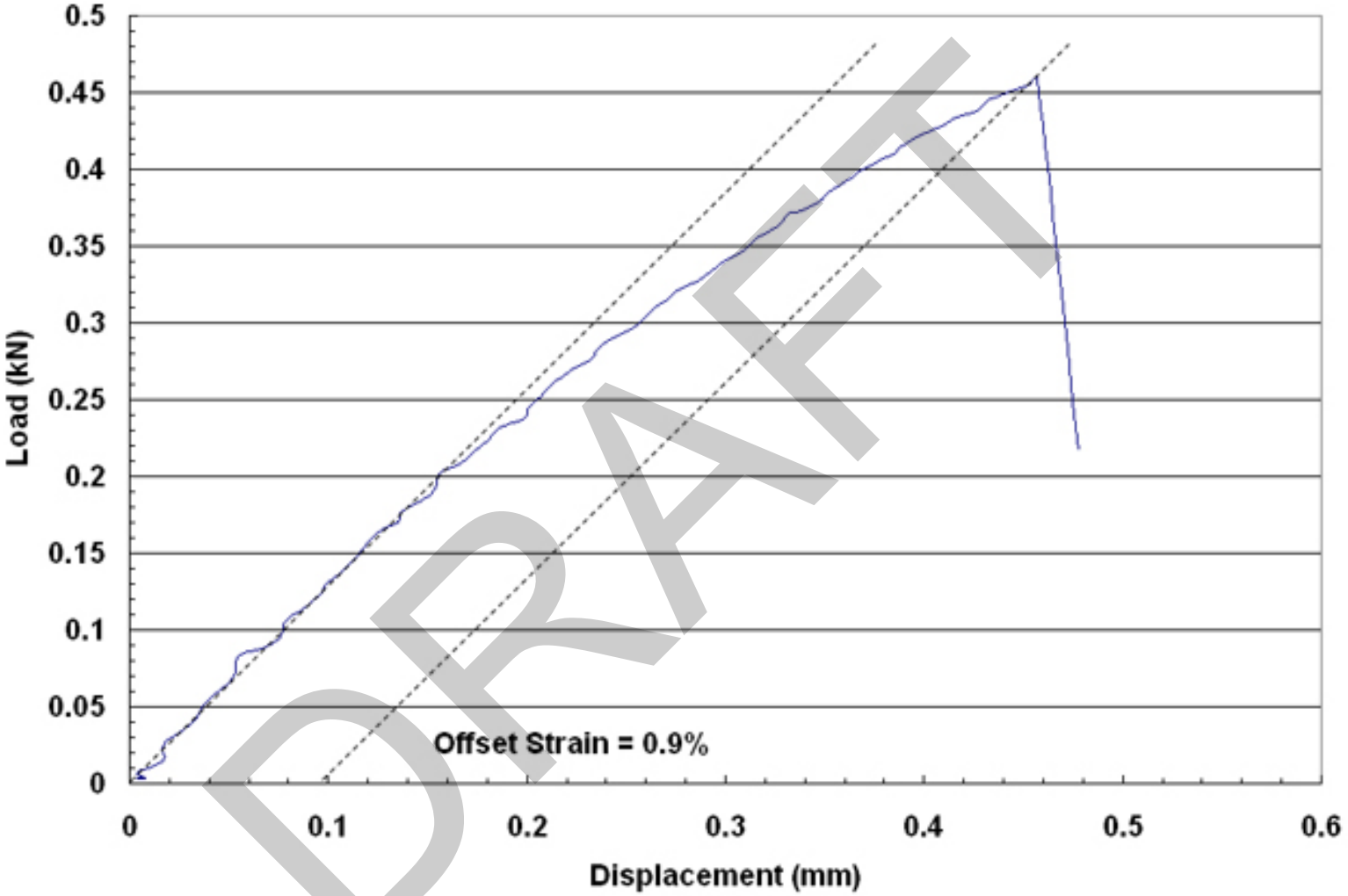

Figure 157. Load-displacement curve for HBRI#12 sample one-side oxidized to 7.1% CP-ECR at 1200ºC and ring-compressed at 135ºC and 0.0333 mm/s displacement rate. The sample developed a tight through-wall crack along the 8-mm length at the support position, with the crack initiating from the inner surface. Offset displacement was 0.1 mm, and permanent displacement in the loading direction was 0.1 mm.

Table 67 Post-oxidation Ductility Values for High-burnup HBR Zry-4 Cladding Samples Oxidized at ≤1200ºC and Slow Cooled to RT. Test type is indicated by 2-S for two-sided oxidation and 1-S for one-sided oxidation; tests were conducted on ≈8-mm-long rings at 135ºC and 0.0333-mm/s displacement rate; offset and permanent displacements were normalized to the cladding metal outer diameter (10.6 mm) to calculate strains.

Test ID #	Hydrogen Content, wppm	Test Time,[a] s	Test Type,	CP-ECR, %	Maximum Oxidation T, ºC	Plastic Strains, %	
						Offset	Permanent
2	550±100	62	2-S	2.7	1110	>45	>43
1	550±100	93	2-S	4.3	1169	>12 ≈37	--- ---
11	570±70	174	1-S	4.8[b]	1200	3.7	2.5
3	550±100	132	2-S	6.4	1196	4.0	2.6
12	550±70	323	1-S	7.1[b]	1200	0.9	0.9
5	550±100	155	2-S	7.4	1197	4.0	2.9
4	550±100	206	2-S	9.3	1198	0.5	0.6

[a]Includes time for ramp from 300ºC and hold time.
[b]CP-ECR values calculated for one-sided steam oxidation.

The results shown in Figure 158 have been plotted in the usual way vs. CP-ECR; i.e., one-sided values are used for the one-sided tests and two-sided values are used for the two-sided tests. When plotted in this manner, the one-sided-test ductility values fall significantly below the data and trend line for the two-sided-test ductility values. Three factors have been considered to understand the differences.

The first factor is the differences in heating rate and test time at 1200ºC (see Figure 137). The relatively high ductility values for two-side-oxidized HBRI#2 (2.7% CP-ECR) and HBRI#1 (4.3% CP-ECR) can be rationalized by the oxidation temperatures being significantly below 1200ºC. However, for the remaining three two-sided tests and the two one-sided tests, equivalent times at temperature and CP-ECR levels are more comparable. Differences in heating rate and hold time at 1200ºC would not explain the differences in ductility levels observed in Figure 158.

The second factor considered is the additional oxygen source from slow steam leakage inside the cladding during the one-sided tests. Although no oxide layer was observed at the edges of the rings used for the ring compression tests, low-partial-pressure steam in a hydrogen atmosphere can grow an oxygen-stabilized alpha layer without growing an oxide layer. For the 174-s and 323-s samples examined, no oxide layer was observed at the edges of the 8-mm rings used to determine ductility, and the oxygen content in the fuel-cladding bond was sufficiently high to grow the alpha layers observed. For these two test times, steam leakage is not considered to be a significant source of oxygen for embrittlement.

The third factor considered is the effect of the fuel-cladding bond on embrittlement. For the two-sided oxidation tests, the effects of the bond-layer oxygen could not be discerned in the presence of flowing steam. However, for the one-sided steam-oxidation tests, the fuel-cladding bond oxide is considered to be a significant source of oxygen for formation and growth of an alpha layer concurrent

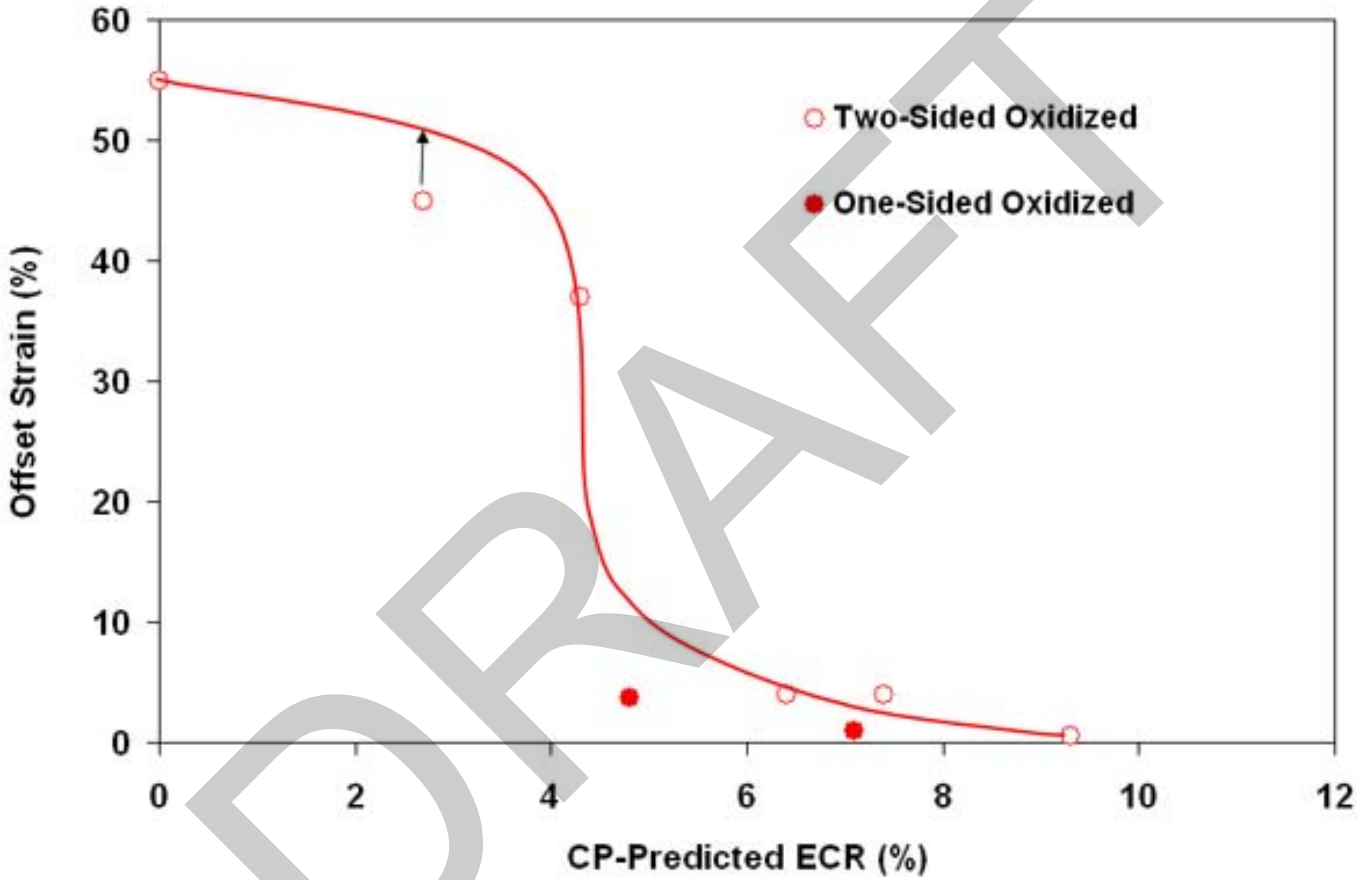

Figure 158. Offset strain data at 135ºC for high-burnup HBR Zry-4 samples with ≈550-wppm hydrogen oxidized to a maximum temperature of 1200ºC and slow cooled. Data are from two-sided and one-sided oxidation tests. Trend curve is based on two-sided-oxidation test results.

with diffusion of oxygen into the beta layer. The samples were brittle enough at the inner surface to initiate and propagate cracks through the wall of the cladding. Of the three factors considered, the fuel-cladding bond oxygen source, which is not accounted for in the one-sided CP-ECR calculation, is considered to be the dominant factor in reducing the ductility of the high-burnup Zry-4 samples from the one-sided tests. Additional embrittlement related to the presence of fuel bonded to the cladding is discussed in Section 6.

The ductile-to-brittle transition CP-ECR for as-fabricated HBR-type Zry-4 oxidized at 1200ºC is 14% following quench at 800ºC. Based on the behavior of modern 17×17 Zry-4, ZIRLO, and M5, this transition CP-ECR is expected to be independent of quench temperature for as-fabricated cladding alloys. For high-burnup HBR-type Zry-4 oxidized under the same conditions (two-sided) at 1200ºC and slow cooled, this transition CP-ECR is reduced to ≈8%. Based on limited results for high-burnup Zry-4 cladding and extensive results for prehydrided Zry-4 cladding (see Section 4), it appears that this transition CP-ECR appears to be ≈6% following quench at 600-800ºC. This value is a reduction of ≈8% CP-ECR due to high-burnup effects (i.e., hydrogen). The corrosion level ECR is ≈5.5% for the high-burnup samples with 550-wppm hydrogen. If the pre-transient corrosion level were used to compensate for the high-burnup effects, it would have to be multiplied by ≈1.5 to compensate for the difference between 14% CP-ECR (as-fabricated) and ≈6% CP-ECR (high-burnup) ductile-to-brittle transition values. Hydrogen contents higher than ≈600 wppm would cause a lower transition CP-ECR for Zry-4 following oxidation at 1200ºC and quench at 600-800ºC. The high-burnup sample with 740-wppm hydrogen and 7%-ECR corrosion level was brittle following oxidation to 7.5% CP-ECR and quench. Quench temperatures below 600ºC may increase the transition CP-ECR and hydrogen content if the cooling time is long enough at <600ºC. With regard to cooling time, note that the cooling rate increases with time between the maximum LOCA temperature and the wetting temperature, while for the ANL and CEA experiments, the cooling rate decreases exponentially with time during this interval. The experimental results for slow cooling without quench or cooling to <600ºC with quench at <600ºC may result in ductility enhancement that would not occur during a LOCA.

For one-sided steam oxidation, which is relevant to cladding outside the balloon region, it was found that the fuel-cladding-bond oxide provides an additional source of oxygen for embrittlement beyond that calculated for single-sided steam oxidation. The ductile-to-brittle transition CP-ECR decreased from ≈8% to ≈6% for slow-cooled high-burnup Zry-4 samples exposed to outer-surface steam flow. The results suggest that calculated CP-ECR values based on one-sided oxidation alone should have a lower ductile-to-brittle transition value, or the calculational method should be revised to account for additional oxygen sources (e.g., fuel-cladding bond and fuel) inside the cladding.

5.2 Results for high-burnup 17×17 ZIRLO cladding

Text, tables and figures to be inserted here.

For high-burnup ZIRLO characterization results and thermal benchmarking results, see letter report:

"North Anna ZIRLO Characterization and LOCA Apparatus Benchmark Results," M. C. Billone, Y. Yan and T. A. Burtseva, May 20, 2008.

For high-burnup ZIRLO ductility results, see letter report:

"Summary of Results for High-Burnup North Anna ZIRLO Cladding Oxidized at ≤1200ºC, Cooled with or without Quench, and Ring-Compressed at 135ºC," Y. Yan, T. Burtseva, R. Daum, and M. Billone, May 20, 2008.

5.3 Results for high-burnup 17×17 M5 cladding

Text, tables and figures to be inserted here.

For high-burnup ZIRLO ductility results, see letter report:

"Summary of Results for High-Burnup Ringhals M5 Cladding Oxidized at 1200ºC, Cooled with or without Quench, and Ring-Compressed at 135ºC," Y. Yan, T. Burtseva, R. Daum, and M. Billone, May 20, 2008.

6 LOCA Integral Test Results

During the development and benchmarking of the LOCA integral test apparatus, numerous tests were conducted with as-fabricated 8×8 and 9×9 Zry-2 filled with zirconia pellets to simulate the heat capacity of the fuel. Four tests have been conducted with high-burnup fuel rod samples from Limerick fuel rods: ICL#1 test was conducted in argon up through ballooning and burst to provide data on ballooning strain and minimum wall thickness; ICL#2 was conducted in steam with a 300-s hold time at 1204ºC, cooling at 3ºC/s to 800ºC, and slower cooling to RT; ICL#3 was conducted under the same conditions as ICL#2 through cooling to 800ºC, followed by quench and rapid cooling from 800ºC to 460ºC; and ICL#4 was conducted through the complete LOCA sequence with quench and rapid cooling from 800ºC to 100ºC. The LOCA test apparatus is shown in Figures 6 (photograph) and 7 (schematic). The LOCA integral test sample, test train, and quartz tube chamber are shown in Figure 15. The LOCA test apparatus, pre-test sample characterization, post-test nondestructive examination results, and post-test destructive examination results are described in detail by Yan et al. [15, 22, 35, 36]. In this section, test results related to post-oxidation and post-quench ductility are emphasized. Some background information is also provided for the convenience of the reader.

6.1 As-fabricated 9×9 Zry-2 oxidized at 1204ºC

6.1.1 Ballooning and burst

In additiona to the numerous tests conducted during the developmental phase of the LOCA integral test apparatus, particular tests were conducted to provide baseline data for the in-cell tests. These out-of-cell tests with as-fabricated 9×9 Limerick cladding (OCL series) parallel the thermal history of the in-cell tests with high-burnup 9×9 Limerick cladding (ICL series). The reference temperature histories for test with slow-cooling from 800ºC and rapid cooling (i.e., quench) from 800ºC are shown schematically in Figure 16. Figure 159 shows the reference internal-pressure and temperature histories for tests with quench at 800ºC. The reference hold time at 1204ºC is 300 s. Tests with as-fabricated Zry-2 were also conducted for hold times of 1 s and 120 s, and ramp-to-burst tests were conducted in argon.

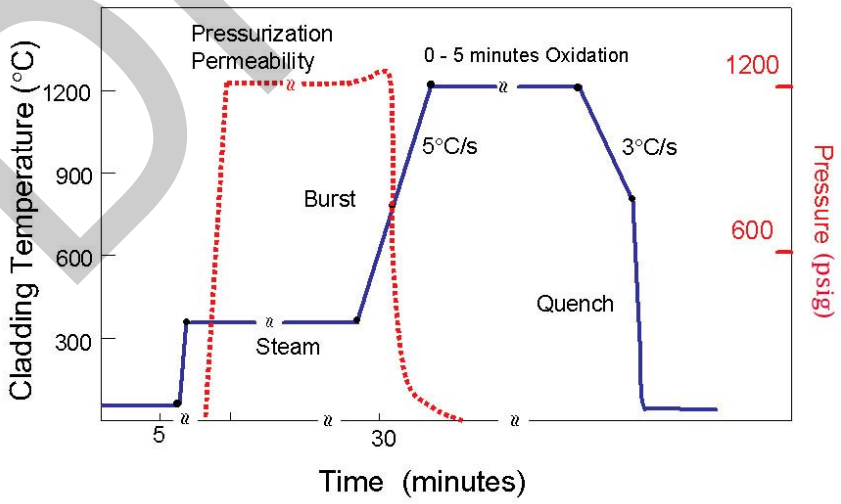

Figure 159. Temperature and pressure histories for full LOCA integral test sequence, including quench from 800˚C to 100˚C.

Table 68 summarizes the out-of-cell tests conducted to parallel the in-cell tests, as well the shorter hold-time tests used to characterize the increase in hydrogen content due to secondary hydriding from inner-surface oxidation. For ballooning and burst characterization, samples from tests such as OCL#8 are the best to use because to capture images of the overall sample geometry, the ballooning diameter and axial extent, the burst length and opening, and the cross section at the midplane burst region where the reference thickness is determined for the ECR calculations. Time at temperature, oxidation, and quench all result in changes in the geometrical details at the time of burst. Figure 160 shows the following: (a) side view of the overall sample geometry, (b) enlarged side view of the ballooned-and-burst region, and (c) enlarged frontal view of the ballooned-and-burst region. Figure 160a shows the bending of the sample that occurred just prior to ballooning during anisotropic creep and plastic deformation of the alpha-phase cladding under internal pressure. Based on real-time videos, the ballooning follows very shortly after bending, and burst follows very shortly after ballooning begins. For all samples tested in the ANL LOCA integral apparatus, the maximum ballooning strain and burst occurred on the concave side of the bending curve. The local bending in the ballooned-and-burst region is imaged in Figure 160b. Figures such as 160c are used to determine the shape (dog bone), the axial length, and maximum opening of the burst.

Following imaging of the sample, outer-diameter measurements were performed for the reference 0º orientation (burst side to 180º from the burst side) and from a diameter orientation 90º from the reference orientation. These measurements were made by using a micrometer at 20-30 axial locations to determine the maximum ballooning diameter and the axial profile for the two orientations. The differences (Δd) between the measured diameters and the as-fabricated diameter (D_o= 11.18 mm, 0.440 in.) were used to determine the ballooning strain ($\Delta d/D_o$). Figure 161 shows the $\Delta d/D_o$ axial profiles for the OCL#8 test sample at the 0º and 90º orientations. The minimum wall thickness (h_{min}) for ECR calculations (averaged over the burst cross section) can be estimated from these data by averaging the strains at the two orientations ([70% + 50%]/2 at the burst midplane), selecting the maximum value (max $\{(\Delta d/D_o)_{avg}\} = \Delta D/D_o = 60\%$), and using the constant-volume plasticity relationship:

$$h_{min} = h_o/(1 + \Delta D/D_o), \quad (8)$$

where h_o is the as-fabricated wall thickness (0.71 mm), and the plastic strain in the axial direction is assumed to be zero at the burst midplane. These assumptions were tested by sectioning the OCL#8 sample at the burst midplane and obtaining high magnification images from which the circumferential strain ($\Delta C/C_o$) could be measured directly, as well as the wall thickness. As shown in Figure 162, the wall thickness is maximum at ≈180º from the burst opening and minimum at the edges of the burst opening. The area-averaged wall thickness determined from Figure 162 was 0.434 mm, the circumferential strain around the cladding mid-wall was 60%, and the wall thickness determined from Equation 8 was 0.444 mm. The difference between the precise measurement and the Equation-8 calculation is only 2%. Thus, Equation 8 is a practical algorithm for calculating the minimum wall thickness to be used in ECR calculations corresponding to the minimum wall thickness. The methodology has also been validated for oxidized ballooned-and-burst cladding. Figure 162 has also been used to gain a better appreciation for circumferential variation in cladding thickness, for the local effects of two-sided oxidation, and for interpretation of the effects of quench on burst opening. The thin cladding at the edges of the burst region experiences a high level of oxidation during a LOCA-type transient as compared to the thicker cladding 180º from the burst region. Locally, this cladding will be highly brittle and the edges will most likely fragment during quench, resulting in a larger post-test burst width. Such behavior has no consequence relative to the current LOCA criteria, which apply to average rather than local behavior of the burst cross section. However, the Figure 162 results are useful in order to rationalize observed changes to the burst region due to oxidation and quench.

Table 68 Summary of LOCA Integral Test Results for Out-of-cell Tests with Near-archival As-fabricated (Unirradiated) 9×9 Zry-2 Samples Filled with Zirconia Pellets. Outer diameter and wall thickness of as-fabricated cladding are 11.18 mm and 0.71 mm, respectively.

Parameter	OCL#5	OCL#8	OCL#22	OCL#17	OCL#11	OCL#13
Environment	Argon	Argon	Steam	Steam	Steam	Steam
Hold Temperature, °C	---	---	1204	1204	1204	1204
Hold Time, s	---	---	1	120	300	300
Quench (Q) at 800ºC or Slow Cooling (SC)	SC	SC	Q-800ºC	Q-800ºC	SC	Q-800ºC
$(P_g)_{max}$, MPa	8.96	8.62	8.87	9.10	8.61	9.09
T at $(P_g)_{max}$, °C	660	687	690	6.83	680	676
Burst Pressure (P_B), MPa	8.26	7.67	6.90	9.07	7.93	6.43
Burst Temperature (T_B), °C	733±5	766±17	747±37	750	753±22	766±25
Burst Center Relative to Specimen Midplane, mm	+20	-10	+25	-13	+35	28
Burst Shape	Dog Bone	Dog Bone	Dog Bone	Dog Bone	Dog Bone	Dog Bone
Burst Length, mm	13	17	17	10	11	10
Max. Burst Width, mm	2.5	2.5	1	0.8	1	1
Length of Balloon, mm	100	140	140	145	140	150
$(\Delta D/D_o)_{max,}$ [a] %	44±10	60±10	54	49±11	43±10	43±8
$(\Delta C/C_m)_{max,}$ [b] %	---	60	---	---	---	---
Reference Minimum Wall Thickness for ECR, mm	≈0.50	0.434	0.46	0.48	0.50	0.50
Maximum CP-ECR, %	0	0	9	15	21	21

[a]From profilometry at 0° and 90° relative to burst orientation.

[b]Midwall circumferential strain determined from low-magnification photomicrographs.

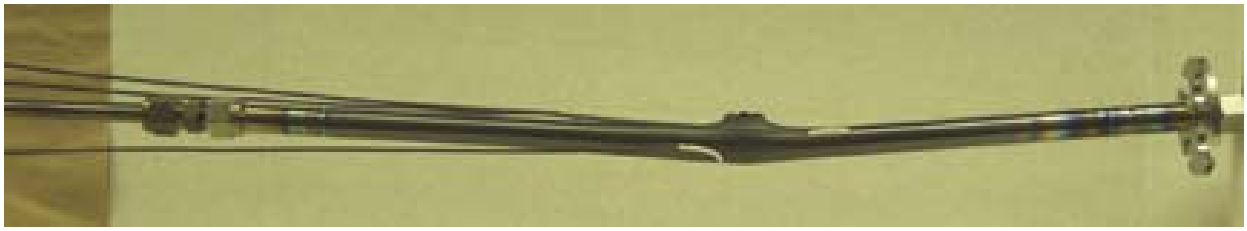

(a)

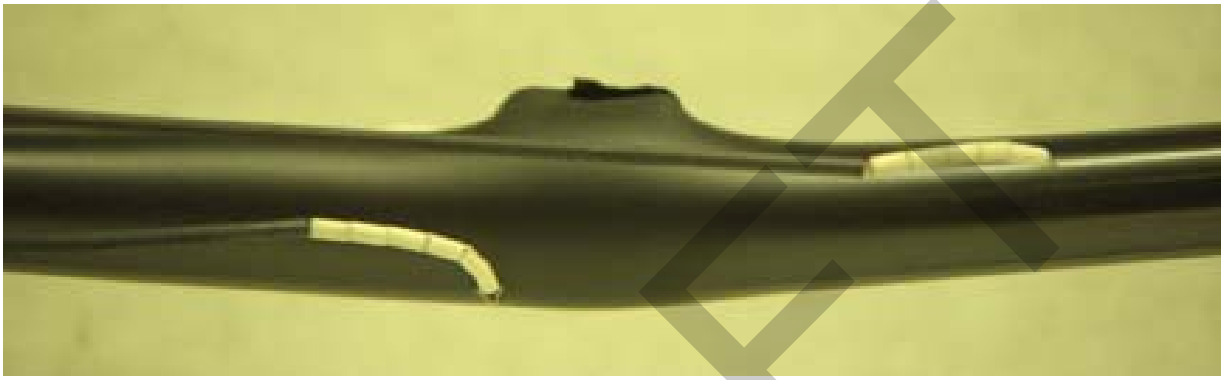

(b)

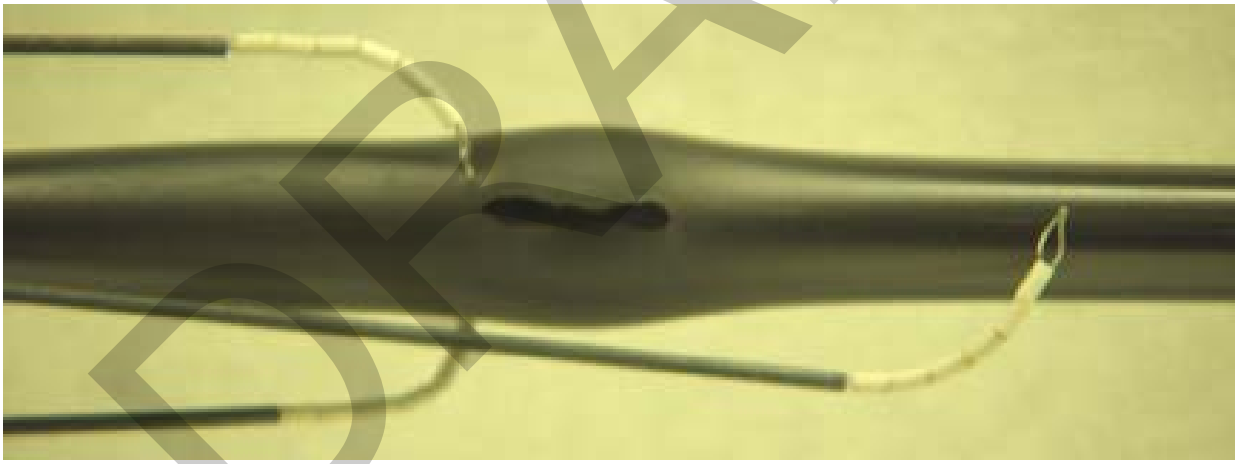

(c)

Figure 160. Images of the OCL#8 test sample after heating in argon to burst at ≈770ºC (due to a maximum internal pressure of 8.62 MPa [gauge] and an estimated pressure of ≈7.7 MPa just prior to burst) and slow cooling: (a) low magnification of side view of sample, (b) higher magnification of side view of ballooned-and-burst region, and (c) higher magnification of frontal view of burst opening. Top of the sample, from which the thermocouples were inserted prior to welding, is to the left in these photographs.

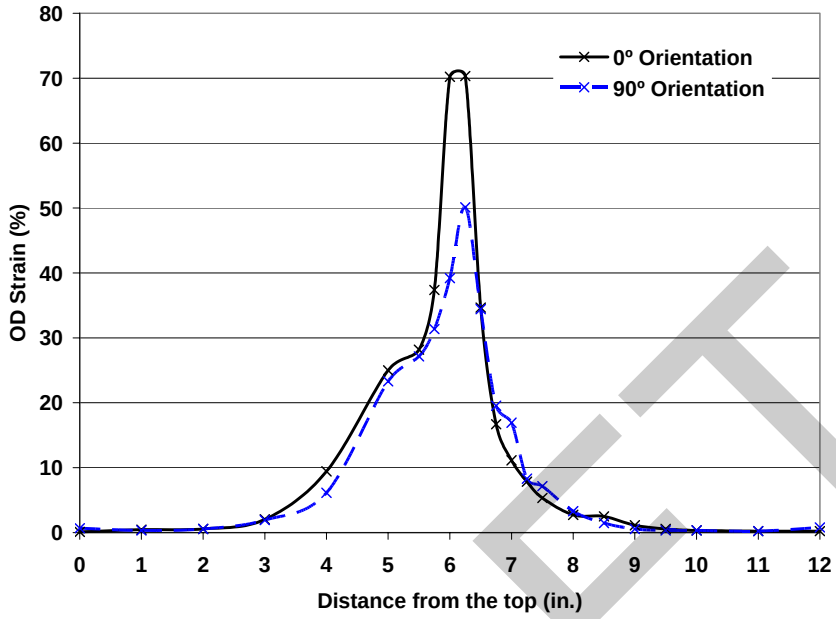

Figure 161. Axial profile of the diametral ballooning strain at 0º and 90º relative to the burst opening for test sample OCL#8 heated under internal pressure in argon up to burst at ≈770ºC and slow cooled to RT.

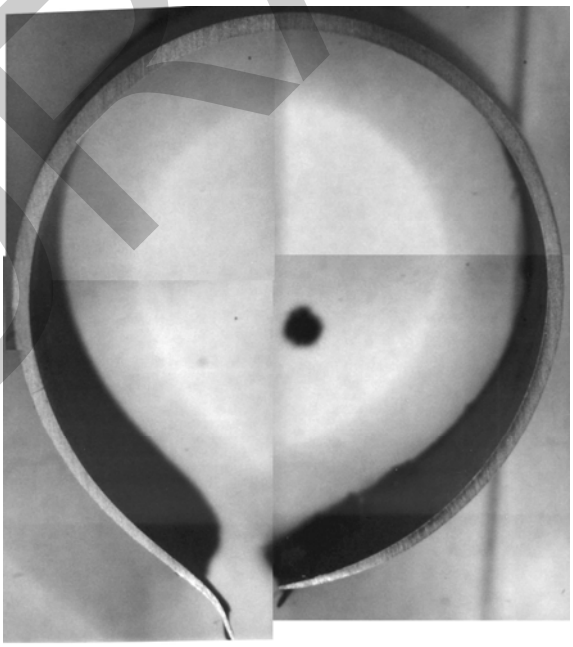

Figure 162. Cladding cross section at burst midplane for OCL#8 sample (see Figure 161).

The axial distribution of cladding strain shown in Figure 161 is typical of samples that developed a single balloon (e.g., OCL#5 and OCL#11). Ballooning and burst are instability phenomena. Differences were observed in maximum ballooning strain (≈40% to 60%), axial extent of ballooning (100-150 mm), burst location relative to the sample midplane (-13 mm to +35 mm), burst length (11-17 mm), and maximum burst opening (0.8-2.5 mm). These test-to-test result differences are to be expected for instabilities of this nature. However, later tests (e.g., OCL#13, OCL#17, and OCL#22) exhibited a secondary balloon region in addition to the larger primary balloon region containing the burst opening. Diametral strain profiles for OCL#5 and OCL#6 are shown in Section 6.2 in comparison plots with results from corresponding high-burnup test-sample results (ICL#1 and ICL#2). Diametral profiles for the three test samples with secondary balloon regions are shown in Figures 163-165. The secondary balloons have a maximum diametral strain of 15-30%. However, these secondary balloons appears to have very little influence on the axial extent of ballooning. The criterion for determining this axial extent is ≥2% strain, along with some judgment based on the intersection of the steeply decreasing part of the profile and the flat portion of the profile.

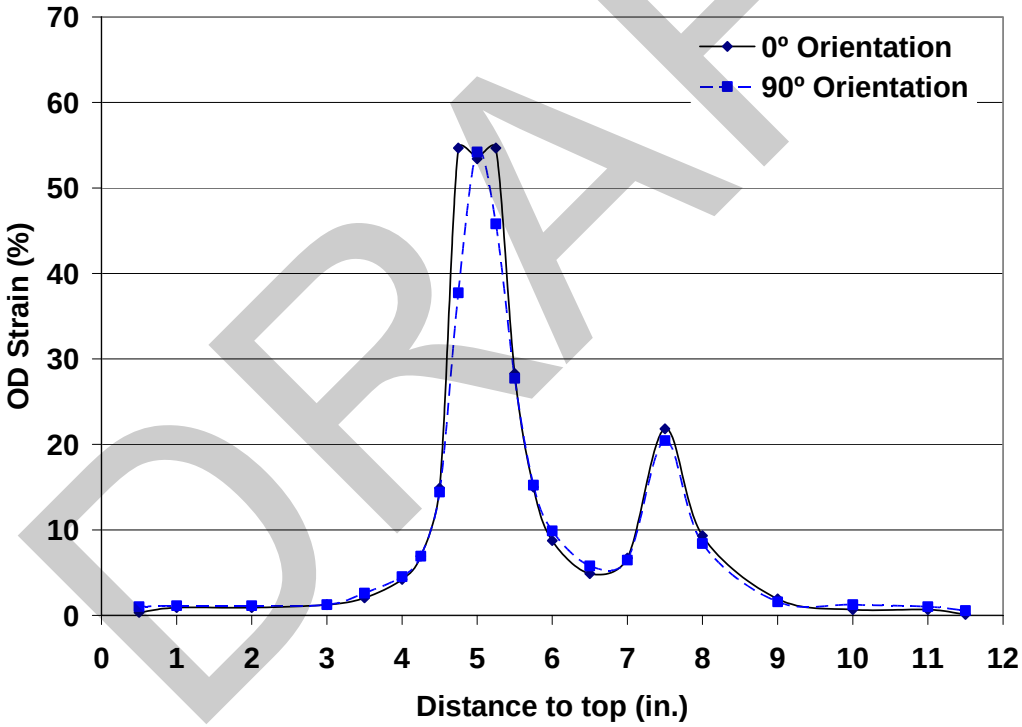

Figure 163. Ballooning strain profile for OCL#22 test sample held for 1 s at 1204ºC, cooled to 800ºC, and quenched.

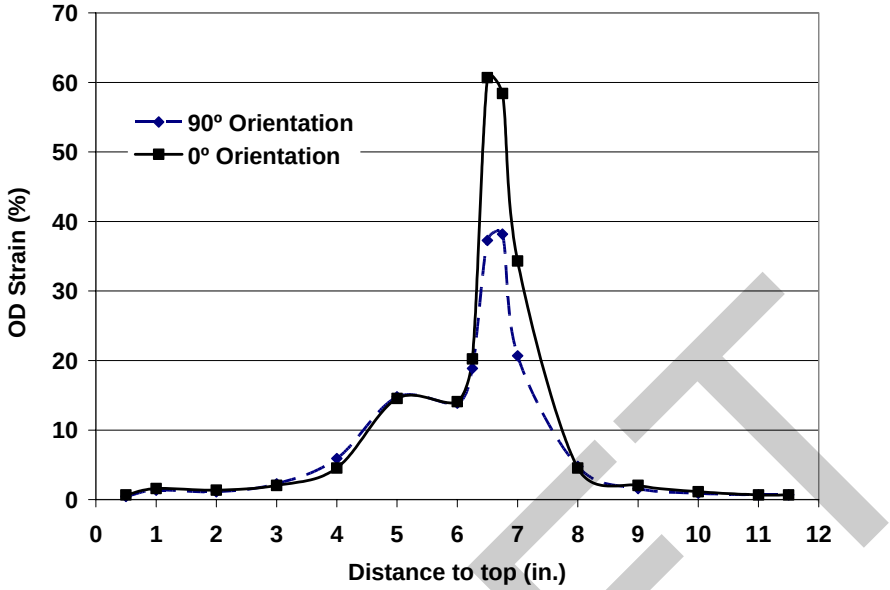

Figure 164. Ballooning strain profile for OCL#17 test sample held for 120 s at 1204ºC, cooled to 800ºC, and quenched.

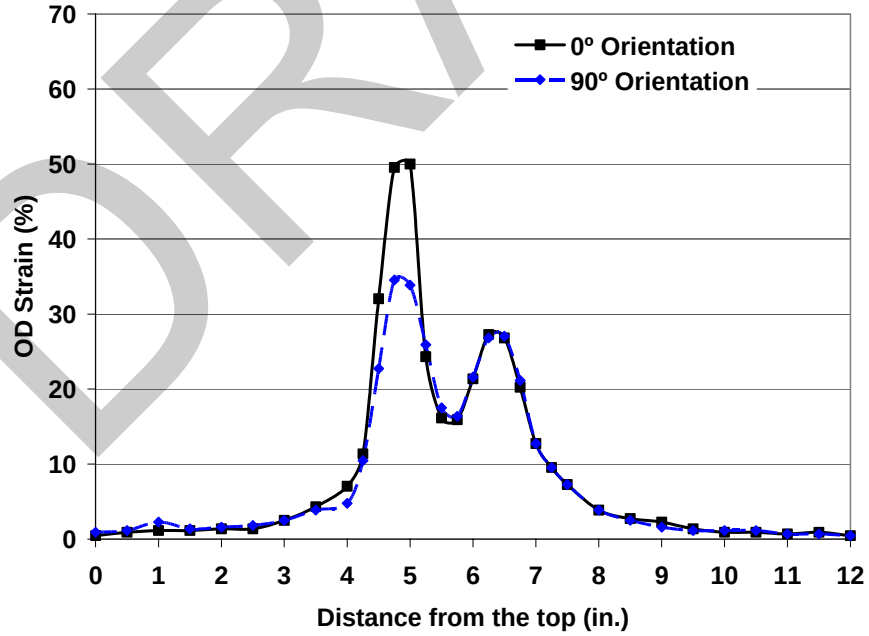

Figure 165. Ballooning strain profile for OCL#13 test sample held for 300 s at 1204ºC, cooled to 800ºC, and quenched.

6.1.2 Oxidation and hydrogen pickup due to secondary hydriding

Due to steam leakage through the burst opening, oxidation within the balloon region is expected to be two-sided. Such oxidation results in hydrogen release to the near-stagnant steam within the test sample. Unlike the outer surface exposed to flowing steam, a large fraction of the released hydrogen is trapped inside the sample and available for pickup by the inner-metal surface in and near the balloon region. Data from quantitative metallography and LECO oxygen-content measurements have been used to determine oxygen pickup (ΔC_O in wt.%) and corresponding ECR (in %). To determine oxygen pickup from the LECO data, two sets of corrections must be made to the raw data. The first set involves renormalizing the LECO oxygen content in wt.% to the weight of the metal prior to oxidation and subtracting the oxygen content in the as-fabricated cladding (C_{Oi} = 0.11 wt.% for 9×9 Zry-2). The second correction accounts for loss of brittle oxide during LECO sample preparation. Some oxide is lost during sectioning of 2-mm-long rings. More is lost during the "snipping" of four arc lengths from the ring. This sample subdivision is needed to prevent exceeding the oxygen-level limit of the LECO detector. In previous work, oxygen pickup has been determined by three means: sample weight gain, quantitative metallography, and refined LECO oxygen-content data. The oxygen content determined from the raw LECO data exhibited lower oxygen pickup than determined by means of sample weight gain and metallography. By multiplying the raw LECO data by a factor of 1.1, good agreement was obtained by all three techniques. The 1.1 factor is used to determine measured ECR. However, the correction factor is not needed to determine hydrogen pickup (ΔC_H). The equations used to convert the raw LECO oxygen (L_O in wt.%) and hydrogen (L_H in wppm) data to ECR and hydrogen pickup are:

$$\Delta C_O = (L_O - C_{Oi})/(1 - L_O/100\%), \text{ wt.\%} \quad (9)$$

$$ECR = 2.85\ (1.1\times L_O - C_{Oi})/(1 - 1.1\times L_O/100\%), \% \quad (10)$$

$$\Delta C_H = (1 + \Delta C_O/100\%)\ L_H - C_{Hi}, \text{ wppm} \quad (11)$$

where C_{Hi} is the hydrogen content (5 wppm) of as-fabricated 9×9 Zry-2.

The LECO data for OCL#22 (1-s hold time at 1204ºC) and OCL#17 (120-s hold time at 1204ºC) – both taken after bend-to-failure tests – are shown in Figures 166 and 167, respectively. For the OCL#22 test sample, the maximum oxygen and hydrogen measurements were 3.95 wt.% and 2105 wppm, respectively. At the axial location where the maximum hydrogen reading was found, the LECO oxygen-content measurement was 2.33 wt.%. Using Equations 9-11, the maximum ECR is calculated to be 11%, and the maximum hydrogen pickup is calculated to be 2150 wppm. The 11% ECR value is higher than the 9% CP-predicted value in Table 68. If the 1.1 factor is not used for such a low-oxidation level sample (i.e., oxide loss during cutting and snipping is smaller than assumed), the measured ECR is reduced to 10%. The maximum hydrogen content measured by LECO was 2700 wppm, where the oxygen pickup was 2.36 wt.%. The hydrogen pickup calculated by Equation 11 is 2760 wppm. The magnitude of the

hydrogen pickup is quite large for such a short hold time at 1204ºC. The results suggest that significant hydrogen pickup occurs early in the LOCA transient. Enough hydrogen is released to the cladding interior due to inner-surface oxidation during the ramp to result in high hydrogen pickup.

The OCL#17 LECO data shown in Figure 167 were taken from half of the sample. The maximum measured oxygen and hydrogen contents were 4.24 wt.% and 2936 wppm, respectively. The ECR determined from Equation 10 is 14%, which agrees with the CP-predicted value. Using 2.39 wt.% oxygen measured by LECO at the peak hydrogen location gives a hydrogen pickup of 3000 wppm. In terms of peak hydrogen content, relatively little is picked up during the 119-s additional hold time at 1204ºC.

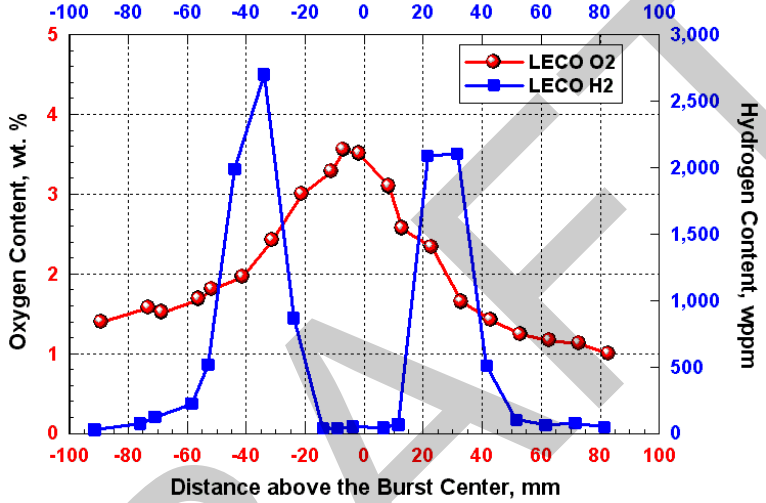

Figure 166. LECO oxygen and hydrogen content for OCL#22 sample ramped in steam from 300ºC to 1204ºC at 5ºC/s, held at 1204ºC for 1 s, cooled at 3ºC/s to 800ºC, and quenched.

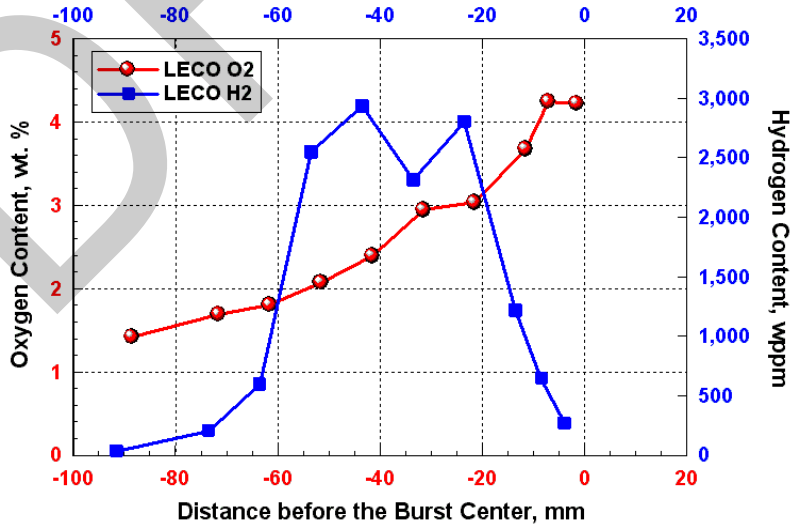

Figure 167. LECO oxygen and hydrogen content for OCL#17 sample ramped in steam from 300ºC to 1204ºC at 5ºC/s, held at 1204ºC for 120 s, cooled at 3ºC/s to 800ºC, and quenched.

LECO data were also obtained for the OCL#11 sample (300-s hold time at 1204ºC). Oxygen pickup from quantitative metallography was also determined. Figure 168 shows (a) the LECO data and (b) the converted data for ECR and hydrogen pickup. The quantitative metallography and LECO results are in excellent agreement. The maximum ECR determined from data is 18.5%, as compared to 21% CP-predicted ECR in Table 68. The maximum hydrogen pickup was 3900 wppm. Thus, >70% of the maximum hydrogen pickup occurs during the ramp to 1204ºC.

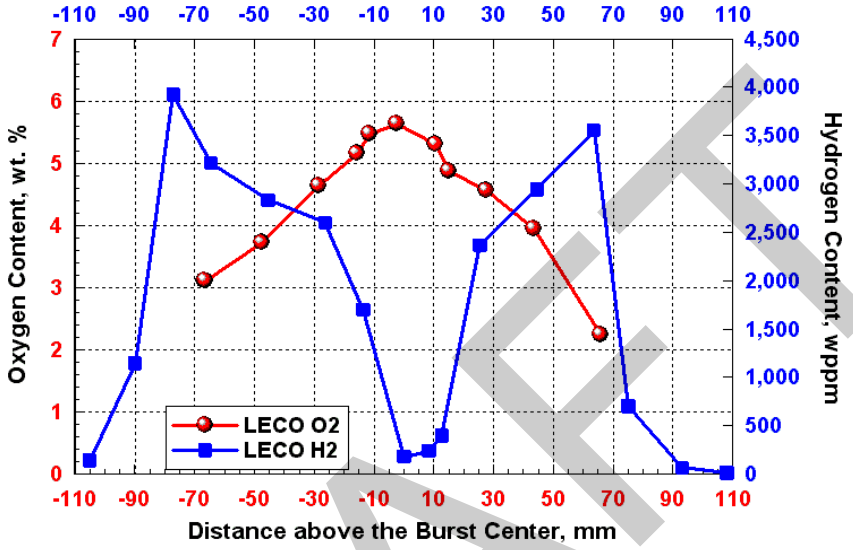

(a)

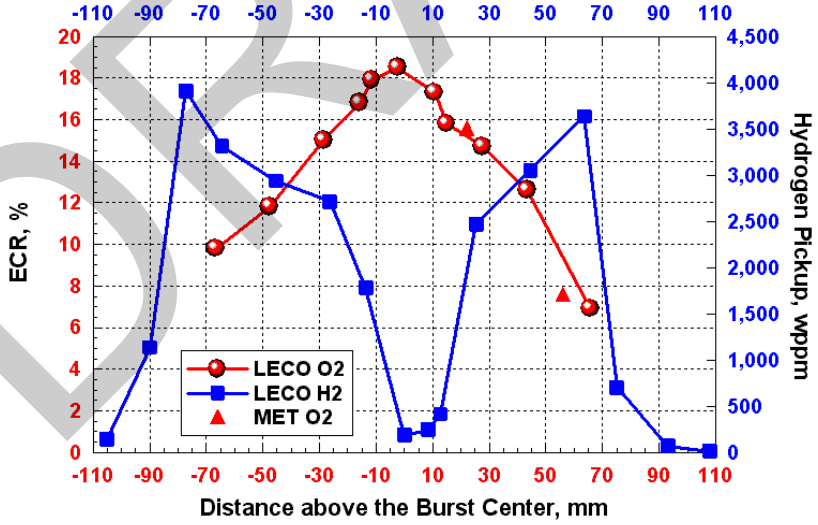

(b)

Figure 168. Data for OCL#11 sample ramped in steam from 300ºC to 1204ºC at 5ºC/s, held at 1204ºC for 300 s, cooled at 3ºC/s to 800ºC, and slow cooled from 800ºC to RT: (a) LECO oxygen and hydrogen content and (b) ECR derived from LECO and metallography data and hydrogen pickup derived from LECO data.

Extensive metallographic characterization was performed for the OCL#11 test sample. The results for the burst midplane are presented in Figure 169 because they lead to insights regarding the post-test strength and ductility corresponding to the maximum ECR. For the LOCA integral test samples, the four-point bend test was used to determine ductility. The four-point-bend fixture (see Section 6.1.3) has a 150-mm span between loading points. Within this span, a uniform bending moment is applied to the sample. The span covers the ballooned region, along with some of the region outside the balloon. Figure 169 shows "local" ECR values determined from quantitative metallography. Although for licensing purposes the maximum ECR in the balloon region is defined in terms of the minimum cross-section-averaged wall thickness, there is considerable variation in percent oxidation and embrittlement around this cross section. The burst tips are highly oxidized and brittle. The oxidation level decreases from >36% ECR at 0º (relative to the burst opening), where the wall is thinnest, to 13% ECR at 180º, where the wall is thickest. In comparing Figure 169 to Figure 162, we concluded that the thin and highly oxidized cladding at the edges around the burst opening was probably lost during handling, cutting, and metallographic mount preparation. Based on Figure 169, if the four-point test is conducted in the traditional way with the flawed region (burst region) under axial tension during the start of the bending test, then the crack will proceed rapidly through that region. Whether or not the sample has any bending ductility will depend on the whether or not the cladding near the back of the burst region (within 150º to 210º relative to the burst) will have sufficient ductility to blunt the crack propagating across the cladding section.

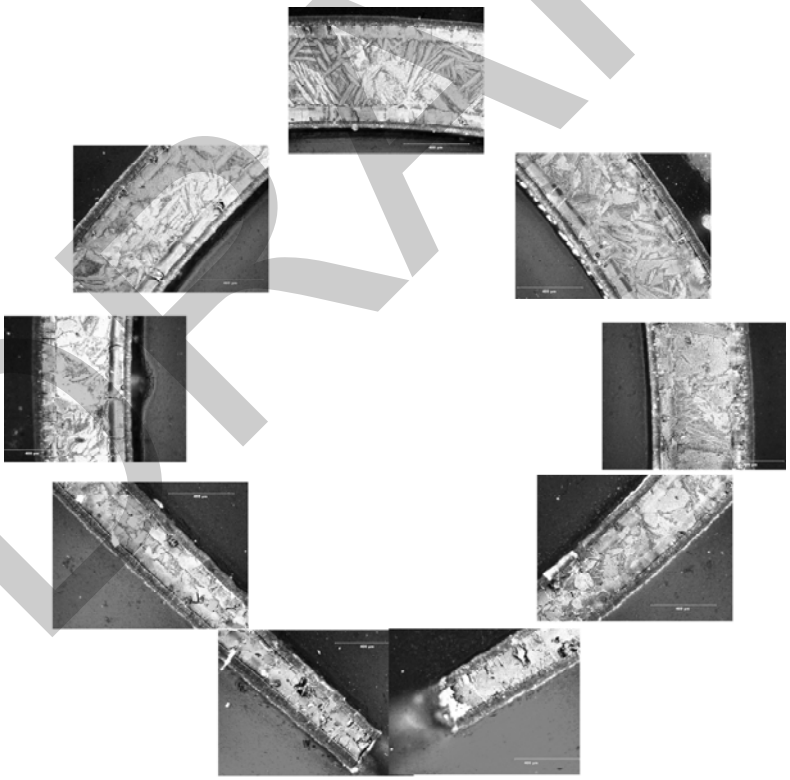

Figure 169. Metallographic images at nine locations around the cross section of the midplane of the burst region of the OCL#11 test sample (300 s at 1204ºC). The cross-section-averaged ECR is 18.5%. Locally, the oxidation level varies from >36% to 13%.

6.1.3 Post-quench ductility for unirradiated LOCA integral samples

The Instron apparatus used to conduct the ring-compression tests was also used to conduct four-point bend tests. A special loading platen and fixture were designed to apply a uniform bending moment over 150 mm of the sample with the burst-region midplane located approximately at the center of the 150 mm. The test apparatus was benchmarked by comparing elastic bending results for as-fabricated HBR-type 15×15 cladding to the textbook solution for bending stiffness (force divided by displacement). The bending tests were conducted in the displacement-controlled mode. Measured displacement corresponds to the displacement at the loading points, ±75 mm from the center of the as-fabricated cladding or ±75 mm from the burst midplane location.

Several four-point-bend demonstrations were conducted with post-test samples with the same temperature history as the OCL#13 test sample listed in Table 68. These samples were weak enough to be bent and broken by hand. With the burst area under bending tension, clean breaks occurred at the burst midplane under the uniform bending moment. With the burst area under compression, an axial crack formed at the burst tip, propagated into the high oxygen-hydrogen region between the burst midplane and the balloon neck, and caused cross-section failure due to bending in this region. Thus, while the burst region is structurally very weak, the thicker cladding region away from the burst is stronger in the unflawed condition, but is brittle enough to fail first in the flawed condition. This behavior illustrates the difficulties that arise from relying on the strength of brittle material. The strength, or resistance to load, decreases dramatically if a flaw is present.

The bending demonstrations were useful for planning purposes. However, the four-point-bend tests were needed for quantitative data. Test samples OCL#22 (1-s hold time at 1204ºC) and OCL#17 (120-s hold time at 1204ºC) were subjected to four-point bending. Figure 170 shows the pre- and post-test sample, along with the Instron load-displacement curve. Most of the burst midplane cross section fails in a brittle mode, as indicated by the sharp load drop of >70% at a bending moment of 21 N·m. However, the region 180º from the burst opening is highly ductile. Within the deflection limits of the apparatus, this back ligament does not fail.

Figure 171 shows the four-point-bend results for the OCL#17 sample, which was oxidized to a higher level than the OCL#22 sample. This higher oxidation level results in a lower maximum bending moment (12 vs. 21 N·m) and brittle failure across the whole cross section. As predicted, by orienting the sample such that the burst region is in bending tension, failure occurs near the burst midplane cross section. Because of the bending orientation, the high-hydrogen cross section with the thicker wall and the lower level of oxidation did not fail even though it was probably more brittle than the weaker burst cross section.

Although additional tests were not conducted at higher oxidation levels (i.e., hold times at 1204ºC), the trend is clear: as the oxidation level increases, the bending resistance of the burst region decreases (i.e., failure bending moment decreases), and the rest of the balloon region outside the burst area continues to embrittle as the oxygen and hydrogen content of this region increases.

From an embrittlement point of view, the hydrogen pickup due to oxidation inside the cladding increases so fast that it would be difficult to find an ECR low enough to guarantee ductility in the balloon region, even if ring-compression tests were performed at 135ºC on rings cut away from the burst region. However, the strength or fracture toughness of the balloon region decreases as the oxidation level increases. The results suggest that some ECR limit would be needed in the balloon region to prevent

(a)

(b)

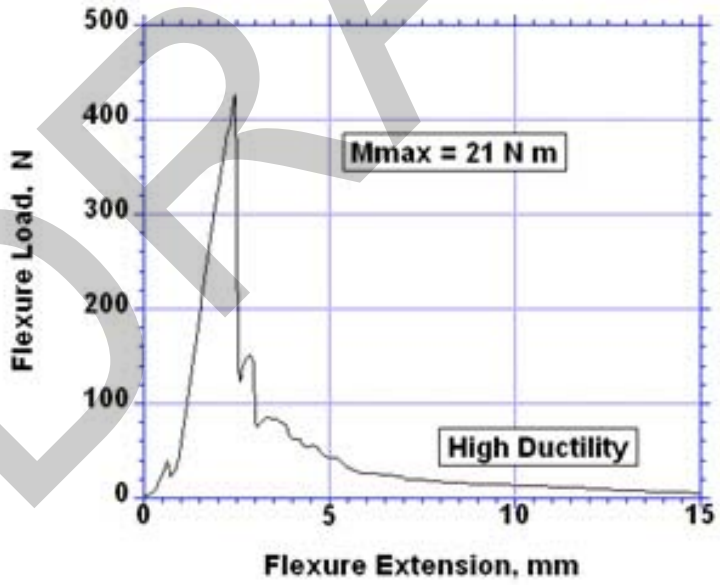

(c)

Figure 170. Bending test results for LOCA integral test sample OCL#22: (a) pretest appearance with burst area on bottom, (b) post-test appearance with burst area on bottom, and (c) bending load vs. displacement (flexure extension) at the loading points.

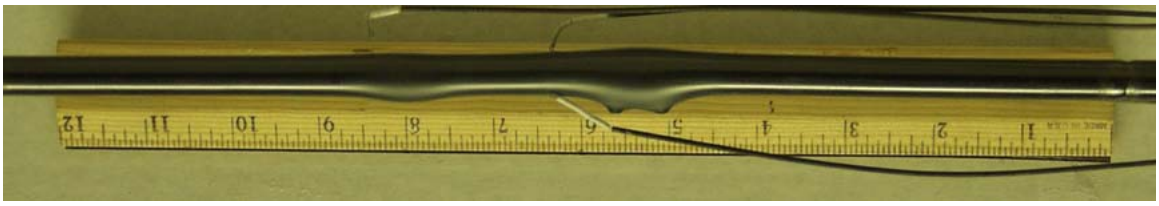

(a)

(b)

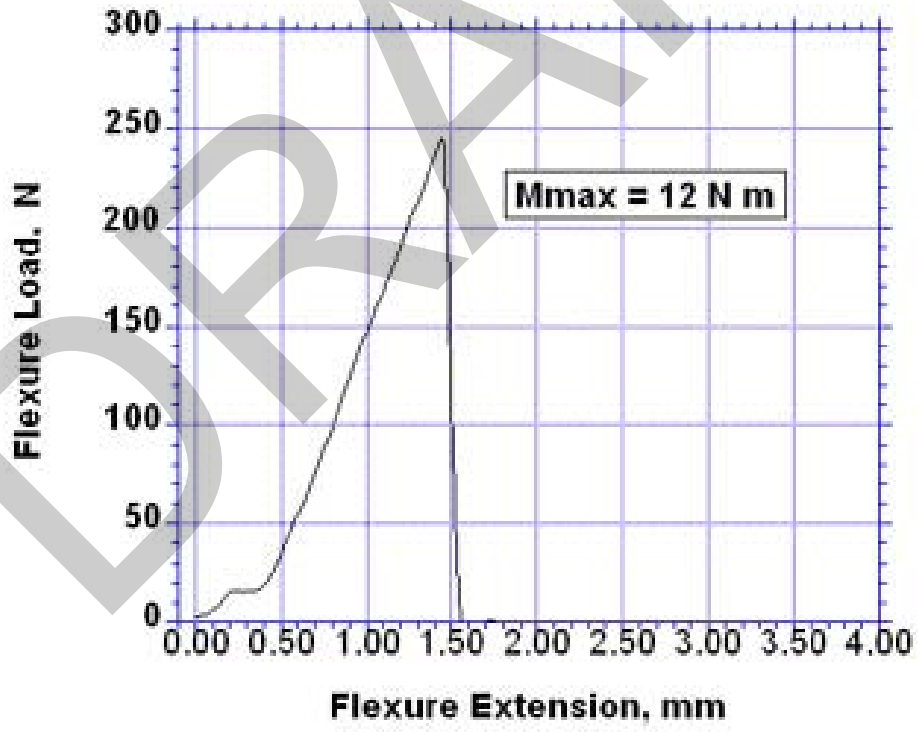

(c)

Figure 171. Bending test results for LOCA integral test sample OCL#17: (a) pretest appearance with burst area on bottom, (b) post-test appearance with burst area on bottom, and (c) bending load vs. displacement (flexure extension) at the loading points.

across-wall failures from occurring due to thermal stresses during quench, side loads due to rod-to-rod impact, and dead-weight loading of the cladding. Based on these studies, that limit would be >14% CP-ECR and <26% CP-ECR. The current 17% limit should be sufficient to guarantee the minimal toughness.

6.2 High-burnup Limerick BWR 9×9 Zircaloy-2 oxidized at 1204ºC

Based on characterization of as-irradiated, high-burnup Limerick cladding (rod F9) at the fuel midplane and at 0.7 m above the midplane, the corrosion layer thickness (≈10 μm), the hydrogen content (≈70 wppm), and the fuel morphology were observed to be relatively constant for these axial locations. These values were assumed for the as-irradiated Limerick sections used for LOCA integral tests. Figures 172 and 173 show the locations of the ICL#1-2 samples from rod F9 and the ICL#3-4 samples from rod J4, respectively. The burnup of these rods was 56-57 GWd/MTU. Additional fuel characterization was performed within the region labeled "Practice Samples" in Figure 172. These samples were used to test the fuel removal device and to verify that removal of 13-25 mm of fuel from the ends of the LOCA sample by means of a hammer drill did not disturb the remaining fuel column.

In-cell LOCA integral tests were conducted with two thermal couples strapped to the outer surface of the cladding 50 mm above the sample centerline. One of these was used to control the furnace power to give a hold temperature of 1204ºC at that location. The other thermocouple, located 180º from the control thermocouple, was used to measure circumferential variation in cladding temperature. Based on benchmark tests (e.g., OCL#14) with unirradiated Zry-2, the difference in output between a strapped and a welded thermocouple (TC) at the same axial elevation is ≈10ºC. Some of this difference may be due to circumferential temperature variation as the two TCs did not have the same circumferential location. Within the expected axial and circumferential variations in high-burnup cladding temperature during and following ballooning and burst, the difference between strapped and welded TC readings is not considered significant.

6.2.1 Ballooning and burst of high-burnup samples

Table 69 summarizes the results of the four in-cell tests with high-burnup fueled Limerick cladding (ICL series), along with companion out-of-cell tests OCL#5 and OCL#11. Both ICL#1 and OCL#5 were ramp-to-burst tests in argon. The burst temperatures, pressures, and maximum diametral strains are remarkably close for these two tests. In terms of these parameters, high-burnup operation had little effect on cladding burst conditions and strains. Hydrogen pickup during normal reactor operation would be expected to affect both the burst conditions and the burst strain. However, high-burnup Limerick cladding had low hydrogen content resulting from its thin corrosion layer.

The primary differences observed between the high-burnup cladding and the unirradiated cladding was in the pre-burst bending (less for high burnup), the axial extent of the balloon region (less for high burnup), and the shape of the burst region (oval for high burnup). Figure 174 shows a comparison of the ballooned-and-burst regions for the ramp-to-burst samples ICL#1 and OCL#5. Figure 175 shows a comparison in burst openings between the ICL#2 and OCL#11 test samples. The profiles of diametral strain for these companion tests are compared in Figure 176.

In Figure 177, the four in-cell test samples are shown. As expected, the partially quenched sample (ICL#3) and the fully quenched sample (ICL#4) have wider burst openings due to loss of thin, brittle cladding near the edges of the burst opening.

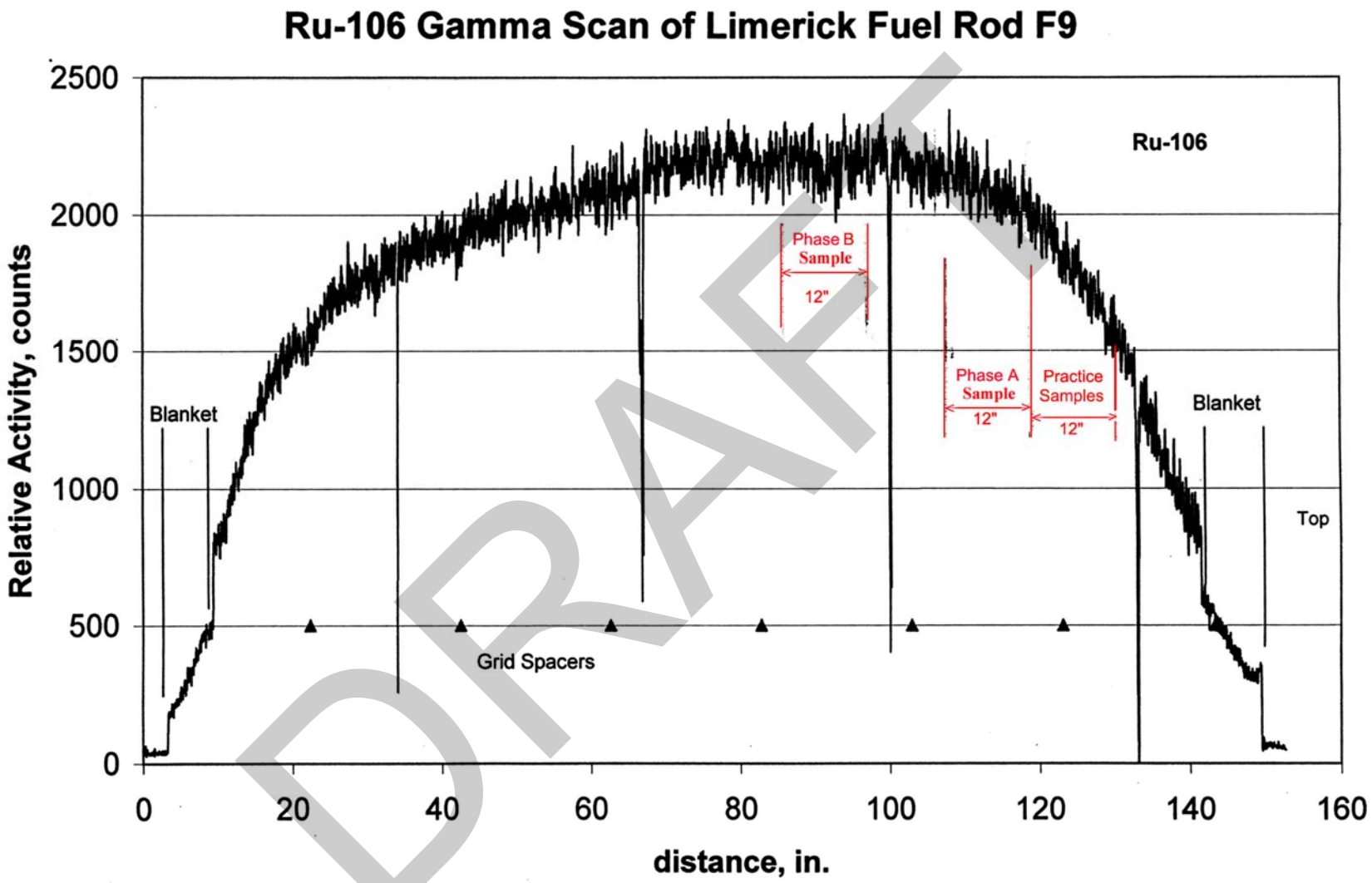

Figure 172. Gamma scan profile for high-burnup Limerick rod F9 showing locations of LOCA integral samples ICL#1 (labeled Phase A) and ICL#2 (labeled Phase B). Fuel and cladding characterization were performed at the fuel midplane, at 0.7 m above the midplane, and at ≈1.1 m above fuel midplane.

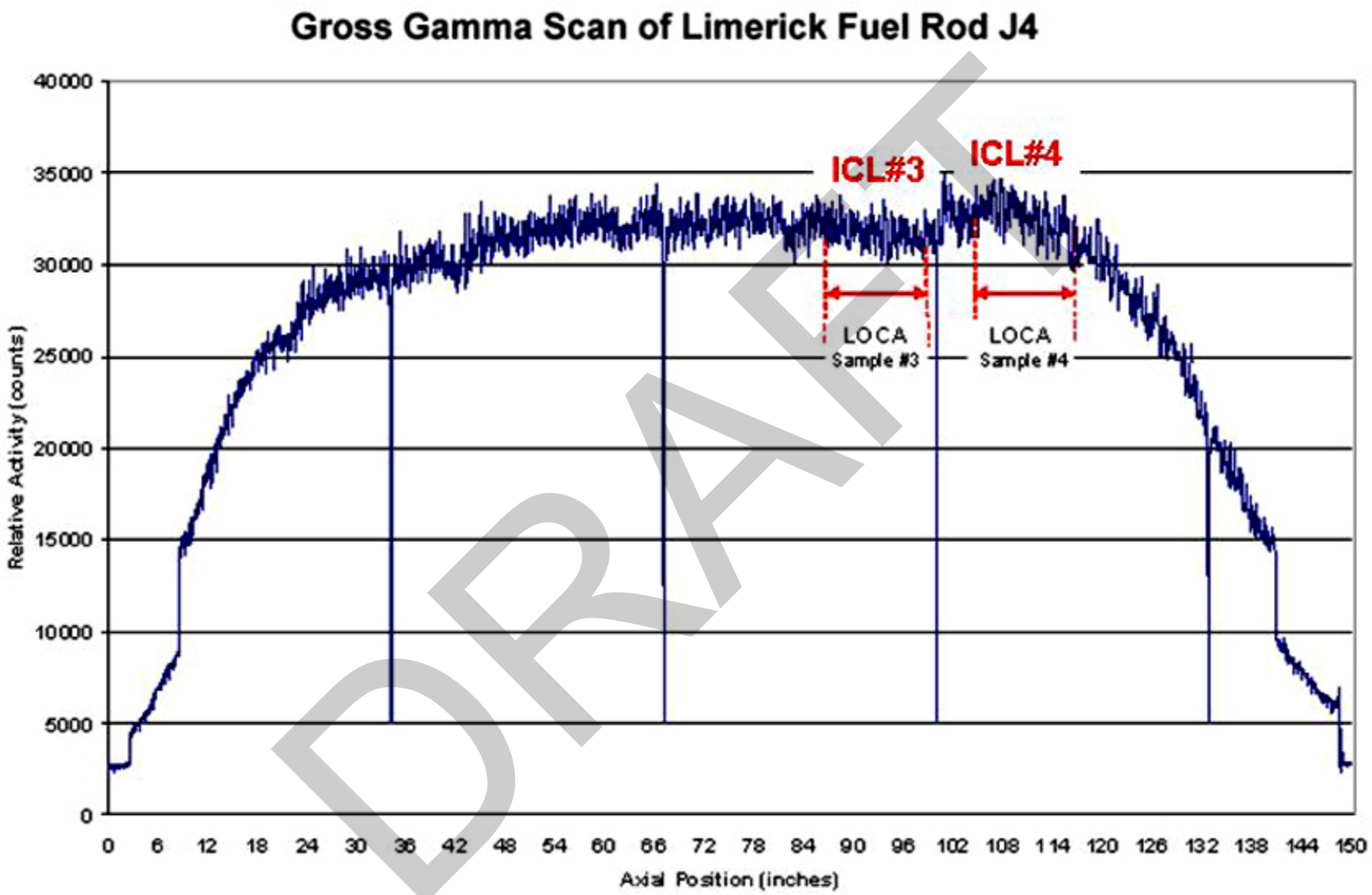

Figure 173. Gamma scan profile for high-burnup Limerick rod J4 showing axial locations of LOCA integral samples ICL#3 and ICL#4.

Table 69 Summary of In-cell LOCA Integral Tests (ICL) with High-burnup Fueled Cladding Specimens from Limerick BWR. Also shown are the results of companion out-of-cell tests OCL#5 and OCL#11 with non-irradiated Zry-2 cladding.

Parameter	ICL#1	OCL#5	ICL#2	OCL#11	ICL#3	ICL#4
Environment	Argon	Argon	Steam	Steam	Steam	Steam
Hold Temperature, ºC	---	---	1204	1204	1204	1204
Hold Time, s	0	0	300	300	300	300
Quench (Q) at 800ºC or Slow Cooled (SC)	SC	SC	SC	SC	Q-800ºC to 460ºC	Q-800ºC
Max. Pressure, MPa	8.96	8.96	8.87	8.61	9.00	8.86
Burst Pressure, MPa	8.61	8.28	8.01	7.93	8.60	8.00
Burst Temperature, °C	≈755	733	≈750	753	≈730	≈790
Burst Shape	Oval	Dog Bone	Oval	Dog Bone	Oval	Oval
Burst Length, mm	13	13	14	11	11	15
Max. Burst Width, mm	3	2.5	3.5	1	4.6	5.1
Length of Balloon, mm	≈70	100	≈ 90	≈ 140	≈ 100	≈ 80
$(\Delta D/D_o)max$, %	38±9	44±10	39±10	43±10	43±9	36±9
Max. Calculated ECR, %	0	0	≈20	≈21	≈21	≈20

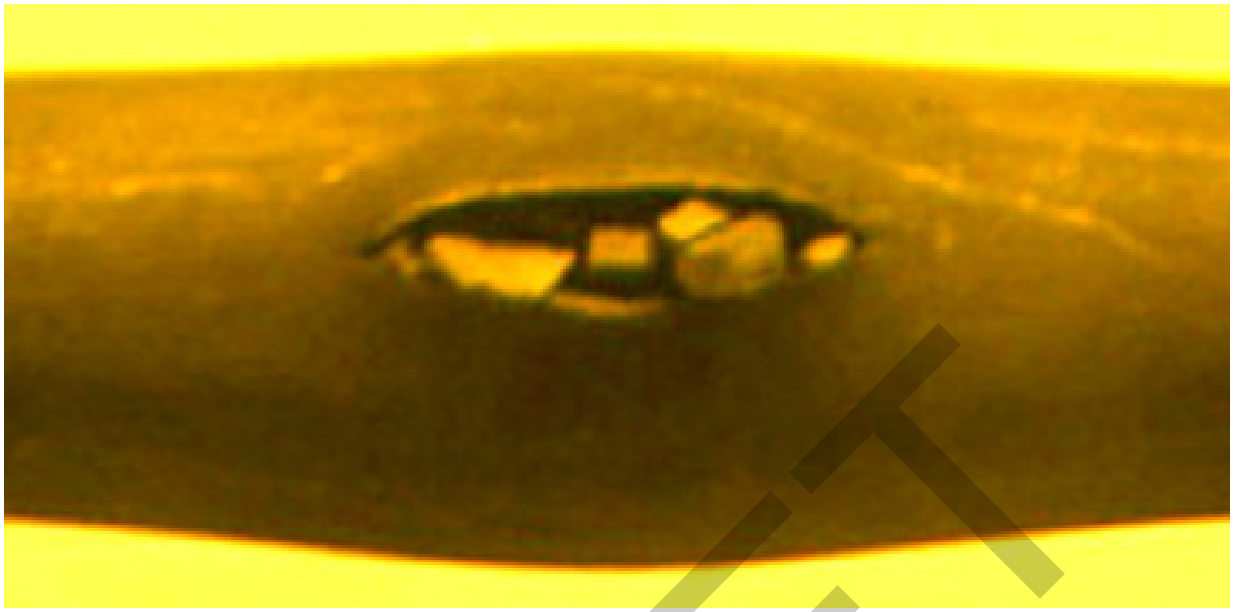

(a)

(b)

Figure 174. Comparison of burst openings for (a) in-cell LOCA integral test ICL#1 specimen from high-burnup Limerick rod F9 and (b) out-of-cell companion test OCL#5 specimen from unirradiated Zry-2 cladding. Burst lengths are both ≈13-mm long for these ramp-to-burst test samples.

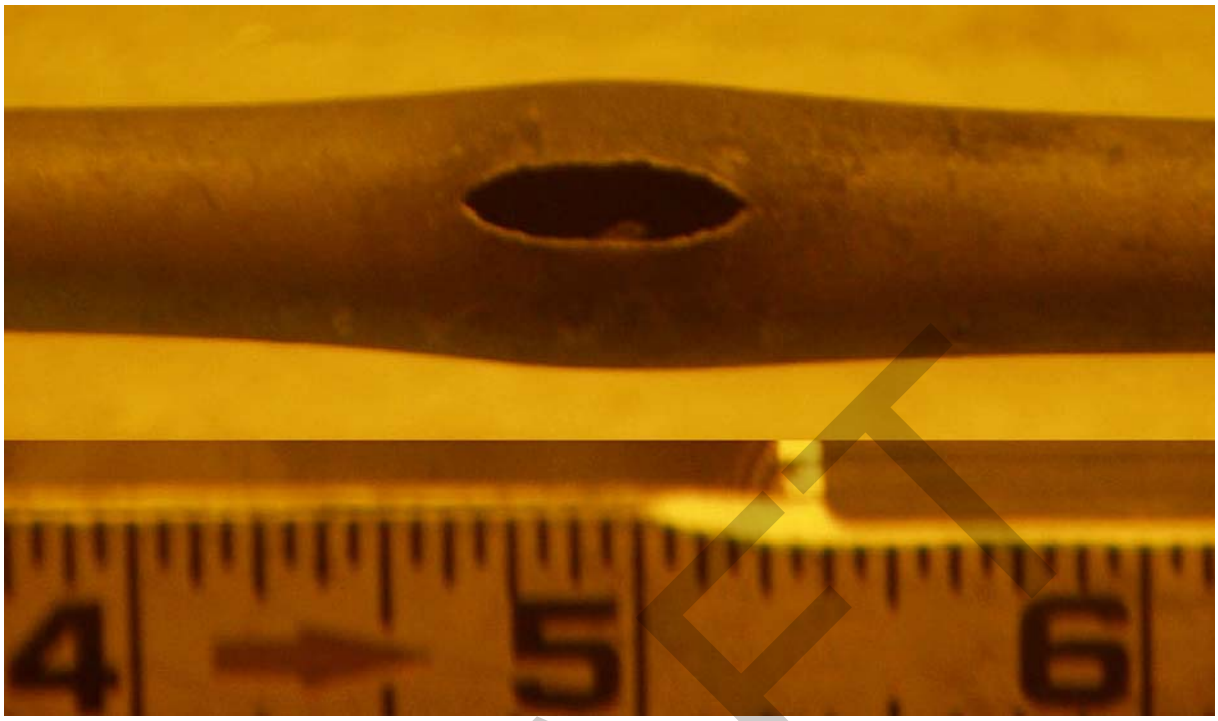

(a)

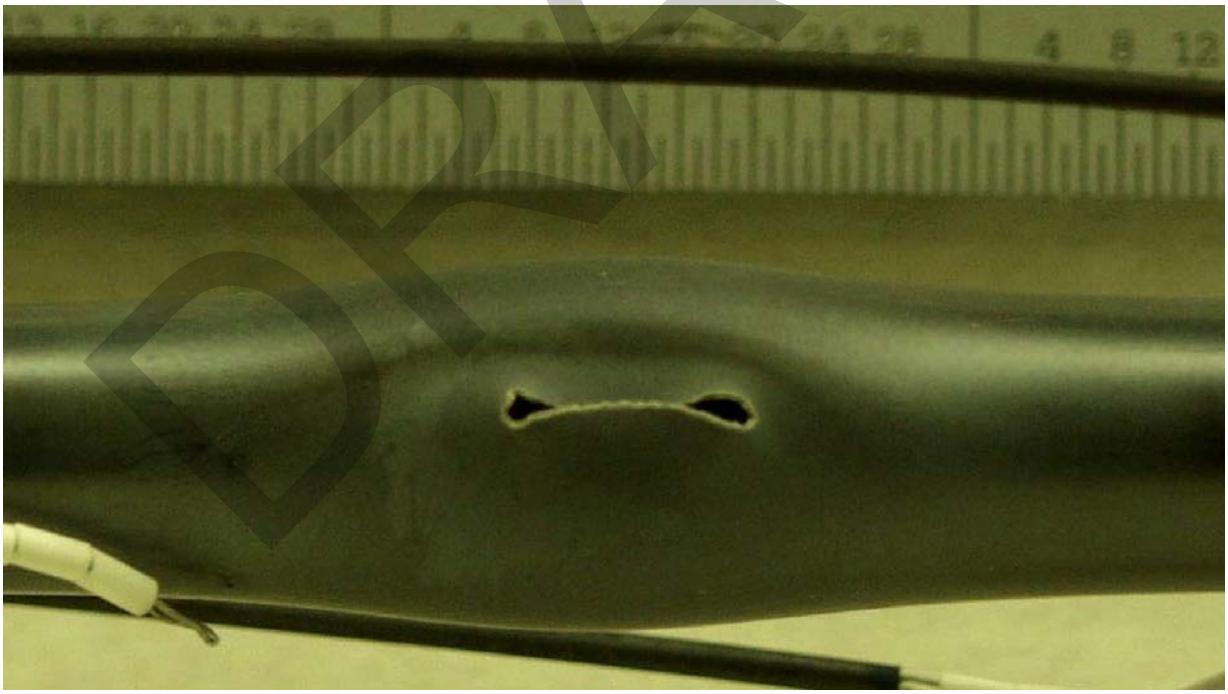

(b)

Figure 175. Comparison of burst openings for (a) high-burnup Limerick ICL#2 specimen and (b) unirradiated OCL#11 Zry-2 specimen after 300-s exposure to steam at 1204°C, followed by slow cooling to RT.

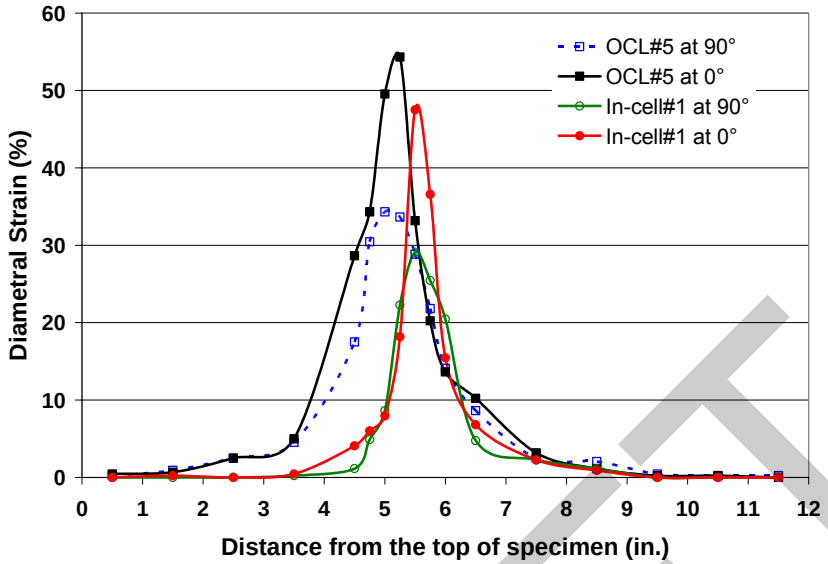

Figure 176a. Outer-diameter strain for in-cell test ICL#1 sample (high-burnup Limerick fueled Zry-2) and companion out-of-cell test OCL#5 sample (unirradiated Zry-2 filled with zirconia pellets). Both tests were ramp-to-burst tests in argon, followed by slow cooling to RT.

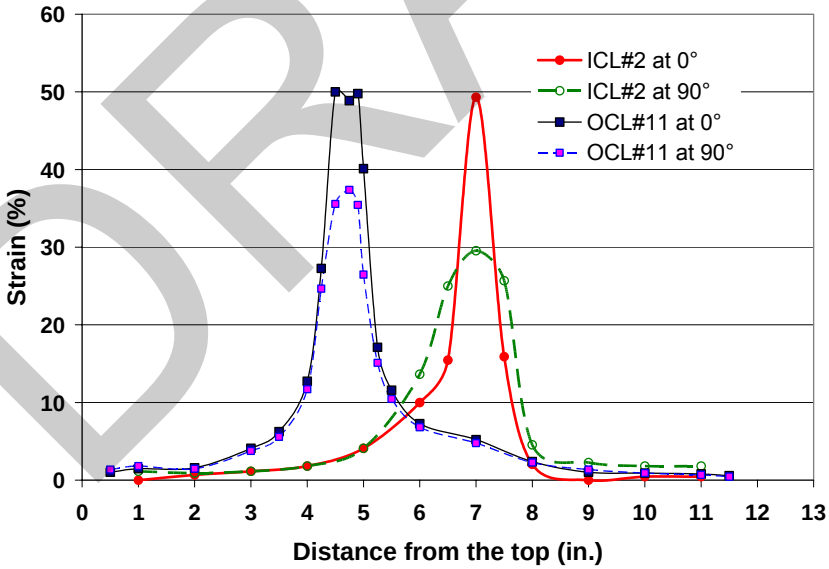

Figure 176b. Outer-diameter strain for in-cell test ICL#2 sample (high-burnup Limerick fueled Zry-2) and companion out-of-cell test OCL#5 sample (unirradiated Zry-2 filled with zirconia pellets). Both samples were ramped to 1204ºC in steam, held at 1204ºC for 300 s, and slow cooled to RT.

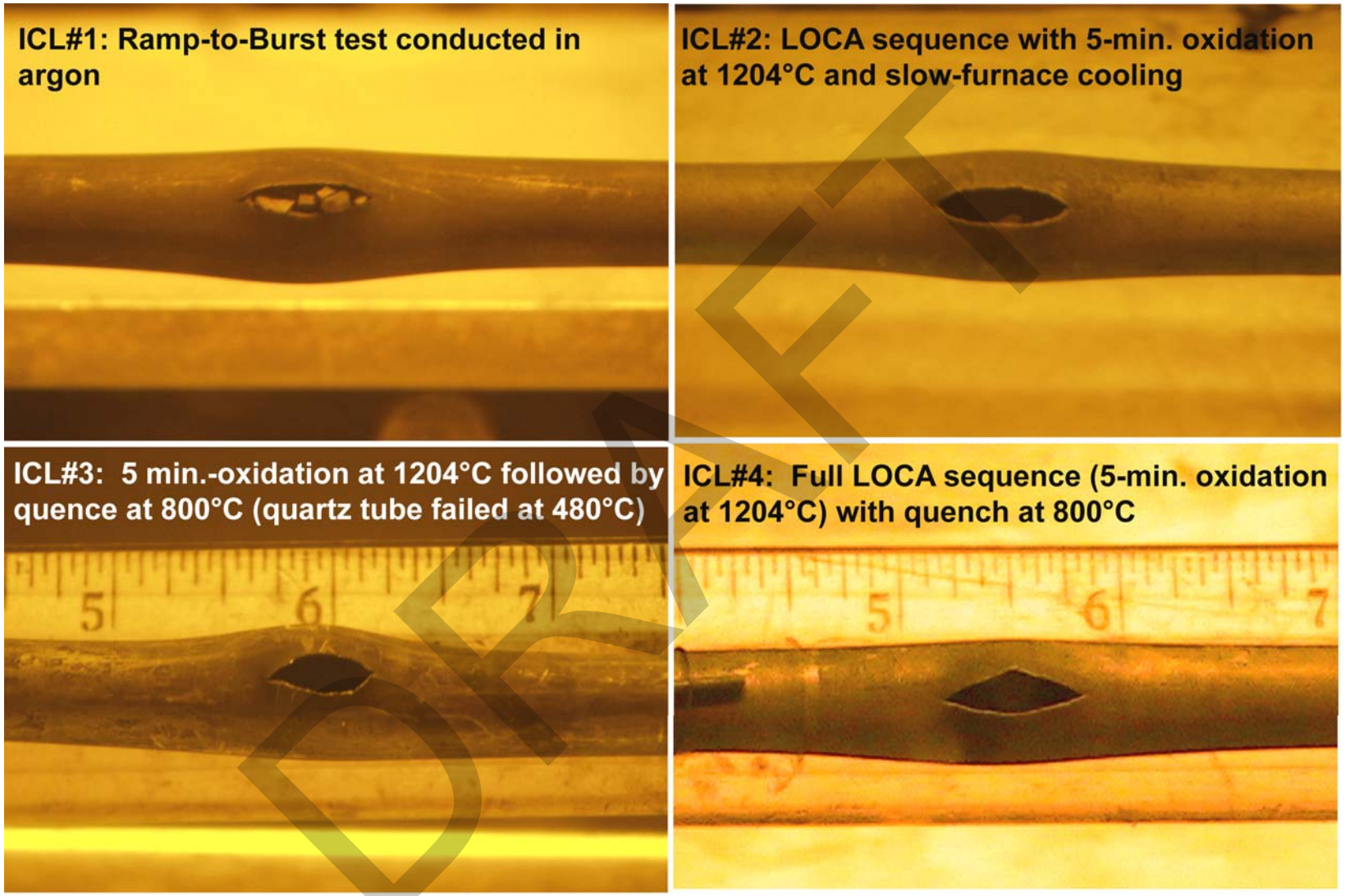

Figure 177. Comparison of ballooned-and-burst regions of four in-cell LOCA integral test samples.

6.2.2 Oxidation and hydrogen pickup due to secondary hydriding for high-burnup samples

For ICL test samples #2 and 3, extensive metallographic characterization and LECO measurements were performed within ±50 mm of the burst midplane to determine the degree of steam oxidation (two-sided vs. one-sided and OD vs. ID oxide-layer thickness within the balloon region), the axial profile of oxygen pickup determined by means of LECO and metallography, and the axial profile of hydrogen pickup. Low-magnification images were obtained for the fuel morphology within ±50 mm and outside the balloon region (see Section 6.3).

For the ICL#2 sample, whose burst opening had to be epoxied to prevent fuel falling out during movement of high-dose-rate samples to allow for shield-window maintenance, LECO hydrogen and oxygen samples were limited to those away from the epoxied region, which extended away from the burst opening into the balloon. The sectioning diagram for ICL#2 metallography is shown in Figure 178, along with a compressed view of the diametral strain profile to show the location of the burst midplane and the axial extent of the balloon region. LECO hydrogen and oxygen measurements were made at locations H_1 and H_2, both regions that contained no epoxy.

The ICL#3-sample sectioning diagram, along with the diametral strain profile, is shown in Figure 179. The sample fractured at three locations during handling: bending failure at A, impact failure at C, and failure due to removal of tape from the burst opening region at B. These locations were initially designated for metallography only. Following the handling failures, however, two of the surfaces were imaged by SEM for fractographic analysis. Not shown in the figure are the locations for LECO oxygen and hydrogen measurements.

The results from LECO hydrogen and oxygen measurements, the ECR determined from oxygen pickup from LECO and metallographic data, and the hydrogen pickup are emphasized because hydrogen and oxygen pickup have a significant influence on ductility. Figure 180 shows the LECO results for oxygen and hydrogen concentrations for the ICL#2 and ICL#3 test samples with axial locations referenced to the burst midplane. Equations 9-11 were used to convert the LECO data to oxygen pickup, ECR, and hydrogen pickup. The pre-test hydrogen and oxygen contents for high-burnup Limerick cladding (0.7-wt.% oxygen and 70-wppm hydrogen) were used in these calculations. The results are shown in Figure 181. The ECR determined from LECO and metallographic data are reasonably close. Based on a reasonable extrapolation of these two off-center locations, the maximum ECR for the ICL#3 sample is ≈18%. This value is in good agreement with the 20% CP-ECR for two-sided steam oxidation. The hydrogen pickup (maximum >3000 wppm) is as high as the values measured for unirradiated cladding. The hydrogen peaks are closer to the center of the burst region, consistent with the shorter axial extent of ballooning for the high-burnup cladding. However, the hydrogen pickup near the burst midplane is significantly larger for high-burnup cladding than for unirradiated cladding. The combination of high-hydrogen and high-oxygen pickup in most of the balloon region (±40 mm) suggests that the cladding should be quite brittle within this region. Recall that the unirradiated LOCA test samples had very low hydrogen pickup in the burst region.

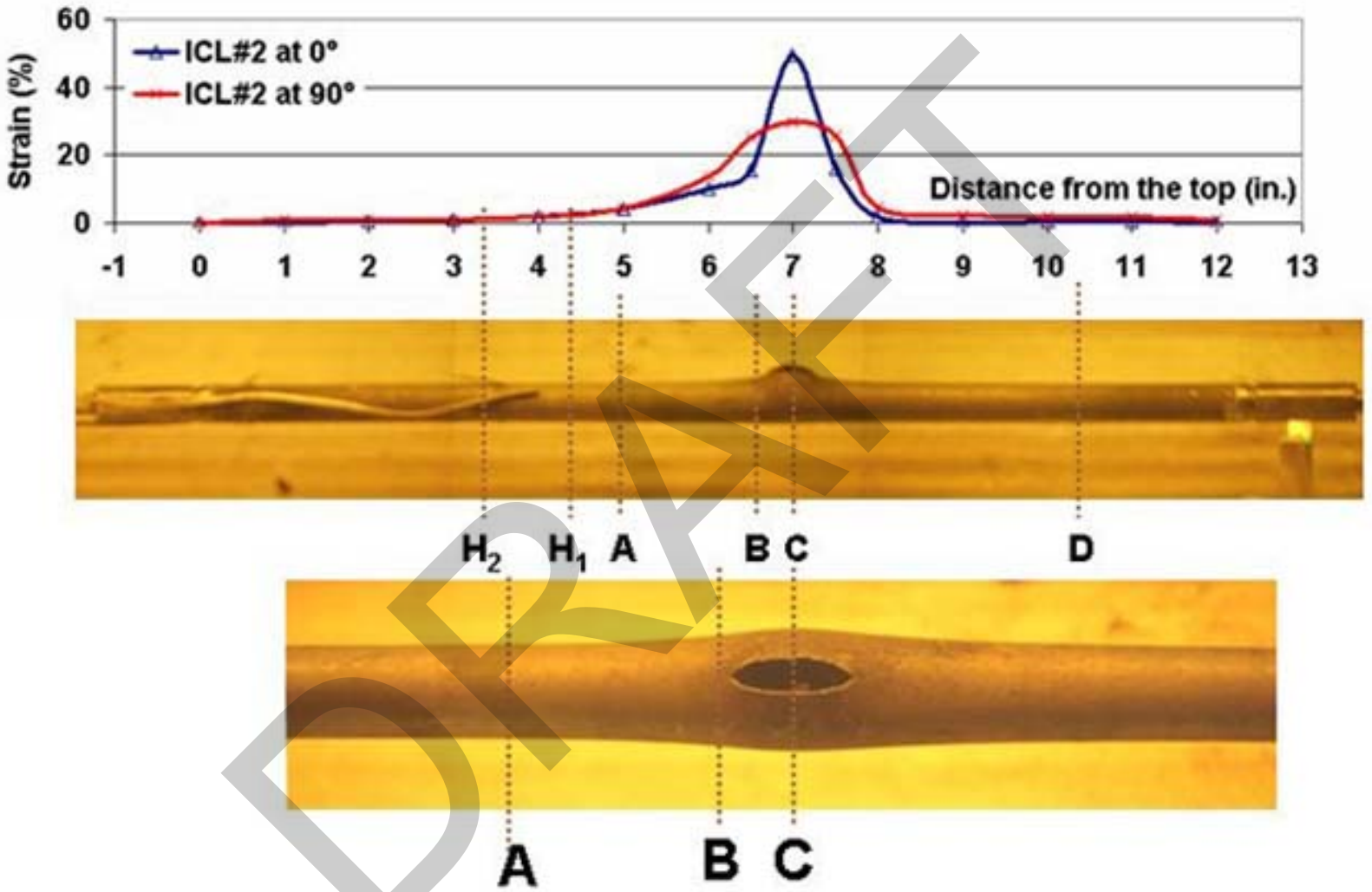

Figure 178. Sectioning diagram for ICL#2 (300 s at 1204ºC, slow cooling to RT) sample. Locations A, B, and C are metallography locations. H_1 and H_2 are locations for LECO hydrogen and oxygen measurements.

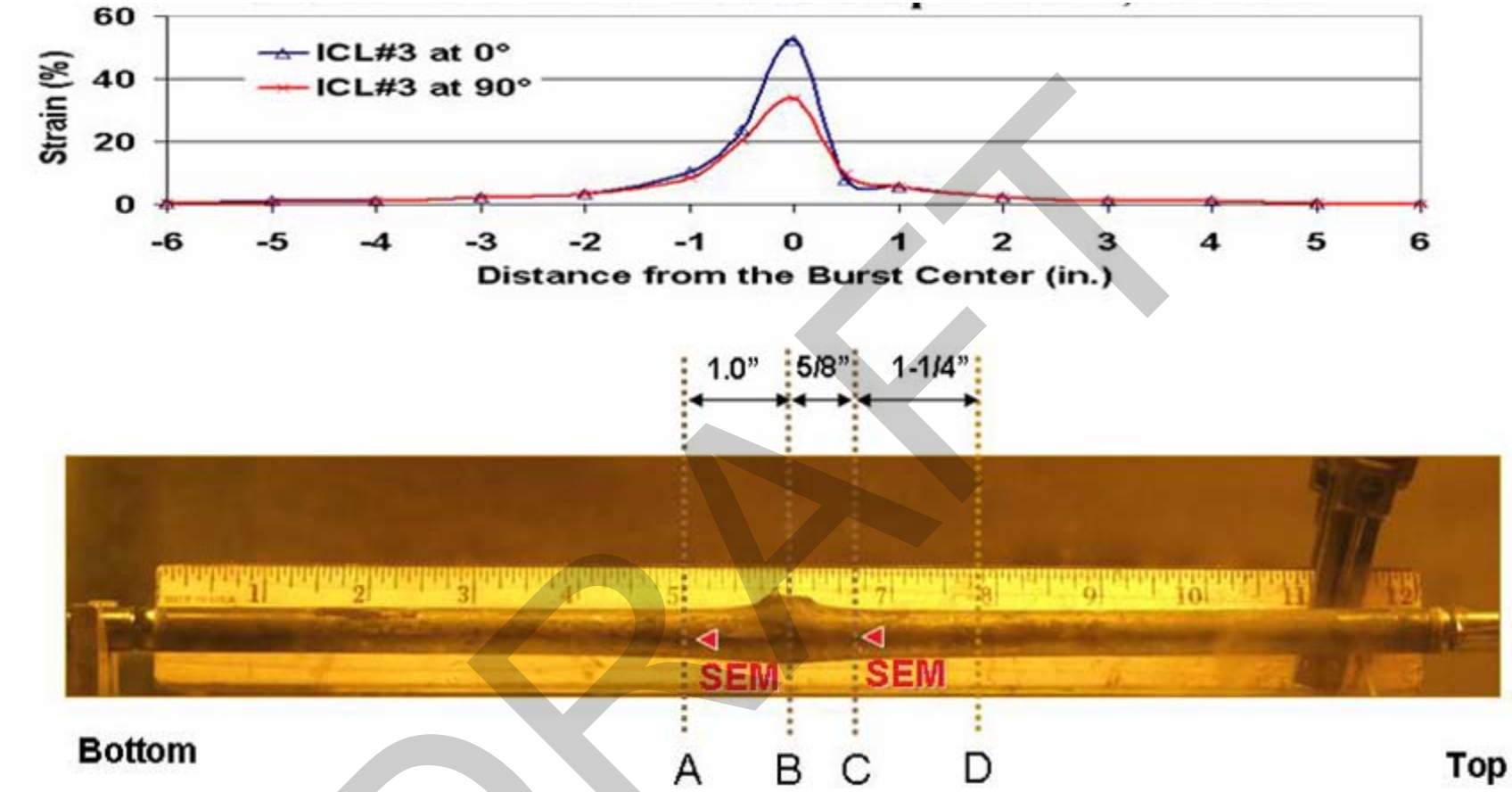

Figure 179. Sectioning diagram for ICL#3 (300 s at 1204ºC, quench from 800ºC to 460ºC, slow cooling to RT) sample. The sample fractured at locations A, B, and C during handling prior to the sectioning at D. LECO hydrogen and oxygen samples not shown.

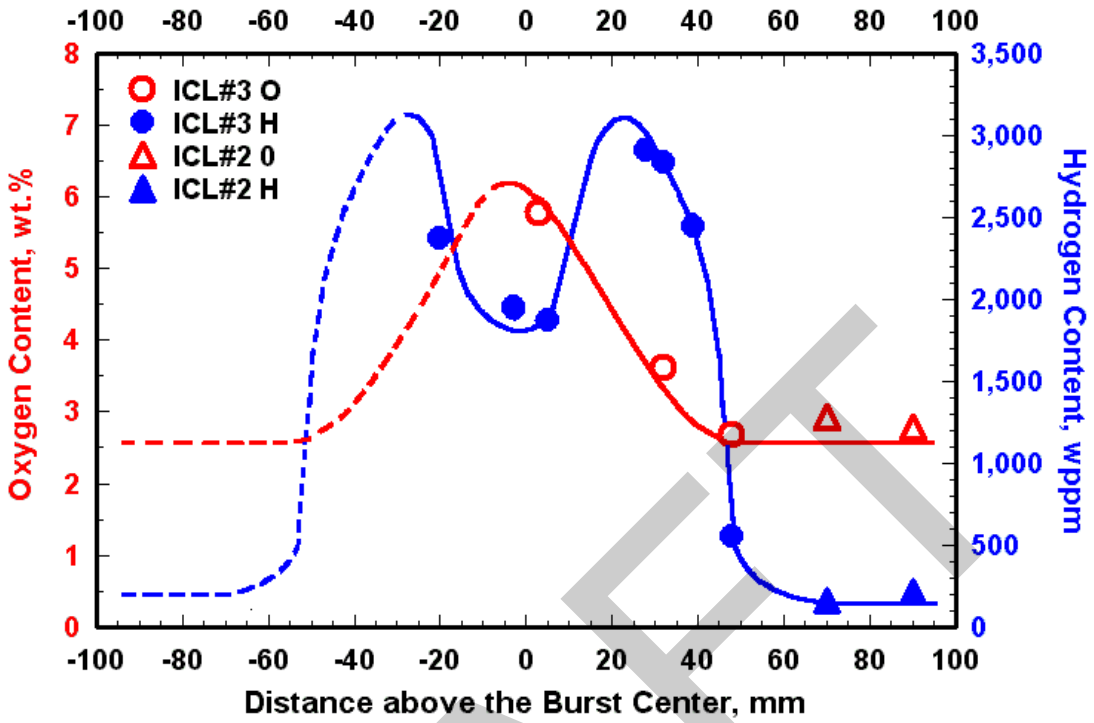

Figure 180. LECO oxygen-and hydrogen content for ICL#2 and ICL#3 test samples, both oxidized for 300 s at 1204ºC. Concentrations are referenced to the weight of the oxidized samples.

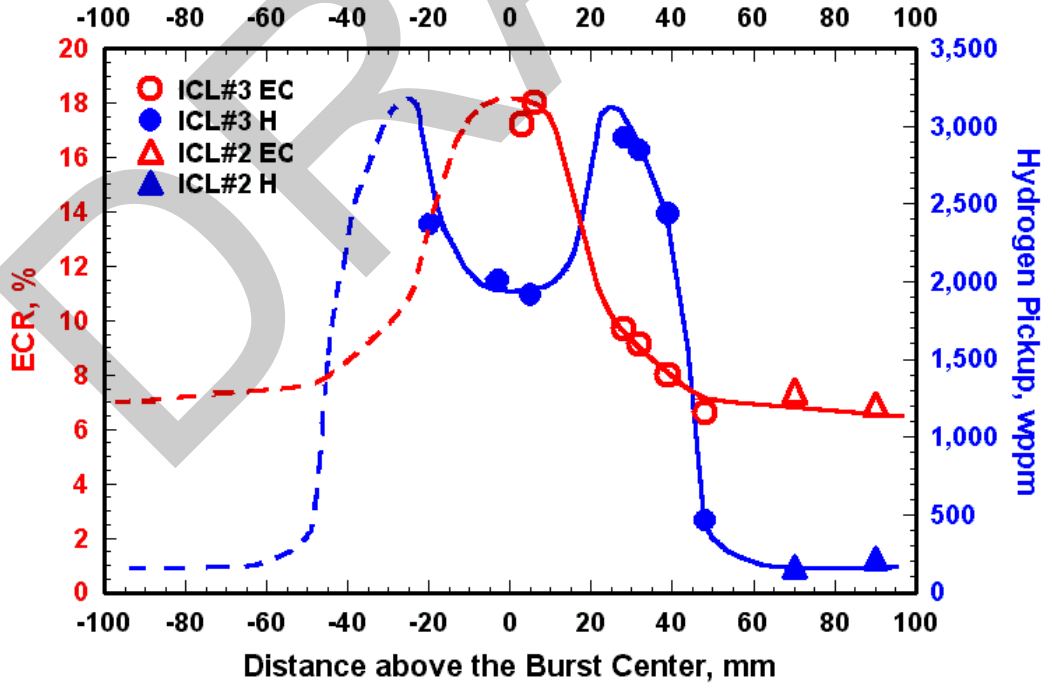

Figure 181. Axial distribution of ECR (based on LECO oxygen and metallographic data) and hydrogen pickup (based on LECO data in Figure 180) for ICL#2 and ICL#3 test samples.

6.2.3 Post-quench ductility of high-burnup samples

The LOCA test samples were not subjected to four-point-bend tests. However, based on optical microscopy and SEM imaging, along with hydrogen and oxygen pickup, embrittlement of these samples can be inferred. The SEM fractography was performed at two locations (A and C) of the ICL#3 test sample that failed during handling. The results for location C (≈20 mm above the burst midplane) are shown in Figure 182. The morphology of the fracture surface supports the contention that the ring-test failure was due to brittleness. Similar results were obtained at location A. Given the high combinations of ECR and hydrogen pickup at these locations (≈25 mm below the burst midplane for A), these locations would very likely have failed in a brittle mode even if they were tested at 135ºC.

It is encouraging that all four LOCA integral samples remained intact during and following quench. However, thermal stresses due to quench are relatively low. The samples were fixed at the top and free to expand and contract in the axial direction. If contraction during quench were partially constrained and/or if impact loads due to rod-to-rod contact during quench vibration were high enough to cause failure, then it is predicted that the failure mode would be brittleness. It is also predicted, based on ANL bend test results and JAEA axial constraint tests, that such loading would result in a clean break across the cladding wall, rather than fragmentation. Except for the highly oxidized cladding at the edges of the burst region, the brittle cladding within the balloon region does not appear to be susceptible to fragmentation for maximum CP-ECR values < 20%.

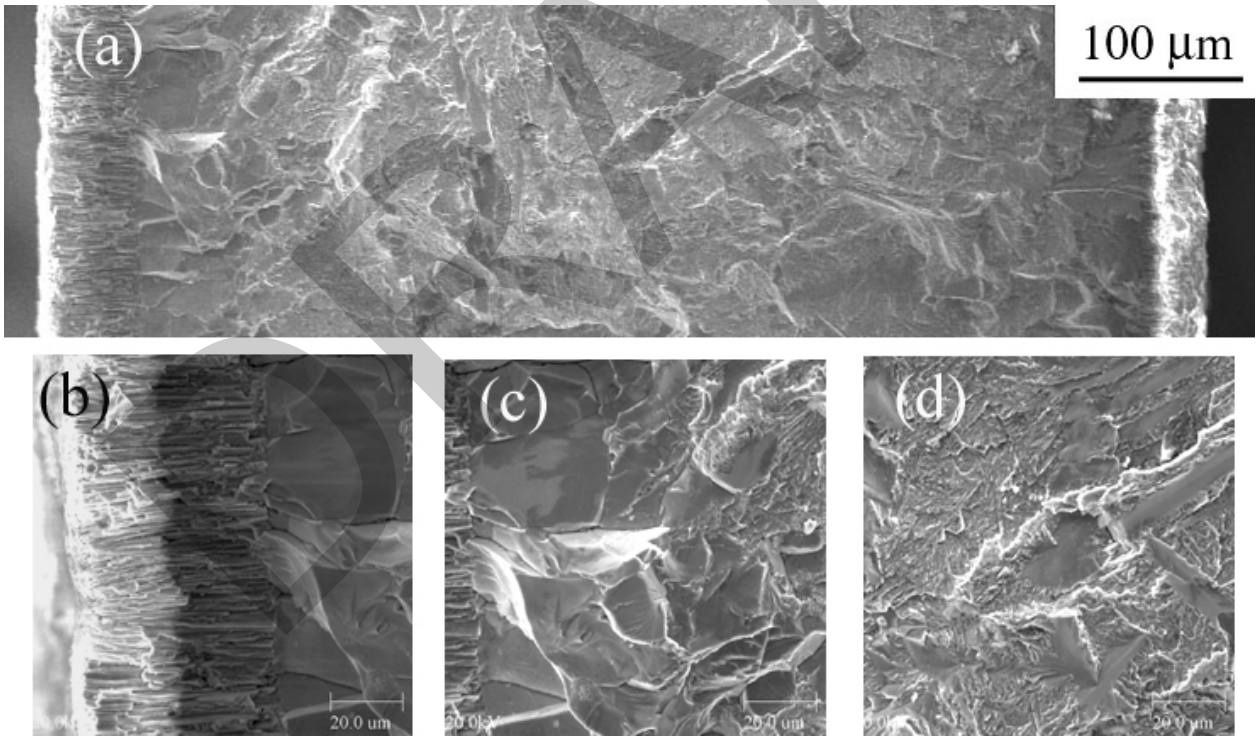

Figure 182. SEM fractography for ICL#3 samples at axial location C in Figure 179 (≈20 mm above the burst midplane): (a) cladding cross section, (b) oxide layer, (c) oxygen-stabilized alpha layer, and (d) prior-beta layer. Interpolating from the results in Figure 181, the estimated hydrogen pickup is ≈3000 wppm, and the estimated measured ECR is ≈10%.

6.3 Cladding inner-surface oxygen pickup from fuel-cladding bond and fuel

As shown in Figure 126, high-burnup Limerick cladding has a fuel-cladding bond thickness of 10±5 μm. For this BWR fuel, the bond thickness is not uniform around the inner surface of the cladding. For the one-sided oxidation tests with defueled Limerick cladding, Figure 126b shows that the bond layer remains after defueling in nitric acid. The minimum hold time at 1200ºC for the Limerick one-side oxidized samples was 300 s. Figure 183 shows one of eight micrographs taken at the midplane of the high-burnup Limerick sample oxidized for 300 s at 1200ºC. The post-test sample,shows no indication of an inner-surface bond-oxide layer or of the oxygen-stabilized alpha layer that would have formed during reduction of the bond layer. Based on the estimate in Section 5 that such a bond layer would be reduced after ≈100 s during the ramp from 300ºC to 1200C, oxygen from the alpha layer would have continued to diffuse into the beta layer until its oxygen content were too low to stabilize the alpha phase at 1200ºC. This observation is consistent with the results of the shorter-time HBRI one-sided oxidation tests.

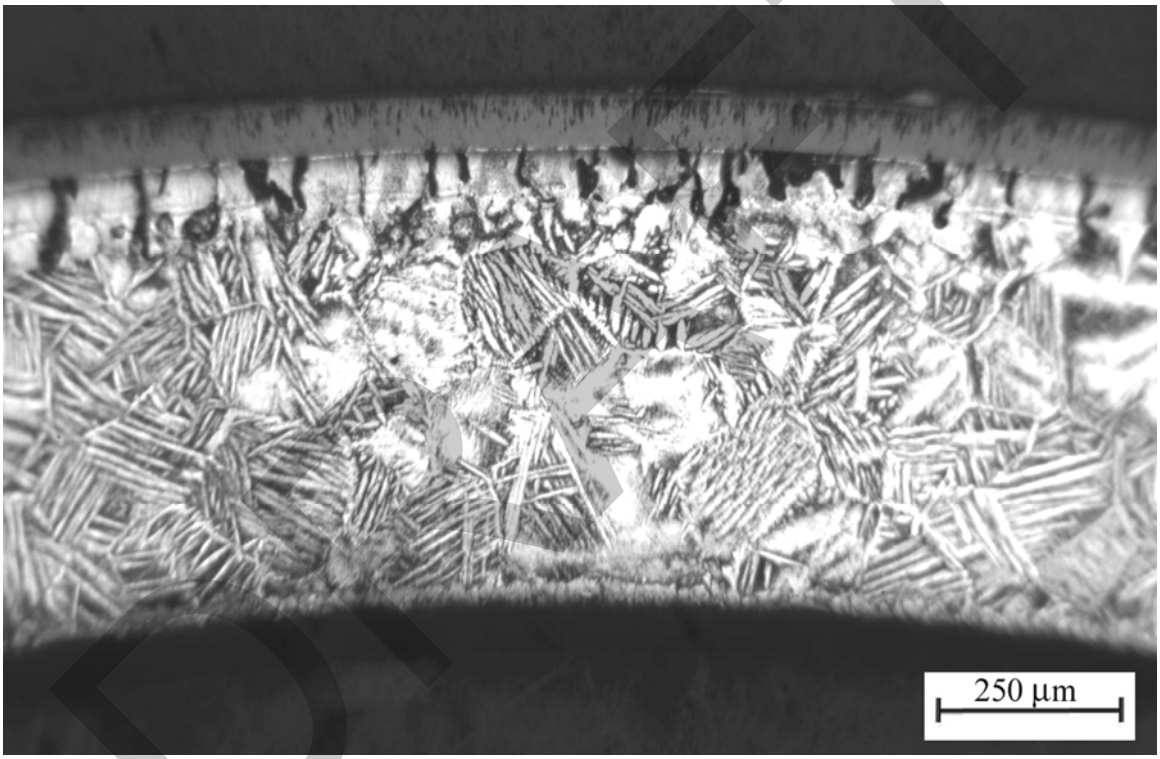

Figure 183. High-burnup Limerick oxidation sample following one-sided oxidation in steam at 1200ºC for a 300-s hold time.

The degree to which the Zircaloy metal will pick up oxygen from the fuel depends on how much fuel remains attached to the bond during the outward expansion of the cladding. The fuel-to-bond strength is greater than the fuel strength; thus, some fuel will remain bonded as the cladding deforms outward. Figure 184 shows one circumferential location at the burst midplane for the ICL#3 sample where there are chunks of fuel still bonded to the cladding. However, there is ample steam at this location to oxidize the cladding inner surface. The presence of this fuel does not appear to influence the growth of the high-temperature steam-oxide layer; the outer-surface oxide is about as thick as the inner-surface oxide.

The fuel morphology for the ICL#2 sample at locations 180 mm below (b) and 50 mm above (c) the burst midplane is shown in Figure 185 and compared to the fuel morphology of the as-irradiated rod (a). The cladding strain at 180 mm below the burst is <2%, while the cladding strain at 50 mm above is ≈5%. Most of the fuel appears to have pulled away from the cladding at 50 mm above the burst, while there is little change in fuel morphology at 180 mm below the burst region, which is outside the uniformly heated zone.

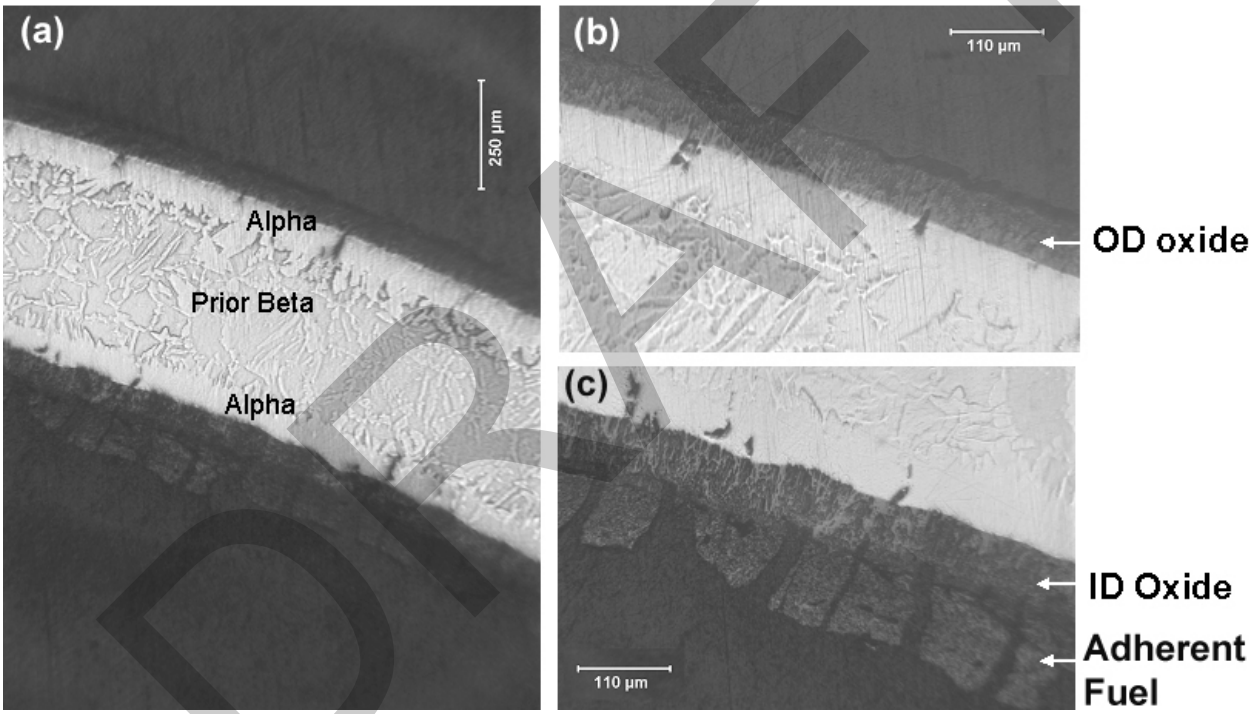

Figure 184. Metallographic results for a circumferential location at the burst midplane of the ICL#3 sample, oxidized for 300 s at 1204ºC. Fuel particles adherent to the cladding inner surface are shown in (c).

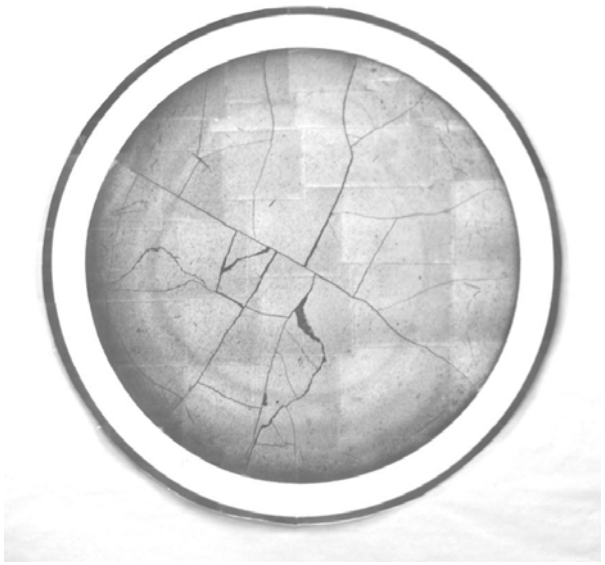

(a)

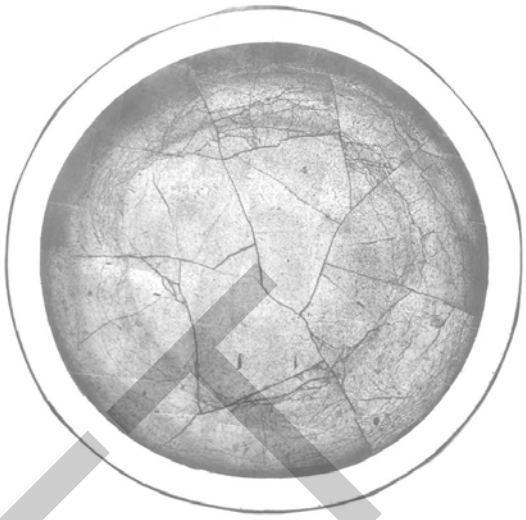

(b)

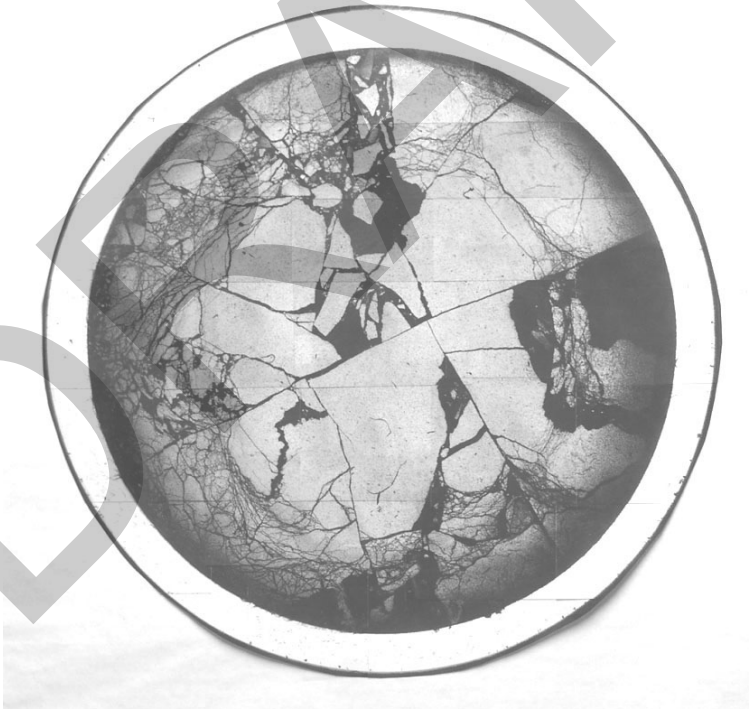

(c)

Figure 185. Fuel morphology for ICL#2 LOCA sample: (a) as-irradiated, pre-test condition; (b) post-test condition 180 mm below burst midplane; and (c) post-test condition at 50 mm above the burst midplane.

Except for local regions on the inner surface of the ICL#2 cladding, no oxygen-stabilized alpha layer is observed. This finding suggests that whatever oxygen has been picked up from the fuel-cladding bond layer and fuel particles or chunks adherent to the bond layer have been reduced after 300 s at 1200ºC near the edges of the balloon. One local area of oxygen-stabilized alpha found at 50 mm above the burst midplane for the ICL#2 sample (see Figure 185c for fuel morphology) is shown in Figure 186. Although this alpha layer could have been caused by local steam leakage, it is likely that it formed through oxygen pickup from the fuel.

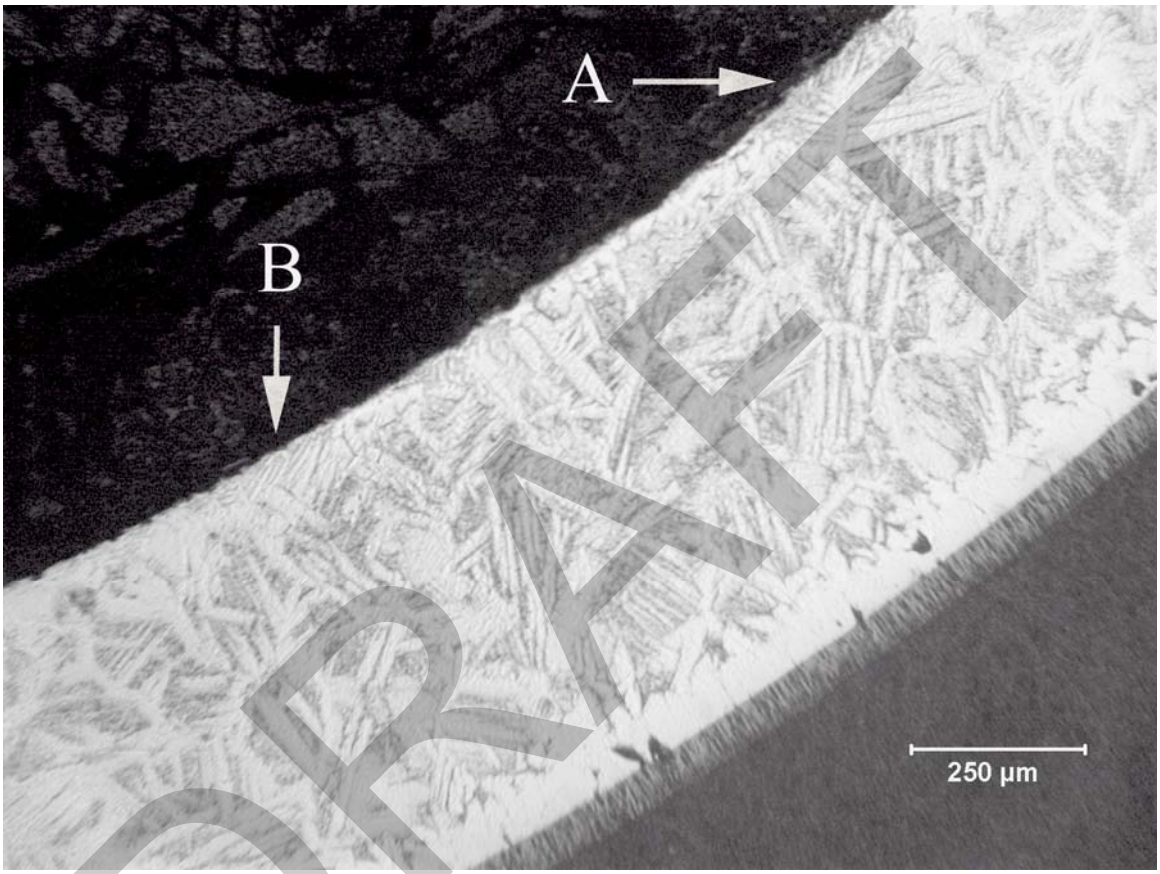

Figure 186. Evidence of local area on cladding inner surface of oxygen-stabilized alpha (B) for ICL#2 sample at 50 mm above the burst midplane. The inner-surface region indicated by "A" does not have such an alpha layer and is more typical of what is observed for most of the inner surface at this axial location.

Although the observations from the LOCA integral test samples are not substantial, it is well known that UO_2 fuel can be the source of oxygen for diffusion into the cladding metal. Hobbins and coworkers made such an observation in one of the Power-Coolant Mismatch tests in the Power Burst Facility [37]. In that test, in which the cladding collapsed onto the fuel, an ID alpha layer was observed. Hobbins et al. concluded that the thickness of the ID alpha layer was of comparable magnitude to the OD alpha layer that came from the reaction with steam. They also gave some evidence that this condition would only happen when hard contact exists between the cladding and the pellet.

Two years later, Hofmann and Politis [14] confirmed Hobbins et al. observations. Hofmann and Politis put fresh UO_2 pellets inside sealed unirradiated Zircaloy tubes and heated them in argon under various pressures. They found an ID alpha layer and also concluded that the uptake of oxygen due to the interaction with UO_2 was approximately as high as that by the reaction with steam. These tests confirmed that solid contact was necessary and that the rate of oxygen transport via the gas phase is too low.

Taken together, these observations support the schematic in Figure 5. The fact that the alpha layers near the ID are always about the same thickness as those observed near the OD when an ID oxygen source is present suggests that oxygen diffusion in the cladding metal is the rate-limiting step – provided the oxygen source is in intimate contact with the surface of the metal.

Typical analyses show no hard contact between fuel pellets and cladding during a LOCA transient at very low burnups, so ID oxygen pickup would not be expected in low-burnup fuel. However, fuel bonding occurs at high burnups after the fuel-to-cladding gap has been closed for a long time, and bonding appears to provide the intimate contact that is needed.

Bonding occurs earlier in PWR fuel than in BWR fuel because the higher system pressure in PWRs results in more cladding creep-down. Bonding between the fuel and the cladding eventually occurs in BWRs as well. From ANL characterization work performed for Limerick BWR high-burnup (57 GWd/MTU) fuel, Surry low-burnup (36 GWd/MTU) fuel, TMI-1 PWR intermediate-burnup (48 GWd/MTU), and H. B. Robinson PWR high-burnup (63-67 GWd/MTU) fuel, bonding (and hence ID oxygen ingress during a LOCA) appear to begin at ≈30 GWd/t in PWR fuel and be complete around ≈50 GWd/t, whereas it would not begin in BWRs until ≈40-50 GWd/t.

7 Conclusions and Recommendations

Six mechanisms for cladding embrittlement during a LOCA are described in Section 1. Data relevant to these mechanisms are summarized and evaluated in this section.

7.1 Beta-layer embrittlement of unirradiated cladding

Because diffusion of oxygen into metal is much faster at high temperatures than at low temperatures, oxygen-induced embrittlement in the beta layer occurs in much shorter times at high temperatures than at low temperatures. For as-fabricated cladding alloys, it was found that ductility and embrittlement threshold correlated better with oxidation levels calculated with the Cathcart-Pawel (CP) weight-gain correlation than with measured weight gain or best-estimate correlations for weight. This CP-predicted weight gain has been converted to CP-ECR in percent using Equations 5 or 6 for one- and two-sided oxidation, respectively.

At oxidation temperatures of 1000ºC and 1100ºC, the modern U.S. alloys tested did not experience embrittlement within the range of CP-ECR values (≤20%) investigated, even when tested at room temperature. The ANL criterion used to assess ductile vs. brittle behavior is ≥2% offset strain (determined from ring-compression load-displacement curves) implies ductile behavior and <2% offset strain implies brittle behavior. The 2% offset strain is based on the uncertainty determined both experimentally and analytically in the unloading slope just prior to failure (through-wall crack along the whole length of the 8±1 mm long ring).

As-fabricated cladding alloys do embrittle at ≤20% CP-ECR following oxidation at 1200ºC. Initially, these alloys were ring-compressed at room temperature, which is highly conservative relative to the calculated core temperature (135ºC or 275ºF) following LOCA-quench cooling. These alloys oxidized at 1200ºC were retested at 135ºC. Also, tests were interrupted following the first significant load drop (>30%), to allow a direct measurement of the diameter of the deformed sample in the loading direction. Based on the normalized diameter change, permanent strain could be measured directly for samples that failed with a single, tight through-wall crack. In general, these permanent strains were less than the offset strains within the ductile region. Based on an error analysis of the permanent strain measurements, rings exhibiting ≥1% permanent strain were characterized as ductile and rings with <1% permanent strain were classified as brittle. For load-displacement curves with a very rapid load drop of 80-100%, the rings cracked into multiple pieces (usually two), and it was not possible to measure post-test diameter. For these rings, the 2% offset strain criterion was used.

Table 70 summarizes the results for embrittlement threshold for cladding alloys oxidized at 1200ºC, quenched at 800ºC, and ring-compressed at 135ºC. For three of these alloys (17×17 Zry-4, ZIRLO and M5), additional tests were conducted with samples cooled without quench. The results indicate that the embrittlement threshold for these alloys is not sensitive to quench temperatures ≤800ºC. From Table 70, it can also be noticed that different batches of one alloy (Zry-4) exhibited a range of embrittlement thresholds (16-19%), whereas some batches of four different alloys (Zry-2, Zry-4, ZIRLO and M5) exhibited almost the same threshold (19-20%). These results suggest that the embrittlement threshold is sensitive to manufacturing variables, but no significant effects of alloy constituents on embrittlement thresholds were observed for the alloys tested in this program.

In order to generate the embrittlement threshold data in Table 70, numerous tests were conducted with each alloy. In general, alloys were oxidized at 5, 10, 13, 17 and 20% CP-ECR values. Additional

Table 70 Embrittlement Threshold (CP-ECR) for As-fabricated Cladding Alloys Oxidized at 1200ºC, Cooled at 11-13ºC/s to 800 ºC, Quenched at 800ºC and Ring-compressed at 135ºC. For CP-ECR values 1% higher than the embrittlement threshold, the alloys are classified as brittle. Results are rounded off to the nearest whole-number percent.

Alloy and Geometry	Manufacturer	Vintage	Embrittlement Threshold CP-ECR, %	Permanent (Offset) Strain, %
Zircaloy-4 15×15	Siemens	Old, Low Tin H.B. Robinson	16	1.1±0.4 (2.9±0.6)
Zircaloy-4 15×15	AREVA	Current Low Tin	19	1.5±0.3 (3.3±0.6)
Zircaloy-4 17×17	Westinghouse	Current Low Tin	17	1.1±0.4 (2.5±0.5
Zircaloy-2 10×10	Global Nuclear Fuel	Current ID Zr Liner	19	2.2 (3.3±0.4)
ZIRLO 17×17	Westinghouse	Current Standard Tin	19	1.1±0.1 (2.5±0.5)
M5 17×17	AREVA	Current	20	1.0 (3.5±0.4)

tests were then conducted in the range of 13-20% CP-ECR to better determine the embrittlement threshold based both on the strain criteria and the shapes of the strain vs. CP-ECR curves.

For all but one of the alloys listed in Table 70, the embrittlement threshold was determined based on the results of 2-to-3 ring-compression tests sectioned from one or two oxidation-quench samples at a given CP-ECR level. This approach is adequate for evaluating the embrittlement threshold for a number of different alloys. For HBR-type Zry-4, this scoping approach led to the conclusion that the embrittlement oxidation threshold was about 14% (14.3% based on interpolation of strain data at 13% and 15% CP-ECR). Additional tests were conducted with HBR-type Zry-4 samples oxidized at 1200ºC to 13-16% CP-ECR. Based on 6 sets of strain data at 15.2% CP-ECR and 8 sets of strain data at 16.0% CP-ECR, embrittlement was found to occur at 15.6% CP-ECR based on interpolation. Thus, the more statistically significant database let to an increase of 1.3% in embrittlement CP-ECR. Based on this experience, the uncertainty in the threshold oxidation levels for the other alloys listed in Table 70 can be taken as ±1%. For more precise (e.g., ±0.5%) determination of embrittlement threshold, the approach used for HBR-type Zry-4 is recommended.

Although the range of embrittlement thresholds listed in Table 70 is relatively narrow (17-20% for current alloys), the ductility vs. CP-ECR curves below the embrittlement threshold exhibited a wide spread from one cladding to another. As shown in Figure 48, current 17×17 Zry-4 showed a sharp decrease in ductility between 11 and 13% CP-ECR, while current 15×15 Zry-4 exhibited a sharp decrease in ductility between 13 and 15% CP-ECR. The 10×10 Zry-2 cladding exhibited a more gradual decrease in ductility with increasing CP-ECR up to the embrittlement threshold.

7.2 Beta-layer thinning of unirradiated cladding

Embrittlement due to beta-layer thinning will not occur if the time at temperature is sufficiently limited. Within the test times used in this experimental work, beta-layer thinning was not a limiting phenomenon. At 1200ºC, the beta-layer thickness at the ductile-to-brittle-transition CP-ECR ranged from 0.2 to 0.4 mm. Limiting the CP-ECR based on beta-layer embrittlement for oxidation at 1200ºC is sufficient to preclude embrittlement due to beta-layer thinning. For test temperatures of 1000ºC and 1100ºC, modern, belt-polished 17×17 alloys remained ductile at RT up to 20% CP-ECR with beta-layer thicknesses of 0.2-0.3 mm. For 1000ºC, limiting the time based on breakaway oxidation is sufficient to preclude embrittlement due to beta-layer thinning. For 1100ºC, neither oxygen-induced embrittlement nor breakaway oxidation appears to be limiting. Beta-layer thinning is the most likely embrittlement mechanism at 1100ºC. However, for all alloys tested, this limit would occur at CP-ECR values > 20%. Therefore, by limiting the CP-ECR based on ductility loss for 1200ºC oxidation, beta-layer thinning would not be a factor in cladding embrittlement. As pointed out in Ref. 1, beta-layer thinning does result in a decrease in strength and fracture toughness (as determined by impact tests). However, based on the results in the current study, post-quench ductility appears to be relatively insensitive to beta-layer thickness for ≥0.2-mm-thick prior-beta layers.

7.3 Localized embrittlement in a balloon

Current industry practice uses the average of an enlarged cladding diameter and a corresponding reduced wall thickness in a balloon to calculate two-sided oxidation of the cladding (and two-sided oxygen pickup). The calculated CP-ECR is then compared with a limiting value. As shown in Section 6.2.1, this procedure does not guarantee ductility in a balloon. Hydrogen absorption at the cladding inner surface is so pronounced that we have not found a practical limit that could be used to ensure ductility. This was observed for both fresh and high-burnup cladding.

Nevertheless, the current practice does limit oxygen concentrations in the balloon wall and maintains some material toughness. When this practice is used, as was seen in Sections 6.2 and 6.3, the cladding survived quenching without fracture. Also, the failure bending moment increases within the balloon region as the CP-ECR value decreases. Although this is a less conservative condition than retaining ductility, quench survival is an important step in maintaining a coolable geometry following a LOCA and is considered sufficient in licensing in some countries (e.g., Japan [40]).

7.4 Hydrogen-enhanced beta-layer embrittlement

Hydrogen, which enters the outer cladding surface during normal lifetime operation, increases oxygen solubility and pickup rate in the beta layer even at temperatures below 1200ºC. This reduces ductility compared with unirradiated cladding, as seen in Figure 187. For HBR-type Zry-4 oxidized at 1200ºC, about 550-wppm hydrogen in the cladding reduces the embrittlement threshold from 16% for fresh cladding to 8% for high-burnup cladding cooled without quench to ≈5% for high-burnup cladding quenched at 800ºC. The higher the hydrogen pickup during normal operation, the larger will be the decrease in embrittlement threshold. Embrittlement results for both prehydrided Zry-4 and high-burnup alloys (Zry-4, ZIRLO and M5) are summarized in the following.

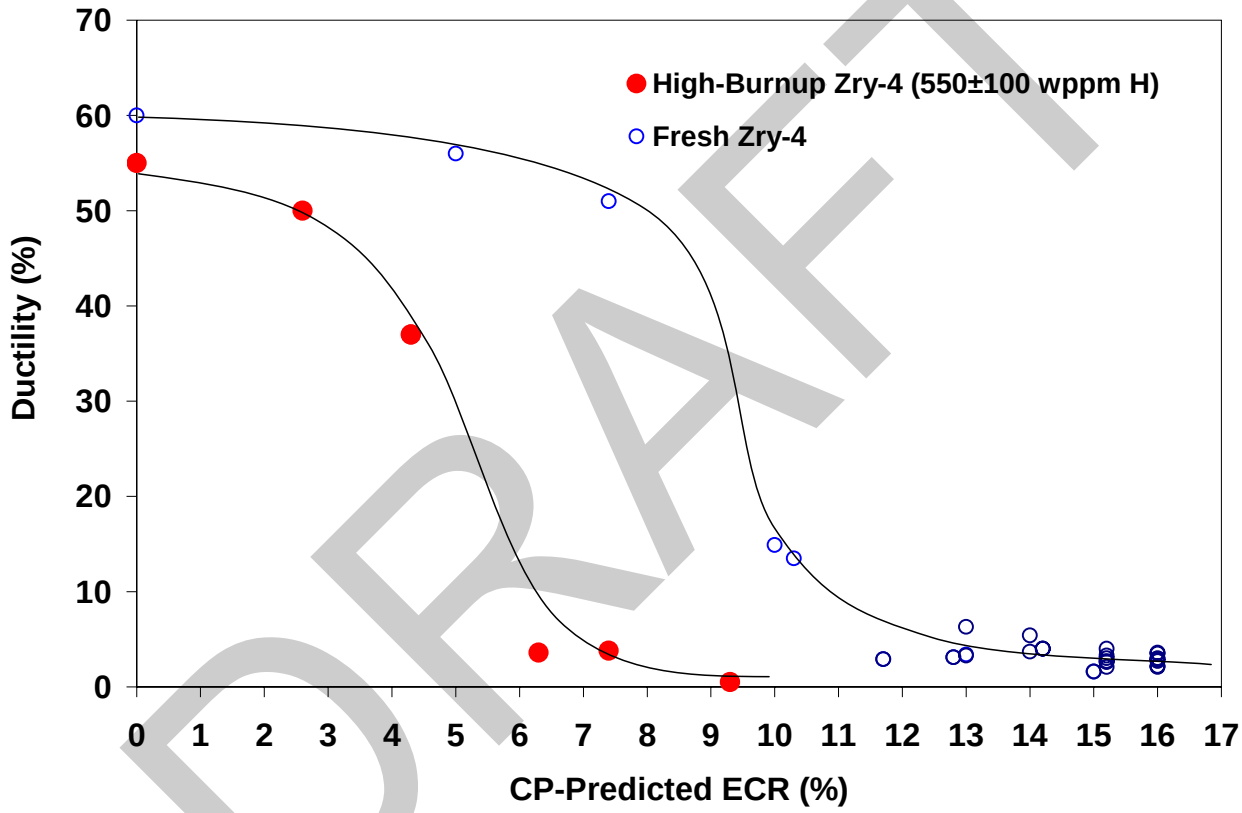

Figure 187. Offset strains for high-burnup Zry-4 (71-74 μm corrosion-layer thickness) and as-fabricated (fresh) HBR-type 15×15 Zry-4. Cladding samples were two-side oxidized at ≈1200ºC and cooled at ≈11ºC/s to 800ºC. As-fabricated samples were quenched at 800ºC, while the high-burnup samples were slow cooled from 800ºC to RT.

Hydrogen-enhanced embrittlement for prehydrided Zry-4

Numerous LOCA embrittlement tests were conducted with prehydrided 17×17 Zry-4 and 15×15 HBR-type Zry-4 to map out regions of hydrogen concentration and oxidation levels resulting in embrittlement. Most of the tests were conducted using prehydrided HBR-type Zry-4 because more of this material was available. Ductility tests were performed for 1200ºC-oxidized samples, which were cooled at ≈11ºC/s to 800ºC and either quenched at 800ºC, further cooled with quench at 600ºC and 700ºC, or cooled from 800ºC without quench. No ductility enhancement was observed by lowering the quench temperature from 800ºC to 600ºC. A small, but significant, enhancement in ductility was observed for samples cooled without quench. The data sets in Section 4 were used to generate Figure 188, which shows the oxidation threshold for embrittlement vs. average hydrogen content in the samples. The samples used in these tests were prehydrided with relatively low circumferential variations (less than ±30 wppm) in hydrogen concentration. A few tests were conducted with samples exhibiting higher variation (±100 wppm) in hydrogen content in the circumferential direction. Based on average hydrogen content, it was anticipated that these samples would be ductile. However, the samples with 510±100 wppm hydrogen and 610±100 wppm hydrogen were brittle at 5.2% CP-ECR and 4.7% CP-ECR, respectively. Two major findings in this work are: high-burnup cladding with >500 wppm average hydrogen content generally has large circumferential variation (±100 wppm) in hydrogen content; and hydrogen does not diffuse fast enough in the presence of oxygen to homogenize in the circumferential direction during the short LOCA transients leading to embrittlement. More testing would be needed to determine the effects of circumferential variation in hydrogen content on the embrittlement threshold.

Hydrogen-enhanced embrittlement for high-burnup alloys

Determining the embrittlement threshold vs. hydrogen content for high-burnup cladding is very challenging because the average hydrogen content varies with axial location over short distances, the circumferential variation in hydrogen can be as high as ±100 wppm (Zry-4 and ZIRLO), and the measured pre-test hydrogen can be 100 wppm higher (ZIRLO) than the post-test measured hydrogen. For practical reasons, testing of high-burnup cladding was initiated with a series of tests cooled without quench to map out the ductility vs. oxidation level. This allowed determination of the ductile-to-brittle transition oxidation level for oxidation at 1200ºC and cooling without quench. Based on the results shown in Figure 188, this transition level should be higher than the transition level for samples quenched at 800ºC. The results helped to focus the tests with quench to within a narrow CP-ECR range. Table 71 and Figures 189 and 190 summarize the results of these studies.

For high-burnup (64 GWd/MTU) H. B. Robinson Zry-4, tests were conducted in the AGHCF. Based on tests conducted without quench, the transition CP-ECR oxidation level was determined to be 8% for samples with 550±100 wppm (see Figure 188). Only one quench test was performed, but the hydrogen (740±100 wppm) and the oxidation (7.7% CP-ECR) levels were above the embrittlement threshold. No additional quench tests were conducted with this alloy. However, based on the results for prehydrided HBR-type Zry-4, the embrittlement threshold for this high-burnup alloy cooled with quench at 800ºC can be estimated to be 5% CP-ECR.

High-burnup ZIRLO (70 GWd/MTU) and M5 (63 GWd/MTU) cladding samples were tested in a beta-gamma cell in the Irradiated Materials Laboratory. Based on the results of three tests, the embrittlement threshold for high-burnup ZIRLO with 670±40 wppm pretest hydrogen and 540±100 wppm post-test hydrogen was determined to be 9%. Based on three tests cooled with quench at 800ºC, the embrittlement threshold was determined to be 5% for samples with 620±100 wppm pretest hydrogen and about 540±100 wppm post-test hydrogen. For ZIRLO, it appears that about 100 wppm of hydrogen

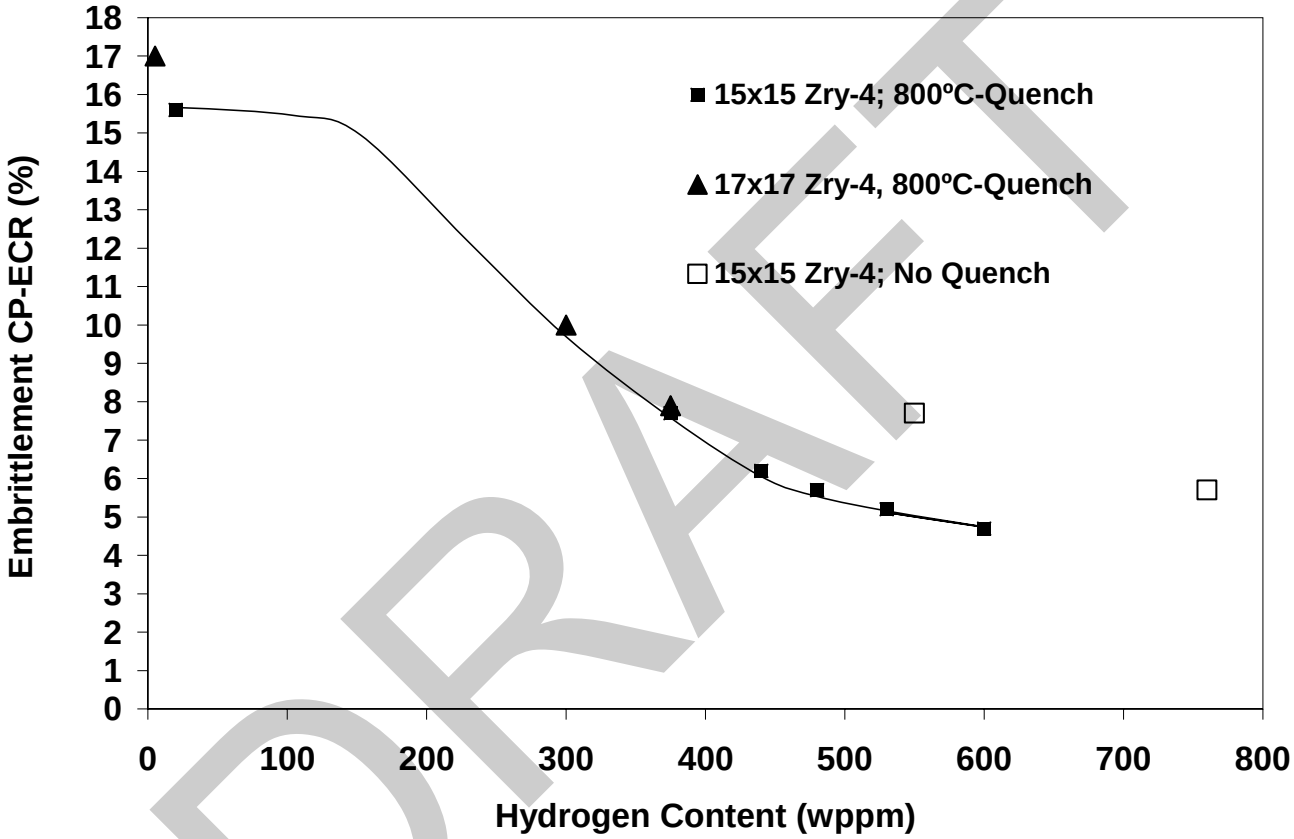

Figure 188. Embrittlement oxidation level (CP-ECR) vs. hydrogen content for 17×17 Zry-4 and 15×15 HBR-type Zry-4 oxidized at ≤1200ºC, cooled at 11-13ºC/s to 800ºC and quenched. Results for samples with large circumferential distributions in hydrogen content (±100 wppm) are not included in this figure.

Table 71 Embrittlement Threshold (CP-ECR) for High-burnup Cladding Alloys Oxidized at ≤1200ºC, Cooled at 11-13ºC/s to 800ºC, and either Quenched (Q) at 800ºC or cooled without quench. Ring-compression tests were performed at 135ºC. For CP-ECR values 1% higher than the embrittlement threshold, the alloys are brittle. Results are rounded off to the nearest whole-number percent. SC = slow cooling without quench.

High-Burnup Alloy	Hydrogen Content, wppm		Cooling	Maximum Temperature ºC	CP-ECR, %
	Pretest	Post-test			
H. B. Robinson	550±100	---	SC	1200	8
15×15 Zry-4			Q	1180	5
North Anna	670±40	540±100	SC	1200	9
17×17 ZIRLO	620±140	540±100	Q	1162	5
Ringhals	110±10	110±10	SC	1200	18
17×17 M5	110±10	140±15	Q	1200	15±1

may be in the corrosion layer (40-45 μm thick). Hydrogen in the corrosion layer would be released to the flowing steam during the LOCA transient and it would not contribute to embrittlement. For high-burnup M5 with 110±100 wppm, the transition CP-ECR values were determined to be 18% without quench and 15±1% with quench.

The best-linear-fit lines drawn in Figures 189 and 190 are intended as a guide for the reader. More data at additional hydrogen levels would be needed to establish the shape of the embrittlement threshold vs. hydrogen curve.

Prehydrided cladding vs. high-burnup cladding

The ductility and embrittlement data generated for prehydrided HBR-type Zry-4 were very useful in pretest planning and post-test analysis for LOCA testing of high-burnup HBR Zry-4. In Figure 146, it is demonstrated that the ductility of both materials is comparable for similar hydrogen concentrations and oxidation levels when both materials are cooled without quench. The embrittlement thresholds for prehydrided and high-burnup Zry-4 are also comparable for oxidation samples cooled without quench. This is shown in Figure 191, which simply adds the one data point for high-burnup Zry-4 to Figure 188. We are unable to make the same comparison for samples cooled with quench at 800ºC. The one high-burnup Zry-4 sample cooled with quench had a high hydrogen concentration (740 wppm) and a relatively high CP-ECR (7.5%). The fact that the sample was brittle under these conditions is consistent with the data for prehydrided Zry-4. However, many more tests would be needed to assess the adequacy of using prehydrided cladding as a surrogate for high-burnup cladding.

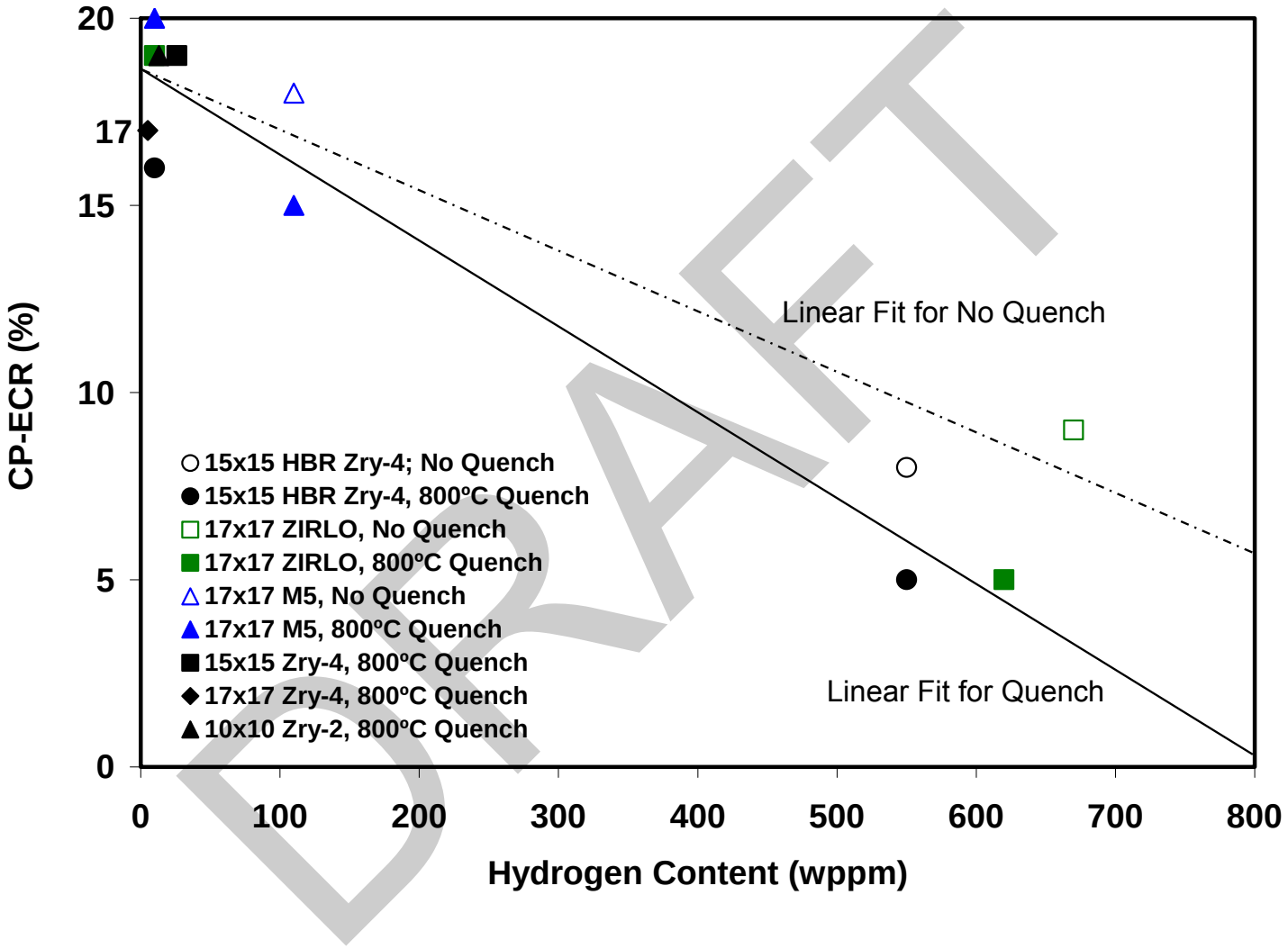

Figure 189. Embrittlement oxidation level (CP-ECR) vs. pre-test hydrogen content for high-burnup 15×15 Zry-4, 17×17 ZIRLO and 17×17 M5 oxidized at ≤1200ºC, cooled at 11-13ºC/s to 800ºC and either quenched or cooled without quench.

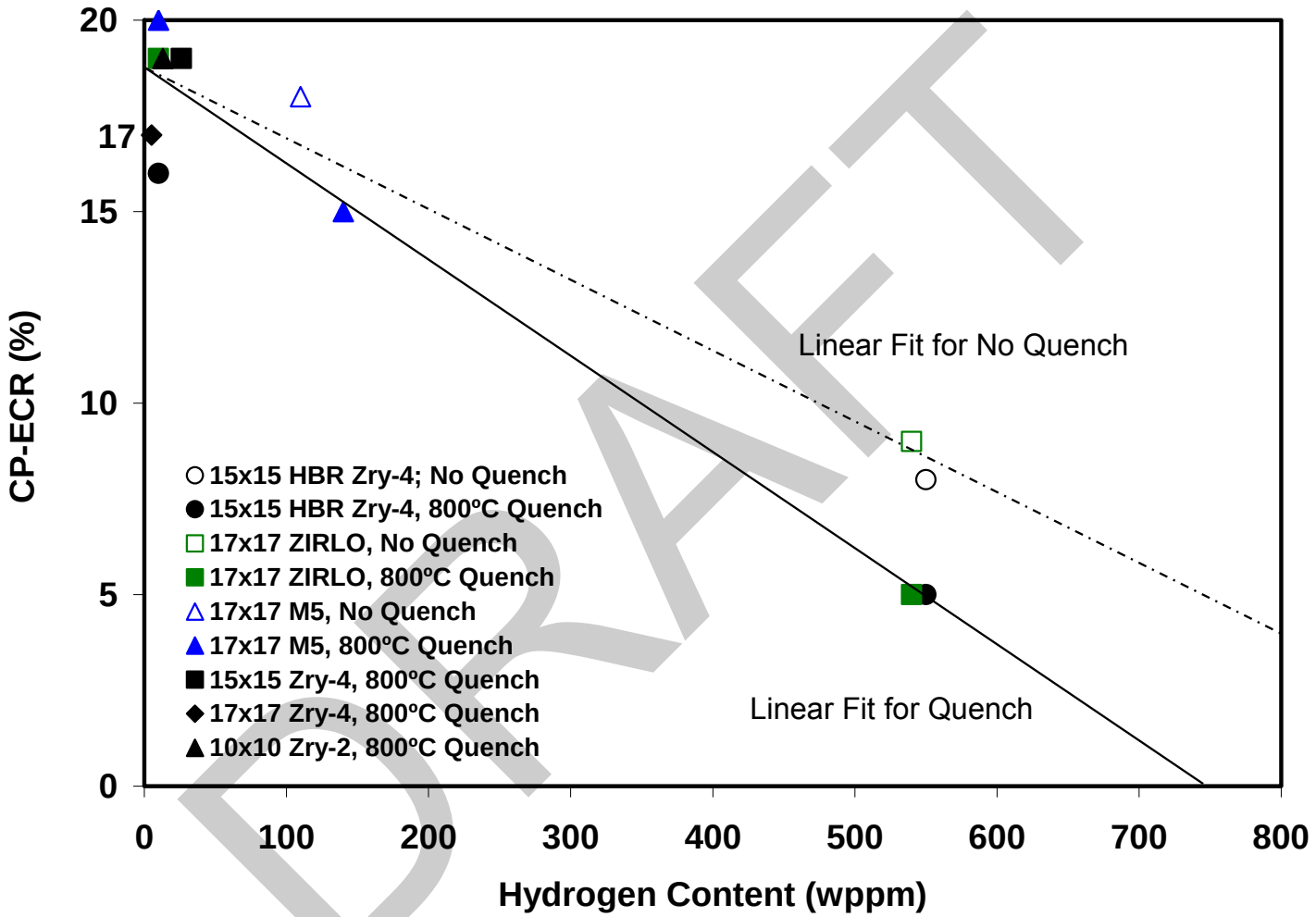

Figure 190. Embrittlement oxidation level (CP-ECR) vs. post-test hydrogen content for high-burnup 15×15 Zry-4, 17×17 ZIRLO and 17×17 M5 oxidized at ≤1200ºC, cooled at 11-13ºC/s to 800ºC and either quenched or cooled without quench.

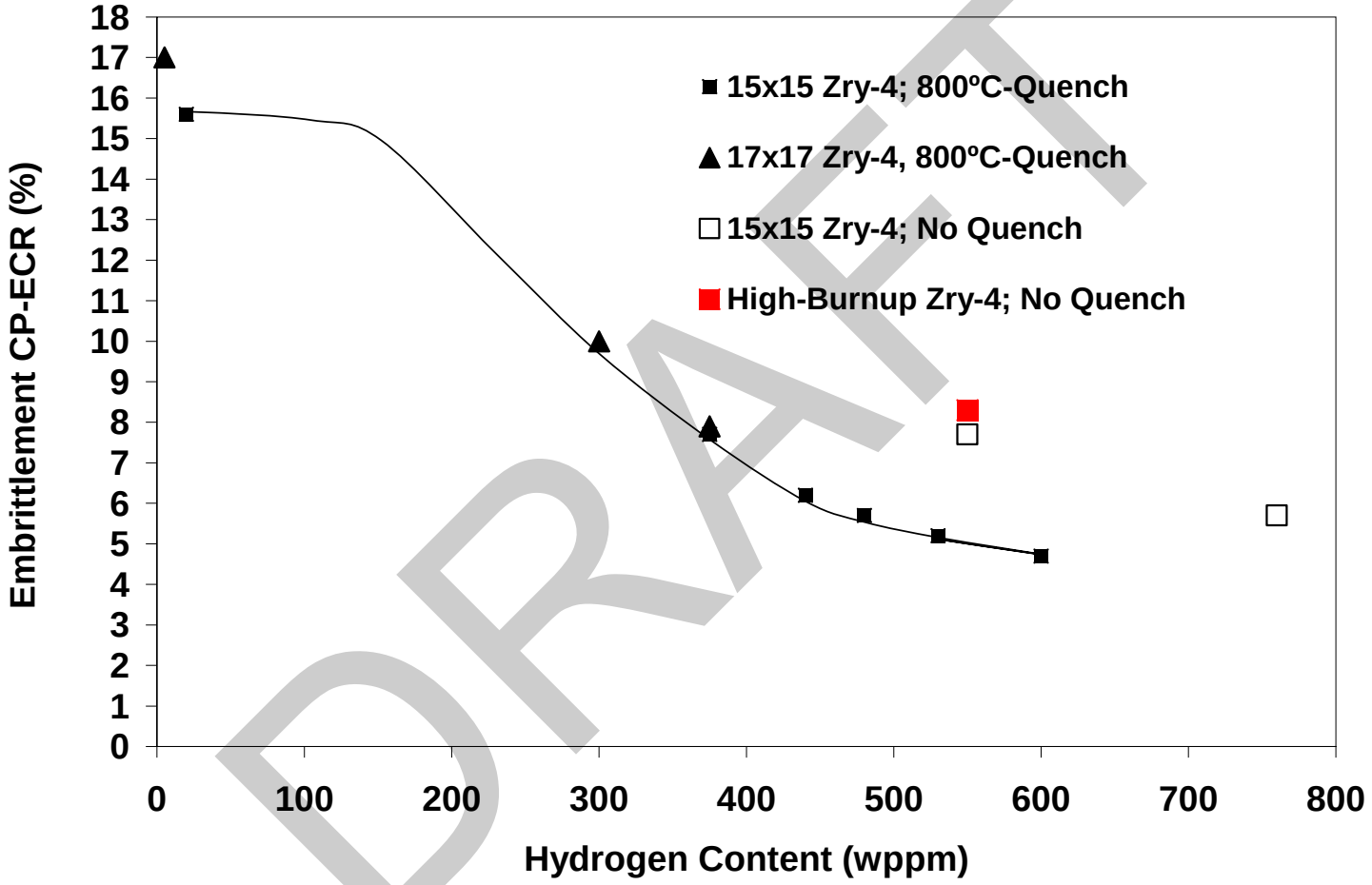

Figure 191. Embrittlement oxidation level (CP-ECR) vs. hydrogen content for high-burnup HBR Zry-4 and prehydrided 17×17 Zry-4 and 15×15 HBR-type Zry-4 oxidized at ≤1200ºC, cooled at 11-13ºC/s to 800ºC and either quenched or cooled without quench.

7.5 Breakaway oxidation

Figure 29 indicates that the minimum time for breakaway oxidation in Zircaloy-4 occurs around 1000ºC. The picture is about the same for other cladding alloys, but the minimum does not always occur exactly at 1000ºC. Nevertheless, the minimum can be found by searching in the neighborhood of 1000ºC, and the minimum time can be determined by using a hydrogen pickup concentration of 200 wppm as the threshold for breakaway. There is another temperature range (around 775ºC) with relatively low breakaway times. However, the oxidation rate is very slow at the lower temperatures, as is the hydrogen generation rate, and it takes a much longer time after breakaway oxidation to pick up 200 wppm of hydrogen. Although this lower temperature region should be characterized, the time for embrittlement at ≈775ºC would probably not be higher than the time to embrittle at ≈1000ºC.

Diffusion of oxygen in the metal is of course very slow at lower temperatures. Further, there will be no beta material in any of these zirconium-tin-niobium alloys at temperatures below about 650ºC because that is the lowest phase transition temperature of the alloys. Hence, a relatively low concentration of oxygen will remain in solution in the alpha-phase metal below 650ºC, and the cladding will remain ductile. It should not be necessary to consider temperatures below the phase transition. Therefore, if the total time spent above 650ºC is less than the measured breakaway time described above, breakaway will not occur.

Tables 20, 23, 29, and 36 indicate that the minimum breakaway times for belt-polished Zry-4, Zry-2, ZIRLO, and M5 are about 5000, >5000, 3000, and 6000 seconds, respectively. It is also seen from Table 18 that older rough-surface Zry-4 has a breakaway time of about 3800 seconds. Breakaway oxidation times may be important for some small-break LOCAs with lower oxidation temperatures and much longer oxidation times above 650ºC. On the other hand, the breakaway time for E110 can be seen in Figure 9 to be only about 500-700 seconds, which is much shorter than the duration of small-break LOCAs.

7.6 Oxygen pickup from the cladding inside diameter (ID)

The ID oxygen pickup can be accounted for in an analysis rather than with criteria *per se*. Because ID oxygen pickup is already accounted for within the ballooned region using the current industry practice, we need only modify the analysis for cladding locations away from a balloon to account for the more general ID oxygen pickup in high-burnup fuel.

For fresh cladding that experiences LOCA conditions, there is no oxygen pickup from the cladding ID away from the balloon, and Equation 5 for one-sided oxidation will give the appropriate CP-ECR. For moderate-to-high burnup fuel, however, oxygen pickup at the inner cladding surface will be bounded by the oxygen pickup due to steam oxidation. Thus, two-sided oxidation will give a reasonable upper bound on the transient CP-ECR to be compared to the transient CP-ECR limit.

The exact burnup for a transition from Equation 5 to Equation 6 is not well defined. For burnups above 30 GWd/MT in PWRs and 40 GWd/MT in BWRs, there will be some fuel-to-cladding bonding, which indicates some ID oxygen pickup will occur during a LOCA. By 50 GWd/MT for PWRs (60 GWd/MT for BWRs), fuel bonding is likely to be well developed, and ID oxygen pickup from the bond and fuel may be as high as the OD oxygen pickup from flowing steam.

7.7 Recommendations

During the course of this investigation, interesting phenomena were discovered that may be worth further investigation to thoroughly understand these phenomena and to determine their relevance to cladding behavior during and following LOCA-type transients, as well as embrittlement limits.

7.7.1 Circumferential and axial variations in hydrogen content

Variation of hydrogen content across the radius of the cladding (hydride rim effect) and over short axial distances (pellet-pellet interface effect) has been observed by many investigators. Based on studies using prehydrided Zry-4 with dense hydride rims, it has been demonstrated that at temperatures ≥900ºC, there is a very rapid homogenization of hydrogen across the radius of the cladding due to the affinity of the beta phase for hydrogen, as well as the high solubility of hydrogen in this phase. However, most studies reported in the literature are for prehydrided cladding samples with relatively uniform hydrogen content in the circumferential and axial directions.

In the Argonne work, significant circumferential variation (±100-140 wppm) in hydrogen content has been measured (by LECO vacuum fusion) and observed (by optical microscopy) for high-burnup Zry-4 and ZIRLO. For oxidation test times at 1200ºC up to the embrittlement CP-ECR level, no significant diffusion of hydrogen in the circumferential direction was observed. Hydrogen-concentration variations of 450 to 750 wppm measured for cladding quarter-segments prior to LOCA testing remained after LOCA testing. The same behavior was observed for prehydrided Zry-4 oxidized under similar LOCA conditions. In addition, axial variations of ±50 wppm along 25-mm-long prehydrided LOCA samples were measured both before and after LOCA testing.

Additional testing could be performed to assess the effects of circumferential variation in hydrogen content on the embrittlement threshold.

7.7.2 Embrittlement oxidation level as a function of hydrogen content for high-burnup cladding

Additional tests could be performed to determine the shape of the embrittlement oxidation level vs. hydrogen content. It is recommended that these tests be performed with high-burnup ZIRLO cladding. Within the uniform-burnup region of high burnup ZIRLO rods, the corrosion layer varies from about ≈20-70 μm. The samples tested in this program had corrosion level thicknesses of about 40-45 μm. Cladding samples with lower and higher corrosion levels should give a wide range of hydrogen contents. Testing of these samples would certainly add valuable embrittlement data points between 110 wppm (M5) and 550 wppm (in Zry-4 and ZIRLO metal), as well as possible data points above 550 wppm.

7.7.3 Assessment of prehydrided cladding as a surrogate for high-burnup cladding

In parallel to the tests recommended in 7.7.2, a series of tests could be performed using prehydrided ZIRLO with the same average hydrogen content as the high-burnup samples tested. The prehydriding can be performed to generate samples with relatively uniform hydrogen concentrations, as well as samples with large circumferential variations in hydrogen to address the recommendation in 7.7.1.

7.7.4 Sensitivity of breakaway oxidation to sample preparation and test conditions

Breakaway oxidation is an instability phenomenon that may be sensitive to sample preparation and test conditions. In order to standardize such testing, additional tests would be needed to determine the sensitivity of results to sample length and cleaning, steam flow rates, heating ramp rate and method, and circumferential temperature variation. As shown in Table 19, breakaway oxidation was observed to occur for belt-polished 15×15 Zry-4 at 5000 s for 985ºC oxidation temperature in the standard 686-mm-long quartz-tube test chamber used to test all the cladding alloys in this program. However, when the same material was retested under these conditions using a shorter (610-mm-long) test chamber, no breakaway was observed at test times as high as 5400 s. This could mean that repeated tests (minimum of 5) may be needed and/or subtle differences in test conditions affect the results. Similar results were obtained using ZIRLO test samples, which exhibited breakaway oxidation at 3000 s for 970ºC oxidation temperature in the longer test train but exhibited no breakaway at 4000 s for 970ºC in the shorter test train.

In addition, Westinghouse has an independent data set indicating that ZIRLO breakaway oxidation time for 950-1000ºC oxidation is >4400 s. Westinghouse and Argonne used different sample cleaning methods, different furnaces (resistance-heating vs. radiant-heating), and different temperature control and monitoring. It is recommended that these differences be evaluated before breakaway oxidation tests are standardized.

References

1. G. Hache and H. M. Chung, "The History of LOCA Embrittlement Criteria," NUREG/CP-0172, May 2001, pp. 205-237.

2. L. Yegorova, K. Lioutov, N. Jouravkova, A. Konobeev, V. Smirnov, V. Chesanov, and A. Goryachev, "Experimental Study of Embrittlement of Zr-1%Nb VVER Cladding under LOCA-Relevant Conditions," NUREG/IA-0211, Mar. 2005.

3. *Annual Book of ASTM Standards*, "Standard Specification for Wrought Zirconium Alloy Seamless Tubes for Nuclear Reactor Fuel Cladding," Vol. 02.04 (1997).

4. R. J. Comstock, G. Schoenberger, and G. P. Sabol, "Influence of Processing Variables and Alloy Chemistry on the Corrosion Behavior of ZIRLO Nuclear Fuel Cladding," *Zirconium in the Nuclear Industry: Eleventh International Symposium, ASTM STP 1295,* E. R. Bradley and G. P. Sabol, Eds., American Society for Testing and Materials, 1996, pp. 710-725.

5. W. J. Leech, "Ductility Testing of Zircaloy-4 and ZIRLO™ Cladding after High Temperature Oxidation in Steam," NEA/CSNI/R(2001)18, Dec. 2001, pp. 135-143.

6. J.-P. Mardon, D. Charquet, and J. Senevat, "Influence of Composition and Fabrication Process on Out-of-Pile and In-Pile Properties of M5 Alloy," *Zirconium in the Nuclear Industry: Twelfth International Symposium, ASTM STP 1354,* G. P. Sabol and G. D. Moan, Eds., American Society for Testing and Materials, West Conshohocken, PA, 2000, pp. 505-524.

7. P. V. Shebaldov, M. M. Peregud, A. V. Nikulina, Y. K. Bibilashvilli, A. F. Lositski, N. V. Kuz'menko, V. I. Belov, and A. E. Novoselov, "E1110 Alloy Cladding Tube Properties and Their Interrelation with Alloy Structure-Phase Condition and Impurity Content," *Zirconium in the Nuclear Industry: Twelfth International Symposium, ASTM STP 1354,* G. P. Sabol and G. D. Moan, Eds., American Society for Testing and Materials, West Conshohocken, PA, 2000, pp. 545-559.

8. O. Kubaschewski, *Metallurgical Thermochemistry*, Pergamon Press, Oxford, 1967.

9. James P. Coughlin, "Contributions to the Data on Theoretical Metallurgy," XII, *Heats and Free Energies of Formation of Inorganic Oxides*, U.S. Government Printing Office, 1954.

10. G. M. O'Donnell, H. H. Schott, and R. O. Meyer, "A New Comparative Analysis of LWR Fuel Designs," NUREG-1754, Nov. 2001.

11. L. Yegorova, K. Lioutov, N. Jouravkova, O. Nechaeva, A. Salatov, V. Smirnov, A. Goryachev, V. Ustinenko, and I. Smirnov, "Experimental Study of Narrow Pulse Effects on the Behavior of High Burnup Fuel Rods with Zr-1%Nb Cladding and UO_2 Fuel (VVER type) under Reactivity-Initiated Accident Conditions: Program Approach and Analysis of Results," NUREG/IA-0213, Vol. 1, May 2006.

12. L. Baker and L. C. Just, "Studies of Metal-Water Reactions at High Temperatures; III. Experimental and Theoretical Studies of the Zirconium-Water Reaction," ANL-6548, May 1962.

13. J. V. Cathcart, R. E. Pawel, R. A. McKee, R. E. Druscel, G. J. Yurek, J. J. Cambell, and S. H. Jury, "Zirconium Metal-Water Oxidation Kinetics IV. Reaction Rate Studies," ORNL/NUREG-17, Aug. 1977.

14. P. Hofmann and C. Politis, "Chemical Interaction Between Uranium Oxide and Zircaloy-4 in the Temperature Range Between 900 and 1500˚C," *Zirconium in the Nuclear Industry (Fourth Conference),* ASTM STP 681, American Society for Testing and Materials, West Conshohocken, PA, 1979, pp. 537-560.

15. Y. Yan, R. V. Strain, T. S. Bray, and M. C. Billone, "High Temperature Oxidation of Irradiated Limerick BWR Cladding," NUREG/CP-0176, May 2002, pp. 353-372.

16. D. O. Hobson, "Ductile-Brittle Behavior of Zircaloy Fuel Cladding," *Proc. ANS Topical Meeting on Water Reactor Safety*, Salt Lake City, Mar. 26, 1973, pp. 274-288.

17. D. O. Hobson and P. L. Rittenhouse, "Embrittlement of Zircaloy-Clad Fuel Rods by Steam during LOCA Transients," ORNL-4758, Jan. 1972.

18. H. M. Chung and T. F. Kassner, "Pseudobinary Zircaloy-Oxygen Phase Diagram," J. Nucl. Matls. 84 (1979) 327-339.

19. S. Leistikow and G. Schantz, "The Oxidation Behavior of Zircaloy-4 in Steam between 600 and 1600˚C," Werkstoffe und Korrosion 36 (1985) 105-116.

20. S. Leistikow and G. Schanz, "Oxidation Kinetics and Related Phenomena of Zircaloy-4 Fuel Cladding Exposed to High Temperature Steam and Hydrogen-Steam Mixtures under PWR Accident Conditions," Nucl. Eng. and Des. 103 (1987) 65-84.

21. J. P. Mardon, J. C. Brachet, L. Portier, V. Maillot, T. Forgeron, A. Lesbros, and N. Waeckel, "Influence of Hydrogen Simulating Burn-Up Effects on the Metallurgical and Thermal-Mechanical Behavior of M5™ and Zircaloy-4 Alloys under LOCA Conditions," ICONE13-50457, *13th Intl. Conf. on Nucl. Eng.*, Beijing, China, May 16-20, 2005, pp. 1-9.

22. Y. Yan, R. V. Strain, and M. C. Billone, "LOCA Research Results for High-Burnup BWR Fuel," NUREG/CP-0180, Mar. 2003, pp. 127-155.

23. B. Cheng and R. B. Adamson, "Mechanistic Studies of Zircaloy Nodular Corrosion," *Zirconium in the Nuclear Industry: Seventh International Symposium, ASTM STP 939,* R. B. Adamson and L. F. P. Van Swam, Eds., American Society for Testing and Materials, Philadelphia, 1987, pp. 387-416.

24. B. Cheng, H. A. Levin, R. B. Adamson, M. O. Marlowe, and V. L. Monroe, "Development of a Sensitive and Reproducible Steam Test for Zircaloy Nodular Corrosion," *Zirconium in the Nuclear Industry: Seventh International Symposium*, *ASTM STP 939,* R. B. Adamson and L. F. P. Van Swam, Eds., American Society for Testing and Materials, Philadelphia, 1987, pp. 257-283.

25. A. V. Nikulina, L. N. Andreeva-Andrievskaya, V. N. Shishov, and Yu. V. Pimenov, "Influence of Chemical Composition of Nb Containing Zr Alloy Cladding Tubes on Embrittlement under Conditions Simulating Design Basis LOCA," presentation at the *14th Intl. Symp. on Zirconium in the Nuclear Industry*, Stockholm, Sweden, June 13-17, 2004.

26. R. E. Pawel, R. A. Perkins, R. A. McKee, J. V. Cathcart, G. J. Yurek, and R. E. Druschel, "Diffusion of Oxygen in Beta-Zircaloy and the High Temperature Zircaloy-Steam Reaction," *Zirconium in the Nuclear Industry, ASTM STP 633,* A. L. Lowe, Jr. and G. W. Parry, Eds., American Society for Testing and Materials, 1977, pp. 119-133.

27 J. P. Mardon, "Impact of the LOCA Cooling Rates and Pre-corrosion Layer on the Cladding Residual Ductility: Main Learnings from the Recent CEA Experiments," presented at the ACRS Reactor Fuels Subcommittee Meeting, Rockville, MD, July 27, 2005.

28. V. Maillot, J. C. Brachet, J. P. Mardon, A. Lesbos, and N. Waeckel, "Recent CEA Data on the Influence of the Cooling Scenario after Oxidation at 1200ºC on the Post-quench Mechanical Behavior of Pre-hydrided Low Tin Zy-4 (~600 wppm H)," presented at the ANL LOCA Program Review Meeting, Argonne, IL, June 8, 2006.

29. J. C. Brachet, L. Portier, J. Hivroz, D. Hamon, T. Guilbert, T. Bedel, P. Yvon, J. P. Mardon, and P. Jacques, "Influence of Hydrogen Content on the α/β Phase Transformation Temperature and on the Thermal-Mechanical Behavior of Zy-4, M4 (ZrSnFeV), and M5TM (ZrNbO) Alloys During the First Phase of LOCA Transient," *Zirconium in the Nuclear Industry, ASTM STP 1423,* G. D. Moan and P. Rudling, Eds., American Society for Testing and Materials, 2002, pp. 673-701.

30. E. J. Ruzauskas and K. N. Fardell, "Design, Operation, and Performance Data for High Burnup PWR Fuel from the H. B. Robinson Plant for Use in the NRC Experimental Program at Argonne National Laboratory," 1001558, Electric Power Research Institute, Palo Alto, CA (2001).

31. L. F. Van Swam, G. M. Bain, W. C. Dey, D. D. Davis, and H. Heckermann, "BWR and PWR Fuel Performance at High Burnup," *Proceedings of the 1997 Intl. Topical Meeting on LWR Fuel Performance,* Portland, Oregon, March 2-6, 1997, pp. .

32. H. Tsai and M. C. Billone, "Characterization of High-Burnup PWR and BWR Rods, and PWR Rods after Extended Dry-Cask Storage," NUREG/CP-0180, Mar. 2003, pp. 157-168.

33. L. F. Van Swam, A. A. Strasser, J. D. Cook, and J. M. Burger, "Behavior of Zircaloy-4 and Zirconium Liner Zircaloy-4 Cladding at High Burnup," *Proceedings of the 1997 Intl. Topical Meeting on LWR Fuel Performance,* Portland, OR, March 2-6, 1997, pp. 421-431.

34. K. Une, K. Nogita, S. Kashibe, T. Toyonaga, and M. Amaya, "Effect of Irradiation-Induced Microstructural Evolution on High Burnup Fuel Behavior," *Proceedings of the 1997 International Topical Meeting on LWR Fuel Performance*, Portland, OR, March 2-6, 1997.

35. Y. Yan, T. Burtseva, and M. C. Billone, "LOCA Results for Advanced-Alloy and High-Burnup Zircaloy Cladding," NUREG/CP-0185, June 2004, pp. 97-121.

36. Yong Yan, Michael C. Billone, Tatiana A. Burtseva, and Hee M. Chung, "LOCA Integral Test Results for High-Burnup BWR Fuel," NUREG/CP-0192, Oct. 2005, pp. 138-158.

37. R. R. Hobbins, G. R. Smolik, and G. W. Gibson, "Zircaloy Cladding Behavior during Irradiation Tests under Power-Cooling-Mismatch Conditions," *Zirconium in the Nuclear Industry,* ASTM STP 633, A. L. Lowe and G. W. Parry, Eds., American Society for Testing and Materials, 1977, pp. 182-208.

38. B. E. Boyack, A. T. Motta, K. L. Peddicord, C. A. Alexander, J. G. M. Andersen, J. A. Blaisdell, B. M. Dunn, D. Ebeling-Koning, T. Fuketa, G. Hache, L. E. Hochreiter, S. E. Jensen, S. Langenbuch, F. J. Moody, M. E. Nissley, K. Ohkawa, G. Potts, J. Rashid, R. J. Rohrer, J. S. Tulenko, K. Valtonen, N. Waeckel, and W. Wiesenack, "Phenomenon Identification and Ranking Tables (PIRTs) for Loss-of-Coolant Accidents in Pressurized and Boiling Water Reactors Containing High Burnup Fuel," NUREG/CR-6744, Dec. 2001.

39. M. E. Nissley, C. Frepoli, and K. Ohkawa, "Realistic Assessment of Fuel Rod Behavior under Large-Break LOCA Conditions," NUREG/CP-0192, Oct. 2005, pp. 231-273.

40. Fumihisa Nagase and Toyoshi Fuketa, "Results from Studies on High Burn-up Fuel Behavior under LOCA Conditions," NUREG/CP-0192, Oct. 2005, pp. 197-230.

41. F. Nagase and H. Uetsuka, "Hybride Morphology and Hydrogen Embrittlement of Zircaloy Fuel Cladding used in NSRR/HBO Experiment," Proc. 1997 International Topical Meeting on LWR Fuel Performance, Portland, OR, March 2-6, 1997, American Nuclear Society, pp. 677-684.